1-2021

An Experimental Study of Evaporites on Titan: Implications for Lake Composition and Future Missions

Ellen Czaplinski
University of Arkansas, Fayetteville

Citation

Czaplinski, E. (2021). An Experimental Study of Evaporites on Titan: Implications for Lake Composition and Future Missions. *Graduate Theses and Dissertations* Retrieved from https://scholarworks.uark.edu/etd/4165

An Experimental Study of Evaporites on Titan: Implications for Lake Composition and Future Missions

A dissertation submitted in partial fulfillment
of the requirements for the degree of
Doctor of Philosophy in Space and Planetary Sciences

by

Ellen Czaplinski
Purdue University
Bachelor of Science in Planetary Science, 2016

July 2021

This dissertation is approved for recommendation to the Graduate Council.

Vincent Chevrier, Ph.D.
Dissertation Director

Larry Roe, Ph.D.
Committee Member

Colin Heyes, Ph.D.
Committee Member

Timothy Kral, Ph.D.
Committee Member

ABSTRACT

Titan is the only other planetary body in the solar system with liquid on the surface. With a surface temperature and pressure of 89 – 94 K and 1.5 bar (N_2), respectively, Titan's lakes are comprised of liquid hydrocarbons, predominantly methane and ethane. Over time, Titan's lakes may evaporate, leaving behind residual deposits (evaporites). The evaporation processes and composition of the evaporites is poorly understood. I address these outstanding questions by experimentally investigating the physical and spectral properties of evaporites at Titan surface conditions using an experimental chamber.

Chapter 1 addresses the formation of ethylene evaporites. Ethylene evaporites form more quickly with pure methane, because methane readily evaporates at Titan surface conditions. Ethylene absorption bands at 1.630 and 2.121 μm are redshifted after evaporite formation. These results imply that ethylene is a good candidate for Titan's evaporites, although they may be restricted to methane-dominated lakes/seas.

Chapter 2 addresses the ability to detect the formation of the acetylene-benzene co-crystal using FTIR spectroscopy. The co-crystal is easily identifiable upon formation at ~135 K, as evidenced by drastic spectral band shifts, several new bands in the C-H stretching and combination bands regions, and clear morphological changes of the sample. The co-crystal is stable down to Titan temperatures (90 K). Studying co-crystal formation provides insights into co-condensation in Titan's atmosphere, and evaporite formation and composition.

Chapter 3 investigates the formation of evaporites with acetonitrile. Acetylene and acetonitrile form a co-crystal between 118 – 174 K, which is stable down to 90 K. New bands at 1.676 μm and morphological changes to the sample confirm co-crystal formation. We observe new shapes to NIR absorptions that were not previously present in pure component experiments.

These results have implications for astrobiologically relevant co-crystals and where nitrile compounds may accumulate on Titan.

Chapter 4 addresses more complex evaporite experiments (“binary” experiments) with two evaporite molecules combined. Acetylene is the most prominent species in these experiments, and the acetylene-acetonitrile co-crystal is stable before, during, and after methane evaporation. These results and future binary experiments can help assess the validity of evaporite models, and represent a more realistic view of evaporite solutions.

ACKNOWLEDGEMENTS

This work was funded by the NASA Earth and Space Science Fellowship grant #80NSSC17K0603. Personal stipend was awarded by the 2020 Zonta International Amelia Earhart Fellowship. Additional funding and support was awarded and provided by the Arkansas Space Grant Consortium, and the University of Arkansas Summer Research Fellowship.

I would first like to thank my doctoral research advisor, Dr. Vincent Chevrier, for formulating this research project idea and working with me on it throughout graduate school. I would like to thank the remainder of my committee members, Dr. Larry Roe, Dr. Colin Heyes, and Dr. Timothy Kral for their continued support of this research. Additionally, I would like to thank all of my co-authors for their invaluable scientific contributions to my publications.

I would like to specifically thank Walter Graupner Jr., Dr. Kendra Farnsworth, Dustin Laxton, Dr. Sandeep Singh, and Katherine Dzurilla, for their assistance and support with the Titan chamber. Further, I would like to thank Dr. Sara Port for her unwavering support, assistance, and encouragement throughout my graduate career.

Additionally, I would like to thank Dr. Briony Horgan and Dr. David Minton at Purdue University for encouraging me to pursue my planetary science career through undergraduate research and guiding me into graduate school.

Finally, I would like to thank my husband, Woody Gilbertson, for his love and devotion to me while also pursuing his doctorate degree; my parents, siblings, parents-in-law, and grandparents for their love, support, and enthusiasm throughout graduate school; my friends for their encouragement and understanding; and my dogs, Bekka, Daisy, Claira, Gemma, Luna, Stella, Angela, and Heidi for their emotional support during all of my endeavors.

TABLE OF CONTENTS

CHAPTER PUBLICATION STATUS

Published Articles

Chapter 1. Experimental Study of Ethylene Evaporites under Titan Conditions

Czaplinski, E. C., Gilbertson, W. A., Farnsworth, K. K., & Chevrier, V. F. (2019). Experimental Study of Ethylene Evaporites under Titan Conditions. *ACS Earth and Space Chemistry*, *3*, 2353-2362. DOI:10.1021/acsearthspacechem.9b00204

Chapter 2. Experimental Investigation of the Acetylene–Benzene Cocrystal on Titan

Czaplinski, E. C., Yu, X., Dzurilla, K., Chevrier, V. (2020). Experimental Investigation of the Acetylene–Benzene Cocrystal on Titan. *The Planetary Science Journal, 1,* 16pp. DOI:10.3847/PSJ/abbf57

INTRODUCTION

1. Science Background

Titan is Saturn's largest moon, the second largest moon in the solar system, and the only moon in the solar system with a significant atmosphere. The first spacecraft flyby of Titan was *Pioneer 11* (1979), which confirmed Titan's physical properties including mass, temperature, and atmospheric haze. After the *Pioneer 11* mission, the *Voyager 1* and *2* probes (1980 and 1981, respectively) made the next Titan flybys, determining the density, composition, and atmospheric temperature, as well as more precise mass measurements and images of Titan's haze layer (Bell, 2015). However, Titan's thick atmospheric haze prevented direct imaging of the surface by *Voyager 1*.

Later, in 2004, the *Cassini-Huygens* mission (*Cassini* orbiter built by the National Aeronautics and Space Agency (NASA) and *Huygens* atmospheric probe built by the European Space Agency, ESA) revealed Titan's mysterious surface for the first time using RADAR (Elachi et al., 2004), the Imaging Science Subsystem (ISS; Porco et al., 2004), and the Visual and Infrared Mapping Spectrometer (VIMS; Brown et al., 2004). These radar images obtained from a flyby in 2006 show lakes of liquid hydrocarbons (primarily CH_4 and C_2H_6; Stofan et al., 2007), which marked the first discovery of vast quantities of liquid on a body in the solar system aside from Earth. The *Huygens* probe landed on Titan's surface in 2005, highlighting the first landing on a surface in the outer solar system, as well as the first landing on a moon other than Earth's moon. During its descent, *Huygens* imaged various river channels (Owen, 2005) and confirmed large bodies of liquid on the surface with a dynamic coastline including islands (Hofgartner et al., 2016). *Huygens* landed in a vast, dark region near the equator called Shangri-La, which is an extensive field of dark, organic dune deposits (e.g., Malaska et al., 2016). At the landing site, *Huygens* imaged a flat plain covered in rounded pebbles and rocks, further evidence that the area was once covered in liquids which eroded these rocks over time (Tomasko et al., 2005). *Cassini* orbited and studied Titan from 2004 to 2017 and made 127 flybys of Titan. Each flyby taught us more about this unique world, including identifying vast equatorial dune fields (Lorenz et al., 2006; Radebaugh et al., 2008), hydrocarbon lakes and seas of liquid methane and ethane (Stofan et al., 2007; Brown et al., 2008; Mastrogiuseppe et al., 2014, 2016, 2018), numerous river channels (Owen et al., 2005; Lorenz et al., 2008) and valleys (Perron et al., 2006), impact craters (Lorenz et al., 2007; Soderblom et al., 2010; Neish & Lorenz, 2012; Neish et al., 2013; Neish & Lorenz, 2014; Neish et al., 2016; Werynski et al., 2019; Hedgepeth et al., 2020; Solomonidou et al., 2020b), and potential cryovolcanoes (Neish et al., 2006; Lopes et al., 2007; Mitri et al., 2008), as well as a more accurate surface temperature (89 – 94 K) and pressure (1.5 bar; Fulchignoni et al., 2005; Jennings et al., 2009; Cottini et al., 2012). The *Cassini-Huygens* mission left behind a legacy of data and one-of-a-kind discoveries that will propel Titan science forward for years to come.

In the next decade, a new Titan spacecraft will be built and launched; the *Dragonfly* rotorcraft lander (Lorenz et al., 2018; Turtle et al., 2018). Landing in the dune fields just south of Selk Crater (near the *Huygens* landing site; Lorenz et al., 2021), *Dragonfly* will have the opportunity to study the surface up close using a mass spectrometer, gamma-ray and neutron spectrometer, a geophysics and meteorology package, and a high resolution camera suite. *Dragonfly* will give scientists a detailed view of the composition of Titan's surface for the first time. Additionally, since *Dragonfly* has the ability to "hop" to different locations on the surface, it will study a variety of geologic units and seek out potential prebiotic molecules and chemical processes (Lorenz et al., 2018). The mission will study a variety of geologic units and seek out potential prebiotic molecules and chemical processes (Lorenz et al., 2018).

From the *Voyager* and *Cassini-Huygens* missions, we learned that Titan's atmosphere is surprisingly Earth-like, with a composition of 95% nitrogen (N_2), 4% methane (CH_4), and 1% trace species, a surface pressure of 1.5 bar (Earth surface pressure is 1 bar), and a layered atmospheric structure (Figure 1). Solar radiation and charged particles from Saturn's magnetosphere dissociate and ionize atmospheric N_2 and CH_4, allowing them to recombine into new hydrocarbons (ethane (C_2H_6) being the most prevalent (Yung et al., 1984)), nitriles, and a plethora of other organic molecules that cause the atmosphere to be shrouded in a thick haze (e.g., Desai et

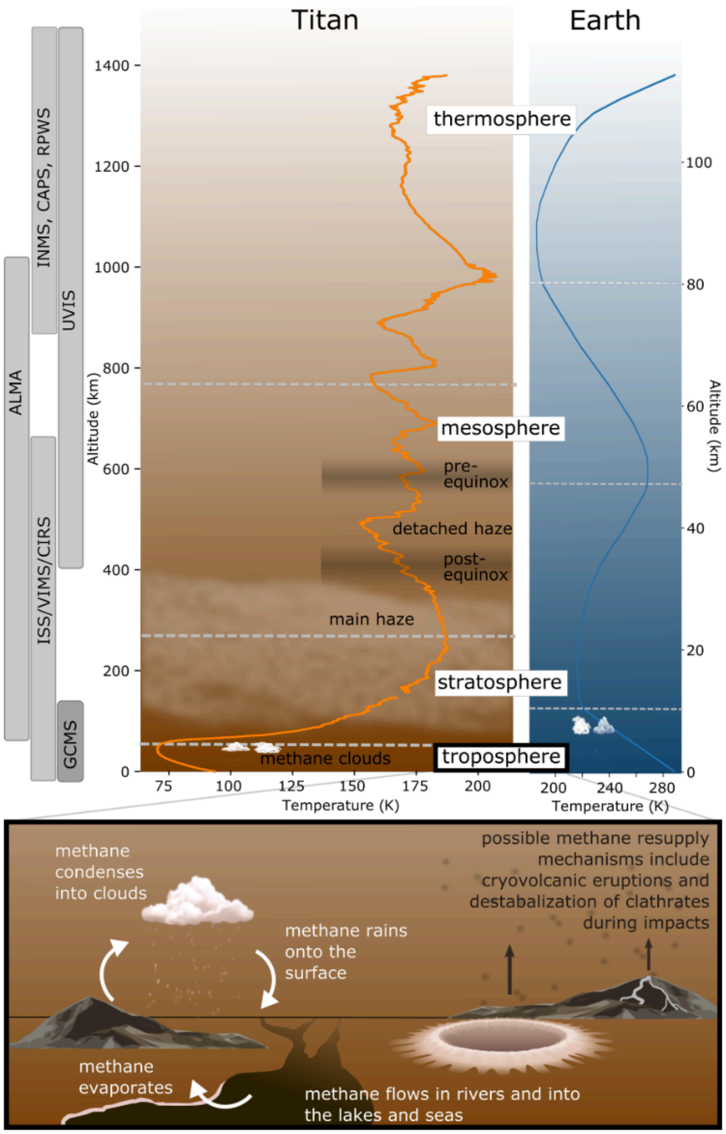

Figure 1. (top) Temperature profile and atmospheric structure comparison between Titan and Earth. Gray, vertical bars show the regions examined by *Cassini* instruments and the Atacama Large Millimeter/submillimeter Array (ALMA) telescope. (bottom) Titan's troposphere includes the methane "hydrological" cycle between the surface and the atmosphere, similar to Earth's hydrosphere. A methane replenishment process is necessary to explain the irreversible methane loss in the thermosphere (Figure and caption from MacKenzie et al., 2021).

al., 2017; Lai et al., 2017). Titan's organic-rich atmosphere is filled with a wealth of molecules that are interesting from an astrobiological perspective, and may represent processes that occurred on prebiotic Earth (Trainer et al., 2006; Palmer et al., 2017).

As these various chemical species condense from gas to solid ices and descend through the atmosphere towards the surface, they may also condense as ice layers onto haze particles and form ice clouds (Anderson et al., 2018), or fall directly to the surface in the liquid (e.g., CH_4, C_2H_6) or solid (acetylene, C_2H_2) phase. These particles may deposit onto Titan's dry plains, into the polar lakes and seas, or be transported across the surface via fluvial networks as part of Titan's CH_4 "hydrologic" cycle.

Titan's liquids are restricted to the north and south poles in the form of lakes and seas, where colder temperatures and less volatile species allow for these lakes and seas to persist (Hayes et al., 2016). In Titan's north pole, broad basins filled with liquid make up Kraken Mare, Ligeia Mare, and Punga Mare, as well as larger lakes (Jingpo and Bolsena Lacus; see Figure 2). Titan's seas (mare) represent 80% of all liquid-filled surfaces by area (Hayes et al., 2008). The lakes (predominantly in the north) take up 12% of the surface area between 55º to 90ºN, whereas in the south, the small amount of lakes only take up 0.3% of the surface area in the same latitude range (Hayes et al., 2016). In the south lie many broad, empty depressions (Figure 2) that are suggested to be paleoseas that may have been filled with liquid in the past (Aharonson et al., 2009; Hayes et al., 2011), along with the largest liquid body at the south pole, Ontario Lacus (Figure 3). This liquid dichotomy between the north and south poles is mainly due to orbital variations in the Saturn-Titan system, where the southern hemisphere summer has a 25% higher peak solar flux than that of the northern hemisphere summer, which may have led to a net transport of methane and ethane from the south to the north pole (Hayes et al., 2016).

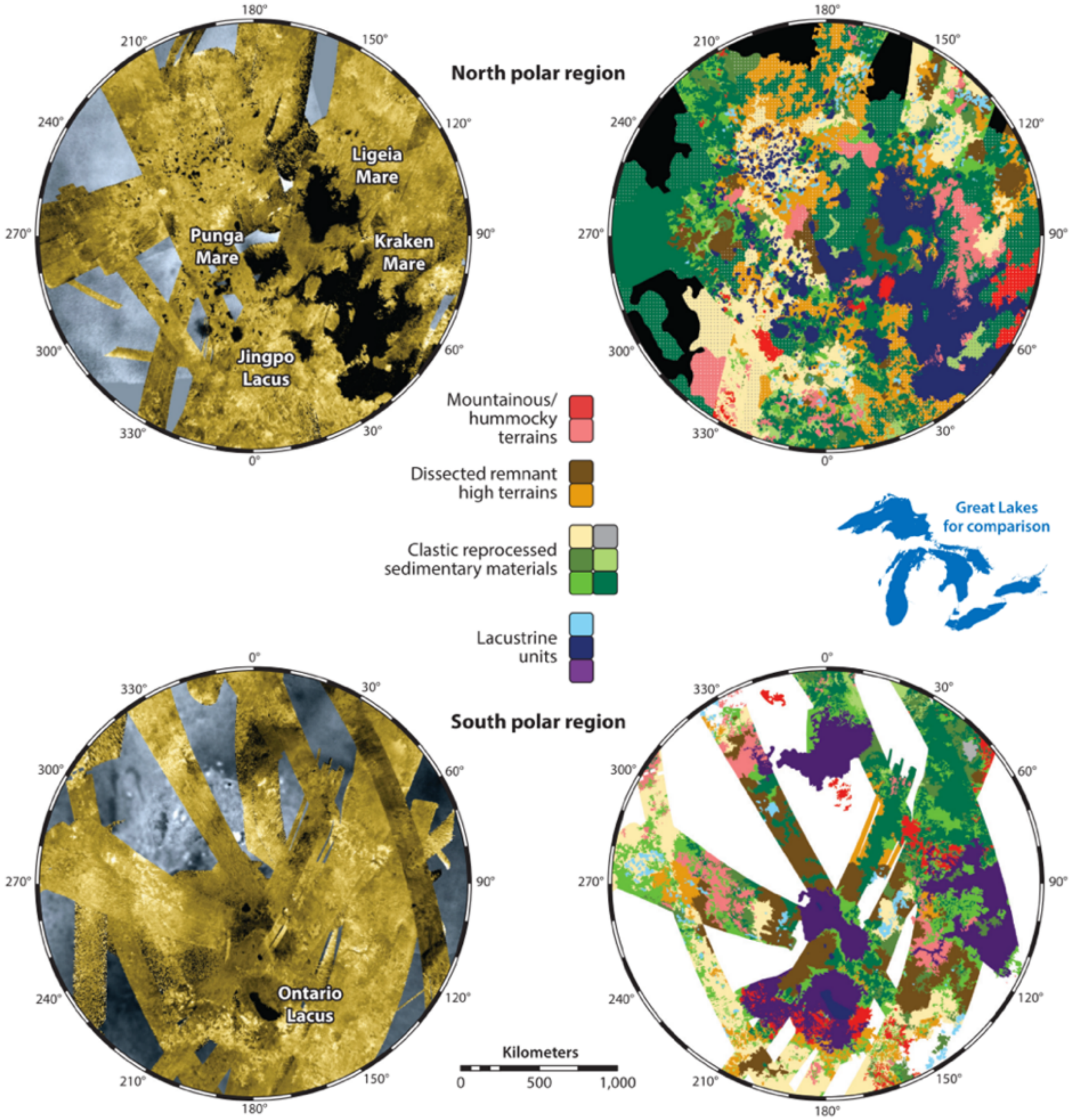

Figure 2. Distribution of polar hydrologic features on Titan derived from Cassini data acquired through January 2015 (Cassini flyby T108). The panels on the left depict false-color Synthetic Aperture Radar (SAR) mosaics (gold overlying near-infrared Imaging Science Subsystem (ISS) maps (gray), with maria and lacus identified. The panels on the right show the morphologic mapping units identified by Birch et al. (2017). The relative topography of the mapped units is represented by the vertical arrangement of boxes in the central legend. An outline of Earth's Great Lakes in North America is included for scale (Figure and caption from Hayes et al., 2016).

The perimeter of Ontario Lacus possesses "bathtub rings" of material (sediments) that exhibit a brighter signal in the 5-µm-region of *Cassini* VIMS spectral data than the surrounding material (Figure 3); these bathtub rings have been interpreted as evaporites (Barnes et al., 2009; Moriconi et al., 2010). Additionally, similar 5-µm-bright deposits were identified in association with a subset of some of the northern lakes (and empty lake basins; see Figures 4, 5; Barnes et al., 2011a). MacKenzie et al. (2014) mapped the global exposures of the 5-µm-bright deposits, and found that they comprise ~1% of Titan's surface (Figure 6). Apart from the polar evaporites, the largest deposits of the 5-µm bright material are near the equator at Hotei and Tui Regions (interpreted as low-latitude paleoseas (Moore & Howard, 2010)). Although we have been fortunate to discover, identify, and globally map such evaporites, *Cassini* data is ultimately limited in the extent of *determining* the composition of such evaporites. Previous studies have measured various hydrocarbon and nitrile compounds in the 5-µm region to shed light on which materials would be more likely to compose Titan's evaporites. For

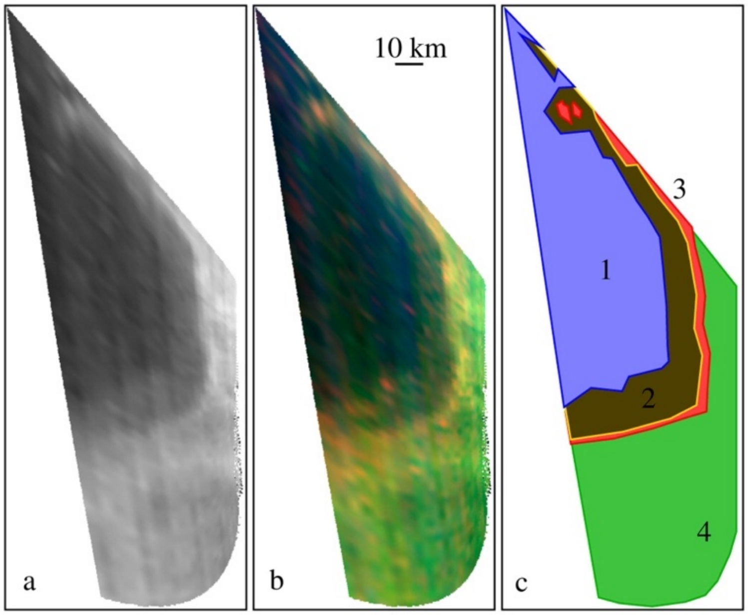

Figure 3. VIMS cube CM_1575506843_1, shown in an orthographic projection from directly above the lake (74ºS, 180ºW). Subfigure (a) is a 2-µm image; (b) is a 3-color image with red as 5 µm, green as 2 µm, and blue as 1.6 µm; and (c) is a unit map, with units numbered. Unit 1 (blue) corresponds to the uniformly dark interior of Ontario Lacus. Unit 2 (yellow/brown) is a less-dark, uniform shelf that surrounds Unit 1. Unit 3 (red) is a narrow, bright annulus that exists at the edge of the lake. Unit 4 (green) represents the area exterior to the lake (the Unit 3/4 border is defined by inspection, and is somewhat arbitrary; Figure and caption from Barnes et al., 2009).

example, Clark et al. (2010) found that the spectra of benzene (C_6H_6), toluene ($C_6H_5CH_3$), cyanoacetylene (C_3HN), and acetonitrile (CH_3CN) all have various degrees of compatibility when compared to the 5-µm bright feature of Titan's evaporites. Further, thermodynamic modeling studies have estimated the chemical composition of the evaporites (Cordier et al., 2009, 2013), and the structure of deposits based on estimated composition (Cordier et al., 2016). However, definitive concentrations, extent, and spatial distribution of Titan's evaporites is still unknown. We shed light on these unanswered questions by providing in-depth experimental constraints on the evaporation process, which will further our understanding of basin formation and evolution on Titan.

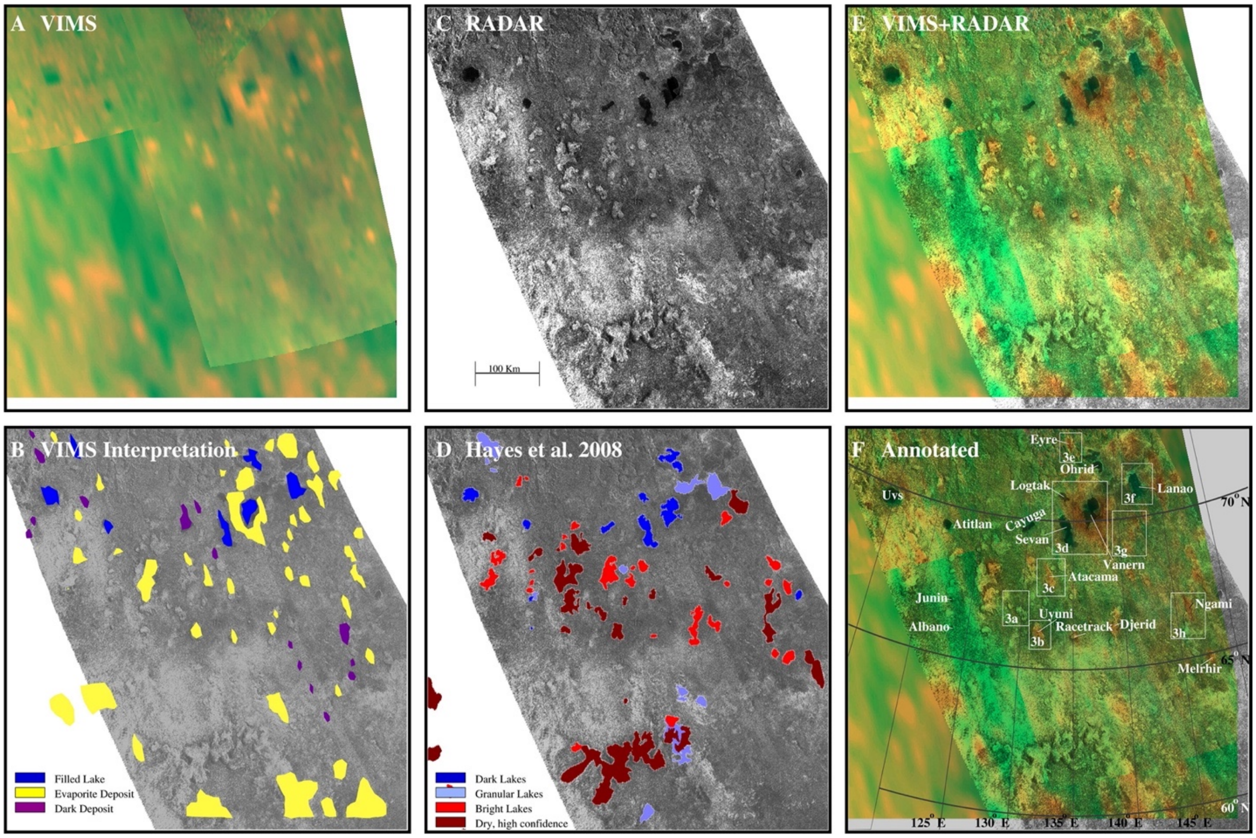

Figure 4. This figure shows the area south of the north-polar sea Ligeia Mare on Titan in orthographic projection using data from both the VIMS and RADAR instruments onboard Cassini. (A) The VIMS view, color-mapped with R =5 µm, G =2 µm, B = 1.3 µm. We show an interpreted map of the VIMS data in (B); here dark blue corresponds to areas where VIMS sees open liquids, yellow to those 5-lm-bright areas that we interpret to be evaporite deposits, and purple to dark areas that may be either wetted sediments or open lakes smaller than a single VIMS pixel in size. Part (C) shows the Synthetic Aperture Radar (SAR) view from Cassini's RADAR instrument, with brightness signifying the radar scattering cross-section parameter σ_0. A map from the RADAR data in (D) shows what Hayes et al. (2008) interpret to be filled lakes (dark blue), ''partially-filled'' lakes (light blue), dry lakebeds (light red), and dry lakebeds with a high level of confidence (dark red). In (E) we show a combined VIMS-RADAR view that allows direct intercomparison between the two datasets. In HSV (hue-saturation-value) colorspace, the VIMS data are used for hue and saturation, and the RADAR data are assigned to value (brightness). (F) An annotated version of the VIMS-RADAR combined view from part (C), with the location of the zoomed-in views from Fig. 2 indicated by the white boxes (Figure and caption from Barnes et al., 2011a).

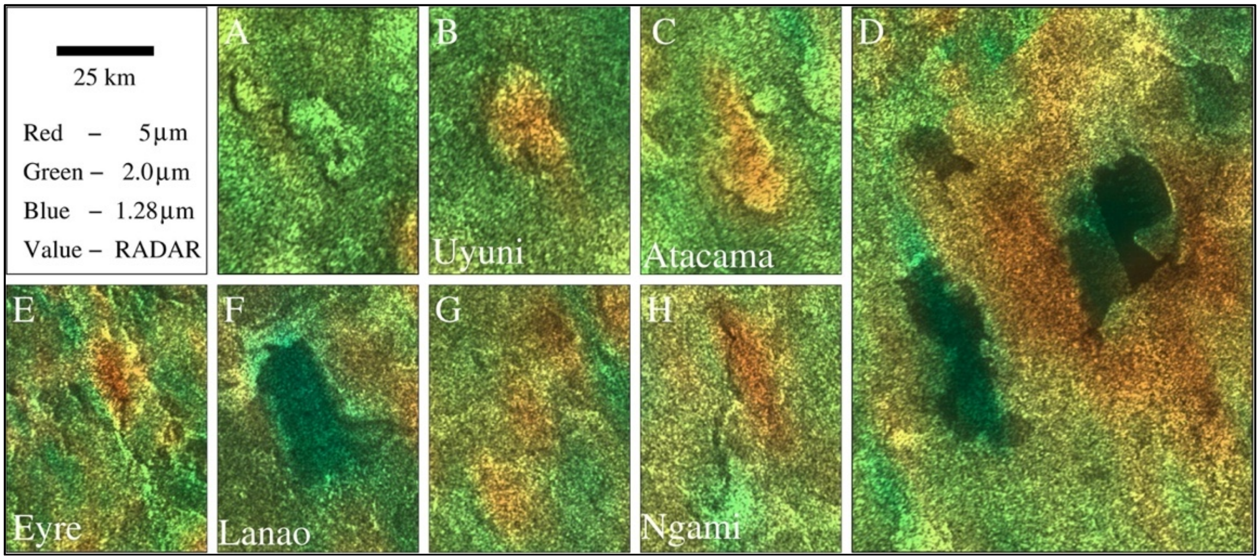

Figure 5. This figure shows zoomed-in versions of various north polar lakes. Part (A) shows unnamed RADAR-empty lakes northwest of Uyuni Lacus that do not have evaporite deposits on their floors. Part (B) shows Uyuni Lacus, which does have evaporite, as does Atacama Lacus in part (C) and Ngami Lacus in part (H). Part (D) shows the complex around Logtak Lacus (in the northwest), Sevan Lacus (in the southwest), and Vänern Lacus (in the east). Vänern Lacus in particular is surrounded by an evaporite deposit 20 km wide. Eyre Lacus in part (E) shows as a dry lakebed in VIMS observations, but was not initially identified as a dry lakebed in the RADAR data (Hayes et al., 2008). It was, however, later shown to be a deep basin by the SARtopo technique (Stiles et al., 2009). Part (F) shows Lanao Lacus, determined to be a shallow filled lake. The 5-µm- bright spectral units in part (G) are evaporites that do not occur in steep-walled depressions identified by RADAR as empty lakes. The southern part of part (H) shows what may be an area presently filled with liquid that was not filled during the T28/T29 RADAR passes 3 years earlier (Figure and caption from Barnes et al., 2011a).

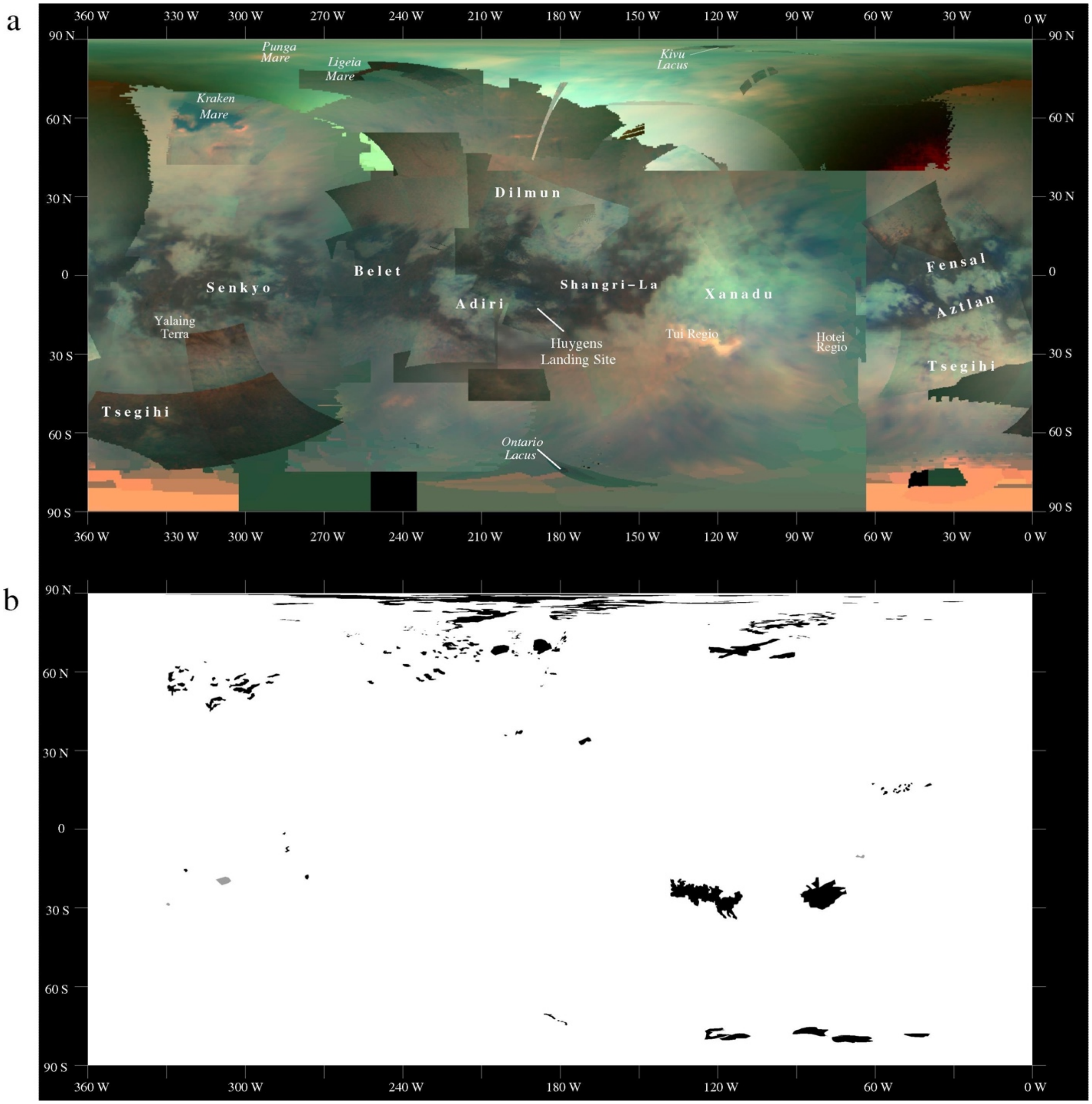

Figure 6. (a) Global cylindrical map of Titan as seen by Cassini VIMS using the color scheme of Barnes et al. (2007a): R =5 µm, G =2 µm, and B = 1.3 µm. This VIMS base map uses data from Cassini flybys T8 to T90. (b) Global distribution of evaporitic deposits in black as well as several 5-µm-bright areas that did not meet sufficient criteria (e.g. not observed twice, no data of high enough resolution) to be considered evaporite candidates in gray. The polygons shown here, created with software designed for the analysis of Barnes et al. (2008), were used to calculate the area covered by evaporite. While many of the new deposits identified in this study are located near liquid (on or near the shores or empty bottoms of polar lakes and seas), the existence of 5-µm-bright material in the equatorial region is evidence for the presence of large scale tropical seas in this area sometime in Titan's past (Figure and caption from MacKenzie et al., 2014).

2. General Methodology

2.1. Titan Surface Simulation Chamber Description

All experiments in this dissertation were performed in the Arkansas Center for Space and Planetary Sciences Titan Surface Simulation Chamber (TSSC; Wasiak et al., 2013). This is a surface-atmosphere chamber that simulates Titan-relevant surface temperature (85 – 110 K) and pressure (1.5 bar N_2 atmosphere). The TSSC is a 2 m tall vertical steel cylinder which maintains Titan atmospheric pressure and houses the Titan Module (TM), a steel housing that rests within the chamber. The Temperature Control Box (TCB; Fig. 7) is the portion of the chamber where the sample is analyzed and Titan temperatures are maintained. N_2 gas (AirGas industrial grade, >99.998%) directly pressurizes the chamber and liquid nitrogen (LN_2) cools the TCB and condenser (inside the TCB; Fig. 7) via stainless steel cooling coils. Chamber pressure is maintained throughout experiments using a Stra-val pressure release valve, and is monitored via a Matheson 63-3161 pressure gauge (0 – 60 psi). Hydrocarbons such as methane, ethane, ethylene, acetylene which are gaseous at standard atmospheric temperature and pressure (SATP) are added to the condenser via gas tubing and are condensed to liquid or solid phase inside the condenser. Compounds which are liquid at SATP (benzene and acetonitrile) follow a different protocol which is described in greater detail in Section 2.2. All gas cylinders and LN_2 dewars are purchased through Airgas®.

Throughout each experiment, liquid and solid samples are analyzed via temperature, mass change over time, optical views, and a Fourier Transform Infrared Spectrometer (FTIR; Fig 8). A glass sample dish (15 cm diameter) is lined with Spectralon®, a fluoropolymer that has its highest diffuse (Lambertian) performance in the infrared, which serves as a background material for FTIR measurements. The sample dish is suspended by three nylon strings which connect to a

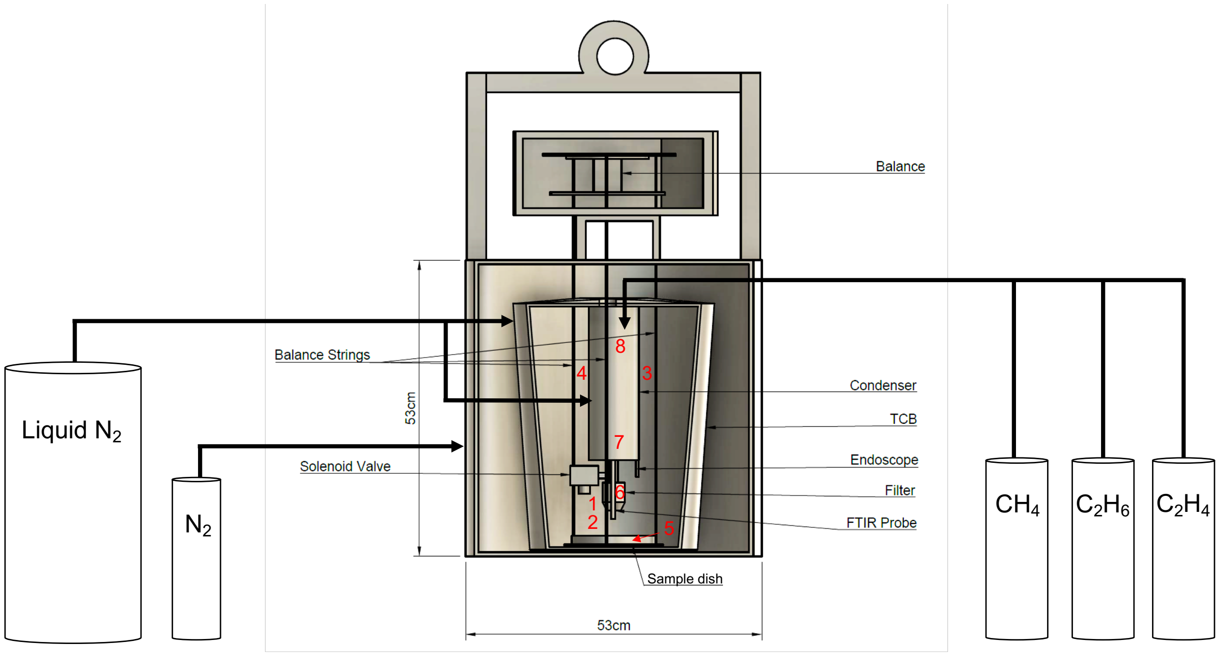

Figure 7. Schematic cross-section view of the Titan Module (TM) and Temperature Control Box (TCB) showing the various components used to simulate and observe the Titan surface environment. The TM and all components inside it are to scale; the external gas cylinders are for reference only, and are not to scale (Figure from Czaplinski et al., 2019).

Sartorius Entris822 digital scale (balance), which has a data connection to the computer. To ensure that the electronic connections of the balance are not affected by the cold temperatures of the chamber, the balance is placed above the TCB inside an insulated container made from pink foam board insulation. A small, metal plate heater (Watlow controller) is placed under the lid of this insulation box to assist with maintaining temperatures inside the balance box above ~220 K. Eight K-type (+/- 2.2ºC) thermocouples are placed throughout the TCB and allow continuous recording of temperatures during experiments: two in the condenser, one near the FTIR probe, one in the filter, two above the sample dish, and two directly touching the mixture in the sample dish. These thermocouples allow precise characterization of the thermal profile in the TCB. A thermocouple is also placed within the balance insulation box to monitor temperatures there. The thermocouples are connected to a computer via an OMEGA® 8-channel USB Thermocouple Data Acquisition Module. A custom made LabVIEW software program reads the inputs from the balance and thermocouple data and outputs this information every second during an experiment. We also have five cameras (one CrazyFire and four KKmoon brand) located at various points above the sample dish to maintain views of the sample throughout experiments. The cameras are connected to the computer via USB. During experiments, we monitor these cameras via CrazyFire software, which allows the user to capture images and videos during experiments (10-20, depending on the experiment). A 40-watt lightbulb is attached to the upper walls of the TCB to allow for manual illumination and temperature control. Spectra are collected using a Thermo Fisher Scientific Nicolet 6700 FTIR Spectrometer equipped with a white light source, CaF_2 beamsplitter, and a TEC InGaAs detector (1-2.5 μm) with a spectral sampling of 4 cm^{-1}. We use the Smart Near-IR FiberPort Accessory (Fig. 8), which connects to the fiber optic probe that has terminal connections ("legs") at the top of the spectrometer and in a nadir orientation a few centimeters above the sample dish. The fiber optic probe is offset by ~10º for experiments conducted in Chapters 2-4 to avoid specular reflections. Thermo Fisher Scientific OMNIC™ Spectra Software is used to collect and analyze spectra from experiments. A background spectrum is collected before every experiments at 450 scans. Approximately 20-40 spectra are collected per experiment, depending on experiment type.

Figure 8. Nicolet 6700 FTIR located below the Titan chamber. Fiber optic "legs" connected to the top of the Smart NIR FiberPort accessory (middle of spectrometer) extend through the chamber with the single terminator end resting just above the sample dish.

2.2. Experimental Protocol

The first step in every experiment is to purge the chamber of any contaminants (water vapor, residuals from previous experiments). To do this, a chamber purge is initiated by flowing N_2 gas through the chamber and out the main exhaust valve for 10 minutes. Next, the condenser is purged by itself for an additional 10 minutes. For each purge, the N_2 outlet pressure is 0.5 bar. After the chamber is purged, a constant flow of LN_2 is used to cool the chamber to the desired temperature (depending on which compound is being added to the condenser; see Table 1). Note that the duration of individual experiments is ultimately limited by the availability of LN_2, as one dewar (180 L, 55 psi) lasts around 3-5 hours. After the purges are complete, and the LN_2 is initiated, we then collect the background spectrum (collected before each new experiment) which is automatically subtracted from each sample spectrum. In tandem, we also start running the LabVIEW data collection, which constantly records temperatures from all eight thermocouples and mass data from the balance. Gases are added to the condenser at the appropriate temperature for 10 – 20 seconds so the compound(s) condense (liquid or gas phase), which generally takes 4 – 5 minutes. A solenoid valve at the bottom of the condenser is then opened, which releases ("pours") the condensed compound(s) into a glass filter (0.4 – 0.6 μm) before reaching the sample dish for analysis. The filter ensures that large amounts of solid particles do not reach the sample dish. This pouring process may take 2 – 8 minutes, depending on how much sample is present. Compounds which are in liquid phase at SATP (benzene, acetonitrile) are added to an Erlenmeyer flask inside a custom-built glove box (Fig. 9) which is connected to both a N_2 cylinder and the condenser/exhaust lines. N_2 gas is then bubbled through the flask until saturated, at which point the N_2-saturated gaseous mixture is delivered through the condenser (kept as close to room temperature as possible) where it deposits onto the sample dish at the bottom of the TCB, which is cold enough for the sample to deposit in solid phase. We call this the "cold trap" method, as the compound is "trapped" in the coldest part of the chamber at that time. This deposition process generally takes 15 – 20 minutes for an appropriate amount of sample to be deposited, as confirmed by visual and spectral analysis. Each research project has its own unique experimental protocol that is described within the methods section of those corresponding chapters.

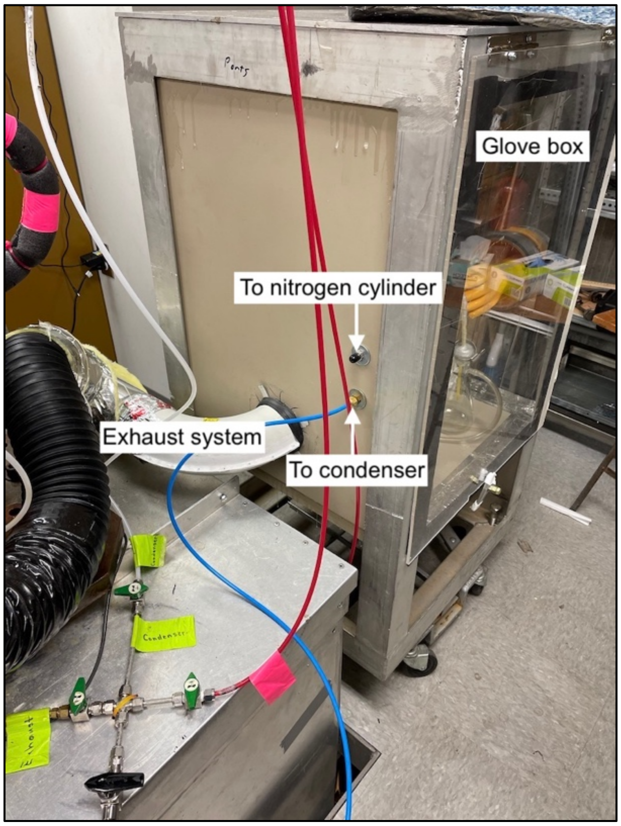

Figure 9. Custom-built glove box shown with connections to the exhaust system, N_2 cylinder, and condenser.

Table 1. Summary of chemical compounds used in this project and their properties.

Compound	Formula	Polarity	Melting T (K)	Boiling T (K)
Methane	CH_4	NP	–*	111.6
Ethane	C_2H_6	NP	89.83	184.6
Acetylene	$HC\equiv CH$	NP	192.3	189.0
Ethylene	$H_2C=CH_2$	NP	104.0	169.5
Benzene	C_6H_6	NP	278.7	353.2
Acetonitrile	$H_3C{-}C\equiv N$	P	228.0	355.0

*Does not freeze under current Titan conditions (89 – 94 K, 1.5 bar N_2 atmosphere) due to the liquid-vapor equilibrium of nitrogen at 1.5 bar and freezing point depression caused by nitrogen dissolution (Farnsworth et al., 2020).
NP: nonpolar
P: polar

2.3. Experimental Datasets

2.3.1. Dataset Types

Dataset outputs for each experiment include temperature as a function of experimental time, mass as a function of experimental time, camera photos and videos, and FTIR spectra.

Temperature vs time plots (Fig. 10) start at room temperature (~300 K). After LN_2 flow is initiated, the temperatures rapidly decrease, taking around 30 minutes to reach the point where the hydrocarbon gas is added to the condenser. Note the temperature increase/peak in T7 and T8 (condenser thermocouples) in Figure 10a. This temperature peak is due to the fact that the gas being added to the condenser is relatively warmer (approximately room temperature) than the temperature of the condenser thermocouples (~100 K to 140 K). However, the gas quickly decreases temperature after condensing inside the condenser. Figure 10a shows an example where Titan surface temperature (~90 K) in T5 was maintained after the sample was poured onto the dish at ~50 minutes (denoted by temperature increase – condenser temperature, T7/8, was slightly warmer than the sample dish, T5). The steady increase in temperature at ~90 minutes indicates the LN_2 dewar became empty. Figure 10b shows an example where the temperature of the TCB was allowed to follow a warming and cooling cycle. This is done to either conserve liquid nitrogen or to induce evaporation of ethane, because ethane evaporation is negligible at Titan surface temperatures.

Mass vs time plots (Fig. 11) start at approximately zero because the sample dish is empty at the beginning of experiments (fluctuations are due to changes in temperature). The increase in mass at ~60 minutes is due to the sample (ethane-ethylene) being poured from the condenser to the sample dish. The second increase is from additional sample being poured onto the dish. Mass remains relatively constant after the second pour. Error can be calculated and the mass plots can be corrected, if needed.

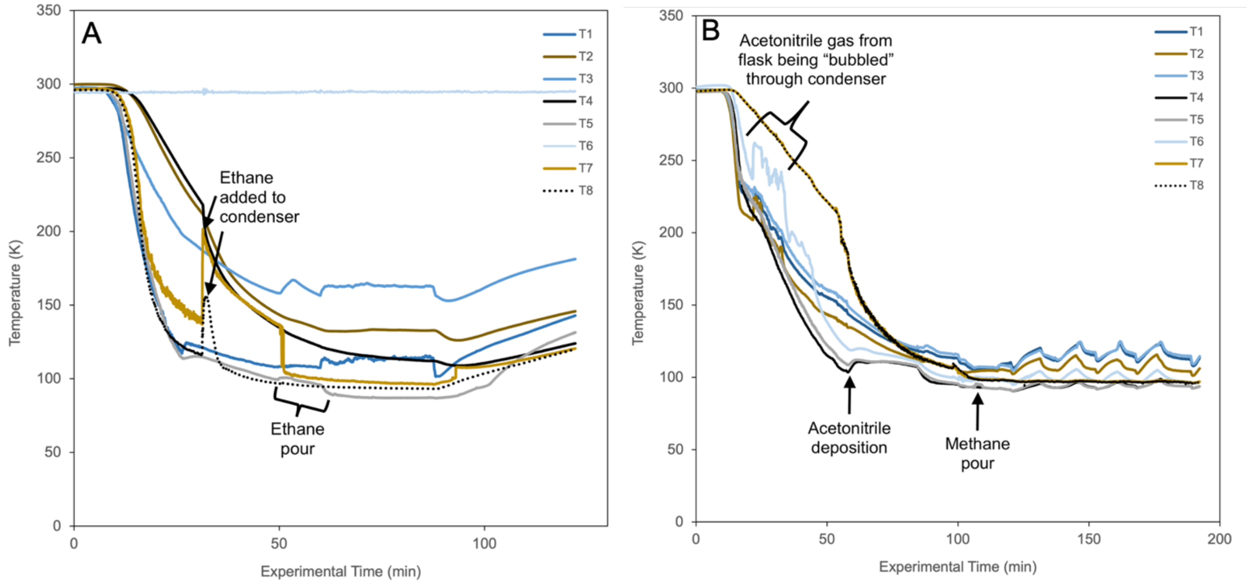

Figure 10. Temperature profiles of two separate experiments showing constant temperatures after the sample is poured (A) compared to fluctuating temperatures after the sample is poured (B). Sample additions and pours are labeled. Notice how the condenser thermocouple temperatures peak when compounds are added to the condenser. Fluctuating temperature (B) conserves LN$_2$ when running multiple experiments in a row.

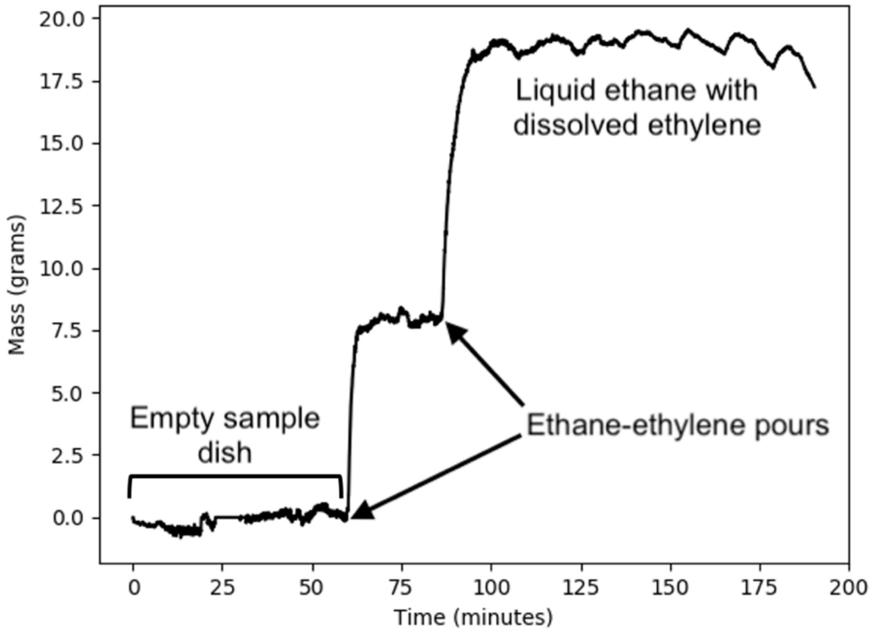

Figure 11. Mass profile of an experiment showing two pours of ethane-ethylene, followed by a relatively stable period (~20 g) after the second pour.

Optical images (Fig. 12) and videos of the sample are recorded during the pouring process to confirm when the sample is being poured onto the dish, as well as during regular intervals during the warming phase of experiments to record any changes in sample morphology. The angle of the cameras are sometimes altered after opening and closing the chamber, therefore images in subsequent chapters may look different from those shown in Fig. 12.

FTIR spectra are recorded during every experiment as a primary source of information about the sample (when the sample is poured, when a certain temperature point is reached, etc.). The spectral range of our setup is from 1 – 2.5 µm, however, due to significant noise at longer wavelengths, we herein present most spectra with an upper wavelength limit of ~2.29 µm for clarity. Figure 13 shows the pure spectra of each compound presented in subsequent chapters: methane, acetylene, ethylene, ethane, benzene, and acetonitrile. Here, the spectra are stacked (using a feature in OMNIC™), which allows each spectrum to be easily compared at the same relative scale.

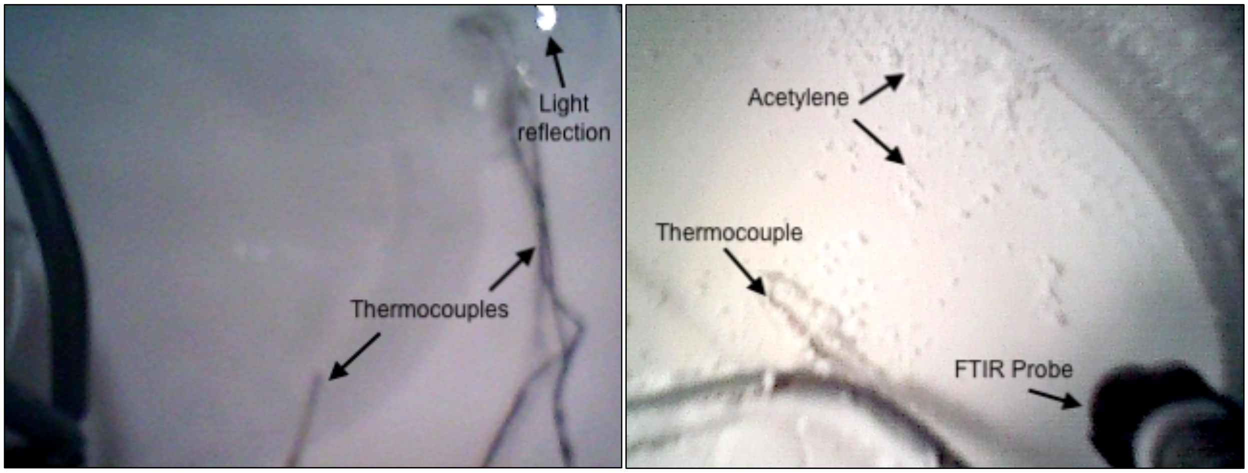

Figure 12. Optical, top-down views of the sample dish showing two slightly different angles. (left) thermocouples can be seen touching the edge of the liquid in the dish. Notice the reflected light on the liquid (upper right) from the lightbulb inside the TCB. (right) different angle showing the FTIR probe and a thermocouple immersed in solid acetylene.

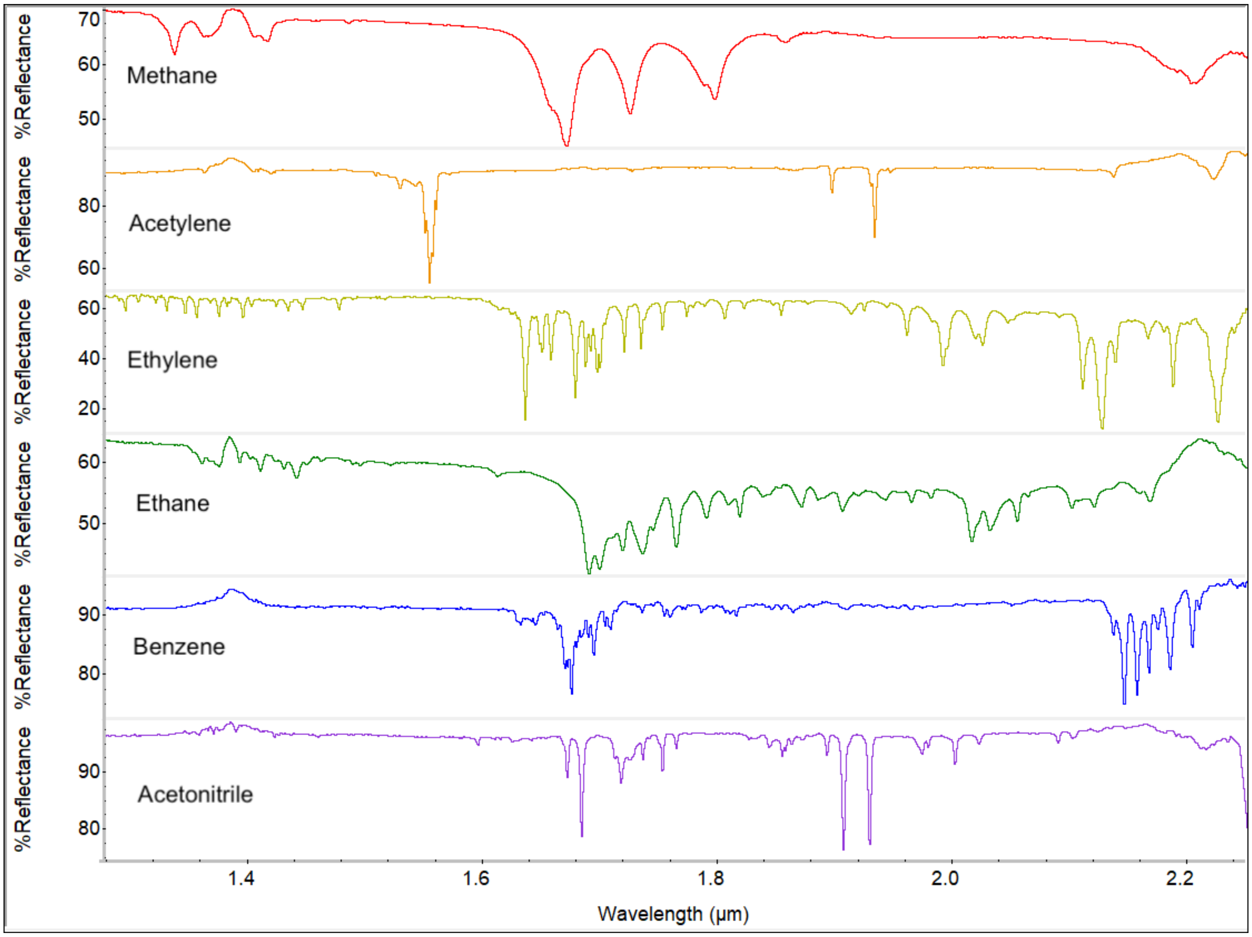

Figure 13. FTIR spectra of pure components presented herein. From top to bottom: methane has a distinct triplet feature in the C–H first overtone region from ~1.7 to 1.8 µm. Acetylene has absorbances at 1.55 µm and 1.93 µm (first overtone region). Ethylene has many different C–H stretch bands (1.6 µm to 2 µm), as well as combination bands beyond 2 µm. Ethane has C – H first overtone bands similar to ethylene, but starting at longer wavelengths, around 1.7 µm. Benzene has C – H aromatic stretch bands around 1.7 µm and C – H aromatic combination bands from 2.1 – 2.3 µm. Acetonitrile has C – H stretch overtones around 1.7 µm and C – N first overtone bands around 1.9 µm.

2.3.2. Data Curation and Repository Information

Experimental datasets for each corresponding chapter will be individually curated via Zenodo. Other experimental datasets will be curated on the University of Arkansas server and will be provided upon reasonable request. The dataset citations for the published chapters are listed below.

Chapter 1: Experimental Study of Ethylene Evaporites Under Titan Conditions

Czaplinski, E. C., Gilbertson, W. A., Farnsworth, K. K., & Chevrier, V. F. (2021). Experimental Study of Ethylene Evaporites under Titan Conditions (Version 1.0) [Data set]. ACS Earth and Space Chemistry. Zenodo. DOI:10.5281/zenodo.4784179

Chapter 2: Experimental Investigation of the Acetylene–Benzene Cocrystal on Titan

Czaplinski, E., Yu, X., Dzurilla, K., & Chevrier, V. (2020). Experimental Investigation of the Acetylene-Benzene Co-Crystal on Titan [Data set]. Zenodo. DOI:10.5281/zenodo.4110814

3. Dissertation Information

3.1. Objectives and Tasks

The overarching science questions are as follows:

- Which combinations of hydrocarbon or nitrile compounds form evaporites?
- Are these evaporites readily detectable using FTIR spectroscopy?

Objective 1. Determine to what extent the ethylene evaporite forms in liquid methane, liquid ethane, and liquid methane-ethane solutions.

Task 1: Conduct laboratory experiments to determine ethylene solubility, solvent evaporation rates, and evaporite production.

Objective 2. Determine if acetylene-benzene co-crystal can be detected via FTIR spectroscopy.

Task 1: Conduct laboratory experiments to determine if the co-crystal forms and document how the NIR absorption bands change as a function of temperature.

Task 2: Identify the primary absorbance features of the co-crystal in the NIR.

Objective 3. Determine if the acetylene-acetonitrile co-crystal can be detected via FTIR spectroscopy.

Task 1: Conduct laboratory experiments to determine if the co-crystal forms and document how the NIR absorption bands change as a function of temperature.

Task 2: Identify the primary absorbance features of the co-crystal in the NIR.

Objective 4. Determine how multiple evaporite compounds combined with methane and ethane solvents affects the formation and behavior of evaporites.

Task 1: Conduct laboratory experiments with multiple evaporite compounds.

Task 2: Observe how differential solubility of multiple evaporite compounds affects evaporite formation.

3.2. Dissertation Outline

This dissertation is divided into four chapters corresponding to four separate studies and four articles in various stages of the publication process. Chapter 1 was accepted and published in *ACS Earth and Space Chemistry* in 2019, and Chapter 2 was accepted and published in *The Planetary Science Journal* in 2020 (see the *Chapter Publication Status* section for more information). Each chapter contains specifically detailed information for the corresponding set of experiments, as well as a separate abstract, introduction, methods, results, discussion, implications for Titan, conclusions, acknowledgements, and references. Following the four research chapters, the section titled *Dissertation Conclusions and Synthesis* combines the motivation for this research study, the conclusions of the four research chapters, and further discusses the relevance to Titan and missions. The dissertation concludes with an *Appendix*, which includes the *Primary Author Contribution Statement* signed by the coauthors of each chapter, as well as the *Primary Author Curriculum Vitae.*

3.3. Primary Author Contribution

I certify that over 51% of the work presented in this document was completed by the primary author, Ellen Czaplinski. More specifically, below is the contribution I deem credible for the work completed. Missing percentages are awarded for intellectual contribution by coauthors listed within the provided research chapters.

- Chapter 1: 80%
- Chapter 2: 85%
- Chapter 3: 95%
- Chapter 4: 95%

4. References

Aharonson, O., Hayes, A.G., Lunine, J.I., Lorenz, R.D., Allison, M.D., Elachi, C., 2009. An asymmetric distribution of lakes on Titan as a possible consequence of orbital forcing. Nat. Geosci. 2, 851–854. https://doi.org/10.1038/ngeo698

Anderson, C.M., Samuelson, R.E., Nna-Mvondo, D., 2018. Organic Ices in Titan's Stratosphere. Space Sci. Rev. 214, 125. https://doi.org/10.1007/s11214-018-0559-5

Barnes, J.W., Bow, J., Schwartz, J., Brown, R.H., Soderblom, J.M., Hayes, A.G., Vixie, G., Le Mouélic, S., Rodriguez, S., Sotin, C., Jaumann, R., Stephan, K., Soderblom, L.A., Clark, R.N., Buratti, B.J., Baines, K.H., Nicholson, P.D., 2011. Organic sedimentary deposits in Titan's dry lakebeds: Probable evaporite. Icarus 216, 136–140. https://doi.org/10.1016/j.icarus.2011.08.022

Barnes, J.W., Brown, R.H., Soderblom, J.M., Soderblom, L.A., Jaumann, R., Jackson, B., Le Mouélic, S., Sotin, C., Buratti, B.J., Pitman, K.M., Baines, K.H., Clark, R.N., Nicholson, P.D., Turtle, E.P., Perry, J., 2009. Shoreline features of Titan's Ontario Lacus from Cassini/VIMS observations. Icarus 201, 217–225. https://doi.org/10.1016/j.icarus.2008.12.028

Barnes, J.W., Brown, R.H., Soderblom, L., Buratti, B.J., Sotin, C., Rodriguez, S., Le, S., Baines, K.H., Clark, R., 2007. Global-scale surface spectral variations on Titan seen from Cassini/VIMS. Icarus 186, 242–258. https://doi.org/10.1016/j.icarus.2006.08.021

Barnes, J.W., Brown, R.H., Soderblom, L., Sotin, C., Le, S., Rodriguez, S., Jaumann, R., Beyer, R.A., Buratti, B.J., Pitman, K., Baines, K.H., Clark, R., Nicholson, P., 2008. Spectroscopy, morphometry, and photoclinometry of Titan's dunefields from Cassini/VIMS. Icarus 195, 400–414. https://doi.org/10.1016/j.icarus.2007.12.006

Birch, S.P.D., Hayes, A.G., Dietrich, W.E., Howard, A.D., Bristow, C.S., Malaska, M.J., Moore, J.M., Mastrogiuseppe, M., Hofgartner, J.D., Williams, D.A., White, O.L., Soderblom, J.M., Barnes, J.W., Turtle, E.P., Lunine, J.I., Wood, C.A., Neish, C.D., Kirk, R.L., Stofan, E.R., Lorenz, R.D., Lopes, R.M.C., 2017. Geomorphologic mapping of titan's polar terrains: Constraining surface processes and landscape evolution. Icarus 282, 214–236. https://doi.org/10.1016/j.icarus.2016.08.003

Brown, R.H., Baines, K.H., Bellucci, G., Bibring, J.-P., Buratti, B.J., Capaccioni, F., Cerroni, P., Clark, R.N., Coradini, A., Cruikshank, D.P., Drossart, P., Formisano, V., Jaumann, R., Langevin, Y., Matson, D.L., McCord, T.B., Mennella, V., Miller, E., Nelson, R.M., Nicholson, P.D., Sicardy, B., Sotin, C., 2004. The Cassini Visual And Infrared Mapping Spectrometer (VIMS) Investigation. Space Sci. Rev. 115, 111–168. https://doi.org/10.1007/s11214-004-1453-x

Brown, R.H., Soderblom, L.A., Soderblom, J.M., Clark, R.N., Jaumann, R.N., Barnes, J.W., Sotin, C., Buratti, B.J., Baines, K.H., Nicholson, P.D., 2008. The identification of liquid ethane in Titan's Ontario Lacus. Nature 454, 607–610. https://doi.org/10.1038/nature07100

Clark, R.N., Curchin, J.M., Barnes, J.W., Jaumann, R., Soderblom, L., Cruikshank, D.P., Brown, R.H., Rodriguez, S., Lunine, J., Stephan, K., Hoefen, T.M., Le Mouélic, S., Sotin, C., Baines, K.H., Buratti, B.J., Nicholson, P.D., 2010. Detection and mapping of hydrocarbon deposits on Titan. J. Geophys. Res. E Planets 115. https://doi.org/10.1029/2009JE003369

Cordier, D., Barnes, J.W., Ferreira, A.G., 2013. On the chemical composition of Titan's dry lakebed evaporites. Icarus 226, 1431–1437. https://doi.org/10.1016/j.icarus.2013.07.026

Cordier, D., Cornet, T., Barnes, J.W., MacKenzie, S.M., Le Bahers, T., Nna-Mvondo, D., Rannou, P., Ferreira, A.G., 2016. Structure of Titan's evaporites. Icarus 270, 41–56. https://doi.org/10.1016/j.icarus.2015.12.034

Cordier, D., Mousis, O., Lunine, J.I., Lavvas, P., Vuitton, V., 2009. An estimate of the chemical composition of titan's lakes. Astrophys. J. 707, L128-131. https://doi.org/10.1088/0004-637X/707/2/L128

Cottini, V., Nixon, C.A., Jennings, D.E., Kok, R. de, Teanby, N.A., Irwin, P.G.J., Flasar, F.M., 2012. Spatial and temporal variations in Titan's surface temperatures from Cassini CIRS observations. Planet. Space Sci. 60, 62–71. https://doi.org/10.1016/j.pss.2011.03.015

Czaplinski, E.C., Gilbertson, W.A., Farnsworth, K.K., Chevrier, V.F., 2019. Experimental Study of Ethylene Evaporites under Titan Conditions. ACS Earth Sp. Chem. 3, 2353–2362. https://doi.org/10.1021/acsearthspacechem.9b00204

Desai, R.T., Coates, A.J., Wellbrock, A., Vuitton, V., Crary, F.J., Shebanits, O., Jones, G.H., Lewis, G., Waite, J., Cordiner, M., Taylor, S., Kataria, D., Wahlund, J.-E., Edberg, N., Sittler, E., 2017. Carbon Chain Anions and the Growth of Complex Organic Molecules in Titan's Ionosphere. Astrophys. J. Lett. 844, L18. https://doi.org/10.3847/2041-8213/aa7851

Elachi, C., Allison, M.D., Borgarelli, L., Encrenaz, P., Im, E., Janssen, M.A., Johnson, W.T.K., Kirk, R.L., Lorenz, R.D., Lunine, J.I., Muhleman, D.O., Ostro, S.J., Picardi, G., Posa, F., Rapley, C.G., Roth, L.E., Seu, R., Soderblom, L.A., Vetrella, S., Wall, S.D., Wood, C.A., Zebker, H.A., 2004. RADAR: The Cassini Titan RADAR Mapper. Space Sci. Rev. 115, 71–110.

Farnsworth, K., 2020. An Experimental Investigation of Liquid Hydrocarbons in a Simulated Titan Environment. University of Arkansas.

Fulchignoni, M., Ferri, F., Angrilli, F., Ball, A.J., Barucci, M.A., Bettanini, C., Bianchini, G., Borucki, W., Colombatti, G., Coradini, M., Coustenis, A., Debei, S., Falkner, P., Fanti, G., Flamini, E., Gaborit, V., Grard, R., Hamelin, M., Harri, A.M., Hathi, B., Jernej, I., Leese, M.R., Lehto, A., Stoppato, P.F.L., 2005. In situ measurements of the physical characteristics of Titan's environment. Nature 438, 785–791. https://doi.org/10.1038/nature04314

Hayes, A., Aharonson, O., Callahan, P., Elachi, C., Gim, Y., Kirk, R., Lewis, K., Lopes, R., Lorenz, R., Lunine, J., Mitchell, K., Mitri, G., Stofan, E., Wall, S., 2008. Hydrocarbon lakes on Titan: Distribution and interaction with a porous regolith. Geophys. Res. Lett. 35, L09204. https://doi.org/10.1029/2008GL033409

Hayes, A.G., 2016. The Lakes and Seas of Titan. Annu. Rev. Earth Planet. Sci. 44, 57–83. https://doi.org/10.1146/annurev-earth-060115-012247

Hayes, A.G., Aharonson, O., Lunine, J.I., Kirk, R.L., Zebker, H.A., Wye, L.C., Lorenz, R.D., Turtle, E.P., Paillou, P., Mitri, G., Wall, S.D., Stofan, E.R., Mitchell, K.L., Elachi, C., Team, R., 2011. Transient surface liquid in Titan's polar regions from Cassini. Icarus 211, 655–671. https://doi.org/10.1016/j.icarus.2010.08.017

Hedgepeth, J.E., Neish, C.D., Turtle, E.P., Stiles, B.W., Kirk, R., Lorenz, R.D., 2020. Titan's impact crater population after Cassini. Icarus 344, 113664. https://doi.org/10.1016/j.icarus.2020.113664

Hofgartner, J.D., Hayes, A.G., Lunine, J.I., Zebker, H., Lorenz, R.D., Malaska, M.J., Mastrogiuseppe, M., Notarnicola, C., Soderblom, J.M., 2016. Titan's "Magic Islands": Transient features in a hydrocarbon sea. Icarus 271, 338–349. https://doi.org/10.1016/j.icarus.2016.02.022

Jennings, D.E., Flasar, F.M., Kunde, V.G., Samuelson, R.E., Pearl, J.C., Nixon, C.A., Carlson, R.C., Mamoutkine, A.A., Brasunas, J.C., Guandique, E., Achterberg, R.K., Bjoraker, G.L., Romani, P.N., Segura, M.E., Albright, S.A., Elliott, M.H., Tingley, J.S., Calcutt, S., Coustenis, A., Courtin, R., 2009. Titan's Surface Brightness Temperatures. Astrophys. J. 691, L103–L105. https://doi.org/10.1088/0004-637X/691/2/L103

Lai, J.C.-Y., Cordiner, M.A., Nixon, C.A., Achterberg, R., Molter, E., Teanby, N., Palmer, M.Y., Charnley, S., JE, L., Kisiel, Z., Mumma, M., Irwin, P., 2017. Mapping Vinyl Cyanide and Other Nitriles in Titan's Atmosphere Using ALMA. Astron. J. 154, 206. https://doi.org/10.3847/1538-3881/aa8eef

Lopes, R.M.C., Mitchell, K.L., Stofan, E.R., Lunine, J.I., Lorenz, R., Paganelli, F., Kirk, R.L., 2007. Cryovolcanic features on Titan ' s surface as revealed by the Cassini Titan Radar Mapper. Icarus 186, 395–412. https://doi.org/10.1016/j.icarus.2006.09.006

Lorenz, R.D., Lopes, R.M., Paganelli, F., Lunine, J.I., Kirk, R.L., Mitchell, K.L., Soderblom, L.A., Stofan, E.R., Ori, G., Myers, M., Miyamoto, H., Radebaugh, J., Stiles, B., Wall, S.D., Wood, C.A., Cassini Radar Team, 2008. Fluvial channels on Titan : Initial Cassini RADAR observations. Planet. Space Sci. 56, 1132–1144. https://doi.org/10.1016/j.pss.2008.02.009

Lorenz, R.D., Mackenzie, S.M., Neish, C.D., Gall, A. Le, Turtle, E.P., Barnes, J.W., Trainer, M.G., Werynski, A., Hedgepeth, J., Karkoschka, E., 2021. Selection and Characteristics of the Dragonfly Landing Site near Selk Crater, Titan. Planet. Sci. J. 2, 24. https://doi.org/10.3847/PSJ/abd08f

Lorenz, R.D., Turtle, E.P., Barnes, J.W., Trainer, M.G., Adams, D.S., Hibbard, K.E., Sheldon, C.Z., Zacny, K., Peplowski, P.N., Lawrence, D.J., Ravine, M.A., Mcgee, T.G., Sotzen, K.S., Mackenzie, S.M., Langelaan, J.W., Schmitz, S., Wolfarth, L.S., Bedini, P.D., 2018. Dragonfly: A Rotorcraft Lander Concept for Scientific Exploration at Titan. APL Tech. Dig. 34, 374–387.

Lorenz, R.D., Wall, S., Radebaugh, J., Boubin, G., Reffet, E., Janssen, M., Stofan, E., Lopes, R., Kirk, R., Elachi, C., Lunine, J., Mitchell, K., Paganelli, F., Soderblom, L., Wood, C., Wye, L., Zebker, H., Anderson, Y., Ostro, S., Allison, M., Boehmer, R., Callahan, P., Encrenaz, P., Ori, G.G., Francescetti, G., Gim, Y., Hamilton, G., Hensley, S., Johnson, W., Kelleher, K., Muhleman, D., Picardi, G., Posa, F., Roth, L., Seu, R., Shaffer, S., Stiles, B., Vetrella, S., Flamini, E., West, R., 2006. The Sand Seas of Titan : Cassini. Science (80-.). 312, 724–728. https://doi.org/DOI: 10.1126/science.1123257

Lorenz, R.D., Wood, C.A., Lunine, J.I., Wall, S.D., Lopes, R.M., Mitchell, K.L., Paganelli, F., Anderson, Y.Z., Wye, L., Tsai, C., Zebker, H., Stofan, E.R., 2007. Titan's young surface: Initial impact crater survey by Cassini RADAR and model comparison. Geophys. Res. Lett. 34, L07204. https://doi.org/10.1029/2006GL028971

MacKenzie, S.M., Barnes, J.W., Sotin, C., Soderblom, J.M., Le Mouélic, S., Rodriguez, S., Baines, K.H., Buratti, B.J., Clark, R.N., Nicholson, P.D., McCord, T.B., 2014. Evidence of Titan's climate history from evaporite distribution. Icarus 243, 191–207. https://doi.org/10.1016/j.icarus.2014.08.022

Mackenzie, S.M., Birch, S P D, Hörst, S.M., Sotin, C., Barth, E., Lora, J.M., Mackenzie, S.M., Birch, Samuel P D, Sarah, H., Trainer, M.G., Corlies, P., Malaska, M.J., Brien, E.S., Thelen, A.E., Turtle, E.P., Radebaugh, J., Hanley, J., Solomonidou, A., Newman, C., Regoli, L., Rodriguez, S., Seignovert, B., Hayes, A.G., Journaux, B., Steckloff, J.K., Nna-Mvondo, D., Cornet, T., Palmer, M.Y., Lopes, R.M.C., Vinatier, S., Lorenz, R.D., Nixon, C., Czaplinski, E., Barnes, J.W., Sittler, E., Coates, A., 2021. Titan: Earth-like on the Outside, Ocean World on the Inside. Planet. Sci. J., 2, 112.

Malaska, M.J., Lopes, R.M., Hayes, A.G., Radebaugh, J., Lorenz, R.D., Turtle, E.P., 2016. Material transport map of Titan: The fate of dunes. Icarus, 270, 183–196. https://doi.org/10.1016/j.icarus.2015.09.029

Mastrogiuseppe, M., Hayes, A., Poggiali, V., Seu, R., Lunine, J.I., Hofgartner, J.D., 2016. Radar Sounding Using the Cassini Altimeter: Waveform Modeling and Monte Carlo Approach for Data Inversion of Observations of Titan's Seas. IEEE Trans. Geosci. Remote Sens. 54, 5646–5656. https://doi.org/10.2190/RM36-JLXA-6WUY-KDQ2

Mastrogiuseppe, M., Poggiali, V., Hayes, A., Lorenz, R., Lunine, J., Picardi, G., Seu, R., Flamini, E., Mitri, G., Notarnicola, C., Paillou, P., Zebker, H., 2014. The bathymetry of a Titan sea. Geophys. Res. Lett. 41, 1432–1437. https://doi.org/10.1002/ 2013GL058618. Received

Mastrogiuseppe, M., Poggiali, V., Hayes, A.G., Lunine, J.I., Seu, R., Di Achille, G., Lorenz, R.D., 2018. Cassini radar observation of Punga Mare and environs: Bathymetry and composition. Earth Planet. Sci. Lett. 496, 89–95. https://doi.org/10.1016/j.epsl.2018.05.033

Mitri, G., Showman, A.P., Lunine, J.I., Lopes, R.M.C., 2008. Resurfacing of Titan by ammonia-water cryomagma. Icarus 196, 216–224. https://doi.org/10.1016/j.icarus.2008.02.024

Moore, J.M., Howard, A.D., 2010. Are the basins of Titan's Hotei Regio and Tui Regio sites of former low latitude seas? Geophys. Res. Lett. 37, L22205. https://doi.org/10.1029/2010GL045234

Moriconi, M.L., Lunine, J.I., Adriani, A., Aversa, E.D., Negrão, A., Filacchione, G., Coradini, A., 2010. Characterization of Titan's Ontario Lacus region from Cassini/VIMS observations. Icarus 210, 823–831. https://doi.org/10.1016/j.icarus.2010.07.023

Neish, C.D., Kirk, R.L., Lorenz, R.D., Bray, V.J., Schenk, P., Stiles, B.W., Turtle, E., Mitchell, K., Hayes, A., Cassini RADAR Team, 2013. Crater topography on Titan: Implications for landscape evolution. Icarus 223, 82–90. https://doi.org/10.1016/j.icarus.2012.11.030

Neish, C.D., Lorenz, R.D., 2014. Elevation distribution of Titan's craters suggests extensive wetlands. Icarus 228, 27–34. https://doi.org/10.1016/j.icarus.2013.09.024

Neish, C.D., Lorenz, R.D., 2012. Titan's global crater population: A new assessment. Planet. Space Sci. 60, 26–33. https://doi.org/10.1016/j.pss.2011.02.016

Neish, C.D., Lorenz, R.D., Brien, D.P.O., Team, R., 2006. The potential for prebiotic chemistry in the possible cryovolcanic dome Ganesa Macula on Titan. Int. J. Astrobiol. 5, 57–65. https://doi.org/10.1017/S1473550406002898

Neish, C.D., Molaro, J.L., Lora, J.M., Howard, A.D., Kirk, R.L., Schenk, P., Bray, V.J., Lorenz, R.D., 2016. Fluvial erosion as a mechanism for crater modification on Titan. Icarus 270, 114–129. https://doi.org/10.1016/j.icarus.2015.07.022

Owen, T., 2005. Huygens rediscovers Titan. Nature 438, 756–757.

Perron, J.T., Lamb, M.P., Koven, C.D., Fung, I.Y., Yager, E., 2006. Valley formation and methane precipitation rates on Titan. J. Geophys. Res. 111, E11001. https://doi.org/10.1029/2005JE002602

Porco, C.C., West, R.A., Squyres, S., McEwen, A., Thomas, P., Murray, C.D., Delgenio, A., Ingersoll, A.P., Johnson, T. V, Neukum, G., Veverka, J., Dones, L., Brahic, A., Burns, J.A., Haemmerle, V., Knowles, B., Dawson, D., Roatsch, T., Beurle, K., Owen, W., 2004. Cassini Imaging Science: Instrument Characteristics and Anticipated Scientific Investigations at Saturn. Sp. Sci Rev 115, 363–497.

Radebaugh, J., Lorenz, R.D., Lunine, J.I., Wall, S.D., Boubin, G., Reffet, E., Kirk, R.L., Lopes, R.M., Stofan, E.R., Soderblom, L., Allison, M., Janssen, M., Paillou, P., Callahan, P., Spencer, C., Cassini Radar Team, 2008. Dunes on Titan observed by Cassini Radar. Icarus 194, 690–703. https://doi.org/10.1016/j.icarus.2007.10.015

Soderblom, J.M., Brown, R.H., Soderblom, L.A., Barnes, J.W., Jaumann, R., Le, S., Sotin, C., Stephan, K., Baines, K.H., Buratti, B.J., Clark, R.N., Nicholson, P.D., 2010. Geology of the Selk crater region on Titan from Cassini VIMS observations. Icarus 208, 905–912. https://doi.org/10.1016/j.icarus.2010.03.001

Solomonidou, A., Neish, C., Coustenis, A., Malaska, M., Gall, A. Le, Lopes, R.M.C., Werynski, A., Markonis, Y., Lawrence, K., Altobelli, N., Witasse, O., Schoenfeld, A., Matsoukas, C., Baziotis, I., Drossart, P., 2020. Astrophysics The chemical composition of impact craters on Titan I. Implications for exogenic processing. Astron. Astrophys. 16, 1–14.

Stiles, B.W., Hensley, S., Gim, Y., Bates, D.M., Kirk, R.L., Hayes, A., Radebaugh, J., Lorenz, R.D., Mitchell, K.L., Callahan, P.S., Zebker, H., Johnson, W.T.K., Wall, S.D., Lunine, J.I., Wood, C.A., Janssen, M., Pelletier, F., West, R.D., 2009. Determining Titan surface topography from Cassini SAR data ☆. Icarus 202, 584–598. https://doi.org/10.1016/j.icarus.2009.03.032

Stofan, E.R., Elachi, C., Lunine, J.I., Lorenz, R.D., Stiles, B., Mitchell, K.L., Ostro, S., Soderblom, L., Wood, C., Zebker, H., Wall, S., Janssen, M., Kirk, R., Lopes, R., Paganelli, F., Radebaugh, J., Wye, L., Anderson, Y., Allison, M., Boehmer, R., Callahan, P., Encrenaz, P., Flamini, E., Francescetti, G., Gim, Y., Hamilton, G., Hensley, S., Johnson, W.T.K., Kelleher, K., Muhleman, D., Paillou, P., Picardi, G., Posa, F., Roth, L., Seu, R., Shaffer, S., Vetrella, S., West, R., 2007. The lakes of Titan. Nature 445, 61–64. https://doi.org/10.1038/nature05438

Stofan, E.R., Lunine, J.I., Lorenz, R.D., Aharonson, O., Bierhaus, E., Clark, B., Griffith, C., Harri, A.-M., Karkoschka, E., Kirk, R., Kantsiper, B., Mahaffy, P., Newman, C., Ravine, M., Trainer, M., Waite, H., Zarnecki, J., 2010. EXPLORING THE SEAS OF TITAN: THE TITAN MARE EXPLORER (TiME) MISSION, in: 41st Lunar and Planetary Science Conference. p. 1236. https://doi.org/10.1038/nature05438.

Tomasko, M.G., Archinal, B., Becker, T., Bézard, B., Bushroe, M., Combes, M., Cook, D., Coustenis, A., Bergh, C. de, Dafoe, L.E., Doose, L., Doute, S., 2005. Rain, winds and haze during the Huygens probe's descent to Titan's surface. Nature 438, 765–778. https://doi.org/10.1038/nature04126

Trainer, M.G., Pavlov, A.A., Dewitt, H.L., Jimenez, J.L., Mckay, C.P., Toon, O.B., Tolbert, M.A., 2006. Organic haze on Titan and the early Earth. Proc. Natinoal Acad. Sci. United States Am. 103, 18035–18042. https://doi.org/10.1073/pnas.0608561103

Turtle, E.P., Barnes, J.W., Trainer, M.G., Lorenz, R.D., Hibbard, K.E., Adams, D.S., Bedini, P., Brinckerhoff, W.B., Ernst, C., Freissinet, C., Hand, K., Hayes, A.G., Johnson, J.R., Karkoschka, E., Langelaan, J.W., Gall, A. Le, Lora, J.M., Mackenzie, S.M., Mckay, C.P., Neish, C.D., Newman, C.E., Palacios, J., Parsons, A.M., Peplowski, P.N., Radebaugh, J., Rafkin, S.C.R., Ravine, M.A., Schmitz, S., Soderblom, J.M., Sotzen, S., Stickle, A.M., Stofan, E.R., Tokano, T., Wilson, C., Yingst, R.A., Zacny, K., Hopkins, J., Physics, A., Spatiales, O., Angeles, L., Field, M., Space, M., Systems, S., Diego, S., Robotics, H., 2018. Dragonfly: In Situ Exploration of Titan's Organic Chemistry and Habitability, in: 49th LPSC. p. Abstract 1641. https://doi.org/10.1109/AERO.2013.6497165.

Wasiak, F.C., Luspay-Kuti, A., Welivitiya, W.D.D.P., Roe, L.A., Chevrier, V.F., Blackburn, D.G., Cornet, T., 2013. A facility for simulating Titan's environment. Adv. Sp. Res. 51, 1213–1220. https://doi.org/10.1016/j.asr.2012.10.020

Werynski, A., Neish, C.D., Gall, A. Le, Janssen, M.A., Team, C.R., 2019. Compositional variations of Titan's impact craters indicates active surface erosion. Icarus 321, 508–521. https://doi.org/10.1016/j.icarus.2018.12.007

Yung, Y.L., Allen, M., Pinto, J.P., 1984. Photochemistry of the Atmosphere of Titan: Comparison Between Model and Observations. Astrophys. J. Suppl. Ser. 55, 465–506.

CHAPTER 1. EXPERIMENTAL STUDY OF ETHYLENE EVAPORITES UNDER TITAN CONDITIONS

Ellen C. Czaplinski[1], Woodrow A. Gilbertson[2], Kendra K. Farnsworth[1], and Vincent F. Chevrier[1]

[1]Arkansas Center for Space and Planetary Sciences, University of Arkansas, Fayetteville, AR 72701, USA
[2]Department of Physics, University of Arkansas, Fayetteville, AR 72701, USA

Czaplinski, E. C., Gilbertson, W. A., Farnsworth, K. K., & Chevrier, V. F. (2019). Experimental Study of Ethylene Evaporites under Titan Conditions. *ACS Earth and Space Chemistry*, *3*, 2353-2362. https://doi.org/10.1021/acsearthspacechem.9b00204

Keywords: Titan, IR spectroscopy, experimental techniques, evaporite, organics

Highlights:

- Ethylene evaporites were created in the laboratory under Titan surface conditions
- Solubility and evaporation rates were measured for three types of experiments
- Evaporite preferentially forms with methane
- Spectral shifts and the presence of a band at 1.666 μm confirms evaporite formation
- Upper limit of ethylene evaporite thickness on Titan is ~9 m

1. Abstract

Titan has an abundance of lakes and seas, as confirmed by Cassini. Major components of these liquid bodies include methane (CH_4) and ethane (C_2H_6); however, evidence indicates that minor components such as ethylene (C_2H_4) may also exist in the lakes. As the lake levels drop, 5 μm-bright deposits, resembling evaporite deposits on earth, are left behind. Here, we provide saturation values, evaporation rates, and constraints on ethylene evaporite formation by using a Titan simulation chamber capable of reproducing Titan surface conditions (89−94 K, 1.5 bar N_2). Experimental samples were analyzed using Fourier transform infrared spectroscopy, mass, and temperature readings. Ethylene evaporites form more quickly in a methane solvent than in an ethane solvent or in a mixture of methane/ethane. We measured an average evaporation rate of $(2.8 \pm 0.3) \times 10^{-4}$ kg m^{-2} s^{-1} for methane and an average upper limit evaporation rate of < 5.5 x

10^{-6} kg m^{-2} s^{-1} for ethane for ethane. Additionally, we observed red shifts in ethylene absorption bands at 1.630 and 2.121 μm and the persistence of a methane band at 1.666 μm.

2. Introduction

Titan's complex lakes of liquid methane/ethane have intrigued scientists for over a decade. In addition to the lakes and seas we observe today, Titan's past details a history of intricate evaporation processes. The identification of probable evaporite deposits at Titan's north pole, south of Ligeia Mare (Barnes et al., 2011; Hayes et al., 2008) included several "dry" lakebeds showing a unique signature that was bright in the 5-μm window of the Visual Infrared Mapping Spectrometer (VIMS).

These 5-μm-bright regions have been extensively studied and classified as non-water ice materials (Barnes et al., 2005; MacKenzie and Barnes, 2016). The 5-μm-bright deposits discovered at Ontario Lacus, described as "bathtub rings" of low water ice condensates, may have been deposited in the past when lake levels were higher (Barnes et al., 2009; Cornet et al., 2012). Although the exact composition of these 5-μm-bright regions is unknown, previous studies indicate they may be evaporitic in origin (Barnes et al., 2011; Cordier et al., 2016, 2013; MacKenzie and Barnes, 2016; MacKenzie et al., 2014). Evaporites form when dissolved solids precipitate out of a saturated solution as that liquid solvent evaporates. Evaporation of the solvent causes the solute to deposit as an evaporite either onto the surface (if all liquid has evaporated), or at the bottom of the saturated liquid (if not all liquid has evaporated; MacKenzie et al., 2014). We therefore sought to study Titan-relevant evaporite materials in the laboratory to better constrain the processes that may be occurring in and around Titan's lakes.

Recent evaporite studies have included models and theoretical work, (Cordier et al., 2016, 2013) and some groups are also experimentally working to constrain potential solvents and solutes that may be active in evaporite formation (Cable et al., 2018, 2014; Czaplinski et al., 2018, 2017; Malaska and Hodyss, 2014; Vu et al., 2014). These previous studies have focused on a number of potential evaporite compounds including: C_6H_6/C_2H_6 and C_2H_2/NH_3, and C_2H_2/C_2H_4. Roe et al. (2004) observed a significant increase of ethylene in Titan's polar stratosphere (late southern spring time), suggesting that ethylene may be a common compound in Titan's polar regions, and a possible constituent dissolved in the polar lakes (Singh et al., 2017). However, the high solubility values of ethylene in methane/ethane indicate that the lakes contain less ethylene than its saturation value (Singh et al., 2017).

Here, we focus on ethylene (C_2H_4) as a potential evaporite, dissolved in liquid methane, ethane, and methane/ethane. The objective of this paper is to provide laboratory context for ethylene evaporite studies on Titan to aid in the understanding of evaporite composition, which is currently unknown. We note that studying a single evaporite compound (e.g. ethylene) is a simplification of what we presume to occur on Titan, however it is important to isolate evaporation rates and detection requirements of simple mixtures before studying more complex scenarios.

3. Experimental Methods

3.1. Titan Simulation Chamber

Experiments were performed using a facility at the University of Arkansas that was designed to simulate surface conditions on Titan (Wasiak et al., 2013). This facility consists of the larger host chamber (Andromeda) with a smaller subsection (the Titan module) where the Temperature Control Box (TCB) sits (Figure 1). Titan-relevant temperatures (89 – 94 K) were produced by liquid nitrogen flow through coils located both inside and outside of the TCB, and inside the condenser. A 1.5 bar atmosphere was maintained via pressurized nitrogen. Once adequate temperatures were reached, the sample was introduced to the condenser where it condensed, then exited the bottom of the condenser through a filter and remained in a sample dish (15 cm diameter x 2 cm deep). We collected Fourier-Transform Infrared (FTIR) spectra of the sample using a Nicolet® 6700 FTIR spectrometer (equipped with a TEC InGaAs® 2.6 µm detector and CaF_2 beam-splitter) operating from 1 to 2.6 µm with a spectral sampling of 4 cm^{-1}, spectral resolution of 0.01 cm^{-1}, and connected to a fiber optic probe located above the sample dish. The bottom of the dish is covered by Spectralon® (from LabSphere), a fluoropolymer that has its highest diffuse (Lambertian) performance in the IR portion of the spectrum, which serves as the background for all FTIR measurements. Sample mass was continuously measured by a Sartorius® GE812 precision balance (precision of 0.01 g). Temperatures of the sample mixture and TCB were constantly monitored via eight K-type (+/- 2.2°C) thermocouples placed throughout (two in the condenser, two on either side of the condenser, one near the FTIR probe, one in the filter, one just above the sample dish, and one directly touching the mixture in the sample dish) and connected to a USB data acquisition module (see Fig. 1 for placement).

3.2. Experimental Protocol

To perform evaporite experiments, we began by purging the Titan chamber with nitrogen (Airgas® industrial grade, >99.998%) for 10 minutes (Singh et al., 2017) to remove any contaminants from previous experiments. Next, the condenser was independently purged with nitrogen by opening the solenoid and exhaust valves for 10 minutes (Singh et al., 2017) to remove any contaminants. We also maintained a pressure of 1.5 bar in the chamber with

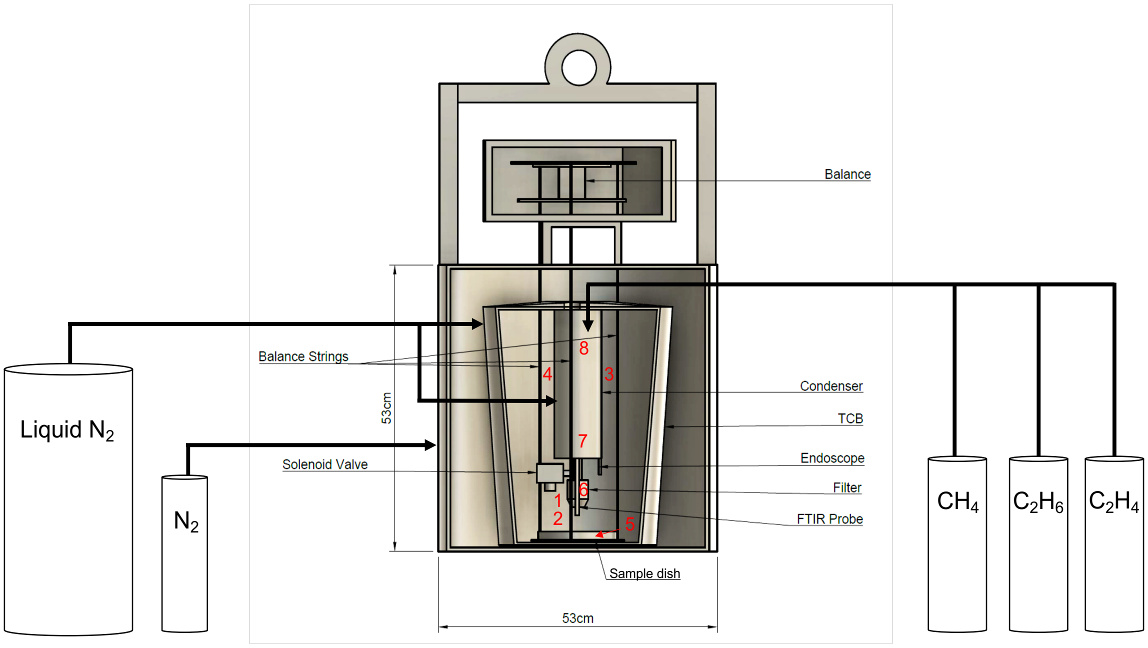

Figure 1. Schematic view of the Titan simulation chamber showing a cross-section of the Titan module, which includes the balance and temperature control box (TCB; to scale). Gas cylinders and feedthroughs are for reference and are not to scale. Red numbers correspond to the locations of different thermocouples. 1 is attached to the FTIR probe (~3 cm above sample), 2 is the atmospheric temperature above the sample (~2 cm), 3 and 4 are the upper atmosphere temperature (~15-20 cm above the sample), 5 is the sample temperature, 6 is the filter temperature, and 7 and 8 are the condenser temperatures. (Modified from Farnsworth et al., 2019).

nitrogen, monitored by a Matheson 63-3161 pressure gauge (0 – 60 psi). After both purges, we started the flow of liquid nitrogen, which cools both the TCB and condenser. We then collected a background FTIR spectrum of the Spectralon® on the sample dish using Omnic^{TM} FTIR software. Next, we started recording temperature and mass data using LabVIEW software. Experimental time (in minutes), which will be referenced herein, is synchronized with the initiation of the LabVIEW software.

During evaporite experiments, ethylene must dissolve in the solvent mixture before it is introduced to the sample dish. To achieve this, we first injected the gaseous solute (Airgas® ultra high purity, 99.9% ethylene) into the condenser, where it condenses to liquid phase below ~104

K. We then introduced gaseous methane (Airgas® chemically pure grade, 99.5%), ethane (Airgas® chemically pure grade, 99.5%), or both into the condenser for approximately 10 seconds, to undergo phase transition below ~113 K. For reference, at 1.5 bar, methane and ethane are in the liquid phase from ~123 K to 90 K and ~ 184 K to 90 K, respectively. After dissolving ethylene throughout a 10 minute equilibration period, (Singh et al., 2017) a solenoid valve was opened, allowing the mixture to exit the bottom of the condenser through a glass-fritted filter (40-60 µm pore size). This filtering process ensures that no solid particles >40 µm in diameter travel through to the sample dish, and was monitored with an endoscope camera. The solenoid valve was closed after all the liquid exited the condenser. After the mixture was transferred to the sample dish, FTIR spectral measurements were acquired every ~10 minutes with a resolution of 4 cm^{-1} and an average of 450 scans. Titan surface temperatures (~89 K – 94 K) were sustained after the mixture was poured onto the Spectralon® in the sample dish to simulate Titan's surface temperature and pressure.

It is important to note that our experimental setup only allows approximate abundances of gases to be added during the experiment, and it is not until after the experiment is finished and the spectra are analyzed by our spectral unmixing model that we can determine the exact percentages of each compound in the experiment (See Spectral Unmixing Model Section). We calculated band depths using the Omnic software, which outputs relative reflectance values. Error from these band depth measurements is from the average noise of the spectrometer, which was calculated by taking the standard deviation of the reflectance values from 1.45 – 1.55 µm, as this is a relatively "flat" portion of our experimental spectra with no absorption bands. These standard deviation values were inserted as error bars to each respective sample point on the band depth graphs.

Evaporite detection required that the solvent (ethane/methane) evaporated gradually, leaving behind some residual solute (ethylene). For the methane experiments, we maintained Titan temperatures in the TCB because methane readily evaporates at Titan conditions (Luspay-Kuti et al., 2015, 2012). However, ethane evaporation on the timescales of our experiments is negligible (Luspay-Kuti et al., 2015), therefore to induce ethane evaporation, the temperature of the sample was increased. For ethane/ethylene mixtures, we maintained Titan temperatures (~94 K) for one experiment, and slowly warmed the sample to ~139 K for a second experiment. Although ethylene is in liquid phase at the warmer temperatures during the forced evaporation experiment, we note that this could be a local mechanism to enrich a lake in ethylene, while further cooling of the lake may allow ethylene to precipitate.

3.3. Spectral Unmixing Model

Various spectra of the pure components (CH_4, C_2H_6, C_2H_4) were recorded before use in these experiments (Fig. 2). The pure spectra recorded included both liquid and solid phases of ethylene and ethane, and the liquid phase of methane. Any compound mixture should have a spectrum that is some combination of the spectra of its components. We wrote a Python code to decompose a given spectrum into a best fit of linear combinations of pure spectra added together. This technique provided the weighted composition of the mixture throughout the evaporation process. For compound spectra (*C*) with *i* components, the Python code breaks down *C* into pure spectra (*P*) as follows:

$$C = A + B\lambda + \sum_i x_i P_i$$

The A and $B\lambda$ terms allowed for the correct of a constant offset and baseline slope, respectively. The spectra tended to increase in reflectance throughout the duration of an experiment, which lead to a vertical offset. Due to instrumental error there was also an occasional slope to the baseline of the reflectance, which was corrected with a simple wavelength (λ) dependent linear term. The mole fraction of a pure spectrum (x_i) was normalized so the sum added to 100%. This process is similar to previous studies (Singh et al., 2017), but is an original process for these experiments. The reflectivity of a component was assumed to be proportional to the number of moles of that component, thus the mole fraction of each pure spectrum can be calculated from the compound spectrum. The component percentages listed in the Results section are all the mole fractions given by this analysis. Also listed is the goodness of fit (Table S1), which is defined by total chi-squared value divided by the degrees of freedom. All of our values are close to 1, which shows that the spectral unmixing model is doing an acceptable job. Values significantly lower than 1 would be a sign of over-fitting the data, and likewise values significantly larger than 1 would be a sign of under-fitting the data. The largest final value for goodness of fit (1.37) shows that our model is, at worst, significant with a critical value of 2.5%. Other goodness of fit values all show significance with critical values of 1%.

We assume that this is an accurate method, as the pure spectra were recorded in both liquid and solid phases stable at Titan temperature and pressure in our chamber. This allowed us to model compound mixtures that are both liquid-liquid, as well as solid-liquid to capture the formation of evaporites. The only error introduced would come from the spectrometer. This error is largely accounted for in the $B\lambda$ term, and utilized in the chi-squared minimization used to find the best fit.

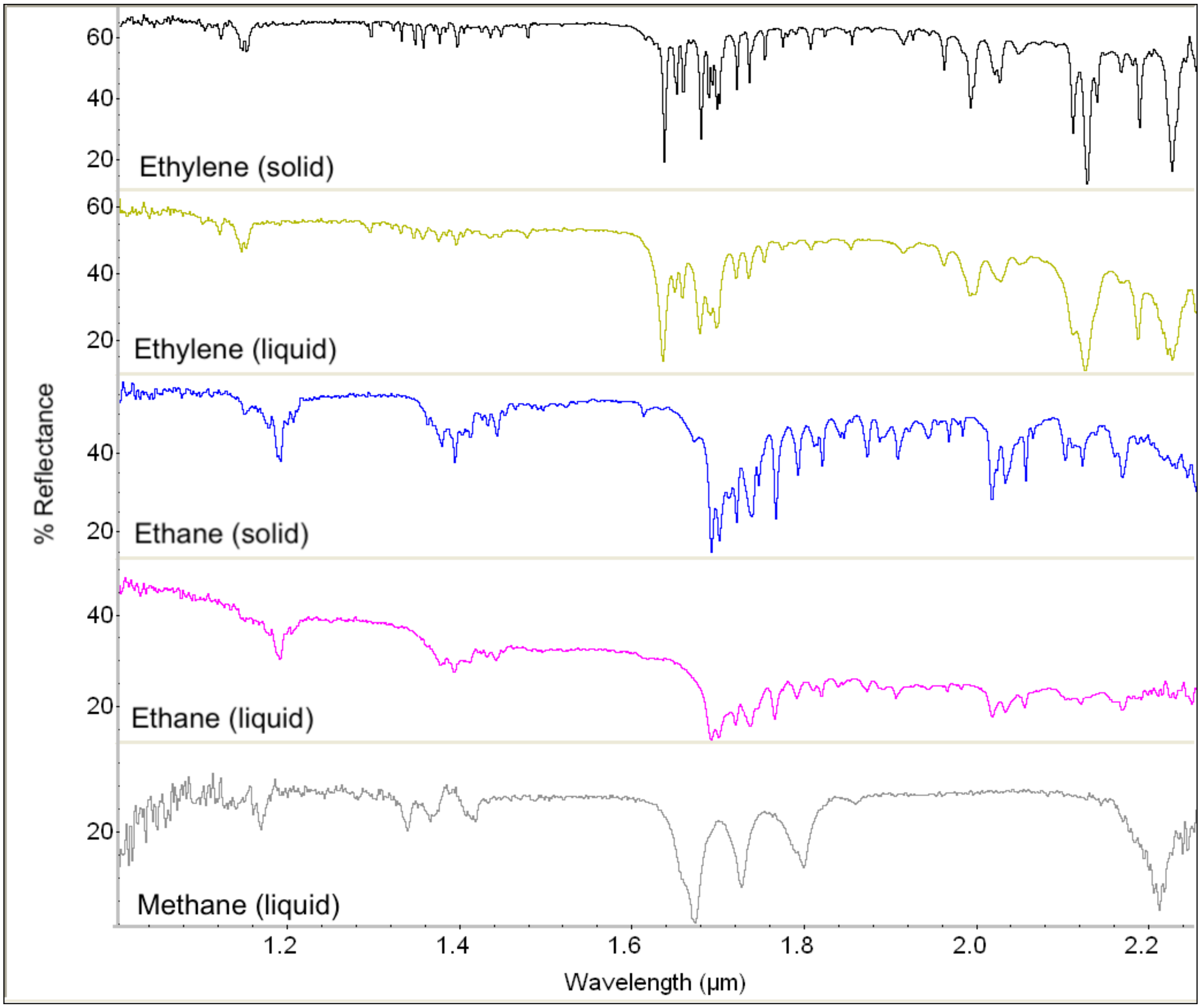

Figure 2. Pure spectra from each species used in this study. Black, solid ethylene; gold, liquid ethylene; blue, solid ethane; magenta, liquid ethane; and gray, liquid methane.

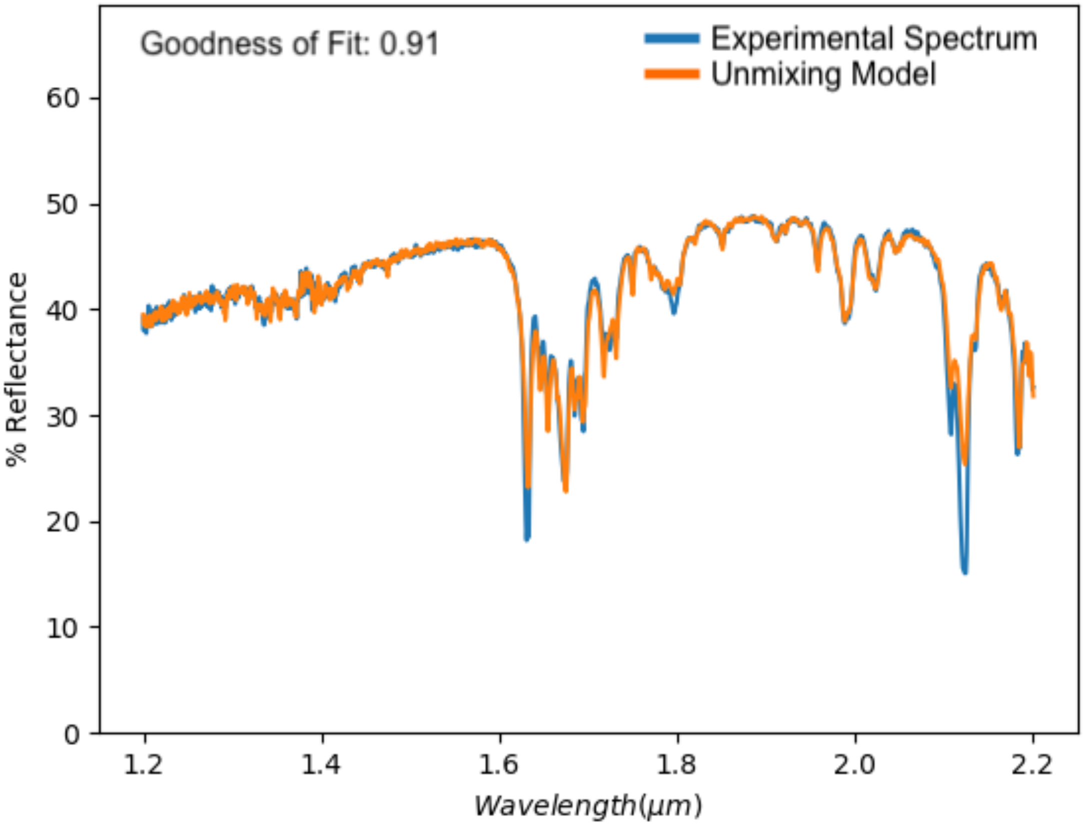

Figure 3. Example of a spectrum from the unmixing model (orange) compared to an experimental spectrum (blue) from a methane/ethylene experiment. This was during the methane evaporation phase with methane and ethylene components at 57% and 43%, respectively. Our model accurately fits highly mixed spectra, as shown.

4. Results

Here, we present NIR reflectance spectra for three types of example experiments: methane/ethylene, ethane/ethylene, and methane/ethane/ethylene. Each experiment has been repeated several times. Additional spectral, mass, and temperature data from repeated experiments can be found in supporting information. Table 1 shows fundamental vibrational frequencies and band assignments for these compounds of interest, as they will be referenced to throughout the paper. Because the edges of our wavelength range show significant noise, we focus on the range from ~1.3 – 2.3 µm, for clarity.

Table 1. Spectral band assignments for the compounds used in this study.

Compound	Assignment	Sample Condition	Freq (cm^{-1})	Freq (μm)	This Study (μm)
CH$_4$	$2v_3$	CH$_4$ in liquid Ar[#]	5991	1.669170422	1.669
	$v_1/v_3 + v_2 + v_4$	CH$_4$ in liquid Ar[#]	5805	1.722652885	1.723
		CH$_4$ liquid[#]	5801	1.723840717	
	$v_1 + 2v_4$	CH$_4$ in liquid Ar[#]	5573	1.794365692	1.796
		CH$_4$ liquid[#]	5564	1.797268152	
C$_2$H$_6$	$v_7 + v_{10}$	room temp, 30 mbar[^]	5948.338	1.681141858	1.688
	$2v_1$	room temp, 30 mbar[^]	5901.3	1.694541881	1.697
					2.014
					2.030
C$_2$H$_4$	$v_5 + v_9$	C$_2$H$_4$ in liquid Ar[+]	6142.5	1.628001628	1.632 (liq)
		C$_2$H$_4$ at 110 K[+]	6126.6	1.632226684	1.634 (sol)
	$v_9 + v_2$	C$_2$H$_4$ in liquid Ar[+]	4723.2	2.117208672	2.123 (liq)
		C$_2$H$_4$ at 110 K[+]	4710.6	2.122871821	2.125 (sol)

[#] From Blunt et al. (Blunt et al., 1997)
[^] From Hepp and Herman (Hepp and Herman, 2000)
[+] From Brock et al. (Brock et al., 1994)

4.1. Methane and Ethylene

For this experiment, we added 76.3% methane and 23.7% ethylene to the condenser. Offset reflectance FTIR spectra from these experiments are shown in Figure 4 (left). The red spectrum in Figure 4 represents the first spectrum of the experiment (t = 81 min), immediately after the mixture was poured onto the sample dish from the condenser. The black spectrum shows an intermediate spectrum (t = 136 min). The blue spectrum in Figure 4 represents the final spectrum of the experiment (t = 230 min), which ended with 2.0% methane and 98.0% ethylene. Throughout the experiment, the baseline reflectance increased, starting around 40% and ending at approximately 80%.

Mass data for the methane/ethylene experiment shows that the sample was poured in the dish at ~70 minutes, reaching a maximum mass of ~11.3 grams before methane began evaporating after ~90 minutes (Fig. 4, right). Herein, we note that all reported mass data has been corrected for a slight mass drift inherent to the balance at these extremely low temperatures (described in detail in Supporting Information). We report a methane evaporation rate of (2.6 ± 0.4) x 10^{-4} kg m^{-2} s^{-1} (Table 2), which is consistent with previously reported experimental values on pure methane evaporation.

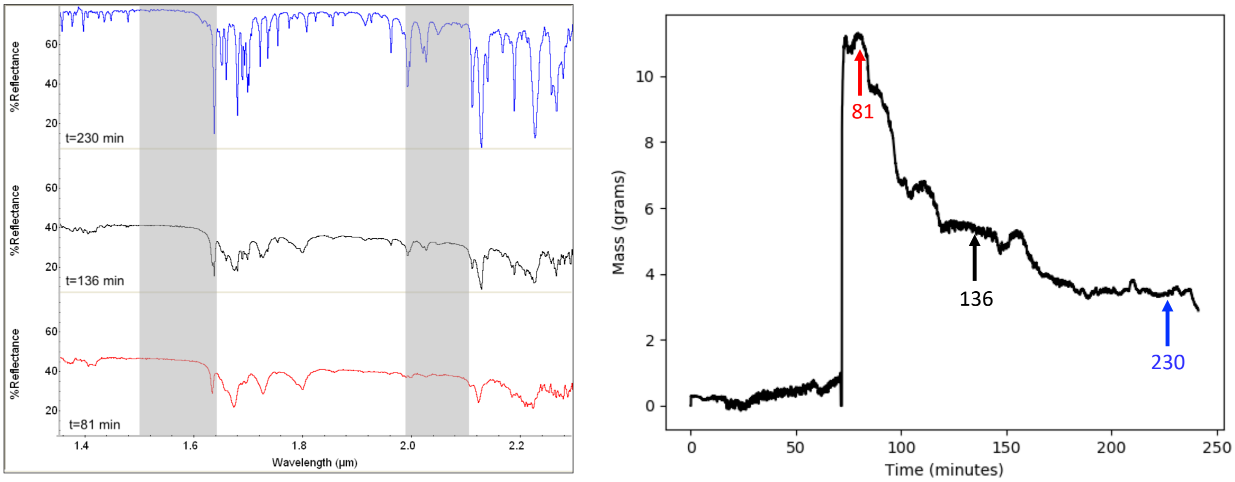

Figure 4. Methane/ethylene spectra, offset for clarity (left). Initial spectrum is shown in red, intermediate in black, and final in blue. Gray vertical bars indicate VIMS windows. Notice the increase in reflectance throughout the experiment. Mass data from the methane/ethylene experiment (right). Mass was approximately zero before the mixture was poured in the sample dish (~70 min), and reached a maximum mass of ~11.3 grams. Methane evaporated throughout the experiment, as seen by the almost immediate decrease in mass after ~90 minutes. Colored arrows correspond with the time each spectrum was taken.

Band depth calculations were performed on the major absorption bands of methane (1.669 μm, 1.723 μm, 1.796 μm) and ethylene (1.630 μm, 2.121 μm). As experiment time increased, the methane bands decreased in depth, while the ethylene bands increased in depth. The 1.669 μm methane band decreased in relative reflectance from 9.9% to 0.0%, the 1.723 μm methane band decreased from 11.0% to 0.3%, and the 1.796 μm methane band decreased from 8.3% to 0.0% (Fig. 5). Ethylene bands at 1.630 μm and 2.121 μm increased in relative reflectance from 12.2% to 57.6%, and 9.2% to 49.7%, respectively (Fig. 5). Notice how this increase coincides with the lowest relative reflectance value of methane before reaching zero. Additionally, the decrease in methane band depths throughout the experiment is relatively linear unlike the sharp, fourfold increase observed in the ethylene band depths at ~150 minutes (Fig. 5).

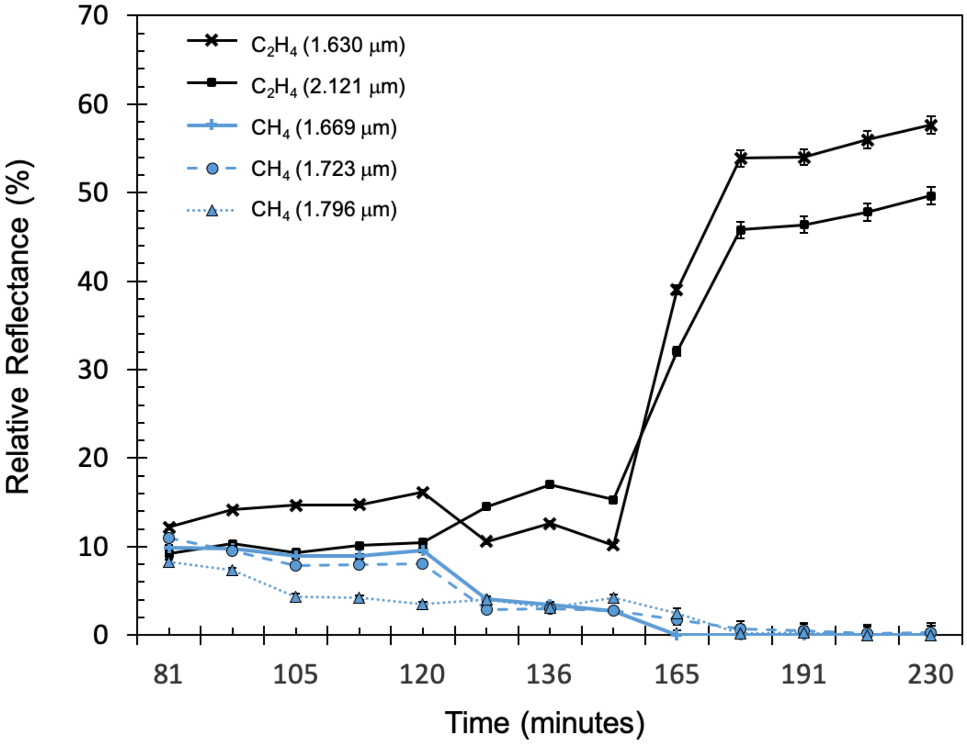

Figure 5. Methane band depths (blue) from the methane/ethylene experiment show a decrease in characteristic methane bands (1.669 µm, 1.723 µm, 1.796 µm), while ethylene band depths (black) show an increase in characteristic ethylene bands (1.630 µm, 2.121 µm). The sudden increase of ethylene band depths at ~150 minutes most likely indicates saturation. Error bars are the same size or smaller than point markers.

We observed red shifts of the 1.630 µm and 2.121 µm ethylene bands by 0.003 µm and 0.004 µm, respectively (Fig. 6 A,B). Given that the spectral resolution of the spectrometer is 0.01cm^{-1} and the 0.003 µm and 0.004 µm red shifts correspond to shifts of 11.271 cm^{-1} and 8.875 cm^{-1}, respectively, these red shifts are well within the resolvable range of the spectrometer. The last spectral measurement taken is shown by the blue spectrum (Fig. 4, left), and nearly matches the pure ethylene spectrum (Fig. 2). It is not an exact match because a band at 1.666 µm is still

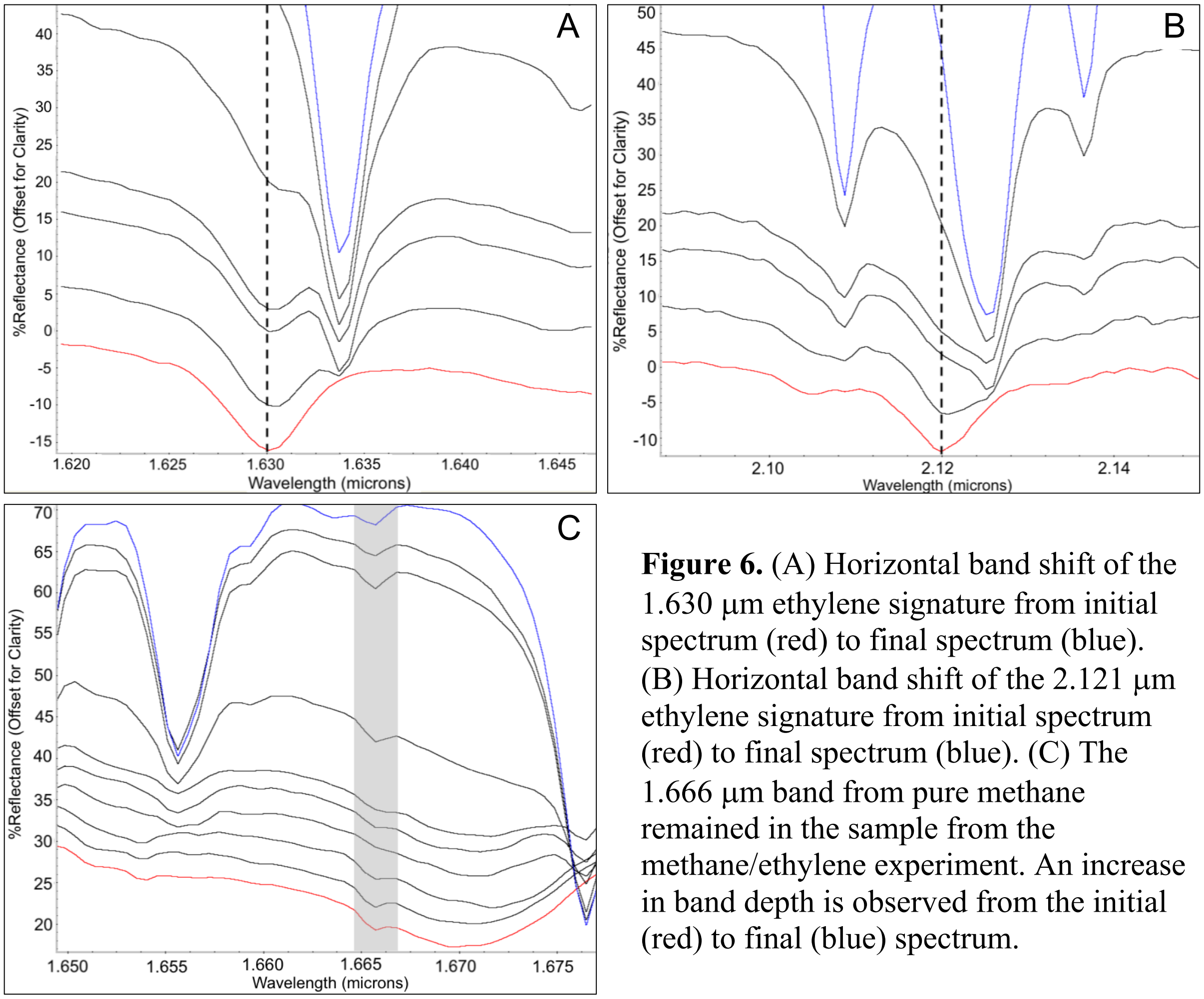

Figure 6. (A) Horizontal band shift of the 1.630 µm ethylene signature from initial spectrum (red) to final spectrum (blue). (B) Horizontal band shift of the 2.121 µm ethylene signature from initial spectrum (red) to final spectrum (blue). (C) The 1.666 µm band from pure methane remained in the sample from the methane/ethylene experiment. An increase in band depth is observed from the initial (red) to final (blue) spectrum.

present in the final spectrum of the experiment (Fig. 6C). This 1.666 µm band originates from the first overtone region of the pure methane spectrum, but does not disappear throughout the duration of the experiment like all other methane bands.

4.2. Ethane and Ethylene

90 K Experiment: This experiment consisted of 87.9% ethane and 12.1% ethylene, initially. Figure 7 (left) shows the offset FTIR spectra. The first spectrum was taken immediately after the mixture was poured onto the sample dish ($t = 95$ min), and is indicated by the red spectrum in Figure 7. An intermediate spectrum was taken at $t = 132$ min. The final spectrum for this experiment is highlighted in blue in Figure 7 ($t = 187$ min) and contained 76.0% ethane, and

24.0% ethylene. The spectrum in Figure 7 shows an approximately constant baseline reflectance around 35% - 40%, and minor variations in band depth.

Figure 7 (right) shows the mass data for this experiment. This experiment included two pours due to nonideal chamber conditions after the first pour. The analyzed ethane/ethylene sample was poured onto the petri dish ~85 minutes after the start of the experiment. After the pour, the mass remained constant (~20 g). We report an upper limit ethane evaporation rate of < 7.0 x 10^{-6} kg m^{-2} s^{-1} (Table 2), which is consistent with the upper limit previously reported by Luspay-Kuti et al. (2015).

No red shifts of any bands are present in the spectra when comparing to the pure endmembers of ethane and ethylene (Fig. 2). Band depth calculations (Fig. 8) were performed on ethane bands (1.688 µm, 1.697 µm, 2.014 µm, and 2.030 µm) and ethylene bands (1.630 µm, 2.121 µm). As time increased, ethylene band depths consistently increased, while ethane band depths remained constant throughout the experiment. The average relative reflectance values of the 1.688 µm, 1.697 µm, 2.014 µm, and 2.030 µm ethane bands were 4.0%, 2.3%, 3.9%, and 2.3%, respectively (Fig. 8). The 1.630 µm ethylene band depths increased in relative reflectance from 1.61% to 6.59%, whereas the 2.121 µm ethylene band depths increased from 1.7% to 3.0% (Fig. 8).

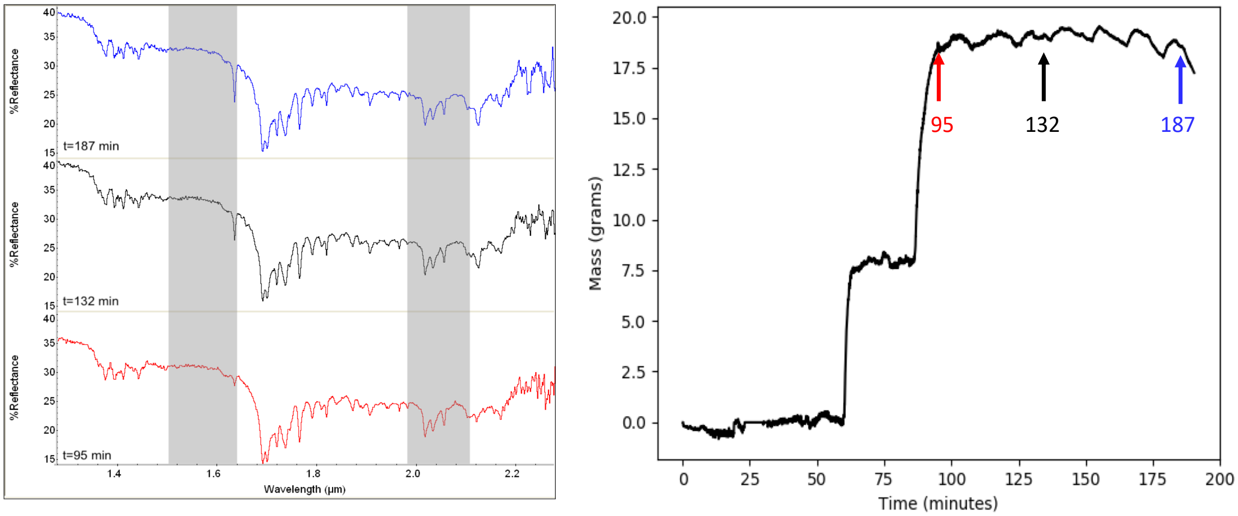

Figure 7: Ethane/ethylene spectra, offset for clarity (left). Initial spectrum is shown in red, intermediate in black, and final in blue. Vertical, gray bars indicate VIMS windows. Notice the increase in reflectance throughout the experiment. Mass data from the ethane/ethylene 90 K experiment (right) shows two separate pours due to nonideal chamber conditions in the first pour: one at ~60 minutes and one at ~80 minutes. Spectral analysis only includes data after the second pour. Notice the relatively stable mass from ~100 minutes to the end of the experiment. Colored arrows correspond with the time each spectrum was taken.

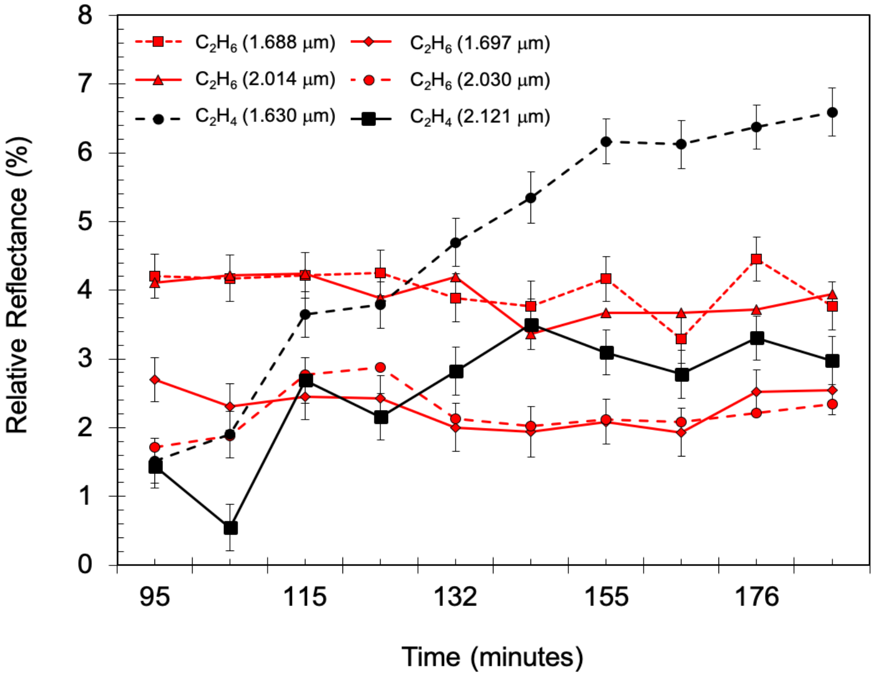

Figure 8. Ethane band depths (red) from the 90 K ethane/ethylene experiment show no overall change in characteristic ethane bands (1.688 μm, 1.697 μm, 2.014 μm, and 2.030 μm), while ethylene band depths (black) show an increase in characteristic ethylene bands (1.630 μm and 2.121 μm).

4.3. Forced Evaporation Experiment

We also performed a second ethane/ethylene experiment, but instead of maintaining Titan temperatures throughout the experiment, the TCB was warmed from ~92 K to ~139 K over a period of 94 minutes to induce evaporation of ethane. See Figure S8 for a temperature profile of the sample over the duration of this experiment.

Figure 9 shows the offset FTIR spectra for this experiment (initial spectrum in red, final spectrum in blue). The spectral results of this experiment show relatively constant band depths for the first ~120 minutes (average temperature of 104 K), then a sudden decrease in both species' band depths starting at 186 minutes (118 K) and ending at 219 minutes (139 K; see Fig. 10). Band depth measurements (Fig. 10) support these spectral results. No red shifts of bands were observed during this experiment.

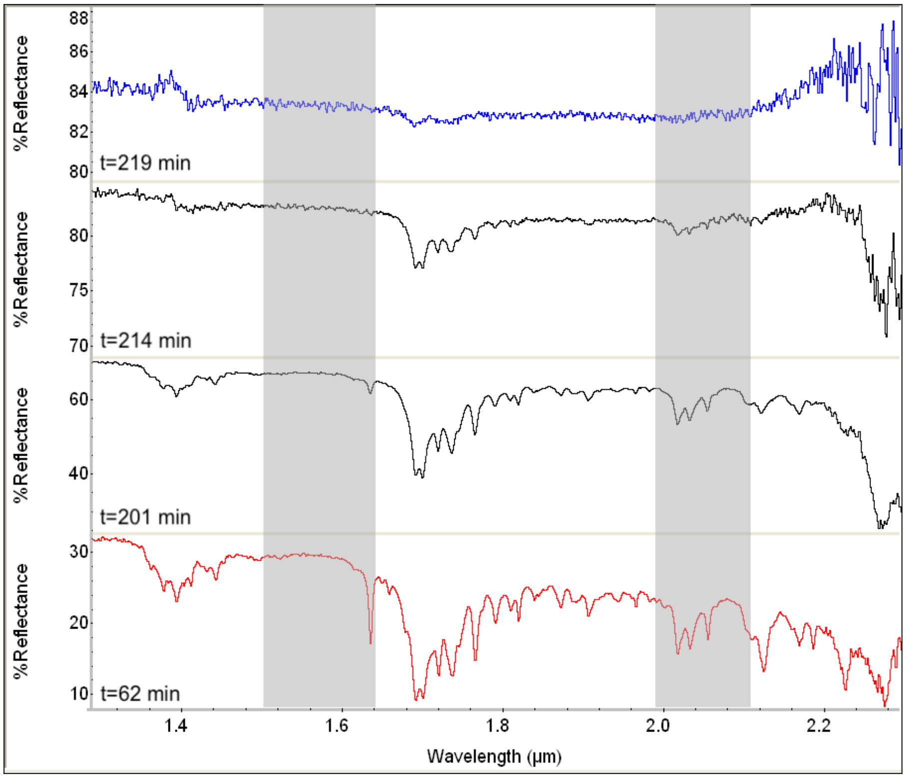

Figure 9. Ethane/ethylene spectra, offset for clarity. Initial spectrum is shown in red, intermediate in black, and final in blue. Vertical, gray bars indicate VIMS windows. Notice the increase in reflectance throughout the experiment.

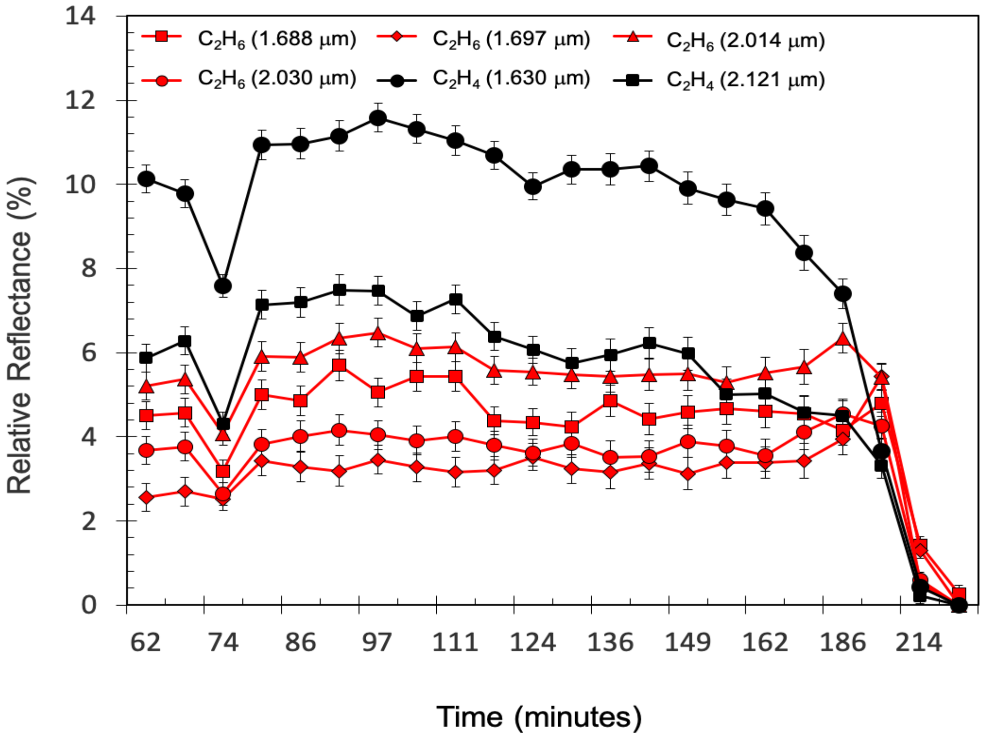

Figure 10. Ethane band depths (red) from the force evaporated experiment show constant band depths until force evaporation (~200 minutes), but ethylene band depths (black) began decreasing sooner, around 150 minutes.

4.4. Methane, Ethane, and Ethylene

Protocol for this experiment included: 50.1% methane, 44.9% ethane, and 5.0% ethylene, initially. Offset reflectance FTIR spectra is shown in Figure 11 (left), with the first sample shown by the red spectrum, and final spectrum shown in blue. The spectra in Figure 11 show variation from the initial spectrum to the final spectrum, which was 0.2% methane, 91.9% ethane, and 7.9% ethylene. The methane in the sample mixture evaporated in this experiment, which explains the percentage difference from initial to final spectrum.

Figure 11 (right) shows the mass data for the methane/ethane/ethylene experiment. The methane/ethane/ethylene sample was poured into the petri dish at ~65 minutes, reaching a maximum mass of ~16 g. An immediate decrease in mass (70-100 minutes) to ~12 g was followed by a stable period (100-150 minutes).

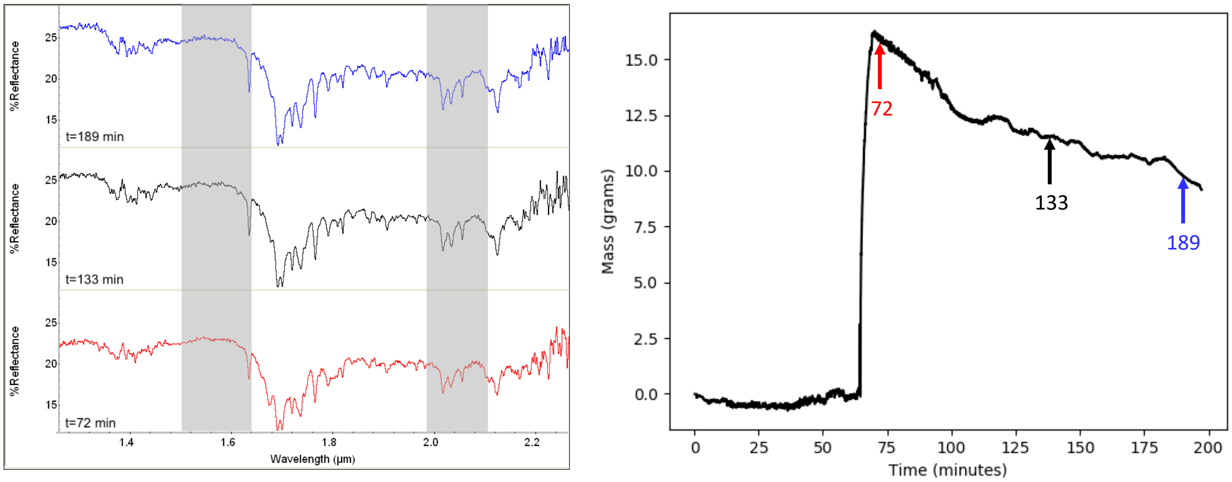

Figure 11. Offset reflectance spectra from the methane/ethane/ethylene experiment (left). The initial spectrum is shown in red, intermediate in black, and final in blue. Notice the disappearance of the 1.669 µm methane band throughout the experiment. Mass data from the methane/ethane/ethylene experiment (right) showing that the sample was poured at ~70 minutes, followed by steady state methane evaporation and a semi-stable period of the ethane/ethylene mixture. Colored arrows correspond with the time each spectrum was taken.

Baseline reflectance slightly increased throughout the experiment, beginning at ~10% and ending at ~25%. The methane band depth (1.669 µm) decreased from 0.6% to 0.0% (Fig. 12). Ethane band depths (1.688 µm, 1.697 µm, 2.014 µm, and 2.030 µm) were almost constant at 2.7%, 1.9%, 2.9%, and 1.8% respectively (Fig. 12). Ethylene (1.630 µm and 2.121 µm) band depths slightly increased in relative reflectance from 3.4% to 5.3% and 26% to 3.3%, respectively (Fig. 12). No red shifts of bands were observed in this experiment.

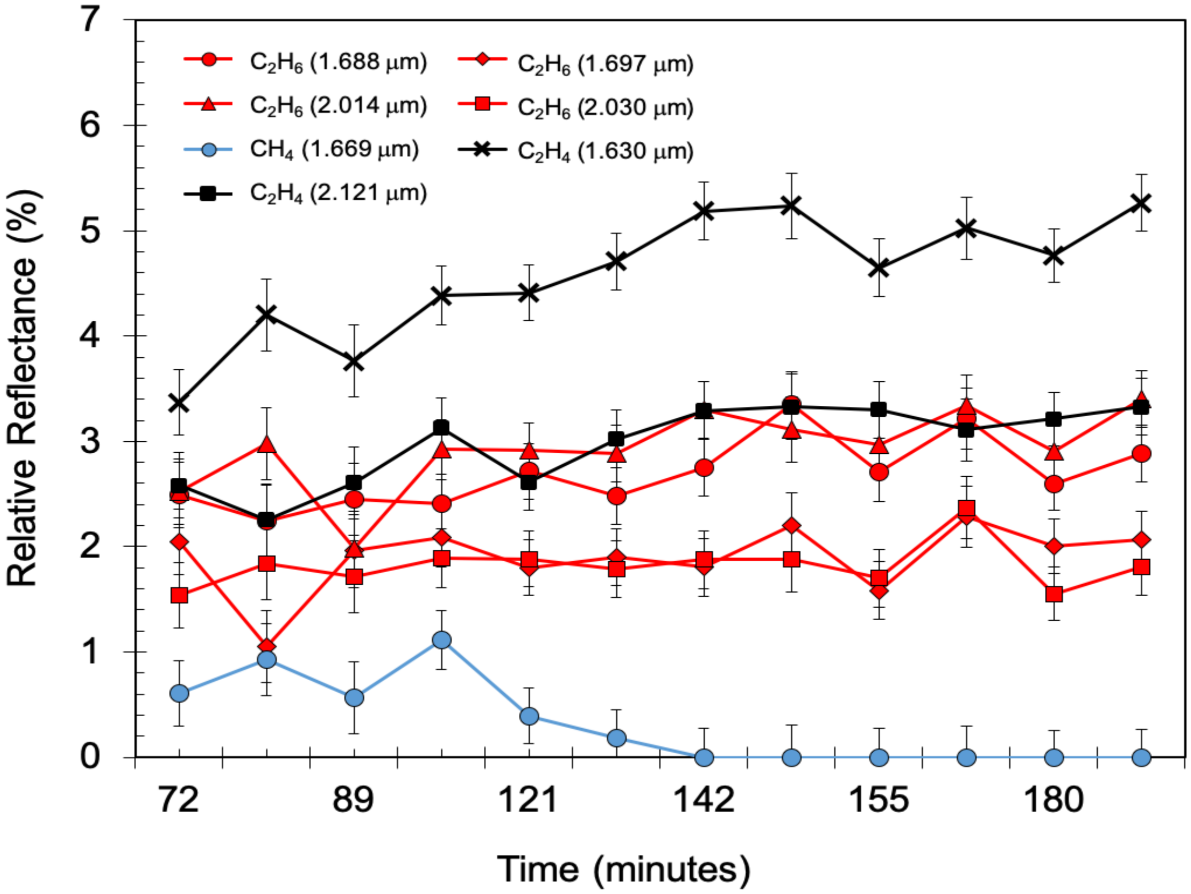

Figure 12. Methane band depths (blue) from the methane/ethane/ethylene experiment show a decrease in the methane band (1.669 μm). Ethane band depths (red) show no significant change in ethane bands (1.688 μm, 1.697 μm, 2.014 μm, and 2.030 μm). Ethylene band depths (black) show an increase in both ethylene bands (1.630 μm and 2.121 μm).

Table 2. Initial/final mole fractions, sample temperature, and evaporation rates from all experiments.

Compounds in Experiment	Initial Mole Fraction (%)	Avg. Sample Temp During Spectral Acquisition (K)	Final Mole Fraction (%)	Methane Evaporation Rate (Earth) ($kg\ m^{-2}\ s^{-1}$)	Methane Evaporation Rate (Titan) ($kg\ m^{-2}\ s^{-1}$)	Ethane Evaporation Rate (Earth) ($kg\ m^{-2}\ s^{-1}$)	Ethane Evaporation Rate (Titan) ($kg\ m^{-2}\ s^{-1}$)
$CH_4:C_2H_4$	80.5:19.5	93.66	40.9:59.1 *	$(3.0\pm0.5) \times 10^{-4}$	$(1.1\pm0.2) \times 10^{-4}$		
$CH_4:C_2H_4$	76.3:23.7	90.43	41.0:59.0 *	$(2.6\pm0.4) \times 10^{-4}$	$(1.0\pm0.2) \times 10^{-4}$		
$C_2H_6:C_2H_4$	87.9:12.1	93.71	76.0:24.0			$<4.9 \times 10^{-6}$	$<1.8 \times 10^{-6}$
$C_2H_6:C_2H_4$	91.8:8.2	93.58	84.6:15.4			$<3.5 \times 10^{-6}$	$<1.3 \times 10^{-6}$
$C_2H_6:C_2H_4$ &	65.1:34.9	109.48	&			&	&
$CH_4:C_2H_6:C_2H_4$	18.1:64.7:17.2	95.39	8.1:76.4:15.5	$(3.4\pm0.7) \times 10^{-4}$	$(1.3\pm0.3) \times 10^{-4}$	$<6.8 \times 10^{-6}$	$<2.5 \times 10^{-6}$
$CH_4:C_2H_6:C_2H_4$	50.1:44.9:5.0	96.02	0.2:91.9:7.9	$(2.7\pm0.6) \times 10^{-4}$	$(1.0\pm0.2) \times 10^{-4}$	$<7.0 \times 10^{-6}$	$<2.6 \times 10^{-6}$
$CH_4:C_2H_6:C_2H_4$	21.8:74.7:3.5	94.37	0.2:93.5:6.3	$(2.5\pm0.9) \times 10^{-4}$	$(0.9\pm0.3) \times 10^{-4}$	$<5.2 \times 10^{-6}$	$<1.9 \times 10^{-6}$

* Second number represents saturation value of ethylene.

& Forced evaporation experiment: evaporation rate not relevant.

5. Discussion

5.1. Evolution of Spectra

Results for the methane/ethylene experiments are as follows: methane being the more volatile solvent (Luspay-Kuti et al., 2015) evaporated out of the system, leaving behind a solid residue of ethylene ice. Immediately after this mixture was poured onto the sample dish, the spectrum resembled a mixture of methane and ethylene in liquid phase. However, as additional spectral samples were taken, this liquid methane began evaporating, resulting in precipitation of solid ethylene (Fig. 5) until the only species left in the sample dish was ethylene. The band depths in Figure 5 show that methane values decreased from beginning of the experiment, while ethylene did not change until ~150 minutes. These results, along with the increase in ethylene band depths after 150 minutes (Fig. 5) indicate ethylene precipitation in conjunction with complete methane evaporation. Increasing reflectance and band depth for ethylene could also indicate ethylene slowly becoming the dominant species in the mixture. The overall increase of reflectance and red shifts, which occurred when dissolved ethylene changed to precipitated (solid) ethylene, suggests that the sample becomes enriched in the solid phase, which stems from the solvent's evaporation. The band at 1.666 µm (Fig. 6C) is associated with pure methane. Initial reports of the IR absorption bands of methane describe a band at 1.666 µm as being the partially resolved first harmonic of the 3.33 µm band (Cooley, 1925; Ellis, 1927), the first overtone of the ν_3 fundamental (Nelson et al., 1948), and was classified as $2\nu_3$ (Moorhead, 1932; Norris and Unger, 1933). However, there are discrepancies as to whether these early studies may be referring to the band at 1.669 µm, which is the most apparent methane band in this study and has also been classified as $2\nu_3$. In either case, our spectral results show the persistence of this 1.666 µm methane band throughout the methane/ethylene experiment. This could mean that a small amount of methane may remain in contact with the ethylene evaporite.

In the 90 K ethane/ethylene experiment, there was no significant evaporation of ethane or ethylene, as shown in the spectra and band depth graphs (Figs. 7, 8). This is due to ethane's low vapor pressure, which prevented it from evaporating at Titan surface conditions in our chamber (Luspay-Kuti et al., 2015). Stable ethane band depths confirm this interpretation. Most differences between the methane and ethane experiments stem from each solvent's individual vapor pressure. A more significant change is seen in the ethylene band depths, as they increased throughout the experiment. Thus, ethylene forms evaporites slowly with ethane since ethane evaporates slowly. This is contrary to methane, which evaporates quickly, allowing the ethylene evaporite to form much quicker.

In the methane/ethane/ethylene experiment, no ethane evaporation occurred, for the same reason as the ethane/ethylene experiment at Titan temperatures. Given the increased and relatively constant band depths of ethane, we assumed that an insignificant amount of ethane evaporated, which is consistent with our calculated upper limit of ethane evaporation (Table 2). Similar to the other experiments, ethylene band depths increased. The 1.669 μm methane band depth decreased to zero, which indicates complete evaporation from the sample, and no apparent precipitation of ethylene.

5.2. Band Shift and Phase Change

One objective of studying a single compound during the evaporation process is to identify the transition between dissolved ethylene and solid ethylene solute/solvent interaction. The red shifts in this study are most clearly defined in the ethylene bands at 1.630 μm and 2.121 μm, however we observe the band shifts throughout the ethylene spectrum. These red shifts are indicative of a transition from dissolved ethylene to solid ethylene, and can be explained by the increased density, stronger interactions and C—H bonds, and closer packing in the solid phase when compared to the liquid phase (Abramczyk and Paradowska-Moszkowska, 2001). Initially, ethylene was dissolved in the methane mixture, but as methane evaporated, ethylene reached saturation. At that point, solid ethylene particles were precipitated in the sample dish to form a residual solid, indicated by the red shifts. This transition from dissolved to solid ethylene was not observed in the ethane/ethylene experiment at Titan temperatures because no significant amount of ethane evaporated. Therefore, ethylene remained in a binary mixture with liquid ethane so long as ethane did not completely evaporate. Further, we detected no transition in the methane/ethane/ethylene experiment either. Although methane evaporated out of the system, ethane was still available as a solvent in which ethylene could remain dissolved. This interpretation is also consistent with the fact that no residual solid formed for this experiment, (i.e. lack of band shifts). Given that we measured an average upper limit of ethane evaporation of $<5.5 \times 10^{-6}$ kg m^{-2} s^{-1}, and modeled ethane evaporation rates on Titan are on the order of 10^{-8} kg m^{-2} s^{-1} (Tokano, 2009), given a long enough period of time, ethane may eventually evaporate completely and leave behind an ethylene evaporite. Alternatively, ethylene may evaporate along with the ethane solvent, as shown in our forced evaporation experiment.

5.3. Solubility

The initial mole fractions for each experiment were calculated using the analysis outlined in the Spectral Unmixing Model section. Given that the solubility is 56% mole fraction for ethylene in methane and 48% mole fraction for ethylene in ethane (Singh et al., 2017), we determined that each of our experiments were well within these solubility limits. The average mole fractions were calculated as 59.1%, 19.7%, and 9.9% in methane, ethane, and a methane/ethane mixtures, respectively. We note that our ethane value is significantly lower than

48% reported in Singh et al. (2017), which is in part due to different experimental protocols between solubility experiments and evaporite experiments. Combining these mole fraction values with the fact that large lakes on Titan may not be saturated in ethylene (Singh et al., 2017), we are confident that the ethylene concentrations in our experiments are appropriate for Titan. However, we note that these experimental conditions may not be truly representative, because the composition of Titan's evaporites is still unknown. In the methane/ethylene experiment, we calculated the mole fraction of ethylene during methane evaporation. Figure 5 shows the final methane evaporation occurring between t = 146 and 185 minutes, since this is when the methane band depths decreased to 0% relative reflectance. During this process (t = 165 minutes), the mole fraction of ethylene was measured at 59.0% mole fraction. When compared to 56% mole fraction (Singh et al., 2017), our value of 59.0% mole fraction indicates that the solution may be slightly supersaturated.

5.4. Implications for Titan's Lakes

On Titan, ethylene evaporite deposits would form quicker in lakes or seas dominated by methane. Titan's northern lakes have been predicted to be dominated by methane during the current season (Luspay-Kuti et al., 2015; Mastrogiuseppe et al., 2019, 2018, 2016, 2014), therefore we may expect the formation of ethylene evaporites in north polar lakes after solvent evaporation. From this, and given the methane and ethane evaporation rates reported in this paper (Table 2), we calculated the time of evaporation and thickness of ethylene evaporite, assuming ethylene dissolution in these lakes. To determine the thickness of an ethylene evaporite layer deposited in one of Titan's northern lakes (e.g. Winnipeg Lacus), we assume lake surface area, depth, and methane-dominated lake composition from (Mastrogiuseppe et al., 2019) methane evaporation rates from Table 2, and a methane density of 452 kg m^{-3} (Malaska et al., 2017). For Winnipeg Lacus, it would take ~5 years to produce an ethylene evaporite with a gross total thickness of ~9 m. In the case of a methane/ethylene lake presented here, we deem an evaporite thickness of ~9 m to be reasonable (albeit high) owing to ethylene's high solubility in methane (Singh et al., 2017; see details in Supporting Information S12). Additionally, this calculated thickness does not take into account erosion by wind or sublimation processes that may occur, and assumes that the lake is saturated in ethylene, thus at the end of the ~5 year timescale the evaporite would ultimately be less than 9 m thick.

Ethane may also be volatile on timescales longer than a season (Lunine et al., 1983; Mousis et al., 2016). Ethylene's approximately equal solubility in both methane and ethane suggests evaporite formation in methane-dominated lakes on a seasonal timescale, but possible evaporite formation in ethane-dominated lakes may occur on longer-than-seasonal timescales (i.e. Croll-Milankovich timescale).

The VIMS 5 μm window allowed for observations of spectral units that represent water-ice-poor material on Titan that are most likely evaporites (Barnes et al., 2011, 2009, 2005; MacKenzie and Barnes, 2016). According to (Clark et al., 2010) ethylene (92 K) has a band center at 4.90 μm, which falls in the VIMS 5 μm window range. Future experimental studies should extend spectral measurements to 5 μm to determine and characterize absorptions that occur at longer wavelengths.

6. Conclusions

By using a unique Titan chamber, we simulated ethylene evaporites in a Titan-like environment. Three types of experiments were performed: methane/ethylene, ethane/ethylene, and methane/ethane/ethylene. Through analysis of spectra, band depths, and temperature, we report that a residual evaporite deposit only formed in the methane/ethylene experiment, due to near complete evaporation of methane. Ethane evaporates much slower than methane at Titan surface conditions, which holds true for our experiments, as no ethylene evaporite formed on the duration of our ethane-dominated experiments. However, these results do not preclude ethylene evaporites from forming in an ethane-dominated lake or sea on Titan, given longer timescales. Our results imply that ethylene may be a good candidate for evaporite deposits at Titan conditions, because ethylene is approximately equally soluble in both methane and ethane solutions. Ethylene evaporites may be restricted to methane-dominated lakes, however, and may not be easily detectable in the 1.6 μm and 2.0 μm VIMS windows.

The recently selected New Frontiers mission, *Dragonfly*, may be able to constrain the composition of equatorially located Tui and Hotei Regiones, proposed paleo seas that contain the largest 5-μm-bright evaporitic features on the satellite (MacKenzie and Barnes, 2016). *Dragonfly* will land in Titan's dune fields (Lorenz et al., 2018; Turtle et al., 2018), which likely contain material sourced from ancient evaporite deposits. If Tui and Hotei Regiones are indeed evaporitic, as previously implied (Barnes et al., 2011; MacKenzie and Barnes, 2016; MacKenzie et al., 2014), our work here could provide initial constraints on the genesis and processing of these proposed evaporites (i.e., thickness, stratification), in addition to understanding the evolution the dune material underwent before becoming incorporated into the dunes that will be sampled by *Dragonfly*.

7. Supporting Information

7.1. Mass Analysis Code

The mass analysis code accomplishes two goals: measuring the evaporation rate of liquid components and correcting for any "drift" in the balance. The cause of the balance drift is most likely due to its interaction with the cold temperatures of our experiments, as the balance appears to slowly change its zero point over the course of an experiment. Fortunately, this scale drift can be modeled as an exponential increase in the mass and thus it can be easily corrected. An example of what our corrected mass data looks like is shown in (Fig. S1).

The starting point for our model is that the evaporation rate ($\dot{M}$) is assumed to be directly proportional to the surface area (A) of the liquid. It is important to note that the constant of proportionality (k) will have units of kg s^{-1} m^{-2}.

$$\dot{M} = -kA$$

This assumption allows us to extrapolate our model to the lakes on Titan. In our experiments the liquid does not take the form of a large lake, but rather that of a small puddle, which we will model as a spherical cap, with the given volume (V) and surface area, based on its height (h), and radius (r).

$$V = \frac{\pi h}{6}(3r^2 + h^2)$$

$$A = \pi\,(r^2 + h^2)$$

The maximum height that a puddle of liquid can reach depends on various physical properties of the liquid, as well as its environment. This can be calculated with the following formula:

$$h = \sqrt{\frac{2\gamma(1 - \cos\theta)}{g\rho}}$$

Here γ is the surface tension of the liquid, θ is the contact angle of the liquid on the surface, g is the acceleration due to gravity, and ρ is the density of the liquid. Because all of these variables are known and fixed in the laboratory setting, we can calculate the maximum height of a puddle of liquid.

With the height now being a fixed number for each experiment, we can find a relationship between mass and surface area. Mass (M) is a function of density and volume, while volume can be rewritten as a function of surface area by solving for radius.

$$A = \frac{2M}{\rho h}$$

This equation can be substituted into the original evaporation rate equation to create an easily solved differential equation, with an exponential form.

$$M = M_0 e^{-\frac{2k}{\rho h}t}$$

This exponential decay as a function of time (t), has the multiplicative constant (M_0) representing the initial mass of the evaporating material.

This reduces the evaporation model down to only two parameters: the multiplicative constant and the exponent. The evaporation rate per unit area can be calculated from the exponent (c) easily:

$$k = -\frac{c\rho h}{2}$$

The final overall fit accounts for the exponential scale drift (with initial error α and exponent β), the evaporation of the liquid, and the constant mass of the evaporite material (M_{EM}). Lastly, as there is some amount of time in the experiment before the components are poured into the sample dish, a time offset is applied to the evaporating liquid and evaporite material mass of t_0.

$$M(t) = \alpha e^{\beta t} + M_0 e^{-\frac{2k}{\rho h}(t-t_0)} + M_{EM}(t - t_0)$$

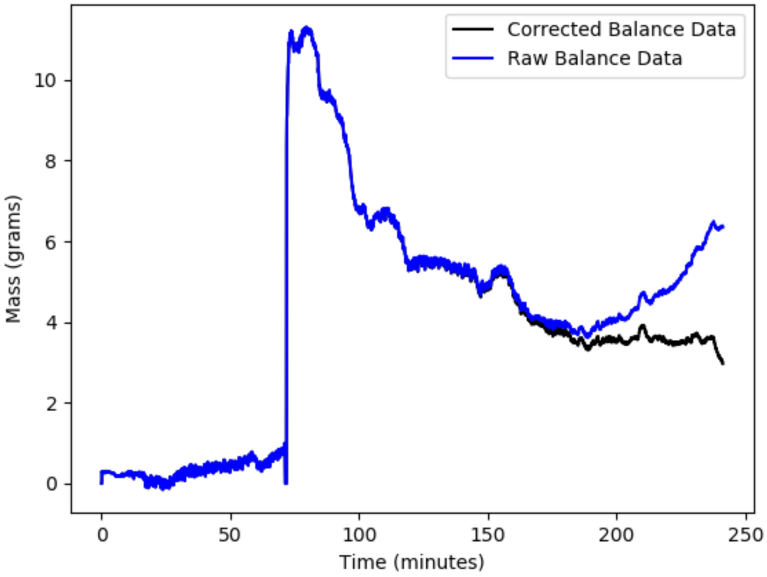

Figure S1. Comparison between raw balance data (blue) and data corrected for the gradual balance drift (black).

7.2. Data from Additional Experiments

7.2.1. Repeated methane/ethylene experiment:

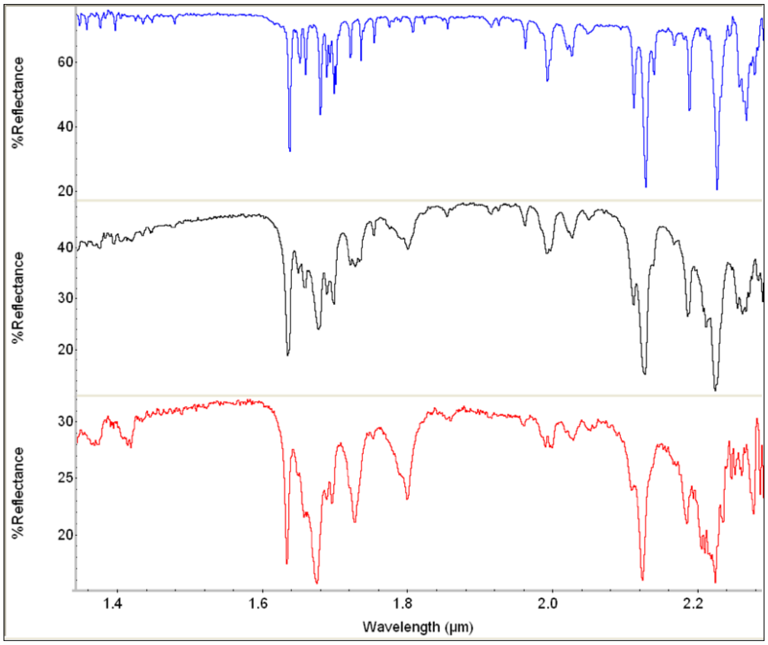

Figure S2. Methane/ethylene spectra from a repeated experiment, offset for clarity. Initial spectrum is shown in red, intermediate in black, and final in blue. Notice the increase in reflectance throughout the experiment and disappearance of the methane triplet

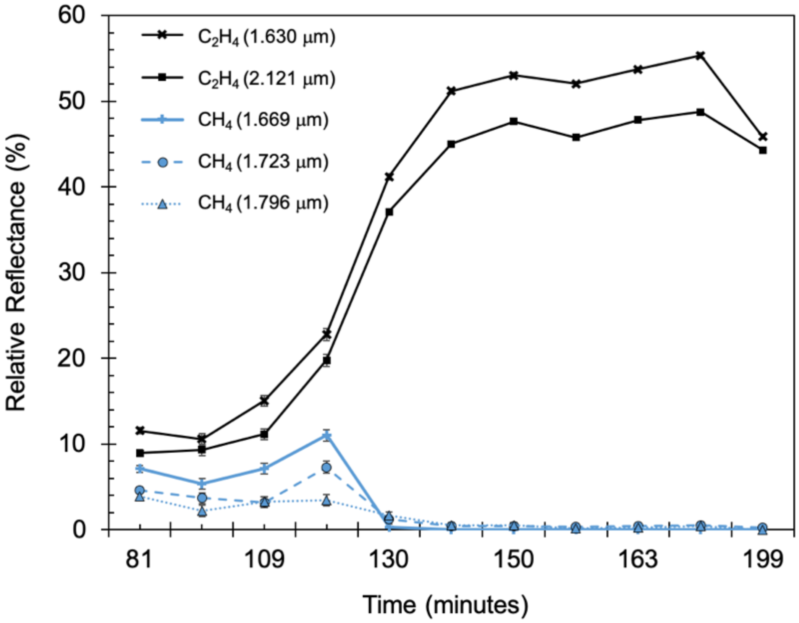

Figure S3. Methane band depths (blue) from a repeated methane/ethylene experiment show a decrease in characteristic methane bands (1.669 µm, 1.723 µm, 1.796 µm), while ethylene band depths (black) show an increase in characteristic ethylene bands (1.630 µm, 2.121 µm). The sudden increase of ethylene band depths at ~120 minutes most likely indicates saturation. Error bars are the same size or smaller than point markers.

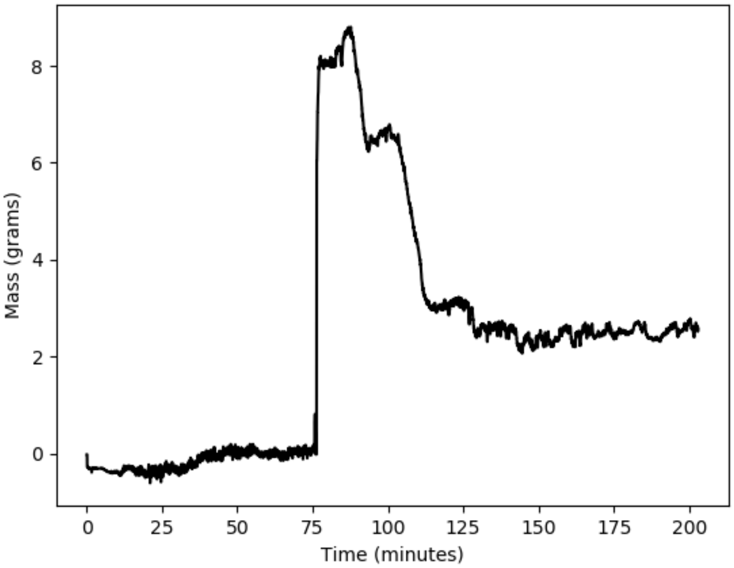

Figure S4. Mass data from a repeated methane/ethylene experiment. Sample was poured onto the sample dish at ~75 minutes and reached a maximum mass of ~8.8 grams. Methane evaporation occurred from ~87-130 minutes, leaving behind ~2.5 grams of ethylene evaporite.

7.2.2. Repeated ethane/ethylene experiment:

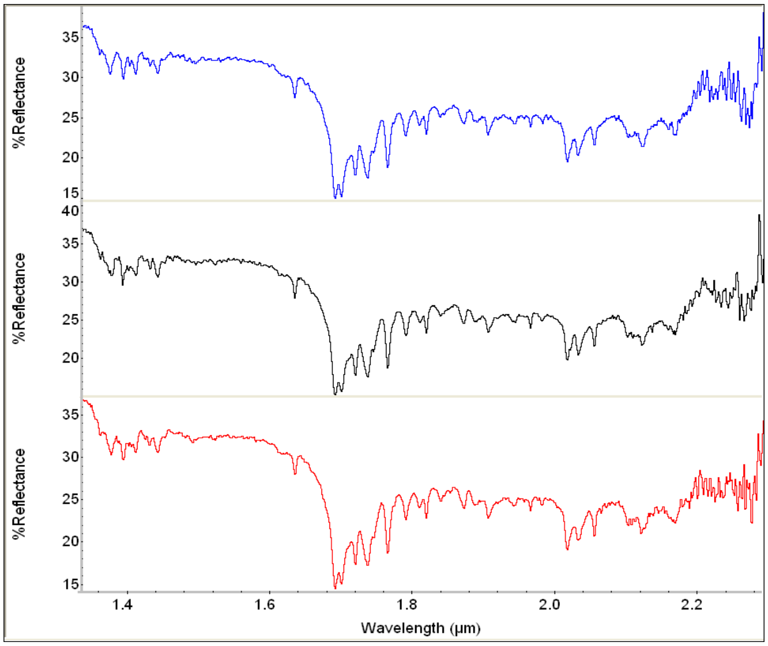

Figure S5. Ethane/ethylene spectra from a repeated experiment, offset for clarity. Initial spectrum is shown in red, intermediate in black, and final in blue. Notice the relatively constant reflectance throughout the experiment, and unchanged ethane bands.

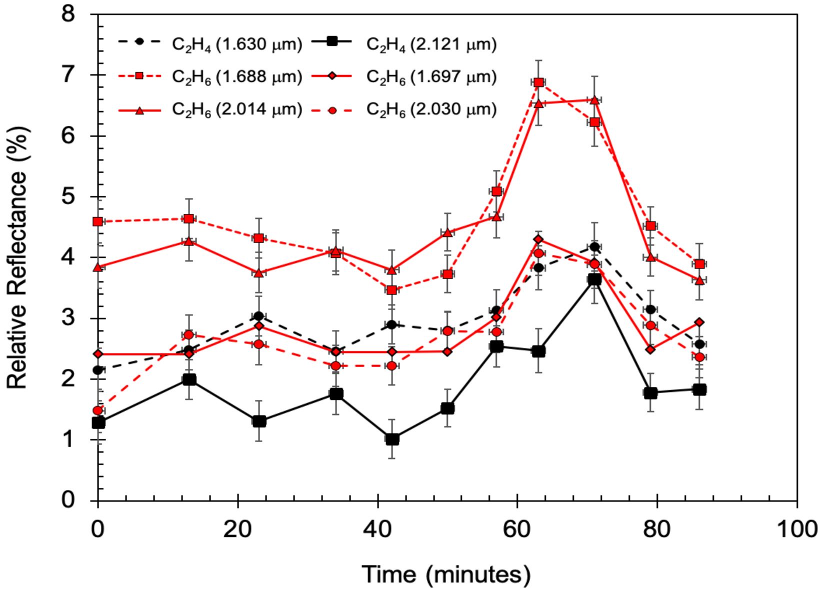

Figure S6. Ethane (red) and ethylene (black) band depths from a repeated 90 K ethane/ethylene experiment. The reflectance increase in all bands around 60-70 minutes is attributed to ethane freezing.

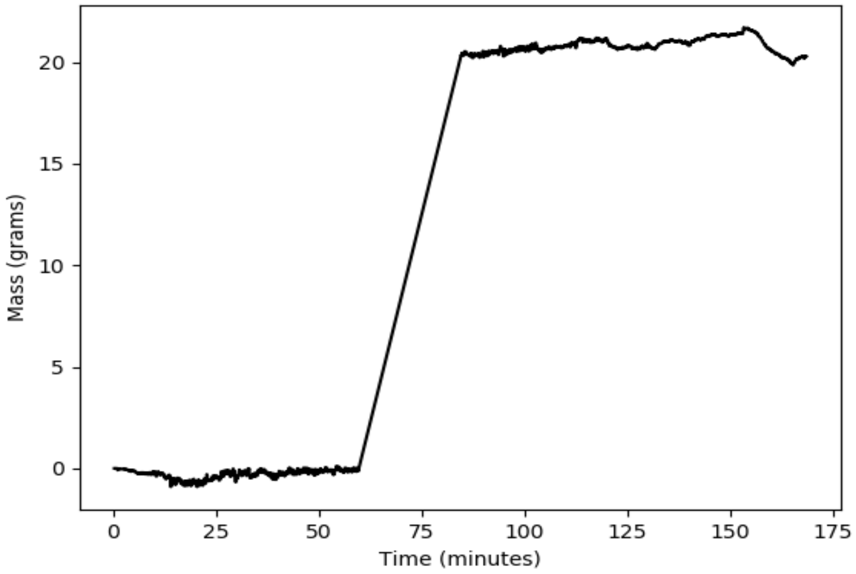

Figure S7. Mass data from a repeated ethane/ethylene experiment. The sample was poured onto the sample dish at ~60 minutes. The balance malfunctioned during this experiment, so the mass data from 60-80 minutes was lost. The connecting line does not represent the pour; it connects what was measured before and after the balance malfunction.

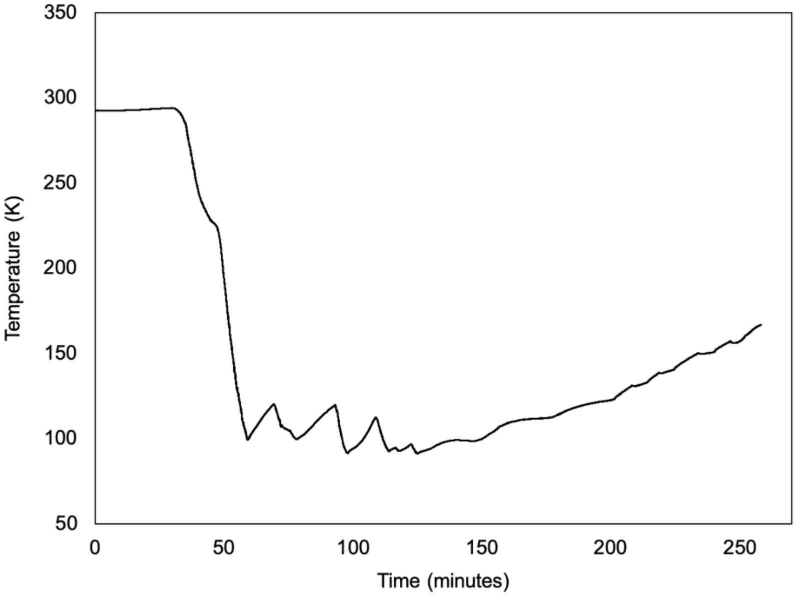

Figure S8. Temperature profile from the ethane/ethylene forced evaporation experiment. The sample was warmed then cooled immediately after pouring (~100 minutes) in an attempt to induce evaporation gradually. Then liquid nitrogen was decreased, which allowed steady warming from ~120 minutes to the end of the experiment.

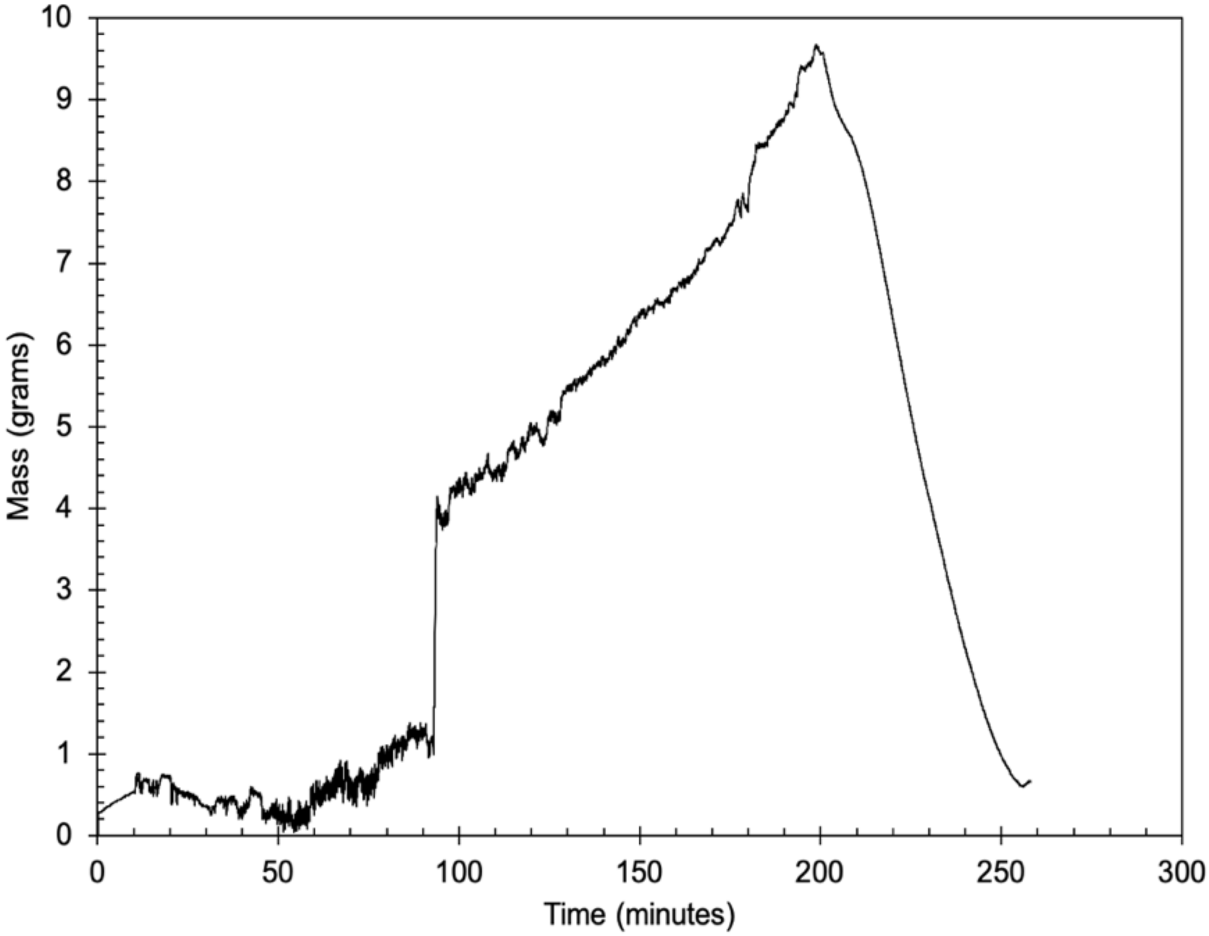

Figure S9. Mass data from the forced evaporated ethane/ethylene experiment. Mass was approximately zero before the mixture was poured at ~100 minutes, reaching a maximum mass of 10 grams before being force evaporated. The increase in mass from ~100 to 200 minutes is due to fluctuations in the readings of the balance from the increase in temperature. Notice how quickly the mass decreases from 200 to 250 minutes, as a result of the mixture evaporating in the warming temperatures of the TCB.

7.2.3. Repeated methane/ethane/ethylene experiments:

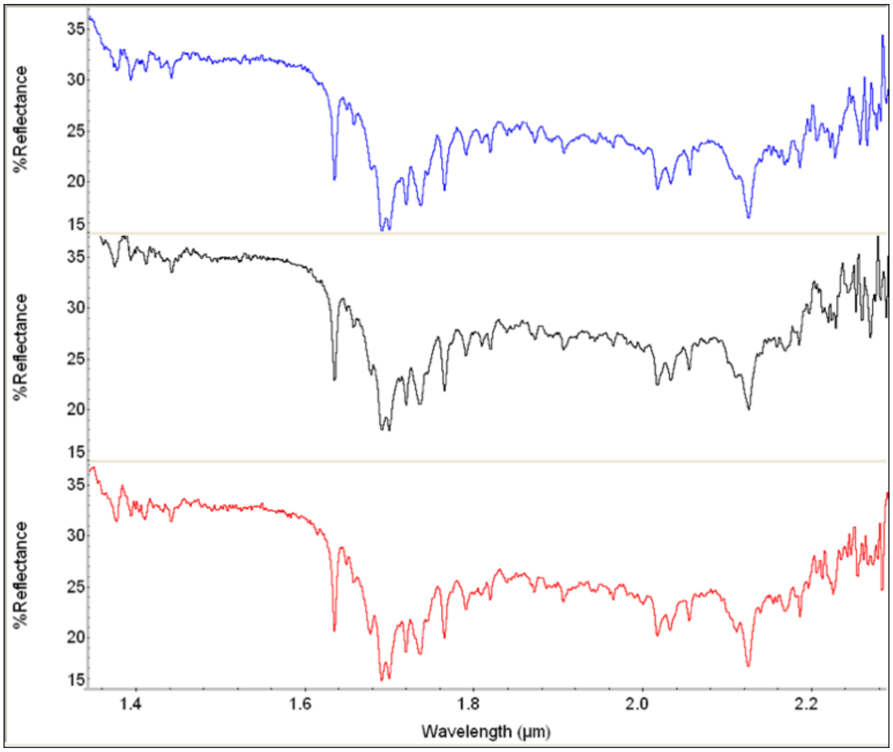

Figure S10. Methane/ethane/ethylene spectra from a repeated experiment, offset for clarity. Initial spectrum is shown in red, intermediate in black, and final in blue. Notice the relatively constant reflectance throughout the experiment.

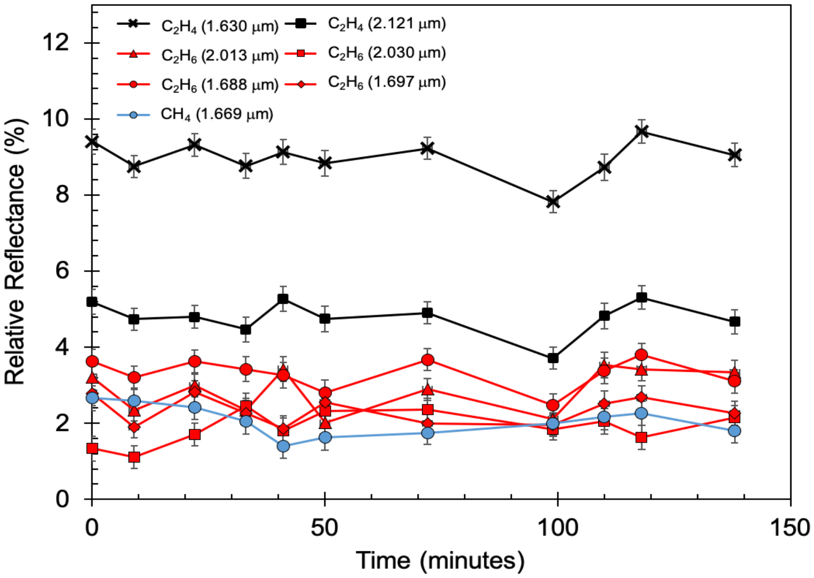

Figure S11. Methane, ethane, and ethylene band depths from a repeated experiment shown in blue, red, and black, respectively.

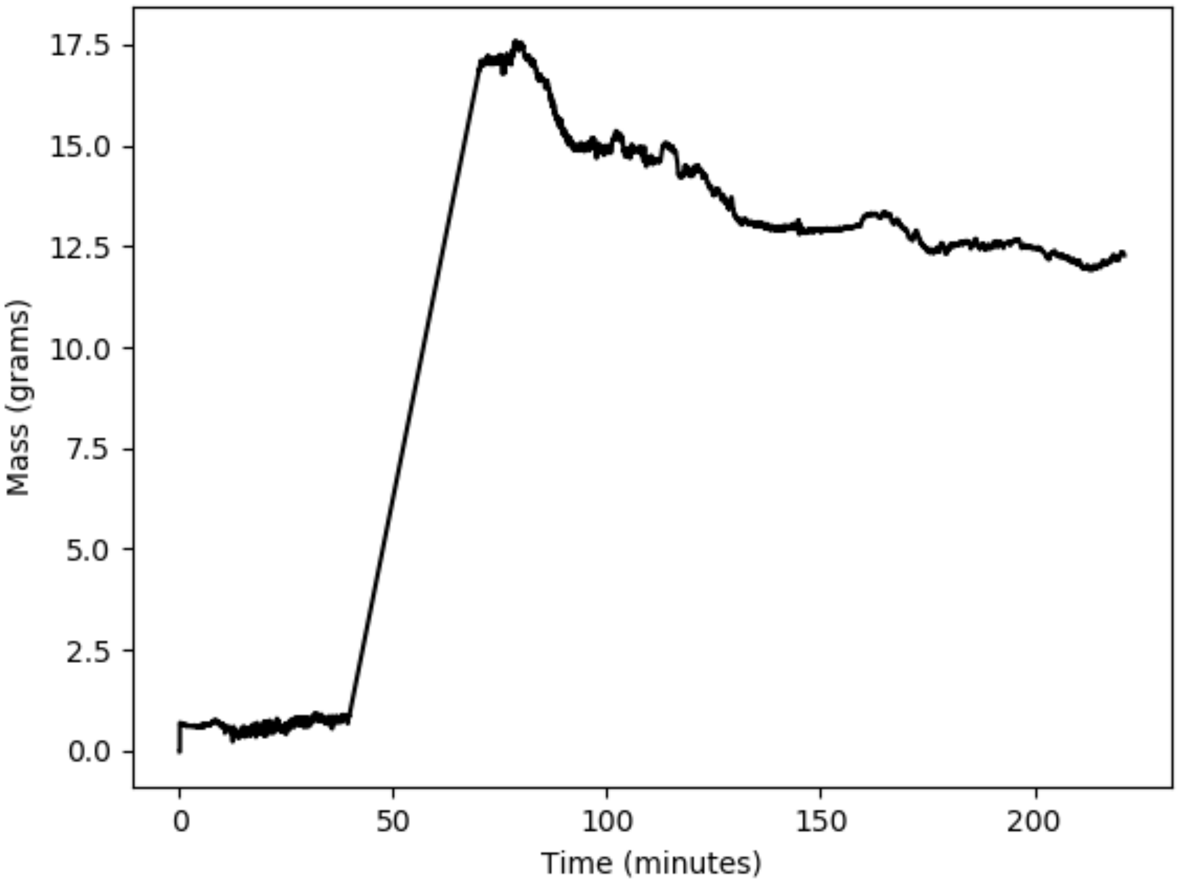

Figure S12. Mass data from a repeated methane/ethane/ethylene experiment. Evaporation of some methane is shown. After ~60 minutes. There were two pours in this experiment – one for just ethane, and one for the methane/ethylene mixture. The increase in mass at ~50 minutes connects the beginning of the first pour to the end of the second pour, in order to properly analyze the balance drift.

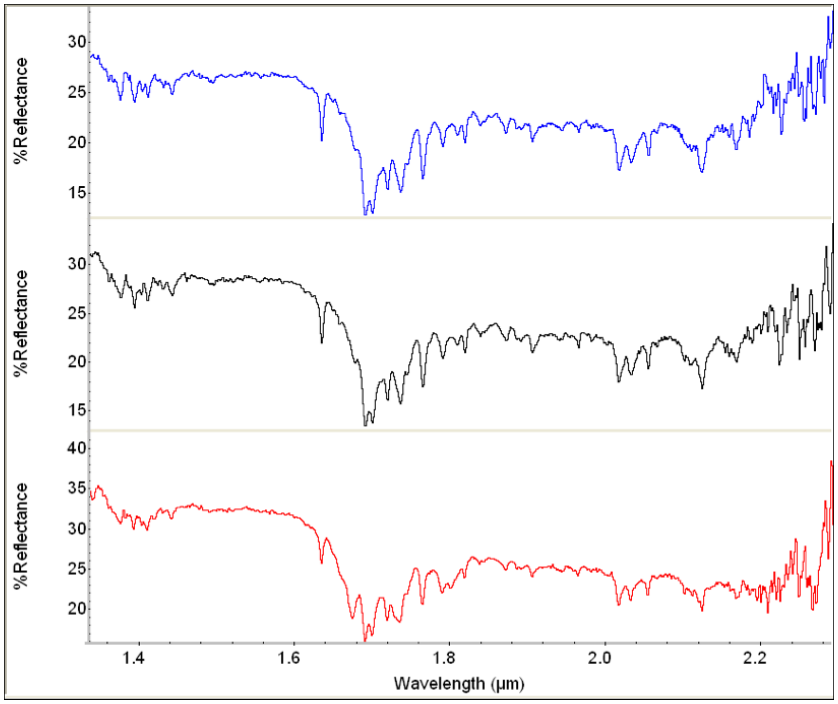

Figure S13. Methane/ethane/ethylene spectra from a repeated experiment, offset for clarity. Initial spectrum is shown in red, intermediate in black, and final in blue. Notice the relatively constant reflectance throughout the experiment, and disappearance of methane bands by the final spectrum.

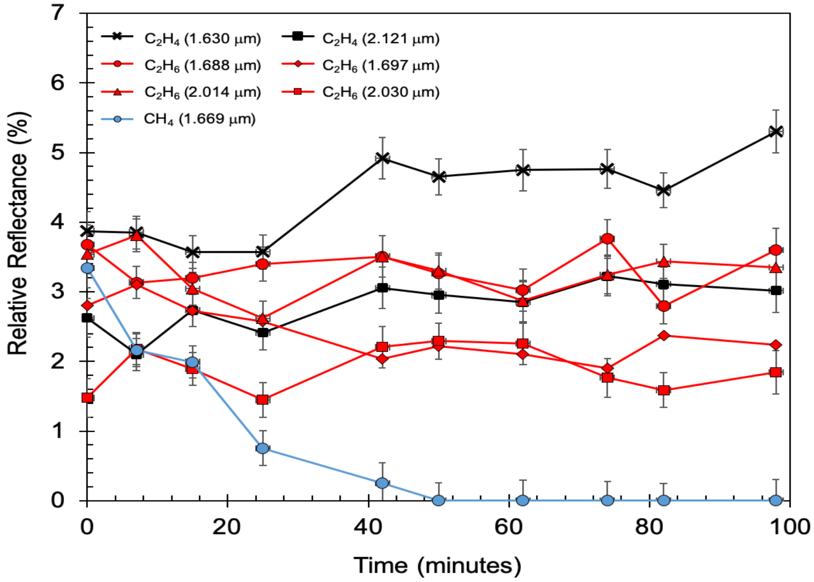

Figure S14. Methane, ethane, and ethylene band depths from a repeated experiment shown in blue, red, and black, respectively. Notice the constant depths of ethane and ethylene bands, but the decrease in methane bands, indicating evaporation.

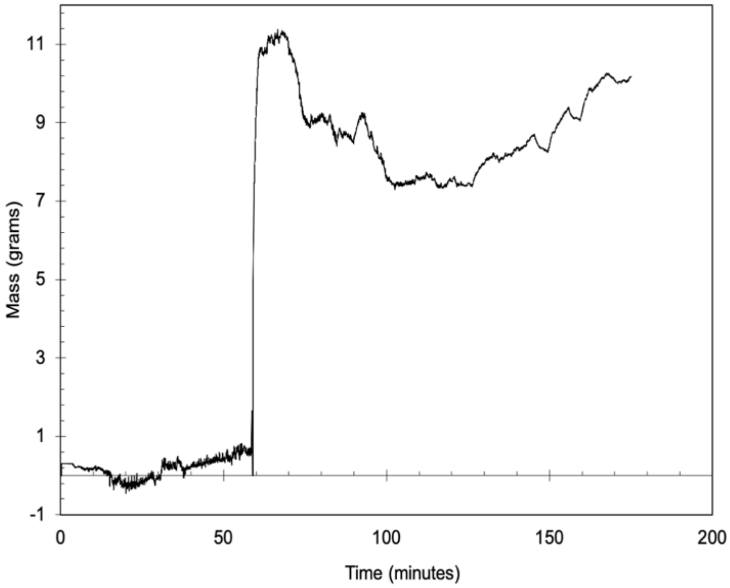

Figure S15. Mass data from a repeated methane/ethane/ethylene experiment showing the sample was poured at ~60 minutes. Evaporation of some methane is shown by the decrease in mass. The increase in mass from ~130 - ~180 minutes is due to drift in the balance and is not indicative of more sample being added to the sample dish.

Table S1. Additional experimental parameters. Goodness of fit parameter described in Spectral Unmixing Model section of the manuscript.

Compounds in Experiment	Spectral Acquisition Times (min)	STDEV of Avg. Sample Temperature	Initial Goodness of Fit	Final Goodness of Fit
CH_4:C_2H_4	81-199	4.82	0.91	1.37
CH_4:C_2H_4	81-230	3.63	1.69	1.31
C_2H_6:C_2H_4	95-187	2.10	1.00	1.33
C_2H_6:C_2H_4	78-164	2.37	1.19	0.99
C_2H_6:C_2H_4 [A]	62-219	11.99	1.03	[A]
CH_4:C_2H_6:C_2H_4	76-214	6.21	0.92	1.18
CH_4:C_2H_6:C_2H_4	72-189	3.48	1.18	1.09
CH_4:C_2H_6:C_2H_4	69-167	3.36	1.26	1.09

[A] Forced evaporation experiment

7.3. Evaporite Calculations

For Winnipeg Lacus, we calculate that it would take ~5 years to produce an ethylene evaporite with a thickness on the order of 9 m. This estimate is an upper limit, as we assume a lake depth of 50 m, and ~18% ethylene, which in reality may be quite high. Additionally, our assumptions do not take into account local, seasonal methane rain that would contribute to the methane abundance in many north polar lakes. Cordier et al. (2016) estimated the total thickness of an evaporite deposit containing six different solutes as 0.324 m for pure methane and 13.65 m for pure ethane. Their differences in evaporite thickness between methane or ethane solvents are attributed to the selected evaporite species being significantly more soluble in ethane than in methane.

8. Acknowledgement

The authors greatly acknowledge Shannon MacKenzie for valuable comments in the review process, Marco Mastrogiuseppe for assistance with calculating lake parameters, Walter Graupner for help in the lab, Dustin Laxton for aiding with initial experiments, and Sandeep Singh for insight on experimental protocol. This work was supported by NASA Headquarters under the NASA Earth and Space Science Fellowship Program – Grant #80NSSC17K0603.

9. References

Abplanalp, M.J., Frigge, R., Kaiser, R.I., 2019. Low-temperature synthesis of polycyclic aromatic hydrocarbons in Titan ' s surface ices and on airless bodies. Sci. Adv. 5, 1–12.

Abramczyk, H., Paradowska-Moszkowska, K., 2001. The correlation between the phase transitions and vibrational properties by Raman spectroscopy : liquid-solid B and solid B-solid a acetonitrile transitions. Chem. Phys. 265, 177–191. https://doi.org/https://doi.org/10.1016/S0301-0104(01)00271-3

Anderson, C.M., Samuelson, R.E., 2011. Titan's aerosol and stratospheric ice opacities between 18 and 500 um: Vertical and spectral characteristics from Cassini CIRS. Icarus 212, 762–778. https://doi.org/10.1016/j.icarus.2011.01.024

Anderson, C.M., Samuelson, R.E., Nna-Mvondo, D., 2018. Organic Ices in Titan's Stratosphere. Space Sci. Rev. 214, 125. https://doi.org/10.1007/s11214-018-0559-5

Anderson, C.M., Samuelson, R.E., Yung, Y.L., Mclain, J.L., 2016. Solid-state photochemistry as a formation mechanism for Titan's stratospheric C4N2 ice clouds. Geophys. Res. Lett. 43, 3088–3094. https://doi.org/10.1002/2016GL067795.Abstract

Barnes, J.W., Bow, J., Schwartz, J., Brown, R.H., Soderblom, J.M., Hayes, A.G., Vixie, G., Le Mouélic, S., Rodriguez, S., Sotin, C., Jaumann, R., Stephan, K., Soderblom, L.A., Clark, R.N., Buratti, B.J., Baines, K.H., Nicholson, P.D., 2011. Organic sedimentary deposits in Titan's dry lakebeds: Probable evaporite. Icarus 216, 136–140. https://doi.org/10.1016/j.icarus.2011.08.022

Barnes, J.W., Brown, R.H., Soderblom, J.M., Soderblom, L.A., Jaumann, R., Jackson, B., Le Mouélic, S., Sotin, C., Buratti, B.J., Pitman, K.M., Baines, K.H., Clark, R.N., Nicholson, P.D., Turtle, E.P., Perry, J., 2009. Shoreline features of Titan's Ontario Lacus from Cassini/VIMS observations. Icarus 201, 217–225. https://doi.org/10.1016/j.icarus.2008.12.028

Barnes, J.W., Brown, R.H., Turtle, E.P., McEwen, A.S., Lorenz, R.D., Janssen, M., Schaller, E., Brown, M.E., Buratti, B.J., Sotin, C., Griffith, C., Clark, R., Perry, J., Fussner, S., Barbara, J., West, R., Elachi, C., Bouchez, A.H., Roe, H.G., Baines, K.H., Bellucci, G., Bibring, J.-P., Capaccioni, F., Cerroni, P., Combes, M., Coradini, A., Cruikshank, D.P., Drossart, P., Formisano, V., Jaumann, R., Langevin, Y., Matson, D.L., McCord, T.B., Nicholson, P.D., Sicardy, B., 2005. A 5-Micron-Bright Spot on Titan: Evidence for Surface Diversity. Science (80-.). 310, 92–95. https://doi.org/10.1126/science.1117075

Bassi, D., Menegotti, L., Oss, S., Scotoni, M., 1993. The 3-0 CH stretch overtone of benzene. Chem. Phys. Lett. 207, 167–172.

Blunt, V.M., Cedeño, D.L., Manzanares I, C., 1997. Vibrational overtone spectroscopy of methane in liquid argon solutions. Mol. Phys. 91, 3–17. https://doi.org/10.1080/002689797171698

Boese, R., Clark, T., Gavezzotti, A., 2003. Cocrystallization with Acetylene. The 1:1 Complex with Benzene: Crystal Growth, X-Ray Diffraction and Molecular Simulations. Helv. Chim. Acta 86, 1085–1100.

Böning, M., Stuhlmann, B., Engler, G., Busker, M., Häber, T., Tekin, A., Jansen, G., Kleinermanns, K., 2013. Towards a Spectroscopic and Theoretical Identification of the Isolated Building Blocks of the Benzene – Acetylene Cocrystal 837–846. https://doi.org/10.1002/cphc.201200701

Brock, A., Mina-camilde, N., I, C.M., 1994. Vibrational Spectroscopy of C-H Bonds of C2H4 Liquid and C2H4 in Liquid Argon Solutions. J. Phys. Chem. 98, 4800–4808.

Busker, M., Häber, T., Nispel, M., Kleinermanns, K., 2008. Isomer-Selective Vibrational Spectroscopy of Benzene – Acetylene Aggregates : Comparison with the Structure of the Benzene – Acetylene. Angew. Chemie 47, 10094–10097. https://doi.org/10.1002/anie.200802118

Cable, M.L., Vu, T.H., Hodyss, R., Choukroun, M., Malaska, M.J., Beauchamp, P., 2014. Experimental determination of the kinetics of formation of the benzene-ethane co-crystal and implications for Titan. Geophys. Res. Lett. 41, 5396–5401. https://doi.org/10.1002/2014GL060531

Cable, M.L., Vu, T.H., Malaska, M.J., Maynard-casely, H.E., Choukroun, M., Hodyss, R., 2020. Properties and Behavior of the Acetonitrile − Acetylene Co-Crystal under Titan Surface Conditions. https://doi.org/10.1021/acsearthspacechem.0c00129

Cable, M.L., Vu, T.H., Malaska, M.J., Maynard-casely, H.E., Choukroun, M., Hodyss, R., 2019. A Co-Crystal between Acetylene and Butane: A Potentially Ubiquitous Molecular Mineral on Titan. ACS Earth Sp. Chem. 3, 2808–2815. https://doi.org/10.1021/acsearthspacechem.9b00275

Cable, M.L., Vu, T.H., Maynard-Casely, H.E., Choukroun, M., Hodyss, R., 2018. The Acetylene-Ammonia Co-crystal on Titan. ACS Earth Sp. Chem. 2, 366–375. https://doi.org/10.1021/acsearthspacechem.7b00135

Clark, R.N., Curchin, J.M., Barnes, J.W., Jaumann, R., Soderblom, L., Cruikshank, D.P., Brown, R.H., Rodriguez, S., Lunine, J., Stephan, K., Hoefen, T.M., Mouélic, S. Le, Sotin, C., Baines, K.H., Buratti, B.J., Nicholson, P.D., 2010. Detection and mapping of hydrocarbon deposits on Titan. J. Geophys. Res. Planets 115, E10005. https://doi.org/10.1029/2009JE003369

Cooley, J.P., 1925. The Infra-red Absorption Bands of Methane. Astrophys. J. 62, 73–83.

Cordier, D., Barnes, J.W., Ferreira, A.G., 2013. On the chemical composition of Titan's dry lakebed evaporites. Icarus 226, 1431–1437. https://doi.org/10.1016/j.icarus.2013.07.026

Cordier, D., Cornet, T., Barnes, J.W., MacKenzie, S.M., Le Bahers, T., Nna-Mvondo, D., Rannou, P., Ferreira, A.G., 2016. Structure of Titan's evaporites. Icarus 270, 41–56. https://doi.org/10.1016/j.icarus.2015.12.034

Cordier, D., Mousis, O., Lunine, J.I., Lavvas, P., Vuitton, V., 2009. An estimate of the chemical composition of titan's lakes. Astrophys. J. 707, L128-131. https://doi.org/10.1088/0004-637X/707/2/L128

Cornet, T., Bourgeois, O., Le Mouélic, S., Rodriguez, S., Lopez Gonzalez, T., Sotin, C., Tobie, G., Fleurant, C., Barnes, J.W., Brown, R.H., Baines, K.H., Buratti, B.J., Clark, R.N., Nicholson, P.D., 2012. Geomorphological significance of Ontario Lacus on Titan: Integrated interpretation of Cassini VIMS, ISS and RADAR data and comparison with the Etosha Pan (Namibia). Icarus 218, 788–806. https://doi.org/10.1016/j.icarus.2012.01.013

Coustenis, A., Achterberg, R.K., Conrath, B.J., Jennings, D.E., Bézard, B., Samuelson, R.E., Carlson, R.C., Lellouch, E., Hubert, A., Orton, G.S., Kunde, V.G., Vinatier, S., 2007. The composition of Titan's stratosphere from Cassini/CIRS mid-infrared spectra. Icarus 189, 35–62. https://doi.org/10.1016/j.icarus.2006.12.022

Coustenis, A., Salama, A., Schulz, B., Ott, S., Lellouch, E., Encrenaz, T., Gautier, D., Feuchtgruber, H., 2003. Titan's atmosphere from ISO mid-infrared spectroscopy. Icarus 161, 383–403.

Coustenis, A., Schmitt, B., Khanna, R.K., Trotta, F., 1999. Plausible condensates in Titan's stratosphere from Voyager infrared spectra 47, 1305–1329. https://doi.org/https://doi.org/10.1016/S0032-0633(99)00053-7

Czaplinski, E., Farnsworth, K., Gilbertson, W., Chevrier, V., 2018. Experimental Studies of Ethylene and Benzene Evaporites on Titan. LPSC XLIX 2018, 1480.

Czaplinski, E., Farnsworth, K., Laxton, D., Chevrier, V., Heslar, M., Singh, S., 2017. Experimental Results of Evaporite Deposits on Titan Using a Surface Simulation Chamber. LPSC XLVIII 2017, 1537.

Czaplinski, E.C., Gilbertson, W.A., Farnsworth, K.K., Chevrier, V.F., 2019. Experimental Study of Ethylene Evaporites under Titan Conditions. ACS Earth Sp. Chem. 3, 2353–2362. https://doi.org/10.1021/acsearthspacechem.9b00204

Ellis, J.W., 1927. New Infra-red Absorption Bands of Methane. Physics (College. Park. Md). 13, 202–207.

Ennis, C., Cable, M.L., Hodyss, R., Maynard-casely, H.E., 2020. Mixed Hydrocarbon and Cyanide Ice Compositions for Titan ' s Atmospheric Aerosols: A Ternary-Phase Co-crystal Predicted by Density Functional Theory. ACS Earth Sp. Chem. 4, 1195–1200. https://doi.org/10.1021/acsearthspacechem.0c00130

Farnsworth, K.K., Chevrier, V.F., Steckloff, J.K., 2019. Nitrogen Exsolution and Bubble Formation in Titan ' s Lakes Geophysical Research Letters. Geophys. Res. Lett. 46, 1–10. https://doi.org/10.1029/2019GL084792

Fujii, A., Morita, S., Miyazaki, M., Ebata, T., Mikami, N., 2004. A Molecular Cluster Study on Activated CH / π Interactions : Infrared Spectroscopy of Aromatic Molecule - Acetylene Clusters 2652–2658. https://doi.org/10.1021/jp049946b

Hanel, R., Conrath, B., Flasar, F.M., Kunde, V., Maguire, W., Pearl, J., Pirraglia, J., Samuelson, R., Herath, L., Allison, M., Cruikshank, D., Gautier, D., Gierasch, P., Horn, L., Koppany, R., Ponnamperuma, C., 1981. Infrared Observations of the Saturnian System from Voyager 1. Science (80-.). 212, 192–200.

Hayes, A., Aharonson, O., Callahan, P., Elachi, C., Gim, Y., Kirk, R., Lewis, K., Lopes, R., Lorenz, R., Lunine, J., Mitchell, K., Mitri, G., Stofan, E., Wall, S., 2008. Hydrocarbon lakes on Titan: Distribution and interaction with a porous regolith. Geophys. Res. Lett. 35, L09204. https://doi.org/10.1029/2008GL033409

Hepp, M., Herman, M., 2000. Vibration-rotation bands in ethane. Mol. Phys. 98, 57–61. https://doi.org/10.1080/00268970009483269

Hörst, S.M., 2017. Titan's atmosphere and climate. J. Geophys. Res. Planets 122, 432–482. https://doi.org/10.1002/2016JE005240

Hudson, R.L., Ferrante, R.F., Moore, M.H., 2014. Infrared spectra and optical constants of astronomical ices : I . Amorphous and crystalline acetylene. Icarus 228, 276–287. https://doi.org/10.1016/j.icarus.2013.08.029

Kaye, W., 1954. Near-infrared spectroscopy: I. Spectral identification and analytical applications. Spectrochim. Acta 6, 257–287.

Khanna, R.K., 2005. Condensed species in Titan's stratosphere: Confirmation of crystalline cyanoacetylene (HC3N) and evidence for crystalline acetylene (C2H2) on Titan. Icarus 178, 165–170. https://doi.org/10.1016/j.icarus.2005.03.011

Koskinen, T.T., Yelle, R. V, Snowden, D.S., Lavvas, P., Sandel, B.R., Capalbo, F.J., Benilan, Y., West, R.A., 2011. The mesosphere and thermosphere of Titan revealed by Cassini/UVIS stellar occultations. Icarus 216, 507–534. https://doi.org/10.1016/j.icarus.2011.09.022

Lorenz, R.D., Turtle, E.P., Barnes, J.W., Trainer, M.G., Adams, D.S., Hibbard, K.E., Sheldon, C.Z., Zacny, K., Peplowski, P.N., Lawrence, D.J., Ravine, M.A., Mcgee, T.G., Sotzen, K.S., Mackenzie, S.M., Langelaan, J.W., Schmitz, S., Wolfarth, L.S., Bedini, P.D., 2018. Dragonfly: A Rotorcraft Lander Concept for Scientific Exploration at Titan. APL Tech. Dig. 34, 374–387.

Lorenz, R.D., Wall, S., Radebaugh, J., Boubin, G., Reffet, E., Janssen, M., Stofan, E., Lopes, R., Kirk, R., Elachi, C., Lunine, J., Mitchell, K., Paganelli, F., Soderblom, L., Wood, C., Wye, L., Zebker, H., Anderson, Y., Ostro, S., Allison, M., Boehmer, R., Callahan, P., Encrenaz, P., Ori, G.G., Francescetti, G., Gim, Y., Hamilton, G., Hensley, S., Johnson, W., Kelleher, K., Muhleman, D., Picardi, G., Posa, F., Roth, L., Seu, R., Shaffer, S., Stiles, B., Vetrella, S., Flamini, E., West, R., 2006. The Sand Seas of Titan : Cassini. Science (80-.). 312, 724–728. https://doi.org/DOI: 10.1126/science.1123257

Lunine, J.I., Hörst, S.M., 2011. Organic chemistry on the surface of Titan. Rend. Lincei 22, 183–189. https://doi.org/10.1007/s12210-011-0130-8

Lunine, J.I., Stevenson, D.J., Yung, Y.L., 1983. Ethane Ocean on Titan. Science (80-.). 222, 1229–1230.

Luspay-Kuti, A., Chevrier, V.F., Cordier, D., Rivera-Valentin, E.G., Singh, S., Wagner, A., Wasiak, F.C., 2015. Experimental constraints on the composition and dynamics of Titan's polar lakes. Earth Planet. Sci. Lett. 410, 75–83. https://doi.org/10.1016/j.epsl.2014.11.023

Luspay-Kuti, A., Chevrier, V.F., Wasiak, F.C., Roe, L.A., Welivitiya, W.D.D.P., Cornet, T., Singh, S., Rivera-Valentin, E.G., 2012. Experimental simulations of CH4 evaporation on Titan. Geophys. Res. Lett. 39, 2–6. https://doi.org/10.1029/2012GL054003

MacKenzie, S., Barnes, J., 2016. Compositional Similarities and Distinctions between Titan's Evaporitic Terrains. Astrophys. J. 821. https://doi.org/10.3847/0004-637X/821/1/17

MacKenzie, S.M., Barnes, J.W., Sotin, C., Soderblom, J.M., Le Mouélic, S., Rodriguez, S., Baines, K.H., Buratti, B.J., Clark, R.N., Nicholson, P.D., McCord, T.B., 2014. Evidence of Titan's climate history from evaporite distribution. Icarus 243, 191–207. https://doi.org/10.1016/j.icarus.2014.08.022

Majumder, M., Kumar, B., Sathyamurthy, N., 2013. CH · · · pi and pi · · · pi interaction in benzene – acetylene clusters. Chem. Phys. Lett. 557, 59–65. https://doi.org/10.1016/j.cplett.2012.12.027

Malaska, M.J., Hodyss, R., 2014. Dissolution of benzene, naphthalene, and biphenyl in a simulated Titan lake. Icarus 242, 74–81. https://doi.org/10.1016/j.icarus.2014.07.022

Malaska, M.J., Hodyss, R., Lunine, J.I., Hayes, A.G., Hofgartner, J.D., Hollyday, G., Lorenz, R.D., 2017. Laboratory measurements of nitrogen dissolution in Titan lake fluids. Icarus 289, 94–105. https://doi.org/10.1016/j.icarus.2017.01.033

Maleev, A. V, Boese, R., 2014. Investigation of topology of intermolecular interactions in the benzene – acetylene co-crystal by different theoretical methods. https://doi.org/10.1007/s11224-014-0413-7

Mastrogiuseppe, M., Hayes, A., Poggiali, V., Seu, R., Lunine, J.I., Hofgartner, J.D., 2016. Radar Sounding Using the Cassini Altimeter: Waveform Modeling and Monte Carlo Approach for Data Inversion of Observations of Titan's Seas. IEEE Trans. Geosci. Remote Sens. 54, 5646–5656. https://doi.org/10.2190/RM36-JLXA-6WUY-KDQ2

Mastrogiuseppe, M., Poggiali, V., Hayes, A., Lorenz, R., Lunine, J., Picardi, G., Seu, R., Flamini, E., Mitri, G., Notarnicola, C., Paillou, P., Zebker, H., 2014. The bathymetry of a Titan sea. Geophys. Res. Lett. 41, 1432–1437. https://doi.org/10.1002/ 2013GL058618. Received

Mastrogiuseppe, M., Poggiali, V., Hayes, A.G., Lunine, J.I., Seu, R., Di Achille, G., Lorenz, R.D., 2018. Cassini radar observation of Punga Mare and environs: Bathymetry and composition. Earth Planet. Sci. Lett. 496, 89–95. https://doi.org/10.1016/j.epsl.2018.05.033

Mastrogiuseppe, M., Poggiali, V., Hayes, A.G., Lunine, J.I., Seu, R., Mitri, G., Lorenz, R.D., 2019. Deep and methane-rich lakes on Titan. Nat. Astron. 3, 535–542. https://doi.org/10.1038/s41550-019-0714-2

Maynard-Casely, H.E., Hodyss, R., Cable, M.L., Vu, T.H., Rahm, M., 2016. A co-crystal between benzene and ethane: a potential evaporite material for Saturn's moon Titan. IUCrJ 3, 192–199. https://doi.org/10.1107/S2052252516002815

Moorhead, J.G., 1932. THE NEAR INFRARED ABSORPTION SPECTRUM OF METHANE. Phys. Rev. 39, 83–88.

Mousis, O., Lunine, J.I., Hayes, A.G., Hofgartner, J.D., 2016. The fate of ethane in Titan's hydrocarbon lakes and seas. Icarus 270, 37–40. https://doi.org/10.1016/j.icarus.2015.06.024

Nelson, B.R.C., Plylerl, E.K., Benedict, W.S., 1948. Absorption Spectra of Methane in the Near Infrared 41, 615–621.

Niemann, H.B., Atreya, S.K., Bauer, S.J., Carignan, G.R., Demick, J.E., Frost, R.L., Gautier, D., Paulkovich, M., Raulin, F., Raaen, E., Way, S.H., 2005. The abundances of constituents of Titan's atmosphere from the GCMS instrument on the Huygens probe. Nature 438, 779–784. https://doi.org/10.1038/nature04122

Niemann, H.B., Atreya, S.K., Demick, J.E., Gautier, D., Haberman, J.A., Harpold, D.N., Kasprzak, W.T., Lunine, J.I., Owen, T.C., Raulin, F., 2010. Composition of Titan's lower atmosphere and simple surface volatiles as measured by the Cassini-Huygens probe gas chromatograph mass spectrometer experiment. J. Geophys. Res. 115, 1–22. https://doi.org/10.1029/2010JE003659

Norris, W. V, Unger, H.J., 1933. Infrared Absorption Bands of Methane. Pysical Rev. 43, 467–472.

Preston, T.C., Firanescu, G., Signorell, R., 2010. Infrared spectroscopy and vibrational exciton modeling of crystalline , polycrystalline and amorphous acetylene aerosol particles. Phys. Chem. Chem. Phys. 12, 7924–7933. https://doi.org/10.1039/c002525a

Reboucas, M. V, de Barros Neto, B., 2001. Near infrared spectroscopic prediction of physical properties of aromatics-rich hydrocarbon mixtures. J. Near Infrared Spectrosc. 9, 263–273.

Reddy, K. V, Berry, M.J., 1982. Highly vibrationally excited benzene: Overtone spectroscopy and intramolecular dynamics of C6H6, C6D6, and partially deuterated or substituted benzenes. J. Chem. Phys. 76, 2814–2837.

Roe, H.G., de Pater, I., McKay, C.P., 2004. Seasonal variation of Titan's stratospheric ethylene (C2H4) observed. Icarus 169, 440–461. https://doi.org/10.1016/j.icarus.2004.01.002

Schwartz, Y.A., Ron, A., Kimel, S., 1969. FarInfrared Spectrum and Phase Transition of Acetylene The farinfrared spectrum of ice VIII Far-Infrared Spectrum and Phase Transition of Acetylene. J. Chem. Phys. 51, 1666–1667. https://doi.org/10.1063/1.1672234

Shemansky, D.E., Stewart, A.I.F., West, R.A., Esposito, L.W., Hallett, J.T., Liu, X., 2005. The Cassini UVIS Stellar Probe of the Titan Atmosphere. Science (80-.). 308, 978–982.

Singh, S., Combe, J.-P., Cordier, D., Wagner, A., Chevrier, V.F., McMahon, Z., 2017. Experimental determination of acetylene and ethylene solubility in liquid methane and ethane: Implications to Titan's surface. Geochim. Cosmochim. Acta 208, 86–101. https://doi.org/10.1016/j.gca.2017.03.007

Singh, S., Cornet, T., Chevrier, V.F., Combe, J., Mccord, T.B., Roe, L.A., Mouélic, S. Le, Menn, E. Le, Wasiak, F.C., 2016a. Near-infrared spectra of liquid / solid acetylene under Titan relevant conditions and implications for Cassini / VIMS detections. Icarus 270, 429–434. https://doi.org/10.1016/j.icarus.2015.11.002

Singh, S., Mccord, T.B., Combe, J., Rodriguez, S., Cornet, T., Mouélic, S. Le, Clark, R.N., Maltagliati, L., Chevrier, V.F., 2016b. Acetylene on Titan 's Surface. Astrophys. J. 828, 1–8. https://doi.org/10.3847/0004-637X/828/1/55

Sundararajan, K., Viswanathan, K.S., Kulkarni, A.D., Gadre, S.R., 2002. H · · · pi complexes of acetylene – benzene: a matrix isolation and computational study. J. Mol. Struct. 613, 209–222.

Tokano, T., 2009. Limnological Structure of Titan's Hydrocarbon Lakes and Its Astrobiological Implication. Astrobiology 9, 147–164. https://doi.org/10.1089/ast.2007.0220

Turtle, E.P., Barnes, J.W., Trainer, M.G., Lorenz, R.D., Hibbard, K.E., Adams, D.S., Bedini, P., Brinckerhoff, W.B., Ernst, C., Freissinet, C., Hand, K., Hayes, A.G., Johnson, J.R., Karkoschka, E., Langelaan, J.W., Gall, A. Le, Lora, J.M., Mackenzie, S.M., Mckay, C.P., Neish, C.D., Newman, C.E., Palacios, J., Parsons, A.M., Peplowski, P.N., Radebaugh, J., Rafkin, S.C.R., Ravine, M.A., Schmitz, S., Soderblom, J.M., Sotzen, S., Stickle, A.M., Stofan, E.R., Tokano, T., Wilson, C., Yingst, R.A., Zacny, K., Hopkins, J., Physics, A., Spatiales, O., Angeles, L., Field, M., Space, M., Systems, S., Diego, S., Robotics, H., 2018. Dragonfly: In Situ Exploration of Titan's Organic Chemistry and Habitability, in: 49th LPSC. p. Abstract 1641. https://doi.org/10.1109/AERO.2013.6497165.

Ulrich, N.W., Seifert, N.A., Dorris, R.E., Peebles, R.A., Pate, B.H., Peebles, S.A., 2014. Benzene Á Á Á acetylene : a structural investigation of the prototypical CH Á Á Á p interaction † 8886–8894. https://doi.org/10.1039/c4cp00845f

Vu, T.H., Cable, M.L., Choukroun, M., Hodyss, R., Beauchamp, P., 2014. Formation of a new benzene-ethane co-crystalline structure under cryogenic conditions. J. Phys. Chem. 118, 4087–4094. https://doi.org/10.1021/jp501698j

Waite Jr., J.H., Niemann, H., Yelle, R. V, Kasprzak, W.T., Cravens, T.E., Luhmann, J.G., Magee, B., Mcnutt, R.L., Ip, W., Gell, D., Haye, V.D. La, Mu, I., Borggren, N., Ledvina, S., Fletcher, G., Walter, E., Miller, R., Scherer, S., Thorpe, R., Xu, J., Block, B., Arnett, K., 2005. Ion Neutral Mass Spectrometer Results from the First Flyby of Titan. Science (80-.). 308, 982–986. https://doi.org/10.1029/2003JE002180

Wasiak, F.C., Luspay-Kuti, A., Welivitiya, W.D.D.P., Roe, L.A., Chevrier, V.F., Blackburn, D.G., Cornet, T., 2013. A facility for simulating Titan's environment. Adv. Sp. Res. 51, 1213–1220. https://doi.org/10.1016/j.asr.2012.10.020

CHAPTER 2. EXPERIMENTAL INVESTIGATION OF THE ACETYLENE–BENZENE COCRYSTAL ON TITAN

Ellen Czaplinski[1], Xinting Yu (余馨婷)[2], Katherine Dzurilla[1], and Vincent Chevrier[1]

[1]Arkansas Center for Space and Planetary Sciences, University of Arkansas, Fayetteville, AR 72701, USA
[2]Department of Earth and Planetary Sciences, University of California Santa Cruz, Santa Cruz, CA 95064, USA

Czaplinski, E. C., Yu, X., Dzurilla, K., Chevrier, V. (2020). Experimental Investigation of the Acetylene–Benzene Cocrystal on Titan. *The Planetary Science Journal, 1,* 16pp. https://doi.org/10.3847/PSJ/abbf57

Keywords: Molecular spectroscopy, experimental techniques, surface ices

Highlights:

- First study of the acetylene-benzene co-crystal under Titan temperature and pressure
- Cocrystal identified based on unique spectral bands and changes in sample morphology
- Cocrystal is stable from 90 K to 135 K
- 5 cm of this cocrystal could have accumulated on Titan's surface over 1 Gyr, based on atmospheric production rates of these species

1. Abstract

Acetylene and benzene are two common molecules formed in Titan's atmosphere, and are likely components of the lake evaporites. It is known that these two molecules can form a cocrystal, a molecule with a structure that is unique from that of the component molecules. Thus, we sought to study this cocrystal using an experimental setup that simulates Titan surface conditions (90 K, 1.5 bar). Using Fourier transform infrared (FTIR) spectroscopy, we characterize new spectral absorptions, band shifts, and morphological sample changes associated with this cocrystal from 1 to 2.6 μm, which overlaps with Cassini VIMS wavelength range (0.35–5.1 μm). This is the first study of the resulting acetylene–benzene cocrystal under Titan-relevant temperature and pressure. The cocrystal forms at 135 K and is stable down to 90 K. Our findings can be applied to the cocondensation process in Titan's atmosphere, as well as the

ongoing effort to better characterize the composition and spectral properties of Titan's lake evaporites. These results can also provide a stepping stone to future surface missions such as Dragonfly, which will closely examine relevant surface materials on Titan.

2. Background

Titan has a plethora of simple and complex organic molecules that are created in the atmosphere by solar ultraviolet rays and energetic particles from Saturn's magnetosphere interacting with atmospheric methane (CH_4) and nitrogen (N_2). A range of simple organics can be produced, including C_2H_6, C_2H_2, C_2H_4, C_6H_6, HCN, etc. (Hörst, 2017), many of which are able to condense or co-condense from gas to solid ices in Titan's atmosphere and potentially form ice clouds (Anderson et al., 2018). These condensation (or co-condensation) byproducts would eventually fall to Titan's surface in the solid phase, where they could either directly deposit into the polar lakes and be dissolved, or they may be transported fluvially across Titan's surface via river channels, and eventually dissolve into the lakes and seas. After lake evaporation, these types of compounds would precipitate out from the lakes in the form of evaporites, as observed by *Cassini* RADAR (Barnes et al. 2011; Cordier et al. 2016; MacKenzie & Barnes 2016). However, in order to fully understand the composition of these observed evaporitic features, additional experimental work is needed. Previous laboratory studies have characterized a number of potential evaporite compounds and co-crystals such as acetylene (C_2H_2; Singh et al., 2017), ethylene (C_2H_4; Czaplinski et al. 2019; Singh et al. 2017) ethane-benzene (C_2H_6-C_6H_6; Cable et al., 2014; Vu et al., 2014), acetylene-butane (C_2H_2-C_4H_{10}; Cable et al., 2019), and acetylene-ammonia (C_2H_2-NH_3; Cable et al., 2018).

Here, we characterize a type of evaporite compound (a co-crystal) formed with C_2H_2 and C_6H_6. Both C_2H_2 and C_6H_6 are relatively abundant photochemical products, with C_2H_2 being the second most abundant hydrocarbon produced in Titan's atmosphere, behind ethane (C_2H_6; Hörst, 2017). Acetylene has been detected in Titan's atmosphere by the infrared radiometer spectrometer (IRIS) on Voyager 1 (Hanel et al., 1981), telescopes such as the Infrared Space Observatory (ISO; Coustenis et al. 2003), *Cassini's* Ion Neutral Mass Spectrometer (INMS; Waite et al. 2005), *Cassini's* Ultraviolet Imaging Spectrometer (UVIS; Shemansky et al. 2005), *Cassini* Infrared Spectrometer (CIRS; Coustenis et al. 2007), and near Titan's surface by the *Huygens* probe (Niemann et al., 2010). Solid acetylene ices have been observed by the *Cassini* Visual and Infrared Mapping Spectrometer (VIMS; Singh et al. 2016b). Acetylene has been linked to the composition of Titan's equatorial dunes (Abplanalp et al., 2019; Lorenz et al., 2006) and is a primary candidate for composing the evaporites that are ever present in Titan's lake district (Cordier et al., 2009). Benzene was first detected at Titan by the ground based telescope ISO (Coustenis et al. 2003), and was also measured by *Cassini*/INMS (Waite et al. 2005), UVIS (Koskinen et al., 2011), CIRS (Coustenis et al. 2007), near the surface by the *Huygens* probe (Niemann et al., 2005), and as surface ices by *Huygens*' Gas Chromatograph Mass Spectrometer (GCMS; Niemann et al. 2005) and *Cassini*/VIMS (Clark et al. 2010).

The formation of the C_2H_2-C_6H_6 co-crystal has been studied in great detail in previous works using infrared-ultraviolet (IR-UV) double resonance spectroscopy (Sundararajan et al. 2002; Fujii et al. 2004; Busker et al. 2008; Böning et al. 2013; Ulrich et al. 2014). In the simplest structure, a hydrogen from the C_2H_2 molecule interacts with the π cloud from the C_6H_6 molecule, forming a C-H ••• π bond in a T-shaped arrangement (e.g., Fig. 1 from Busker et al., 2008; Sundararajan et al., 2002). The driving factor in the T-shaped arrangement of the C_2H_2-C_6H_6 co-crystal is a coulombic-polarization interaction between the electron-deficient H-atom end of the C_2H_2 molecule and the electron-rich C_6H_6 ring (Boese et al., 2003). Strong miscibility and solubility between C_2H_2 and C_6H_6 is the main force for co-crystal formation (Boese et al., 2003). These previously reported techniques have laid the groundwork for characterizing the co-crystal in the mid infrared region. Additionally, X-Ray Diffraction (XRD) and ab initio theoretical calculations (Sundararajan et al. 2002; Majumder et al. 2013; Maleev & Boese 2014;; Ulrich et al. 2014) have also given detailed structural information on the co-crystal.

Recent studies of evaporite-relevant co-crystal formation with C_2H_2-C_4H_{10} and C_2H_2-NH_3 mixtures underscores the importance of studying such molecules under Titan conditions (Cable et al., 2019, 2018). Co-crystal formation in a C_2H_6-C_6H_6 system has also been carried out at Titan temperatures (Cable et al. 2014; Vu et al. 2014; Maynard-Casely et al. 2016), and benzene has been included in the list of probable evaporite molecules (Clark et al., 2010). However, the formation of the C_2H_2-C_6H_6 co-crystal has not yet been tested under Titan atmospheric and surface conditions. Therefore, we sought to study the interactions of the acetylene-benzene aggregate at Titan-relevant temperatures and pressure (~89-94 K, 1.5 bar) using IR spectroscopy (1-2.6 μm).

3. Experimental Methods

To investigate interactions between acetylene and benzene, we conduct laboratory experiments in the Titan Surface Simulation Chamber (TSSC) located at the University of Arkansas (Wasiak et al., 2013). Briefly, a pressure of 1.5 bar is maintained with N_2 gas and temperatures of 89 - 94 K are maintained with liquid nitrogen (LN_2). Organic compounds are condensed from gas phase in a condenser, and are then poured onto a sample dish for further analysis. The TSSC has been used for a number of previous Titan-relevant studies (Luspay-Kuti et al., 2015, 2012; Singh et al., 2017). More recently, several modifications to the TSSC's cooling system, fiber optics, and cameras have allowed for studies of Titan's evaporites

(Czaplinski et al. 2019) and bubble formation in Titan's lakes (Farnsworth et al., 2019). The specific mechanics and protocols of the TSSC are detailed in these previous studies. Relevant details for this set of experiments are provided below.

Prior experimental protocol for the TSSC was designed for compounds that are gas phase at standard ambient temperature and pressure (SATP; e.g., CH_4, C_2H_4, C_2H_6, etc.). However, since C_6H_6 is a liquid at SATP, a refined experimental protocol must be followed when introducing C_6H_6 to the TSSC. First, we restrict LN_2 flow from the condenser, while LN_2 cools the rest of the TSSC temperature control box (TCB) as normal. Inside a custom-built glovebox, an Erlenmeyer flask is filled with 50 mL of >99.7%, OmniSolv® Benzene (C_6H_6, Sigma-Aldrich). The flask has two connections through the glovebox: one to the N_2 gas (Airgas industrial grade, >99.998%), and the other to a valve control on the exterior of the chamber with "exhaust" and "condenser" outlets. Nitrogen is continuously bubbled through the C_6H_6-filled flask to the exhaust system at 20 kPa for ~5 minutes. This flow of N_2 through the flask creates surficial bubbling of the C_6H_6 that is confirmed through optical images. After the flask reaches N_2 saturation and the sample dish reaches ~223 K, we then open the solenoid valve, close the exhaust valve, and open the exterior condenser inlet so that the N_2-C_6H_6 saturated mixture is carried through the condenser where it deposits onto the sample dish in solid phase (referred to here as the cold trap method). The C_6H_6 deposits onto the sample dish for ~15 minutes, or until solid C_6H_6 particles are seen in the TCB's optical cameras and Fourier transform infrared spectroscopy (FTIR) measurements show C_6H_6 vibrational bands. We use a Nicolet 6700 FTIR spectrometer that is equipped with a TEC InGaAs 2.6 µm detector, a CaF_2 beam-splitter, spectral range of 1 to 2.6 µm, spectral sampling of 4 cm^{-1}, spectral resolution of 0.01 cm^{-1}, and connected to a fiber optic probe located above the sample dish. After this allotted time, the N_2 bubbling through the Erlenmeyer flask is stopped, and the external condenser outlet is closed. We leave the solenoid valve open for an additional 5 minutes to prevent any blockages from the C_6H_6. Additional FTIR measurements of the pure C_6H_6 are made for comparisons between the combined mixture later.

After the sample dish has reached 173 K, we begin flowing C_2H_2 (Airgas, 99.6%, acetone added as stabilizer) through the condenser at 50 kPa for 20 minutes, where it deposits on the sample dish in solid phase. Deposition is confirmed by optical TCB cameras and FTIR spectra. After we stop the C_2H_2 gas flow, the solenoid valve is left open for 5 minutes to prevent blockages.

Once both compounds are deposited onto the sample dish (sample thickness on the order of a few mm), the LN_2 flow to the condenser is turned on. Note that at this point, we are finished adding compounds to the condenser; the condenser LN_2 flow merely contributes to the rest of the TCB successfully attaining Titan surface temperatures (89 – 90 K). Depending on the experiment, the TCB temperatures may be warmed later in the experiment in an attempt to speed up reaction times or, in the case of C_2H_2, to identify how the spectra changes with regards to temperature. The mole fraction for the acetylene-benzene experiment was calculated using the same methods reported in Czaplinski et al. (2019; see Spectral Unmixing Model section), a Python code that decomposes a given spectrum into a best fit of linear combinations of the pure spectra (taken at corresponding temperatures) added together. The mole fraction is reflected in the linear weights that each raw component spectrum is given in order to fit the experimental data.

4. Results

Near-infrared (NIR) spectra of acetylene is reported first, then benzene, and lastly we examine the formation of the acetylene-benzene combined aggregate. For clarity, a reduced spectral range (1.45 to 1.96 µm for C_2H_2 and 1.57 to 2.33 µm for C_6H_6) is presented to allow for an enhanced view of the bands described. The full range spectra are included in the Appendix (Figures A1-A4). Regarding the vibrational mode and bond label columns in Tables 1-5, NIR absorption bands arise from overtones and combinations of the fundamental IR molecular vibrations often associated with hydrogen atoms. Changes in the interatomic distance or angle between two atoms are known as stretching or bending vibrations, respectively. The vibrational quantum number, v, describes the energy state of the vibrational motion the molecule, in terms of degrees of freedom.

4.1. NIR Reflectance Spectra of C_2H_2 Ice

Figure 1 shows NIR spectra of acetylene ice from 89 to 184 K. Vibrational modes and band assignments are presented in Table 1. The acetylene was deposited as a solid at 140 K, after which the temperature was lowered to 89 K over the course of 28 minutes, then slowly warmed (temperatures denoted in Fig. 1). The average temperature decrease was -1.73 degrees/minute with the steepest decrease in temperature being -4.61 degrees/minute. At 89 K, the acetylene exhibits a quadruplet feature from 1.54 – 1.55 µm ($\nu_1 + \nu_3$ vibrational mode), as well as two smaller bands around 1.931 µm ($5\nu_4 + 3\nu_5$ vibrational mode; Fig. 1). Significant spectral changes occur as the sample is slowly warmed.

Repeated experiments show the next major change occurs at 140 K, where the quadruplet transforms into a single band (centered at 1.547 µm), and the $5\nu_4 + 3\nu_5$ mode decreases in reflectance by ~13% (Fig. 1). The quadruplet band center is blue shifted to the single band by

0.025 - 0.026 µm from the 89 K spectrum. The last band transition in this study occurs at 184 K (just before acetylene's sublimation point, 189 K, and triple point, 192 K), where the formerly single band at 1.547 µm disappears, leaving only the doublet with band centers at 1.521 and 1.529 µm (Fig. 1). Minor bands at 2.135 and 2.222 µm ($\nu_1 + \nu_4 + \nu_5$ and $\nu_3 + 2\nu_4$, respectively) are presented in the Appendix (Figure A1).

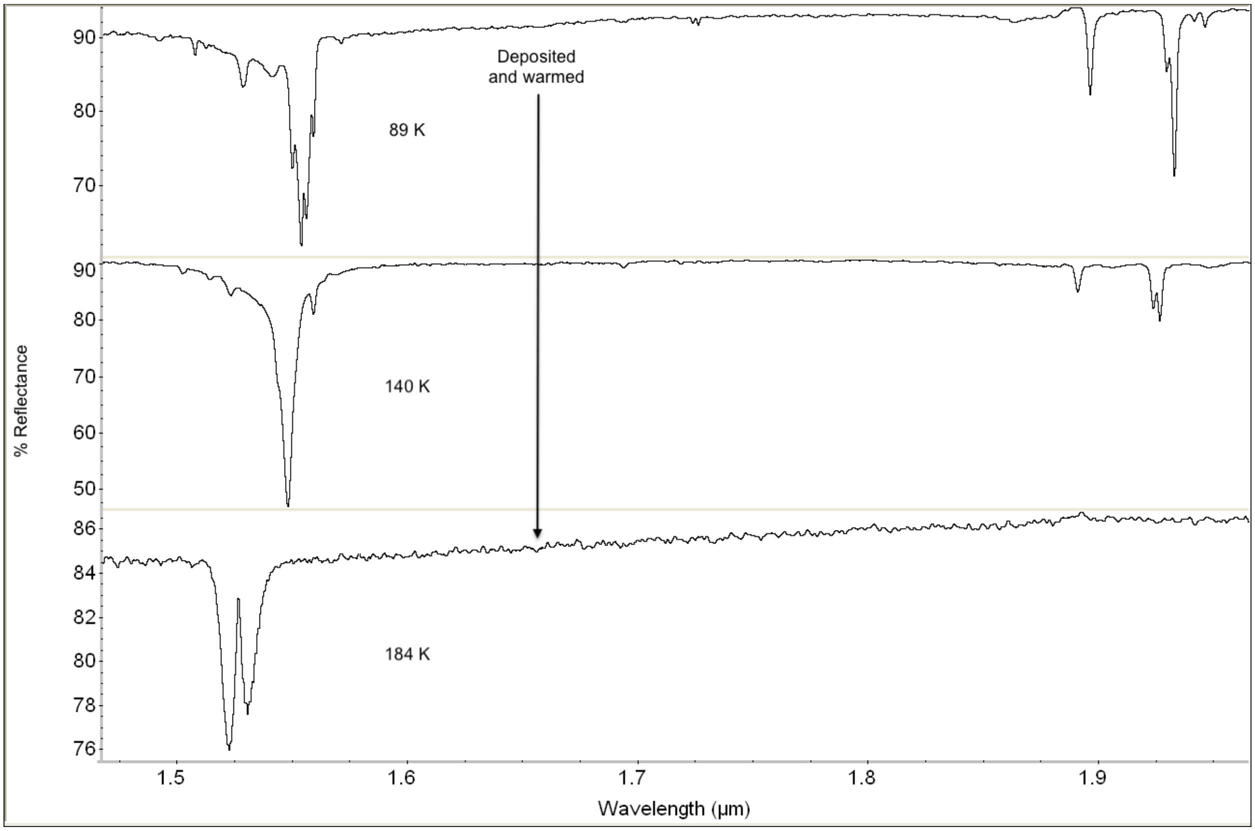

Figure 1. Fourier transform infrared reflectance spectra (1.45 to 1.96 µm) of C_2H_2 from 89 K to 184 K. Acetylene was deposited at 140 K, the sample was cooled to 89 K, then slowly warmed to 184 K. Two transition phases are observed at 140 K and 184 K.

Table 1. Vibrational modes and band assignments of C_2H_2. Band centers from this study at various temperatures are compared to literature values at 15 K (band centers in wavenumbers (cm^{-1}) are listed in brackets).

Vibrational Mode Assignment	Band Centers from the Literature[1]	This Study		
	λ (μm) 15 K [wavenumber (cm^{-1})]	λ (μm) 89 K	λ (μm) 140 K	λ (μm) 184 K
$\nu_1 + \nu_3$ (sym. and asym. C-H stretch)	1.552 [6442]	1.552 [6440]	…	…
$\nu_1 + \nu_3(\nu_2 + \nu_3 + 2\nu_4)$ First overtone of C-H stretch	1.545 [6472]	…	1.547 [6465]	…
	1.549 [6454]	1.548 [6457]	…	…
	1.552 [6442]	1.552 [6440]	…	…
	1.555 [6431]	1.555 [6432]	…	…
	1.557 [6421]	1.558 [6419]	1.558 [6418]	…
$\nu_1 + 2\nu_4 + \nu_5$ (C-H sym., *trans*, and *cis* bend)	1.896 [5275]	1.895 [5276]	1.890 [5291]	…
$5\nu_4 + 3\nu_5$ *(trans* and *cis* bend)	1.929 [5183]	1.928 [5185]	1.923 [5201]	…
	1.933 [5174]	1.932 [5176]	1.925 [5193]	…
$\nu_1 + \nu_4 + \nu_5$ (C-H sym., *trans* and *cis* bend)	2.135 [4684]	2.135 [4682]	2.133 [4689] 2.139 [4674]	…
$\nu_3 + 2\nu_4$ (C-H asym. stretch, *trans* bend)	2.221 [4502]	2.222 [4500]	2.224 [4495]	…

Notes. Band centers from this study at various temperatures are compared with values from the literature at 15 K (band centers in wavenumbers (cm−1) are listed in brackets).
References: [1]Hudson, Ferrante, and Moore 2014

4.2. NIR Reflectance Spectra of C_6H_6 Ice

Figure 2 shows NIR spectra of pure benzene from 85 to 151 K from separate experiments where corresponding temperatures were achieved. Vibrational modes and band assignments of benzene are presented in Table 2. NIR benzene spectra are characterized by C-H aromatic ring first overtones of stretching vibrations in the 1.65 – 1.70 µm region (Fig. 2, Table 2). Various less reflective bands are observed from 1.70 – 2.00 µm, which lead up to the C-H aromatic ring combination bands from 2.14 – 2.20 µm region (Fig. 2).

We do not observe drastic spectral changes with temperature, as with acetylene. The main difference among the benzene spectra is the decrease in reflectance by ~10-15% at warmer temperatures, possibly due to grain size differences, volumetric scattering (Singh et al., 2016a), or a change in thickness due to sublimation or evaporation of the sample as it is heated.

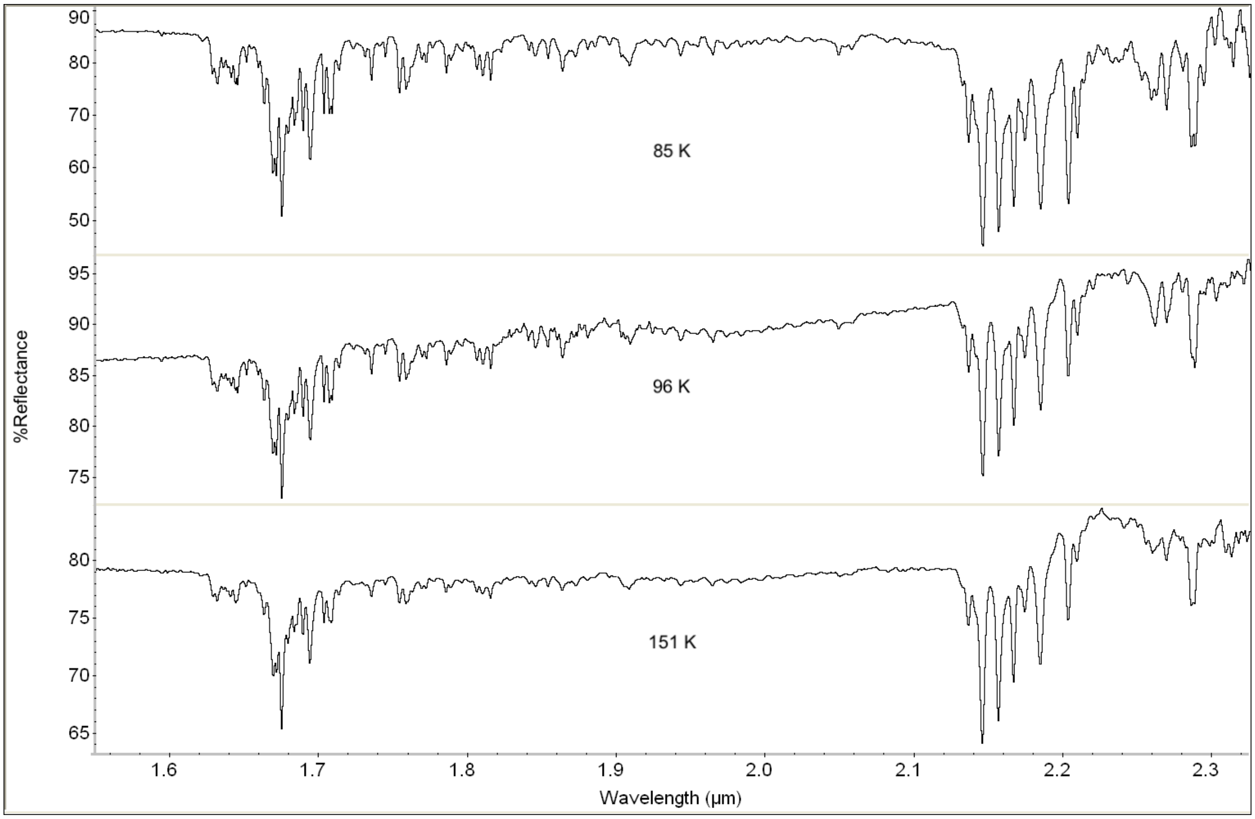

Figure 2. Fourier transform infrared reflectance spectra (1.57 to 2.33 µm) of C_6H_6 from 85 to 151 K. Full range spectra presented in Appendix Figure A2. These spectra represent three separate experiments where the corresponding temperature range was achieved. Notice the decrease in reflectance with increasing temperature.

Table 2. Vibrational modes and band assignments of C_6H_6.

Vibrational Mode Assignment	Band Centers From the Literature		This Study (85 – 151 K)	
	$\tilde{v}$ (cm^{-1})	λ (μm)	$\tilde{v}$ (cm^{-1})	λ (μm)
v_3 (C-H aromatic stretch)	8786[a]	1.138	8793	1.137
$2v_{CH}+2(v_{CC} + v_3)$ (C-H aromatic stretch)	8770[b]	1.140	8774	1.139
$v_{15} + v_5$ (C-H aromatic stretch)	6107[c,d]	1.637	6136	1.63
$v_{12} + v_1$ (C-H aromatic stretch)	5985[c]	1.671	5976	1.673
$v_{15} + v_5$ (C-H aromatic stretch)	5920[c,e]	1.689	5910	1.691
$v_{15} + v_9$ (C-H aromatic combination)	4655[c]	2.141[f]	4663	2.144
$v_{12} + v_{16}$ (C-H aromatic combination)	4642[c]	2.153[f]	4640	2.155
$v_{16} + v_5$ (C-H aromatic combination)	4615[c]	2.163[f]	4618	2.165
$v_{13} + v_1$ (C-H aromatic combination)	4570[c]	2.181[f]	4580	2.183
$v_{13} + v_{15}$ (C-H aromatic combination)	4532[c]	2.200[f]	4541	2.202
$v_{12} + v_3$ Methyl C-H combination)	4360[c]	2.294	4372	2.286
$v_{12} + v_{17}$ (Methyl C-H combination)	4252[c]	2.352	4256	2.349

[a] (Reddy and Berry, 1982), gas phase
[b] (Bassi et al., 1993), 300 K
[c] (Kaye, 1954), no temperature noted
[d] calculated
[e] observed
[f] (Reboucas and de Barros Neto, 2001), 292 K

4.3. NIR Reflectance Spectra of C_2H_2-C_6H_6 Mixture

Figures 3 and 4 show NIR spectra of a C_2H_2-C_6H_6 mixture from 135 to 151 K and 93 to 94 K, respectively. The benzene:acetylene %mol fraction for this experiment is 45:55. Assignments of new bands are presented in Tables 3 and 4. Table A1 lists the temperature at each time a new spectrum was recorded. In this experiment, C_6H_6 was deposited first, from 158 to 132 K, then C_2H_2 was deposited afterward, from 168 to 150 K. The sample was cooled to 94 K, warmed to 173 K, before cooling back to 93 K in order to characterize spectral changes with temperature. The 144 K spectrum (Fig. 3) was taken during C_2H_2 deposition (t = 0). We observe several new bands in the combined spectrum that are not present in either pure C_2H_2 or C_6H_6

spectra (Figs. 1 and 2). These bands are located from 1.569 to 1.598 μm, as well as 1.943 to 2.122 μm (Figs. 3 and 4). We observe an increase in reflectance by up to 20% as temperature decreases. These reflectance changes may be due to changes in sample thickness, as more C_2H_2 and/or C_6H_6 in the "atmosphere" above the sample dish could be condensing on the sample dish.

Additionally, we observe several significant frequency shifts of bands associated with the bare C_2H_2 molecule (Figs. 3 and 4, Tables 3 and 4). The largest shifts associated with C_2H_2 are observed immediately after C_2H_2 has been deposited on the sample dish at 135 K (t = 6). This is observed in the $5\nu_4 + 3\nu_5$ band of C_2H_2 which blueshifts by 30 cm^{-1} upon co-crystal formation. When combined with C_6H_6, the 1.548 μm band ($\nu_1 + \nu_3(\nu_2 + \nu_3 + 2\nu_4)$ mode) redshifts by 45.64 cm^{-1} and the 1.925 μm bands ($5\nu_4 + 3\nu_5$ mode) redshifts by 26.85 cm^{-1} (Table 5). Note that we use the unit cm^{-1} in these shifts to compare values with ones reported in the literature. The $\nu_1 + \nu_3(\nu_2 + \nu_3 + 2\nu_4)$ vibrational mode (quadruplet feature at 1.549 μm and 1.558 μm; see Table 1) blueshifts from 4.12 to 8.35 cm^{-1}, whereas the $5\nu_4 + 3\nu_5$ vibrational mode (1.932 μm) redshifts by up to 10.69 cm^{-1} in the last spectrum of the experiment (t = 168). Figure A5 shows shifts of the 1.558 μm band with temperature. Frequency shifts of bands associated with the bare C_6H_6 molecule are characterized by a 3.60 cm^{-1} blueshift of the C-H aromatic ring first overtones, a 3.58 cm^{-1} redshift of the ν_2 mode, a 3.50 cm^{-1} blueshift of the $\nu_{15} + \nu_5$ mode, and a 2.10 cm^{-1} blueshift of the $\nu_{13} + \nu_1$ mode.

The sample shows significant optical changes after C_2H_2 deposition, as shown in Figure 5. When only C_6H_6 is in the sample dish (Fig. 5 (a), (c)), the sample consists of separated, spherical, white deposits. However, after C_2H_2 is added to the C_6H_6 (Fig. 5 (b), (d)), the sample's appearance changes drastically. Separate white deposits are no longer present, rather, the sample transforms into an ice-like phase with many new morphological features including linear features, dark separation lines, flattening of the sample, and increased reflectivity. These features are not observed in any experiments with solely C_2H_2 or C_6H_6. Knowledge of the unique morphology of the co-crystal may help future Titan surface missions (i.e., *Dragonfly*) identify co-crystals with the microscopic camera of DragonCam (Lorenz et al., 2018).

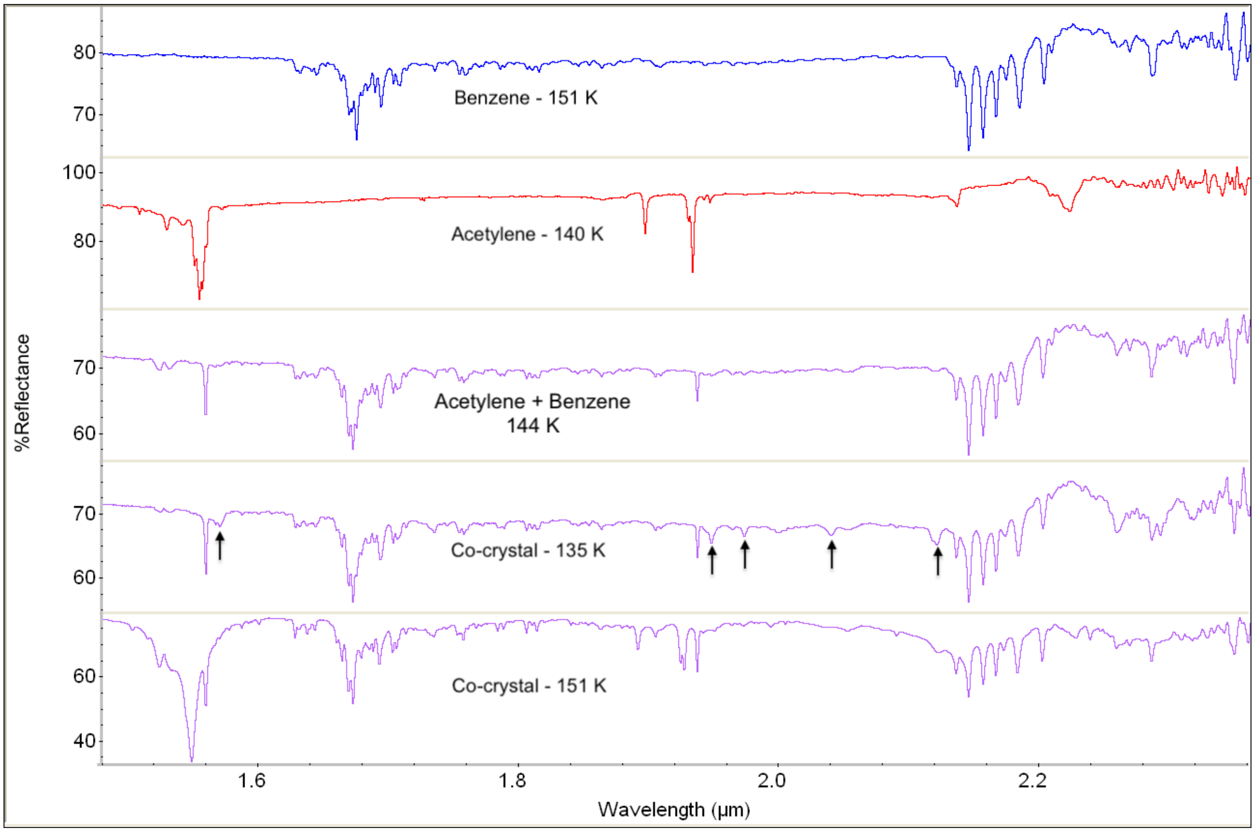

Figure 3. NIR reflectance spectra of pure C_6H_6 (blue) and C_2H_2 (red) compared with the C_2H_2-C_6H_6 co-crystal (purple) from 1.48 to 2.35 µm. Co-crystal spectra are shown in order of increasing time from top to bottom. Only "warm" spectra are shown here (135 – 151 K). The sample was cooled to 94 K, warmed to 173 K, then cooled back to 93 K to characterize changes with temperature ("cold" spectra shown in Fig. 4). The bands denoted by arrows in the 135 K spectrum represent the transition to co-crystal formation, as they are neither present in pure C_6H_6 nor C_2H_2 at similar temperatures.

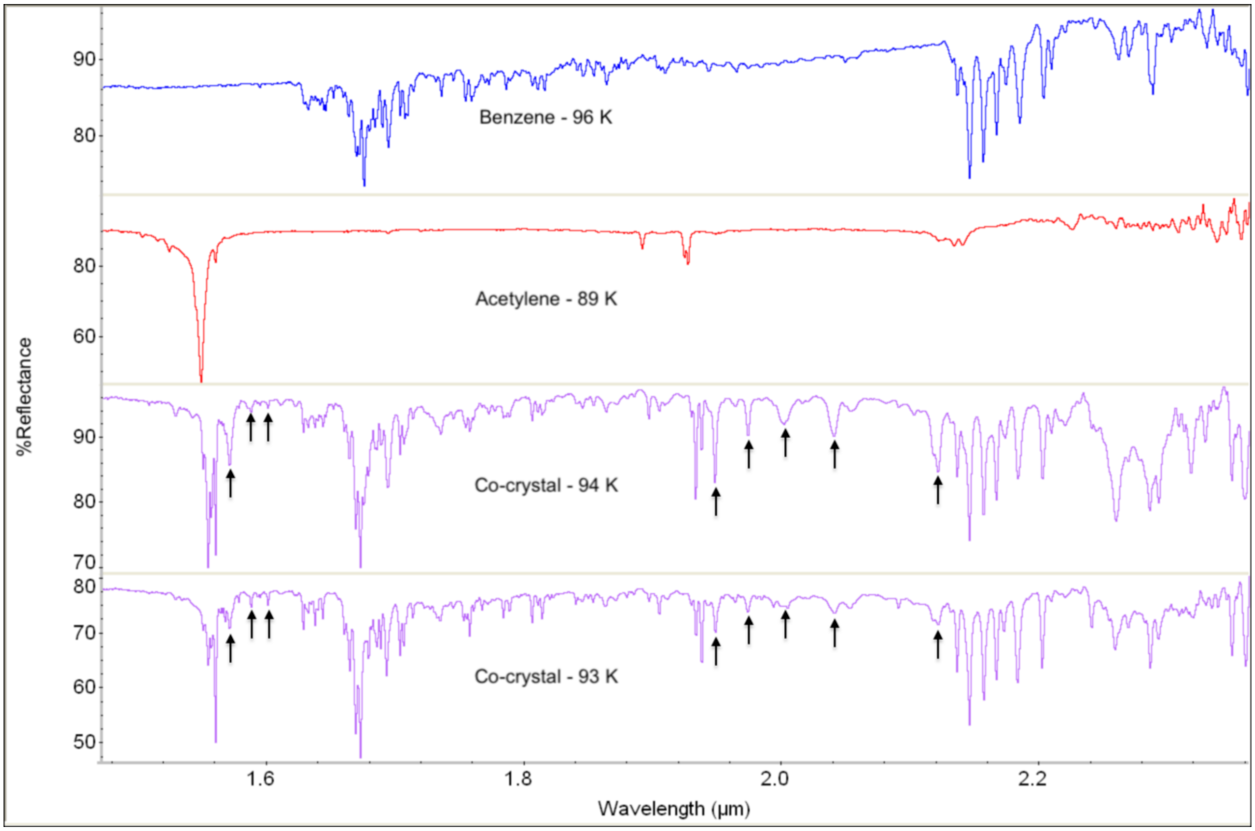

Figure 4. NIR reflectance spectra of pure C_6H_6 (blue) and C_2H_2 (red) compared with the C_2H_2-C_6H_6 co-crystal (purple) from 1.48 to 2.35 µm. Co-crystal spectra are shown in order of increasing time from top to bottom. Only "cold" spectra are shown here (89 - 96 K). The sample was cooled to 94 K, warmed to 173 K ("warm" spectra shown in Fig. 3), then cooled back to 93 K to characterize changes with temperature. Notice the additional new bands (denoted by arrows) associated with the co-crystal that appear at these colder temperatures, when compared with the warmer temperatures of Figure 3.

Table 3. Band centers from pure cubic C_2H_2 (140 K) and pure C_6H_6 (151 K) compared with co-crystal bands at 135 K.

Molecule	Vibrational Mode Assignment	Band Center *λ* (μm) [wavenumber (cm-1)]		
		Pure Component	Co-crystal (135 K)	Δv between Pure and Co-crystal
Acetylene (140 K)	$v_1 + v_3(v_2 + v_3 + 2v_4)$	1.558 [6418]	1.557 [6421]	0.001 [3]
	First overtone of C-H stretch	…	1.568 [6376]	…
	$5v_4 + 3v_5$ (*Trans* and *cis* bend)	1.923 [5201] 1.925 [5193]	1.936 [5166]	0.011 [-35]
	…	…	1.946 [5138]	…
	…	…	1.971 [5072]	…
	…	…	2.038 [4906]	…
Benzene (151 K)	$v_{12} + v_1$ (C-H aromatic stretch)	1.673 [5976]	1.673 [5976]	0
	$v_{15} + v_5$ (C-H aromatic stretch)	1.693 [5908]	1.692 [5911]	0.001 [3]
	$v_{15} + v_9$ (C-H aromatic combination)	2.145 [4662]	2.145 [4662]	0
	$v_{12} + v_{16}$ (C-H aromatic combination)	2.155 [4640]	2.155 [4640]	0
	$v_{16} + v_5$ (C-H aromatic combination)	2.165 [4618]	2.165 [4618]	0
	$v_{13} + v_1$ (C-H aromatic combination)	2.183 [4579]	2.182 [4582]	0.001 [3]
	$v_{13} + v_{15}$ (C-H aromatic combination)	2.202 [4540]	2.201 [4543]	0.001 [3]
	$v_{12} + v_{17}$ (Methyl C-H combination)	2.350 [4256]	2.348 [4258]	0.002 [2]

Note. Only bands present in either the co-crystal or both the co-crystal and pure component are presented. All other bands for C_2H_2 and C_6H_6 are listed in Tables 1 and 2.

Table 4. Band centers from pure orthorhombic C_2H_2 (89 K) and pure C_6H_6 (96 K) compared with co-crystal bands at 94 K. Only bands present in either the co-crystal or both the co-crystal and pure component are presented.

Molecule	Vibrational Mode Assignment	Band Center λ (μm) [wavenumber (cm-1)]		
		Pure Component	Co-crystal (94 K)	Δv between Pure and Co-crystal
Acetylene (89 K)	$v_1 + v_3(v_2 + v_3 + 2v_4)$ First overtone of C-H stretch	…	1.569 [6374]	…
		…	1.585 [6306]	…
		…	1.599 [6254]	…
	$v_1 + 2v_4 + v_5$ (C-H sym., *trans*, and *cis* bend)	1.895 [5276]	1.895 [5276]	0
		…	1.903 [5254]	…
	$5v_4 + 3v_5$ (*Trans* and *cis* bend)	1.928 [5185]	1.928 [5185]	0
		1.932 [5176]	1.931 [5177]	0.001 [1]
	…	…	1.936 [5164]	…
	…	…	1.946 [5137]	…
	…	…	1.972 [5069]	…
	…	…	2.00 [5000]	…
	…	…	2.039 [4904]	…
	$v_1 + v_4 + v_5$ (C-H sym., *trans* and *cis* bend)	2.135 [4682]	2.135 [4684]	0 [2]
	$v_3 + 2v_4$ (C-H asym. stretch, *trans* bend)	2.222 [4500]	2.219 [4506]	0.003 [6]
Benzene (96 K)	$v_{12} + v_1$ (C-H aromatic stretch)	1.673 [5976]	1.673 [5976]]	0
	$v_{15} + v_5$ (C-H aromatic stretch)	1.692 [5909]	1.692 [5910]	0 [1]
	$v_{15} + v_9$ (C-H aromatic combination)	2.144 [4663]	2.144 [4663]	0
	$v_{12} + v_{16}$ (C-H aromatic combination)	2.155 [4640]	2.155 [4640]	0
	$v_{16} + v_5$ (C-H aromatic combination)	2.165 [4617]	2.165 [4618]	0 [1]
	$v_{13} + v_1$ (C-H aromatic combination)	2.183 [4580]	2.182 [4582]	0.001 [2]
	$v_{13} + v_{15}$ (C-H aromatic combination)	2.202 [4541]	2.201 [4543]	0.001 [2]
	$v_{12} + v_3$ Methyl C-H combination)	2.286 [4374]	2.285 [4376]	0.001 [2]
	$v_{12} + v_{17}$ (Methyl C-H combination)	2.349 [4258]	2.349 [4258]	0

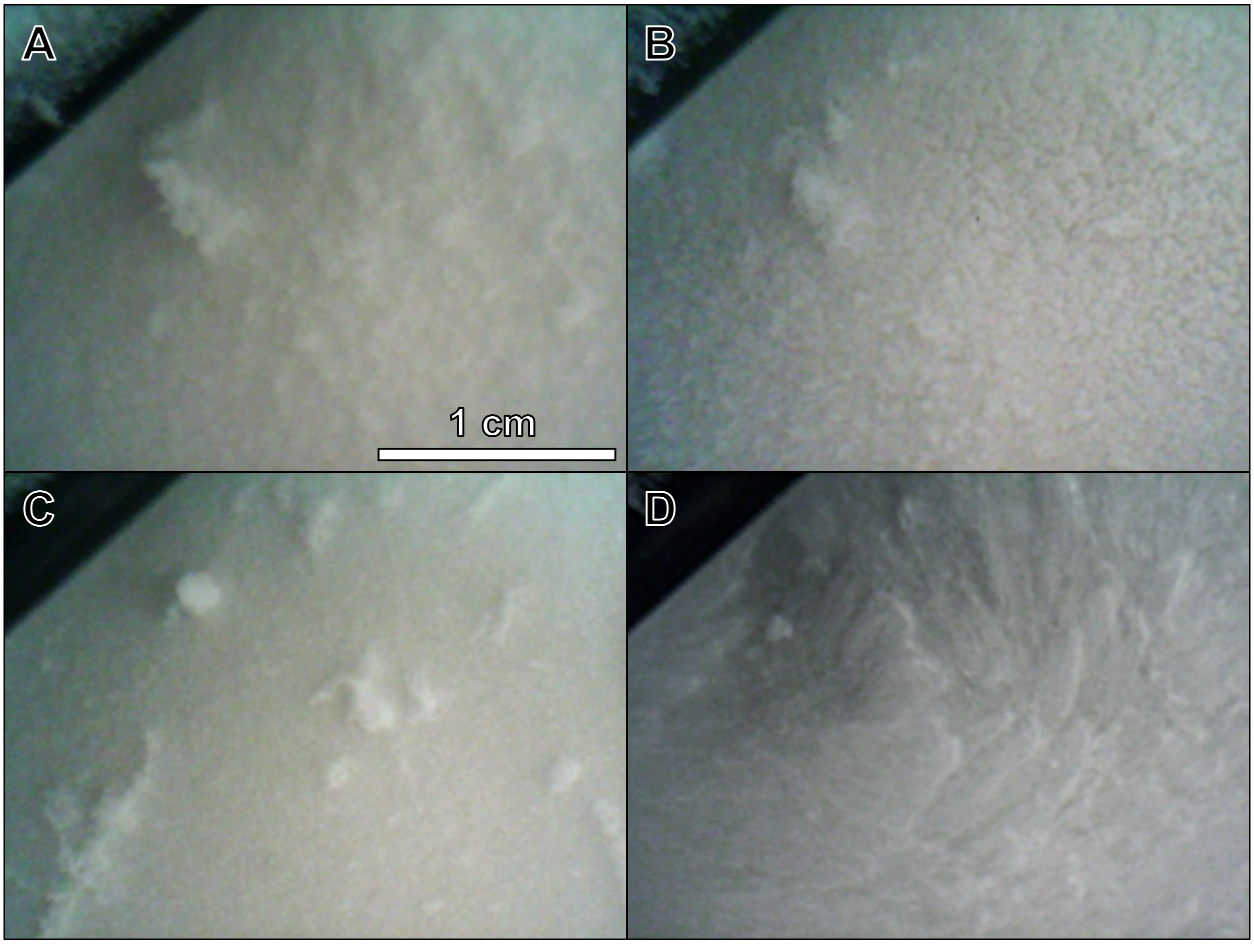

Figure 5. Top-down view of C_2H_2-C_6H_6 mixture in sample dish showing two different C_2H_2-C_6H_6 experiments: (a) and (b) being one, and (c) and (d) being the other. Panel (a) shows the sample at 162 K, before C_2H_2 was added to the dish, panel (b) shows the sample at 140 K (t = 3), after C_2H_2 was added to the C_6H_6 on the dish, cooled, and warmed. Notice the difference in sample appearance and morphology from (a) where the sample lacks defined features, to (b) where distinct separations in the sample start to form. These separations appear as darker "cracks" on the sample surface. Panel (c) shows the sample at 162 K, before C_2H_2 was added to the dish, and panel (d) shows the sample at, 112 K, after C_2H_2 was added to the C_6H_6 on the dish. Notice how both panels (b) and (d) exhibit a more complex morphological structure after both C_2H_2 and C_6H_6 have had time to interact with each other on the dish. The white color of the sample is due to the Spectralon® IR reflectance material upon which the sample is deposited.

5. Discussion

5.1. C_2H_2 and C_6H_6 Spectral Changes

The band shifts observed in the C_2H_2 experiments can be explained by a transition from an ordered, low temperature, orthorhombic form to a disordered, high temperature, cubic form of acetylene's crystal structure (Schwartz et al. 1969; Preston et al. 2010; Hudson et al. 2014). At the lower temperatures, the C_2H_2 molecules exist in a smaller volume orthorhombic structure where there are few thermal vibrations of the molecules. As the C_2H_2 is warmed to the slightly larger volume cubic form, the molecules become rotationally disordered, hence the weaker spectral signals. Previous studies on pure C_2H_2 (Schwartz et al. 1969; Preston et al. 2010) have noted these changes, however at slightly colder temperatures (133 K) than here (139 K). The difference in temperature may be due to differences in experimental setup or the nature of the sample (thin vs. thick film), which is good to be aware of when studying acetylene-bearing materials up close. For example, Titan's equatorial dunes have been hypothesized to have a C_2H_2 component (Lorenz et al. 2006; Lunine & Hörst 2011; Abplanalp et al. 2019). The *Dragonfly* rotorcraft (Lorenz et al., 2018) will land in Titan's dunes and study their composition up close. Additionally, the presence of crystalline C_2H_2 in Titan's lower stratosphere has been suggested (Coustenis et al., 1999; Khanna, 2005). Our measurements could be used to search for C_2H_2 in Titan's clouds to better confirm these suggestions.

Changes in temperature do not drastically affect the pure C_6H_6 spectra, as they do with C_2H_2. The main observation here is a decrease in reflectance by ~10-15% at warmer temperatures. Although the spectra do not change much, knowledge of reflectance variations may still be useful when analyzing Titan surface data from past or future missions.

5.2. C_2H_2-C_6H_6 Co-Crystal

Given the results from these experiments, we believe that the co-crystal has formed in our combined C_2H_2-C_6H_6 experiment (Section 3.3.) through solid-solid interactions between the two molecules. In this experiment, we first observe the transition from two separate molecules (C_2H_2 + C_6H_6) to the co-crystal when the sample is below 135 K, which is in the range where the orthorhombic phase of acetylene is stable. Other co-crystals formed with acetylene are stable above 135 K (e.g., acetylene-butane (Cable et al., 2019), while others are only stable up to 115 K (acetylene-ammonia) and 120 K (acetylene-acetonitrile; Cable et al. 2018, 2020, respectively). This variation in stability ranges for different co-crystals are important to keep in mind for future co-crystal studies in both terrestrial laboratory and Titan in situ environments. While we are not able to investigate the exact crystal structure and orientation of the C_2H_2-C_6H_6 co-crystal with IR spectra alone, we assume a 1:1 ratio (benzene:acetylene 45:55 %mol fraction) formation mechanism consistent with the T-shaped arrangement because this is the simplest scenario.

The spectra are characterized by additional vibrational modes from 1.569 to 1.598 µm, and 1.943 to 2.122 µm that are not observed in spectra from either of the individual components (C_2H_2 or C_6H_6). Similarly, other co-crystal studies have identified co-crystallization by frequency shifts and new bands using Raman spectroscopy (e.g., (Cable et al., 2019) and IR-UV spectra (e.g., Fujii et al. 2004).

Previous IR spectroscopic studies of C_2H_2-C_6H_6 have reported shifts of C_2H_2 bands by up to 15.9 cm^{-1} (Sundararajan et al., 2002), 22 cm^{-1} (Böning et al., 2013; Fujii et al., 2004), and 40 cm^{-1} upon formation of the co-crystal (Fujii et al. 2004; see Table 5). By comparison, redshifts reported here are 10.69 cm^{-1} and 26.85 cm^{-1} for the $5\nu_4 + 3\nu_5$ mode, and 41.52 cm^{-1} and 45.64 cm^{-1} for the 1.548 µm band of the $\nu_1 + \nu_3(\nu_2 + \nu_3 + 2\nu_4)$ vibrational mode, which agree with literature values. C-H aromatic ring first overtone stretching vibrations of C_6H_6 (Table 2) are not shifted upon initial addition of C_2H_2, which also corresponds with what is reported in the literature (Fujii et al., 2004).

Table 5. Co-crystal spectral shifts compared to literature values. Band shifts are reported in wavenumbers (cm^{-1}) for easier comparison to the literature.

Temperature (K)	Previous Work		Temperature (K)	This Study	
	Vibrational Mode	Band Shifts (cm^{-1})		Vibrational Mode	Band Shifts (cm^{-1})
See footnote	C_2H_2 ν_3 band (C—H stretch)	-22[2,3]	144	$5\nu_4 + 3\nu_5$ *Trans*, and *cis* bending	26.85
Jet-cooled	C_2H_2 C—H stretch	40[3]	144	$\nu_1 + \nu_3(\nu_2 + \nu_3 + 2\nu_4)$	41.52
			123	Acetylenic C—H stretch	45.64
12-40	ν_4 of C_6H_6 (C—H bend)	4.4[1]	108	C—H stretch of C_6H_6	-3.6
Jet-cooled	C—H stretch of C_6H_6	no shift within 1 cm^{-1} [3]	123 - 144	C—H stretch of C_6H_6	no shift within 1 cm^{-1}
12-40	ν_5 of C_2H_2	3.2[1]	100	$5\nu_4 + 3\nu_5$ *Trans* and *cis* bend of C_2H_2	-2.68
12-40	ν_3 of C_2H_2	15.9[1]	93	$5\nu_4 + 3\nu_5$	10.69
		13.1[1]		*Trans* and *cis* bend of C_2H_2	

Notes.

[1] Sundararajan et al. 2002 (12-40 K)

[2] Böning et al. 2013 (a few Kelvin)

[3] Fujii et al. 2004 (jet-cooled)

Furthermore, the optical images of the sample show morphological changes after C_2H_2 deposition (Fig. 5) that are not present in repeated pure C_2H_2 or C_6H_6 experiments. These morphological differences may be explained by the change in crystal structure as C_2H_2 molecules are incorporated into the C_6H_6. While our experimental techniques do not allow for microscopic measurements of the C_2H_2-C_6H_6 crystal structure, repeated observations of new bands, band shifts, and sample morphology changes support the claim that a new phase (i.e., a co-crystal) of C_2H_2-C_6H_6 has been identified under Titan-relevant conditions. Microscopic imaging by *Dragonfly* may be able to distinguish between a co-crystal-blanketed surface and a surface dominated by pure hydrocarbon ices by noting similar "cracked" textural features as observed in our experiments. The morphological changes upon co-crystal formation may allow for easier identification on Titan's surface due to the increased reflectance and roughness observed. Furthermore, many material properties of the co-crystal might differ from simpler hydrocarbon ices, such as mechanical properties which could affect surface weathering and erosion. Further work is needed in order to characterize the mechanical properties of this new class of minerals on Titan.

5.3. Relevance to Titan

The spectral transitions observed after the solid-solid interaction between C_2H_2 and C_6H_6 is interesting because it implies that co-crystals can form relatively easily. Past studies have demonstrated that it is common for acetylene co-crystals to form through solid-solid interactions at Titan temperatures (Cable et al. 2018; Cable et al. 2020). These results have strong implications for Titan's surface, where various combinations of hydrocarbons cover the surface in the solid phase. One pathway to co-crystallization may be found in Titan's equatorial sand seas. It is also possible for co-crystals to form as Titan's ice clouds. Previous works have identified CIRS spectral ice signatures that result from species condensing simultaneously (co-condensation; Anderson & Samuelson 2011; Anderson et al. 2016). If C_2H_2 and C_6H_6 co-condense as a solid on Titan haze particles (i.e., refractory organics), they may co-crystallize in the stratosphere at ~130 to 140 K before reaching the dune fields. However, there may be opportunity for a more complex co-crystal composition as the haze particles fall through the atmosphere, allowing accretion of more than just C_2H_2 and C_6H_6 onto the haze particles (Anderson et al., 2018). Future VIMS studies may be able to search for clouds composed of C_2H_2 or C_6H_6 depending on wavelength, altitude, and whether or not the feature is transient. Given that the C_2H_2-C_6H_6 co-crystal forms relatively quickly (within 5 minutes) and is stable under Titan conditions, it is therefore likely that this co-crystal could contribute to Titan's evaporite deposits (Barnes et al. 2011; MacKenzie et al. 2014; Cordier et al. 2016). For example, a layer of solid C_6H_6 could rest at the bottom of a CH_4-dominated lake with C_2H_2 dissolved. Over time, this CH_4 would evaporate, leaving behind a C_2H_2-enriched evaporite layer which then interacts with the C_6H_6 to form the co-crystal.

To estimate the thickness of the acetylene-benzene co-crystal deposit that may have accumulated on Titan's surface over 1 Gyr, we use a net production rate of 1.08×10^{10} molecules m^{-2} s^{-1} for benzene (Cordier 2013; Krasnopolsky, 2009; Vuitton et al. 2008), which is the limiting factor when compared with the net production rate of acetylene, 1.06×10^{13} molecules m^{-2} s^{-1} (Vuitton et al. 2019). This equates to approximately 566 moles of benzene per m^2 after 1 Gyr. Dividing by the density of the acetylene-benzene co-crystal, 1.01 g cm^{-3} (123 K, Boese et al. 2003), and multiplying by the molar masses of acetylene and benzene, gives an approximate thickness of around 5 cm for the acetylene-benzene co-crystal. The net production rates for benzene reported in the literature varies; therefore, we view 5 cm as a rough estimate. Co-crystal formation may also be kinetically hindered due to the relatively low production rates in the atmosphere. Given that *Dragonfly's* DragonCam camera suite can examine surface materials down to a sand grain scale (Lorenz et al. 2017), we predict that *Dragonfly* may be able to detect the acetylene-benzene co-crystal considering the distinct morphological appearance of co-crystals formed in our experiments, as well as others (e.g., Cable et al. 2014). Additionally, *Dragonfly* will also carry a laser-desorption ionization (LDI) mass spectrometer (DraMS) that could provide additional compositional information regarding the presence or absence of co-crystals on the surface of Titan.

6. Summary and Conclusions

In this study, we sought to investigate the interactions of the acetylene-benzene aggregate at Titan-relevant temperatures and pressure (~89-94 K, 1.5 bar) using IR spectroscopy. For the first time under Titan conditions, we have confirmed the formation and stability of the C_2H_2-C_6H_6 co-crystal. The co-crystal formed at 135 K and is stable at Titan surface conditions (89-94 K, 1.5 bar). Identification of the co-crystal using FTIR spectroscopy shows band shifts and new bands that deviate from the individual component molecules, as well as drastic changes in sample morphology.

This high resolution NIR spectra of the C_2H_2-C_6H_6 co-crystal expands upon previous studies of the C_2H_2-C_6H_6 co-crystal to Titan's conditions. First, our experimental study is distinguished because C_6H_6 and C_2H_2 were deposited sequentially. This may represent a situation more applicable to Titan, where molecules like C_2H_2 and C_6H_6 could co-condense in the atmosphere and may comprise the lake evaporites. Our results also complement past works regarding co-crystal formation conducted at Titan-relevant temperatures (Cable et al., 2019, 2018, 2014; Vu et al., 2014) and with recent modeling (Ennis et al., 2020). Experimental investigations in Titan-like environments could enhance our knowledge of the complex chemistry that occurs in Titan's atmosphere and give us clues to interactions that may occur at Titan's lake evaporite beds. Infrared characterization of the co-crystal formation process under Titan's conditions will also be important for future surface missions like *Dragonfly* (Lorenz et al., 2018; Turtle et al., 2018) or other Titan mission concepts to understand the composition of the evaporites. Future experimental investigations on the crystal and chemical structures of the C_2H_2-C_6H_6 co-crystal using techniques such as Raman spectroscopy and X-ray powder diffraction would be helpful to further understand this unique mineral on Titan.

7. Acknowledgement

The authors graciously acknowledge two anonymous reviewers for their invaluable comments and suggestions, Kendra Farnsworth for assistance with thermocouple temperature calibration measurements, Woodrow Gilbertson for mol fraction calculations, Walter Graupner for support in the lab, and Shannon MacKenzie for insight on VIMS detection limits. This work was supported by NASA Headquarters under the NASA Earth and Space Science Fellowship Program – Grant #80NSSC17K0603.

8. References

Abplanalp, M.J., Frigge, R., Kaiser, R.I., 2019. Low-temperature synthesis of polycyclic aromatic hydrocarbons in Titan ' s surface ices and on airless bodies. Sci. Adv. 5, 1–12.

Abramczyk, H., Paradowska-Moszkowska, K., 2001. The correlation between the phase transitions and vibrational properties by Raman spectroscopy : liquid-solid B and solid B-solid a acetonitrile transitions. Chem. Phys. 265, 177–191. https://doi.org/https://doi.org/10.1016/S0301-0104(01)00271-3

Anderson, C.M., Samuelson, R.E., 2011. Titan's aerosol and stratospheric ice opacities between 18 and 500 um: Vertical and spectral characteristics from Cassini CIRS. Icarus 212, 762–778. https://doi.org/10.1016/j.icarus.2011.01.024

Anderson, C.M., Samuelson, R.E., Nna-Mvondo, D., 2018. Organic Ices in Titan's Stratosphere. Space Sci. Rev. 214, 125. https://doi.org/10.1007/s11214-018-0559-5

Anderson, C.M., Samuelson, R.E., Yung, Y.L., Mclain, J.L., 2016. Solid-state photochemistry as a formation mechanism for Titan's stratospheric C4N2 ice clouds. Geophys. Res. Lett. 43, 3088–3094. https://doi.org/10.1002/2016GL067795.Abstract

Barnes, J.W., Bow, J., Schwartz, J., Brown, R.H., Soderblom, J.M., Hayes, A.G., Vixie, G., Le Mouélic, S., Rodriguez, S., Sotin, C., Jaumann, R., Stephan, K., Soderblom, L.A., Clark, R.N., Buratti, B.J., Baines, K.H., Nicholson, P.D., 2011. Organic sedimentary deposits in Titan's dry lakebeds: Probable evaporite. Icarus 216, 136–140. https://doi.org/10.1016/j.icarus.2011.08.022

Barnes, J.W., Brown, R.H., Soderblom, J.M., Soderblom, L.A., Jaumann, R., Jackson, B., Le Mouélic, S., Sotin, C., Buratti, B.J., Pitman, K.M., Baines, K.H., Clark, R.N., Nicholson, P.D., Turtle, E.P., Perry, J., 2009. Shoreline features of Titan's Ontario Lacus from Cassini/VIMS observations. Icarus 201, 217–225. https://doi.org/10.1016/j.icarus.2008.12.028

Barnes, J.W., Brown, R.H., Turtle, E.P., McEwen, A.S., Lorenz, R.D., Janssen, M., Schaller, E., Brown, M.E., Buratti, B.J., Sotin, C., Griffith, C., Clark, R., Perry, J., Fussner, S., Barbara, J., West, R., Elachi, C., Bouchez, A.H., Roe, H.G., Baines, K.H., Bellucci, G., Bibring, J.-P., Capaccioni, F., Cerroni, P., Combes, M., Coradini, A., Cruikshank, D.P., Drossart, P., Formisano, V., Jaumann, R., Langevin, Y., Matson, D.L., McCord, T.B., Nicholson, P.D., Sicardy, B., 2005. A 5-Micron-Bright Spot on Titan: Evidence for Surface Diversity. Science (80-.). 310, 92–95. https://doi.org/10.1126/science.1117075

Bassi, D., Menegotti, L., Oss, S., Scotoni, M., 1993. The 3-0 CH stretch overtone of benzene. Chem. Phys. Lett. 207, 167–172.

Blunt, V.M., Cedeño, D.L., Manzanares I, C., 1997. Vibrational overtone spectroscopy of methane in liquid argon solutions. Mol. Phys. 91, 3–17. https://doi.org/10.1080/002689797171698

Boese, R., Clark, T., Gavezzotti, A., 2003. Cocrystallization with Acetylene. The 1:1 Complex with Benzene: Crystal Growth, X-Ray Diffraction and Molecular Simulations. Helv. Chim. Acta 86, 1085–1100.

Böning, M., Stuhlmann, B., Engler, G., Busker, M., Häber, T., Tekin, A., Jansen, G., Kleinermanns, K., 2013. Towards a Spectroscopic and Theoretical Identification of the Isolated Building Blocks of the Benzene – Acetylene Cocrystal 837–846. https://doi.org/10.1002/cphc.201200701

Brock, A., Mina-camilde, N., I, C.M., 1994. Vibrational Spectroscopy of C-H Bonds of C2H4 Liquid and C2H4 in Liquid Argon Solutions. J. Phys. Chem. 98, 4800–4808.

Busker, M., Häber, T., Nispel, M., Kleinermanns, K., 2008. Isomer-Selective Vibrational Spectroscopy of Benzene – Acetylene Aggregates : Comparison with the Structure of the Benzene – Acetylene. Angew. Chemie 47, 10094–10097. https://doi.org/10.1002/anie.200802118

Cable, M.L., Vu, T.H., Hodyss, R., Choukroun, M., Malaska, M.J., Beauchamp, P., 2014. Experimental determination of the kinetics of formation of the benzene-ethane co-crystal and implications for Titan. Geophys. Res. Lett. 41, 5396–5401. https://doi.org/10.1002/2014GL060531

Cable, M.L., Vu, T.H., Malaska, M.J., Maynard-casely, H.E., Choukroun, M., Hodyss, R., 2020. Properties and Behavior of the Acetonitrile − Acetylene Co-Crystal under Titan Surface Conditions. https://doi.org/10.1021/acsearthspacechem.0c00129

Cable, M.L., Vu, T.H., Malaska, M.J., Maynard-casely, H.E., Choukroun, M., Hodyss, R., 2019. A Co-Crystal between Acetylene and Butane: A Potentially Ubiquitous Molecular Mineral on Titan. ACS Earth Sp. Chem. 3, 2808–2815. https://doi.org/10.1021/acsearthspacechem.9b00275

Cable, M.L., Vu, T.H., Maynard-Casely, H.E., Choukroun, M., Hodyss, R., 2018. The Acetylene-Ammonia Co-crystal on Titan. ACS Earth Sp. Chem. 2, 366–375. https://doi.org/10.1021/acsearthspacechem.7b00135

Clark, R.N., Curchin, J.M., Barnes, J.W., Jaumann, R., Soderblom, L., Cruikshank, D.P., Brown, R.H., Rodriguez, S., Lunine, J., Stephan, K., Hoefen, T.M., Mouélic, S. Le, Sotin, C., Baines, K.H., Buratti, B.J., Nicholson, P.D., 2010. Detection and mapping of hydrocarbon deposits on Titan. J. Geophys. Res. Planets 115, E10005. https://doi.org/10.1029/2009JE003369

Cooley, J.P., 1925. The Infra-red Absorption Bands of Methane. Astrophys. J. 62, 73–83.

Cordier, D., Barnes, J.W., Ferreira, A.G., 2013. On the chemical composition of Titan's dry lakebed evaporites. Icarus 226, 1431–1437. https://doi.org/10.1016/j.icarus.2013.07.026

Cordier, D., Cornet, T., Barnes, J.W., MacKenzie, S.M., Le Bahers, T., Nna-Mvondo, D., Rannou, P., Ferreira, A.G., 2016. Structure of Titan's evaporites. Icarus 270, 41–56. https://doi.org/10.1016/j.icarus.2015.12.034

Cordier, D., Mousis, O., Lunine, J.I., Lavvas, P., Vuitton, V., 2009. An estimate of the chemical composition of titan's lakes. Astrophys. J. 707, L128-131. https://doi.org/10.1088/0004-637X/707/2/L128

Cornet, T., Bourgeois, O., Le Mouélic, S., Rodriguez, S., Lopez Gonzalez, T., Sotin, C., Tobie, G., Fleurant, C., Barnes, J.W., Brown, R.H., Baines, K.H., Buratti, B.J., Clark, R.N., Nicholson, P.D., 2012. Geomorphological significance of Ontario Lacus on Titan: Integrated interpretation of Cassini VIMS, ISS and RADAR data and comparison with the Etosha Pan (Namibia). Icarus 218, 788–806. https://doi.org/10.1016/j.icarus.2012.01.013

Coustenis, A., Achterberg, R.K., Conrath, B.J., Jennings, D.E., Bézard, B., Samuelson, R.E., Carlson, R.C., Lellouch, E., Hubert, A., Orton, G.S., Kunde, V.G., Vinatier, S., 2007. The composition of Titan's stratosphere from Cassini/CIRS mid-infrared spectra. Icarus 189, 35–62. https://doi.org/10.1016/j.icarus.2006.12.022

Coustenis, A., Salama, A., Schulz, B., Ott, S., Lellouch, E., Encrenaz, T., Gautier, D., Feuchtgruber, H., 2003. Titan's atmosphere from ISO mid-infrared spectroscopy. Icarus 161, 383–403.

Coustenis, A., Schmitt, B., Khanna, R.K., Trotta, F., 1999. Plausible condensates in Titan's stratosphere from Voyager infrared spectra 47, 1305–1329. https://doi.org/https://doi.org/10.1016/S0032-0633(99)00053-7

Czaplinski, E., Farnsworth, K., Gilbertson, W., Chevrier, V., 2018. Experimental Studies of Ethylene and Benzene Evaporites on Titan. LPSC XLIX 2018, 1480.

Czaplinski, E., Farnsworth, K., Laxton, D., Chevrier, V., Heslar, M., Singh, S., 2017. Experimental Results of Evaporite Deposits on Titan Using a Surface Simulation Chamber. LPSC XLVIII 2017, 1537.

Czaplinski, E.C., Gilbertson, W.A., Farnsworth, K.K., Chevrier, V.F., 2019. Experimental Study of Ethylene Evaporites under Titan Conditions. ACS Earth Sp. Chem. 3, 2353–2362. https://doi.org/10.1021/acsearthspacechem.9b00204

Ellis, J.W., 1927. New Infra-red Absorption Bands of Methane. Physics (College. Park. Md). 13, 202–207.

Ennis, C., Cable, M.L., Hodyss, R., Maynard-casely, H.E., 2020. Mixed Hydrocarbon and Cyanide Ice Compositions for Titan ' s Atmospheric Aerosols: A Ternary-Phase Co-crystal Predicted by Density Functional Theory. ACS Earth Sp. Chem. 4, 1195–1200. https://doi.org/10.1021/acsearthspacechem.0c00130

Farnsworth, K.K., Chevrier, V.F., Steckloff, J.K., 2019. Nitrogen Exsolution and Bubble Formation in Titan ' s Lakes Geophysical Research Letters. Geophys. Res. Lett. 46, 1–10. https://doi.org/10.1029/2019GL084792

Fujii, A., Morita, S., Miyazaki, M., Ebata, T., Mikami, N., 2004. A Molecular Cluster Study on Activated CH / π Interactions : Infrared Spectroscopy of Aromatic Molecule - Acetylene Clusters 2652–2658. https://doi.org/10.1021/jp049946b

Hanel, R., Conrath, B., Flasar, F.M., Kunde, V., Maguire, W., Pearl, J., Pirraglia, J., Samuelson, R., Herath, L., Allison, M., Cruikshank, D., Gautier, D., Gierasch, P., Horn, L., Koppany, R., Ponnamperuma, C., 1981. Infrared Observations of the Saturnian System from Voyager 1. Science (80-.). 212, 192–200.

Hayes, A., Aharonson, O., Callahan, P., Elachi, C., Gim, Y., Kirk, R., Lewis, K., Lopes, R., Lorenz, R., Lunine, J., Mitchell, K., Mitri, G., Stofan, E., Wall, S., 2008. Hydrocarbon lakes on Titan: Distribution and interaction with a porous regolith. Geophys. Res. Lett. 35, L09204. https://doi.org/10.1029/2008GL033409

Hepp, M., Herman, M., 2000. Vibration-rotation bands in ethane. Mol. Phys. 98, 57–61. https://doi.org/10.1080/00268970009483269

Hörst, S.M., 2017. Titan's atmosphere and climate. J. Geophys. Res. Planets 122, 432–482. https://doi.org/10.1002/2016JE005240

Hudson, R.L., Ferrante, R.F., Moore, M.H., 2014. Infrared spectra and optical constants of astronomical ices : I . Amorphous and crystalline acetylene. Icarus 228, 276–287. https://doi.org/10.1016/j.icarus.2013.08.029

Kaye, W., 1954. Near-infrared spectroscopy: I. Spectral identification and analytical applications. Spectrochim. Acta 6, 257–287.

Khanna, R.K., 2005. Condensed species in Titan's stratosphere: Confirmation of crystalline cyanoacetylene (HC3N) and evidence for crystalline acetylene (C2H2) on Titan. Icarus 178, 165–170. https://doi.org/10.1016/j.icarus.2005.03.011

Koskinen, T.T., Yelle, R. V, Snowden, D.S., Lavvas, P., Sandel, B.R., Capalbo, F.J., Benilan, Y., West, R.A., 2011. The mesosphere and thermosphere of Titan revealed by Cassini/UVIS stellar occultations. Icarus 216, 507–534. https://doi.org/10.1016/j.icarus.2011.09.022

Lorenz, R.D., Turtle, E.P., Barnes, J.W., Trainer, M.G., Adams, D.S., Hibbard, K.E., Sheldon, C.Z., Zacny, K., Peplowski, P.N., Lawrence, D.J., Ravine, M.A., Mcgee, T.G., Sotzen, K.S., Mackenzie, S.M., Langelaan, J.W., Schmitz, S., Wolfarth, L.S., Bedini, P.D., 2018. Dragonfly: A Rotorcraft Lander Concept for Scientific Exploration at Titan. APL Tech. Dig. 34, 374–387.

Lorenz, R.D., Wall, S., Radebaugh, J., Boubin, G., Reffet, E., Janssen, M., Stofan, E., Lopes, R., Kirk, R., Elachi, C., Lunine, J., Mitchell, K., Paganelli, F., Soderblom, L., Wood, C., Wye, L., Zebker, H., Anderson, Y., Ostro, S., Allison, M., Boehmer, R., Callahan, P., Encrenaz, P., Ori, G.G., Francescetti, G., Gim, Y., Hamilton, G., Hensley, S., Johnson, W., Kelleher, K., Muhleman, D., Picardi, G., Posa, F., Roth, L., Seu, R., Shaffer, S., Stiles, B., Vetrella, S., Flamini, E., West, R., 2006. The Sand Seas of Titan : Cassini. Science (80-.). 312, 724–728. https://doi.org/DOI: 10.1126/science.1123257

Lunine, J.I., Hörst, S.M., 2011. Organic chemistry on the surface of Titan. Rend. Lincei 22, 183–189. https://doi.org/10.1007/s12210-011-0130-8

Lunine, J.I., Stevenson, D.J., Yung, Y.L., 1983. Ethane Ocean on Titan. Science (80-.). 222, 1229–1230.

Luspay-Kuti, A., Chevrier, V.F., Cordier, D., Rivera-Valentin, E.G., Singh, S., Wagner, A., Wasiak, F.C., 2015. Experimental constraints on the composition and dynamics of Titan's polar lakes. Earth Planet. Sci. Lett. 410, 75–83. https://doi.org/10.1016/j.epsl.2014.11.023

Luspay-Kuti, A., Chevrier, V.F., Wasiak, F.C., Roe, L.A., Welivitiya, W.D.D.P., Cornet, T., Singh, S., Rivera-Valentin, E.G., 2012. Experimental simulations of CH4 evaporation on Titan. Geophys. Res. Lett. 39, 2–6. https://doi.org/10.1029/2012GL054003

MacKenzie, S., Barnes, J., 2016. Compositional Similarities and Distinctions between Titan's Evaporitic Terrains. Astrophys. J. 821. https://doi.org/10.3847/0004-637X/821/1/17

MacKenzie, S.M., Barnes, J.W., Sotin, C., Soderblom, J.M., Le Mouélic, S., Rodriguez, S., Baines, K.H., Buratti, B.J., Clark, R.N., Nicholson, P.D., McCord, T.B., 2014. Evidence of Titan's climate history from evaporite distribution. Icarus 243, 191–207. https://doi.org/10.1016/j.icarus.2014.08.022

Majumder, M., Kumar, B., Sathyamurthy, N., 2013. CH · · · pi and pi · · · pi interaction in benzene – acetylene clusters. Chem. Phys. Lett. 557, 59–65. https://doi.org/10.1016/j.cplett.2012.12.027

Malaska, M.J., Hodyss, R., 2014. Dissolution of benzene, naphthalene, and biphenyl in a simulated Titan lake. Icarus 242, 74–81. https://doi.org/10.1016/j.icarus.2014.07.022

Malaska, M.J., Hodyss, R., Lunine, J.I., Hayes, A.G., Hofgartner, J.D., Hollyday, G., Lorenz, R.D., 2017. Laboratory measurements of nitrogen dissolution in Titan lake fluids. Icarus 289, 94–105. https://doi.org/10.1016/j.icarus.2017.01.033

Maleev, A. V, Boese, R., 2014. Investigation of topology of intermolecular interactions in the benzene – acetylene co-crystal by different theoretical methods. https://doi.org/10.1007/s11224-014-0413-7

Mastrogiuseppe, M., Hayes, A., Poggiali, V., Seu, R., Lunine, J.I., Hofgartner, J.D., 2016. Radar Sounding Using the Cassini Altimeter: Waveform Modeling and Monte Carlo Approach for Data Inversion of Observations of Titan's Seas. IEEE Trans. Geosci. Remote Sens. 54, 5646–5656. https://doi.org/10.2190/RM36-JLXA-6WUY-KDQ2

Mastrogiuseppe, M., Poggiali, V., Hayes, A., Lorenz, R., Lunine, J., Picardi, G., Seu, R., Flamini, E., Mitri, G., Notarnicola, C., Paillou, P., Zebker, H., 2014. The bathymetry of a Titan sea. Geophys. Res. Lett. 41, 1432–1437. https://doi.org/10.1002/ 2013GL058618. Received

Mastrogiuseppe, M., Poggiali, V., Hayes, A.G., Lunine, J.I., Seu, R., Di Achille, G., Lorenz, R.D., 2018. Cassini radar observation of Punga Mare and environs: Bathymetry and composition. Earth Planet. Sci. Lett. 496, 89–95. https://doi.org/10.1016/j.epsl.2018.05.033

Mastrogiuseppe, M., Poggiali, V., Hayes, A.G., Lunine, J.I., Seu, R., Mitri, G., Lorenz, R.D., 2019. Deep and methane-rich lakes on Titan. Nat. Astron. 3, 535–542. https://doi.org/10.1038/s41550-019-0714-2

Maynard-Casely, H.E., Hodyss, R., Cable, M.L., Vu, T.H., Rahm, M., 2016. A co-crystal between benzene and ethane: a potential evaporite material for Saturn's moon Titan. IUCrJ 3, 192–199. https://doi.org/10.1107/S2052252516002815

Moorhead, J.G., 1932. THE NEAR INFRARED ABSORPTION SPECTRUM OF METHANE. Phys. Rev. 39, 83–88.

Mousis, O., Lunine, J.I., Hayes, A.G., Hofgartner, J.D., 2016. The fate of ethane in Titan's hydrocarbon lakes and seas. Icarus 270, 37–40. https://doi.org/10.1016/j.icarus.2015.06.024

Nelson, B.R.C., Plylerl, E.K., Benedict, W.S., 1948. Absorption Spectra of Methane in the Near Infrared 41, 615–621.

Niemann, H.B., Atreya, S.K., Bauer, S.J., Carignan, G.R., Demick, J.E., Frost, R.L., Gautier, D., Paulkovich, M., Raulin, F., Raaen, E., Way, S.H., 2005. The abundances of constituents of Titan's atmosphere from the GCMS instrument on the Huygens probe. Nature 438, 779–784. https://doi.org/10.1038/nature04122

Niemann, H.B., Atreya, S.K., Demick, J.E., Gautier, D., Haberman, J.A., Harpold, D.N., Kasprzak, W.T., Lunine, J.I., Owen, T.C., Raulin, F., 2010. Composition of Titan's lower atmosphere and simple surface volatiles as measured by the Cassini-Huygens probe gas chromatograph mass spectrometer experiment. J. Geophys. Res. 115, 1–22. https://doi.org/10.1029/2010JE003659

Norris, W. V, Unger, H.J., 1933. Infrared Absorption Bands of Methane. Pysical Rev. 43, 467–472.

Preston, T.C., Firanescu, G., Signorell, R., 2010. Infrared spectroscopy and vibrational exciton modeling of crystalline , polycrystalline and amorphous acetylene aerosol particles. Phys. Chem. Chem. Phys. 12, 7924–7933. https://doi.org/10.1039/c002525a

Reboucas, M. V, de Barros Neto, B., 2001. Near infrared spectroscopic prediction of physical properties of aromatics-rich hydrocarbon mixtures. J. Near Infrared Spectrosc. 9, 263–273.

Reddy, K. V, Berry, M.J., 1982. Highly vibrationally excited benzene: Overtone spectroscopy and intramolecular dynamics of C6H6, C6D6, and partially deuterated or substituted benzenes. J. Chem. Phys. 76, 2814–2837.

Roe, H.G., de Pater, I., McKay, C.P., 2004. Seasonal variation of Titan's stratospheric ethylene (C2H4) observed. Icarus 169, 440–461. https://doi.org/10.1016/j.icarus.2004.01.002

Schwartz, Y.A., Ron, A., Kimel, S., 1969. FarInfrared Spectrum and Phase Transition of Acetylene The farinfrared spectrum of ice VIII Far-Infrared Spectrum and Phase Transition of Acetylene. J. Chem. Phys. 51, 1666–1667. https://doi.org/10.1063/1.1672234

Shemansky, D.E., Stewart, A.I.F., West, R.A., Esposito, L.W., Hallett, J.T., Liu, X., 2005. The Cassini UVIS Stellar Probe of the Titan Atmosphere. Science (80-.). 308, 978–982.

Singh, S., Combe, J.-P., Cordier, D., Wagner, A., Chevrier, V.F., McMahon, Z., 2017. Experimental determination of acetylene and ethylene solubility in liquid methane and ethane: Implications to Titan's surface. Geochim. Cosmochim. Acta 208, 86–101. https://doi.org/10.1016/j.gca.2017.03.007

Singh, S., Cornet, T., Chevrier, V.F., Combe, J., Mccord, T.B., Roe, L.A., Mouélic, S. Le, Menn, E. Le, Wasiak, F.C., 2016a. Near-infrared spectra of liquid / solid acetylene under Titan relevant conditions and implications for Cassini / VIMS detections. Icarus 270, 429–434. https://doi.org/10.1016/j.icarus.2015.11.002

Singh, S., Mccord, T.B., Combe, J., Rodriguez, S., Cornet, T., Mouélic, S. Le, Clark, R.N., Maltagliati, L., Chevrier, V.F., 2016b. Acetylene on Titan 's Surface. Astrophys. J. 828, 1–8. https://doi.org/10.3847/0004-637X/828/1/55

Sundararajan, K., Viswanathan, K.S., Kulkarni, A.D., Gadre, S.R., 2002. H · · · pi complexes of acetylene – benzene: a matrix isolation and computational study. J. Mol. Struct. 613, 209–222.

Tokano, T., 2009. Limnological Structure of Titan's Hydrocarbon Lakes and Its Astrobiological Implication. Astrobiology 9, 147–164. https://doi.org/10.1089/ast.2007.0220

Turtle, E.P., Barnes, J.W., Trainer, M.G., Lorenz, R.D., Hibbard, K.E., Adams, D.S., Bedini, P., Brinckerhoff, W.B., Ernst, C., Freissinet, C., Hand, K., Hayes, A.G., Johnson, J.R., Karkoschka, E., Langelaan, J.W., Gall, A. Le, Lora, J.M., Mackenzie, S.M., Mckay, C.P., Neish, C.D., Newman, C.E., Palacios, J., Parsons, A.M., Peplowski, P.N., Radebaugh, J., Rafkin, S.C.R., Ravine, M.A., Schmitz, S., Soderblom, J.M., Sotzen, S., Stickle, A.M., Stofan, E.R., Tokano, T., Wilson, C., Yingst, R.A., Zacny, K., Hopkins, J., Physics, A., Spatiales, O., Angeles, L., Field, M., Space, M., Systems, S., Diego, S., Robotics, H., 2018. Dragonfly: In Situ Exploration of Titan's Organic Chemistry and Habitability, in: 49th LPSC. p. Abstract 1641. https://doi.org/10.1109/AERO.2013.6497165.

Ulrich, N.W., Seifert, N.A., Dorris, R.E., Peebles, R.A., Pate, B.H., Peebles, S.A., 2014. Benzene Á Á Á acetylene : a structural investigation of the prototypical CH Á Á Á p interaction † 8886–8894. https://doi.org/10.1039/c4cp00845f

Vu, T.H., Cable, M.L., Choukroun, M., Hodyss, R., Beauchamp, P., 2014. Formation of a new benzene-ethane co-crystalline structure under cryogenic conditions. J. Phys. Chem. 118, 4087–4094. https://doi.org/10.1021/jp501698j

Waite Jr., J.H., Niemann, H., Yelle, R. V, Kasprzak, W.T., Cravens, T.E., Luhmann, J.G., Magee, B., Mcnutt, R.L., Ip, W., Gell, D., Haye, V.D. La, Mu, I., Borggren, N., Ledvina, S., Fletcher, G., Walter, E., Miller, R., Scherer, S., Thorpe, R., Xu, J., Block, B., Arnett, K., 2005. Ion Neutral Mass Spectrometer Results from the First Flyby of Titan. Science (80-.). 308, 982–986. https://doi.org/10.1029/2003JE002180

Wasiak, F.C., Luspay-Kuti, A., Welivitiya, W.D.D.P., Roe, L.A., Chevrier, V.F., Blackburn, D.G., Cornet, T., 2013. A facility for simulating Titan's environment. Adv. Sp. Res. 51, 1213–1220. https://doi.org/10.1016/j.asr.2012.10.020

9. Appendix

Here, we provide the full spectral range of pure C_2H_2 (Fig. A1), pure C_6H_6 (Fig. A2), a temperature versus time table (Table A1) for the cocrystal experiment in the main text, the full spectral range of the C_2H_2-C_6H_6 cocrystal experiment in the main text (Fig. A3, A4), and band center shifts versus temperature (Fig. A5) for the cocrystal experiment in the main text. Spectra from repeat cocrystal experiment 1 (Fig. A6, A7) and repeat cocrystal experiment 2 (Fig. A8), as well as optical views from repeat experiment 2 (Fig. A9) are also presented.

It should be noted that the C_2H_2 cylinder used in these experiments is not pure C_2H_2; rather, it is C_2H_2 dissolved in acetone ($(CH_3)_2O$) for stabilization purposes. While we do not observe any $(CH_3)_2O$ bands in our "pure C_2H_2" experiment (Fig. 1) or the experiment presented in the main text (section 3.3.) due to experimental techniques using the cold trap method, it is possible that trace amounts of $(CH_3)_2O$ were incorporated into one of the repeat experiments. The pure $(CH_3)_2O$ spectrum is characterized by a sharp doublet centered at 1.677 and 1.694 μm, as well as a broad doublet at 1.732 and 1.780 μm (Fig. A10). Singh et al. (2016a) also reports an acetone spectrum with matching bands. These four vibrational modes are observed in our spectra, however, they are shifted from 0.001 – 0.004 μm when compared to pure $(CH_3)_2O$ (Fig. A10).

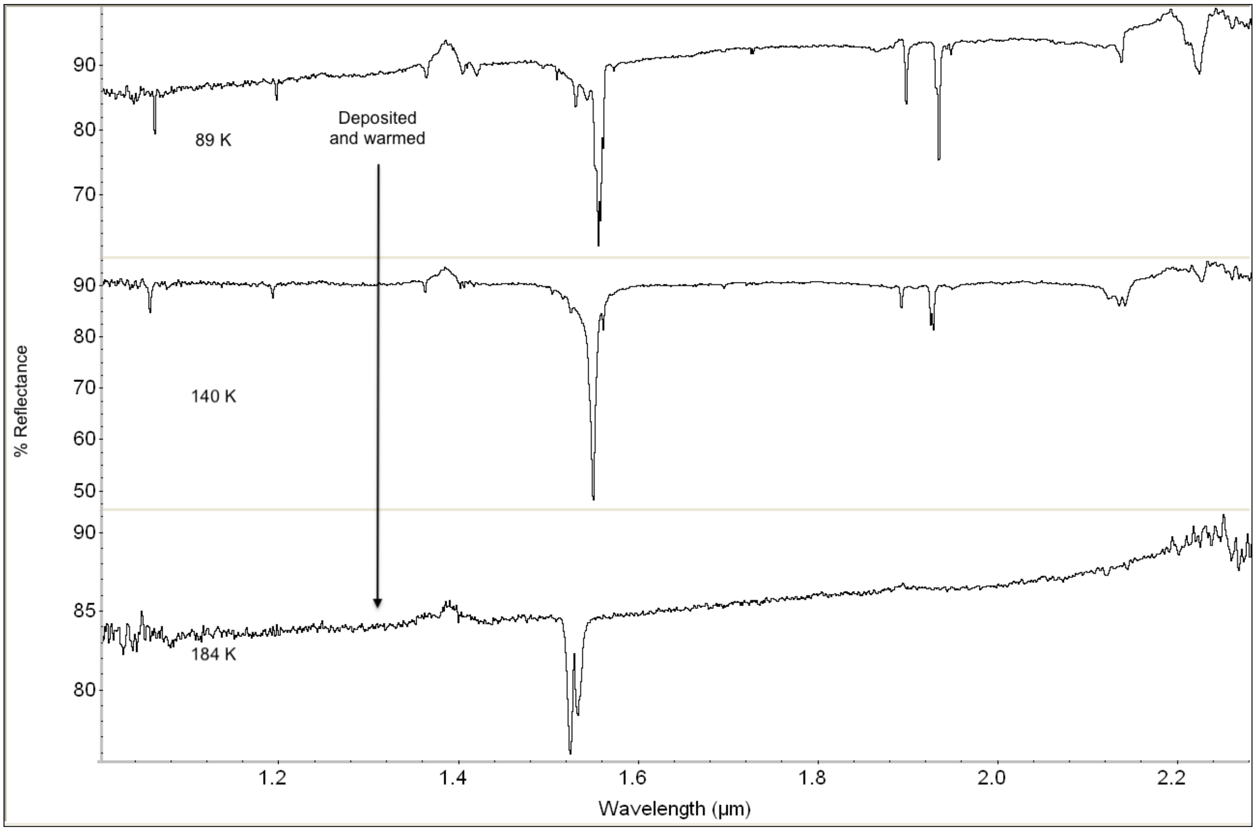

Figure A1. Full spectral range from C_2H_2 experiment presented in the manuscript.

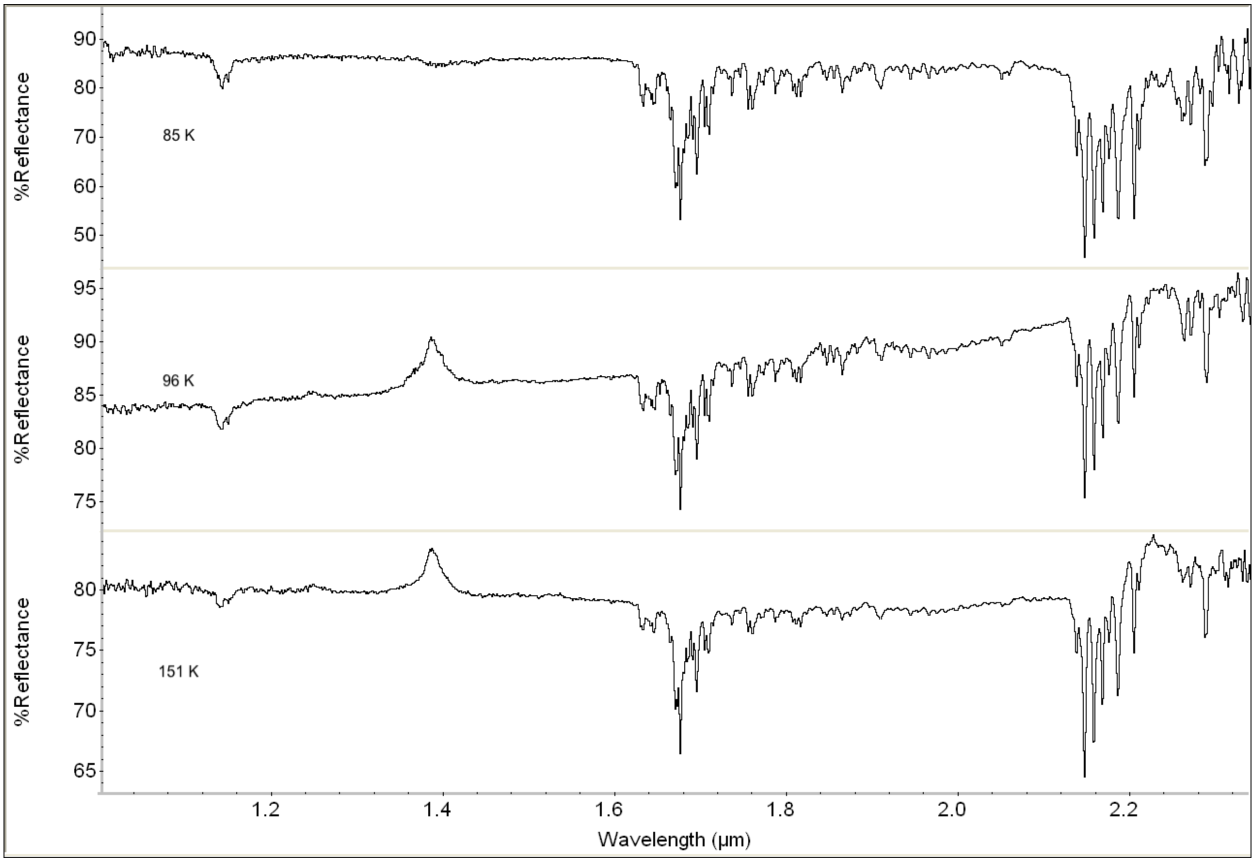

Figure A2. Full spectral range from C_6H_6 experiment presented in the manuscript.

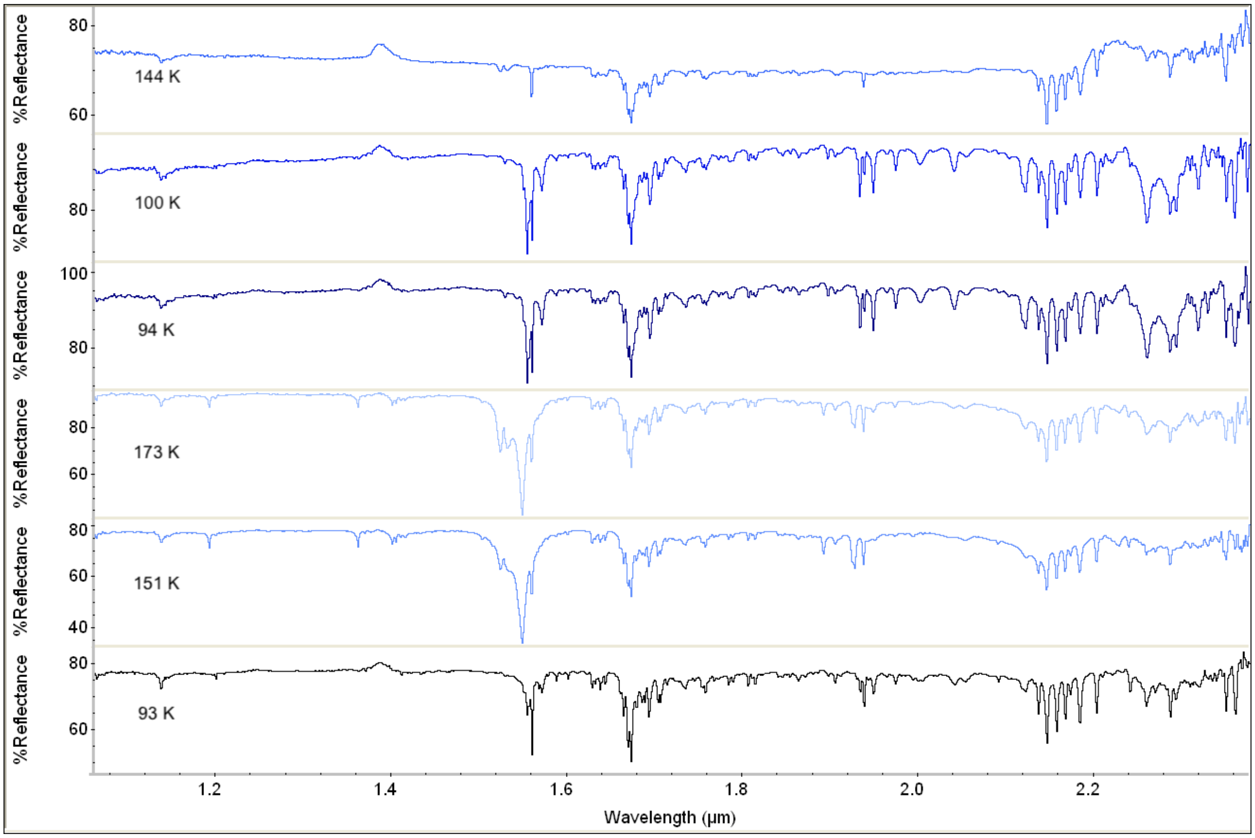

Figure A3. Full spectral range from C_2H_2-C_6H_6 experiment presented in the manuscript.

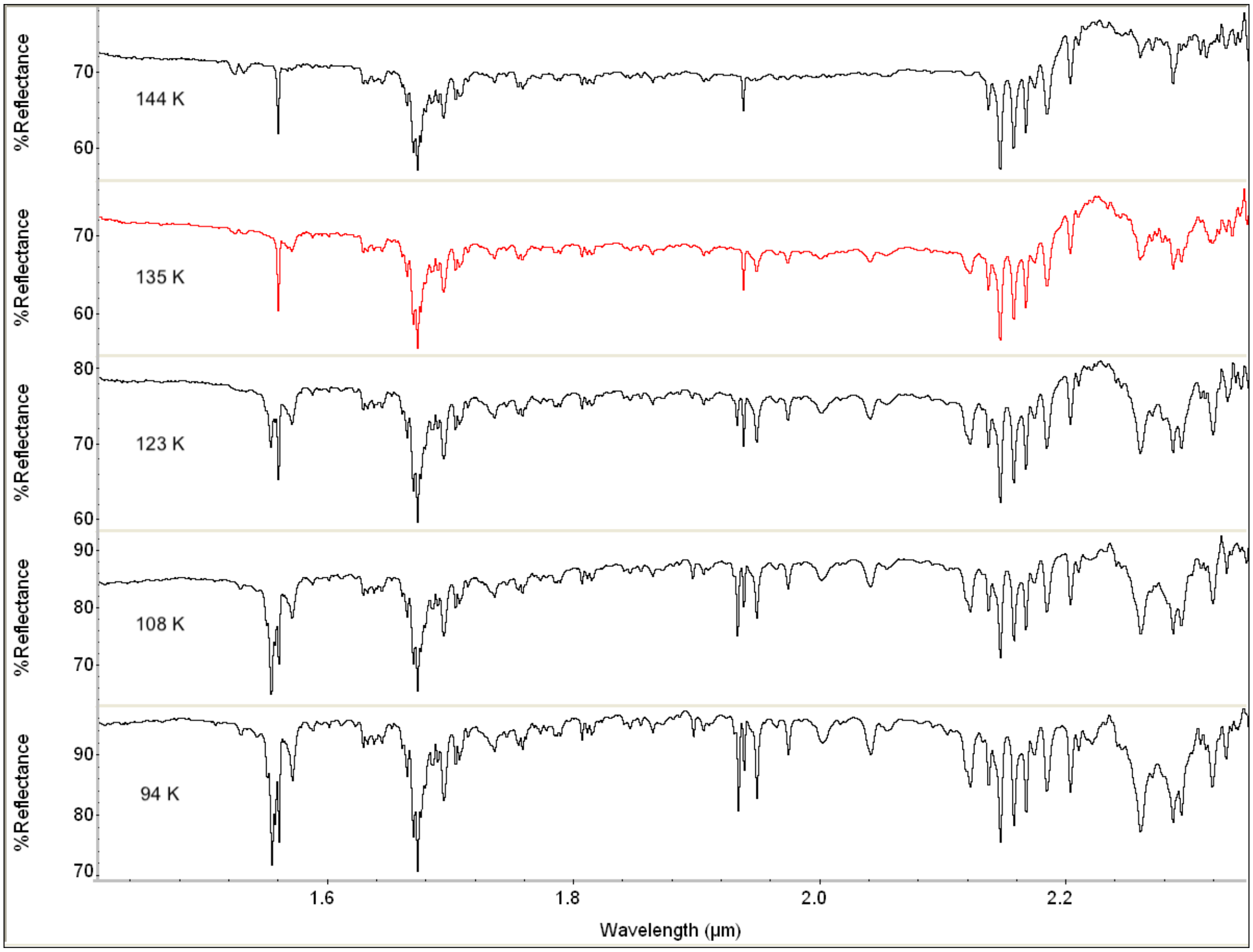

Figure A4. Full range spectra from C_2H_2-C_6H_6 experiment presented in the manuscript showing co-crystal formation initiates around 135 K (red spectrum), as this is the first appearance of one of the new bands at 1.569 µm.

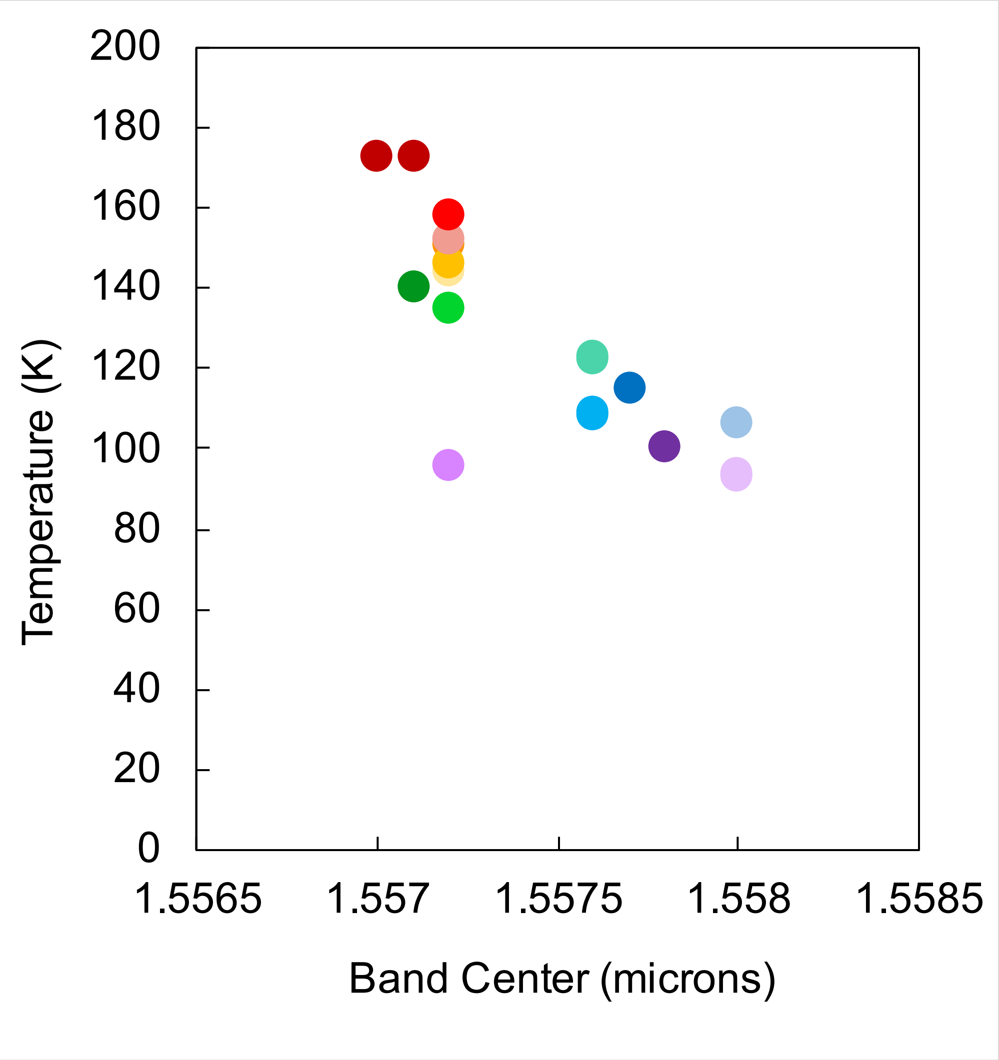

Figure A5. Band center shifts versus temperature for the C_2H_2-C_6H_6 experiment presented in the manuscript.

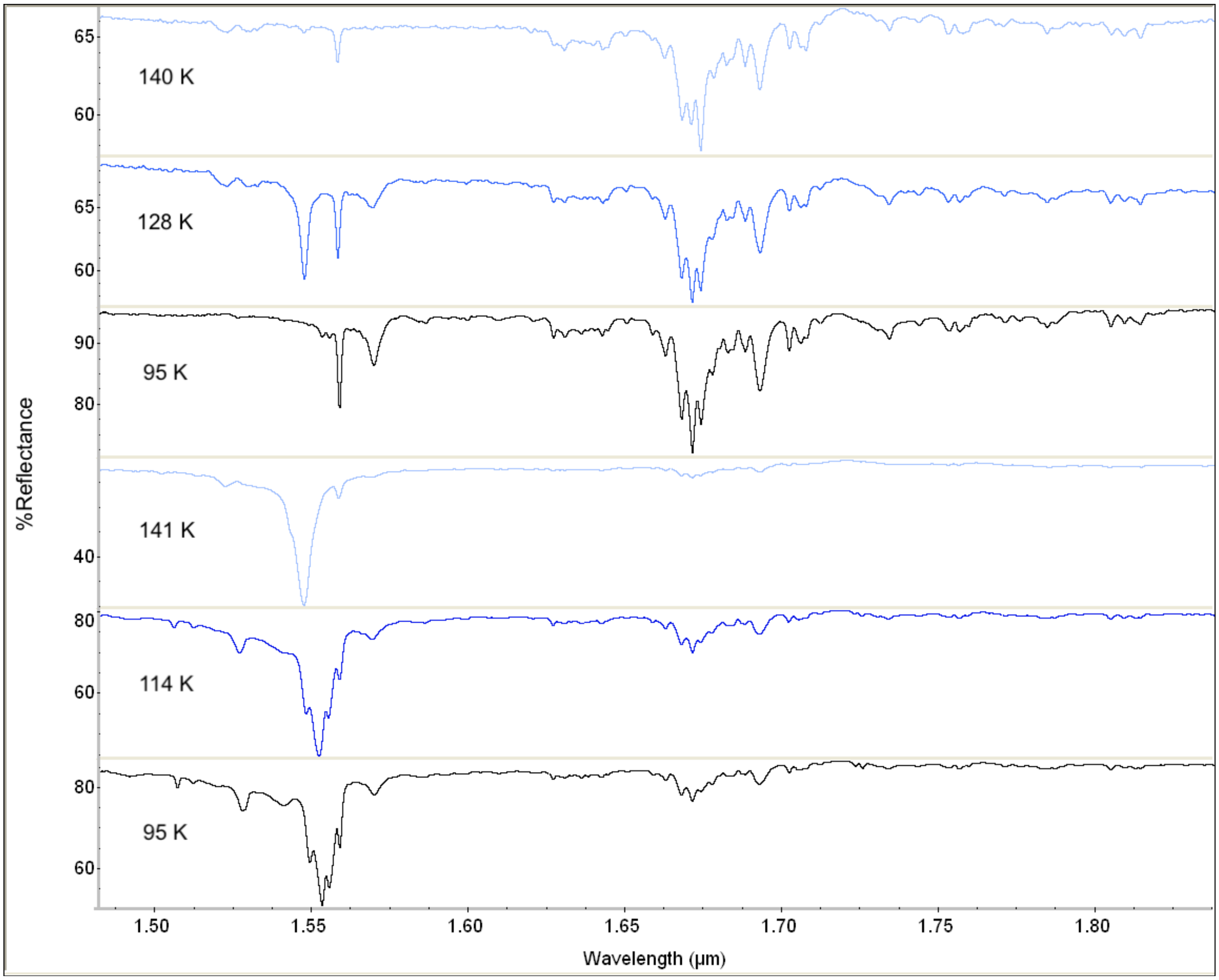

Figure A6. NIR reflectance spectra from repeat experiment 1 of C_2H_2-C_6H_6 (1.5 to 1.85 µm). Spectra are shown in order of increasing time from top to bottom. Co-crystal formation initiated between 136 K and 128 K.

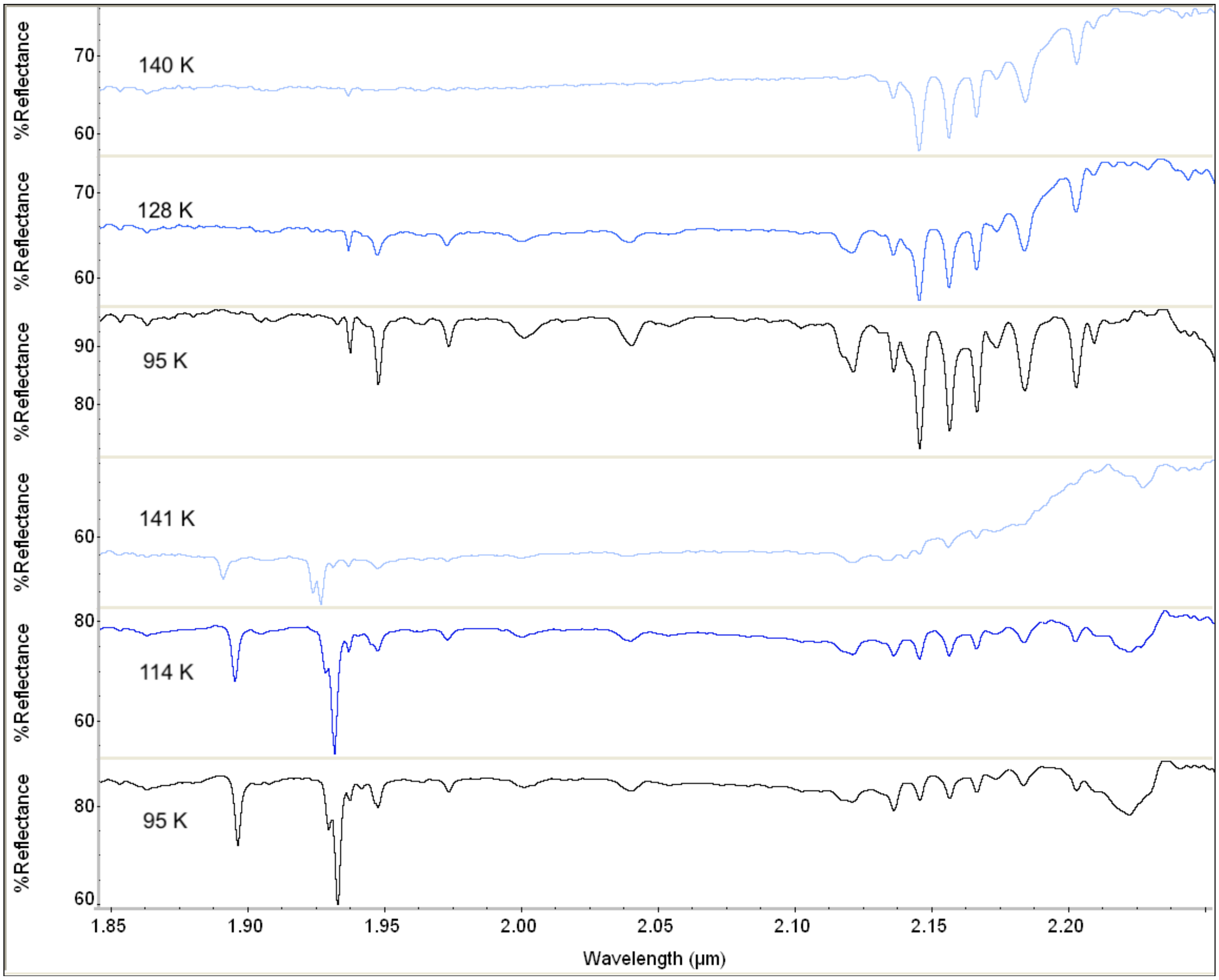

Figure A7. NIR reflectance spectra from repeat experiment 1 of C_2H_2-C_6H_6 (1.85 to 2.22 µm). Spectra are shown in order of increasing time from top to bottom. Co-crystal formation initiated between 136 K and 128 K.

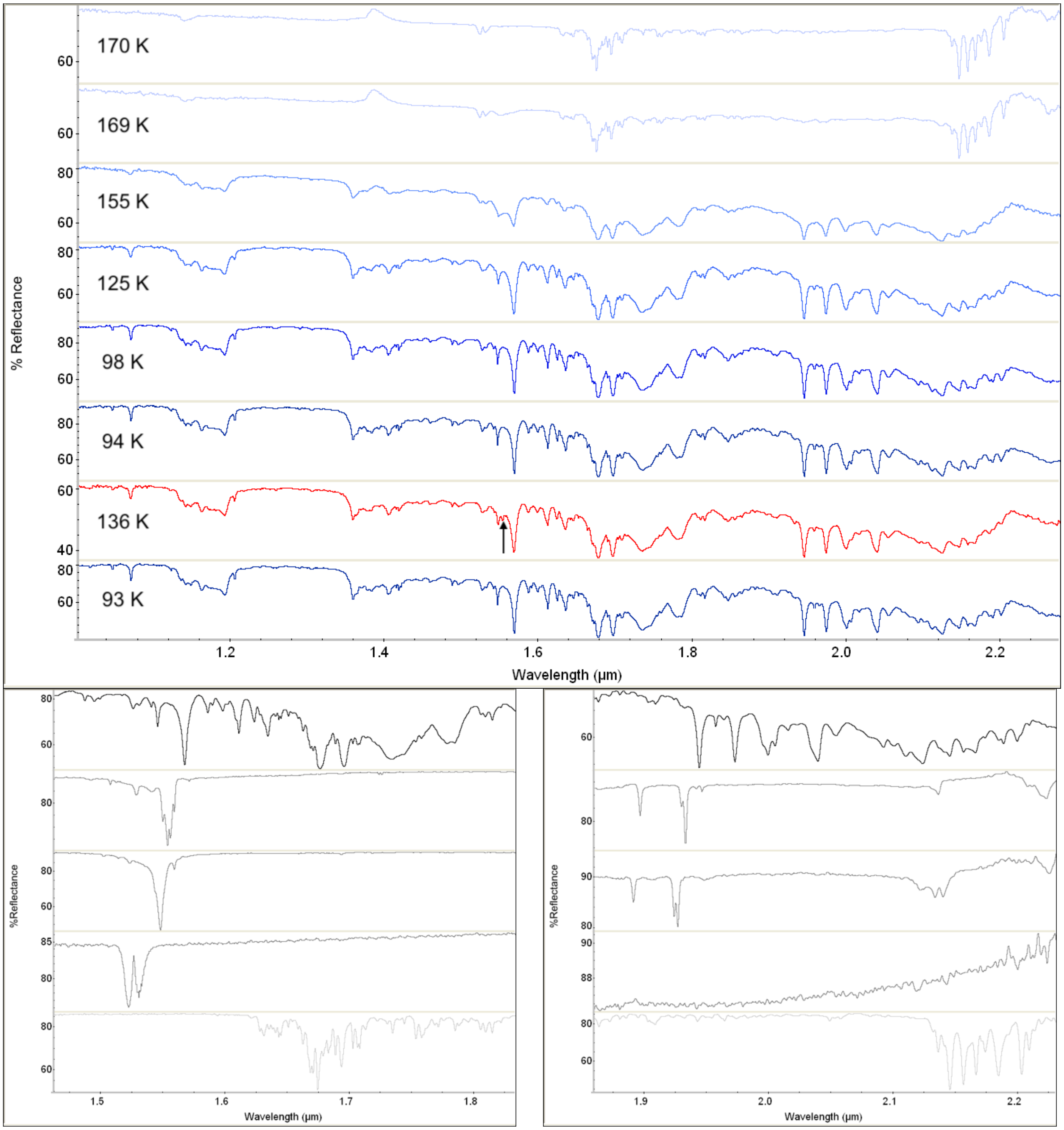

Figure A8. (a) NIR reflectance spectra from repeat experiment 2 of C_2H_2-C_6H_6 mixture after both compounds have been deposited. Benzene was deposited from 214 to 176 K (not shown), then acetylene was deposited from 170 to 167 K. The sample was cooled to 94 K, warmed to 136 K (red spectrum), then cooled back down to 93 K. Bands located at 1.585 to 1.780 µm, as well as 1.943 to 2.122 µm are not observed in either of the single component spectra of C_2H_2 or C_6H_6. Notice the small band at 1.551 µm in the 136 K spectrum (denoted by arrow). (b,c) Zoomed comparison among the C_2H_2-C_6H_6 mixture (black), C_2H_2 (dark gray), and C_6H_6 (light gray) showing new bands from 1.585 to 1.780 µm, as well as 1.943 to 2.122 µm (c).

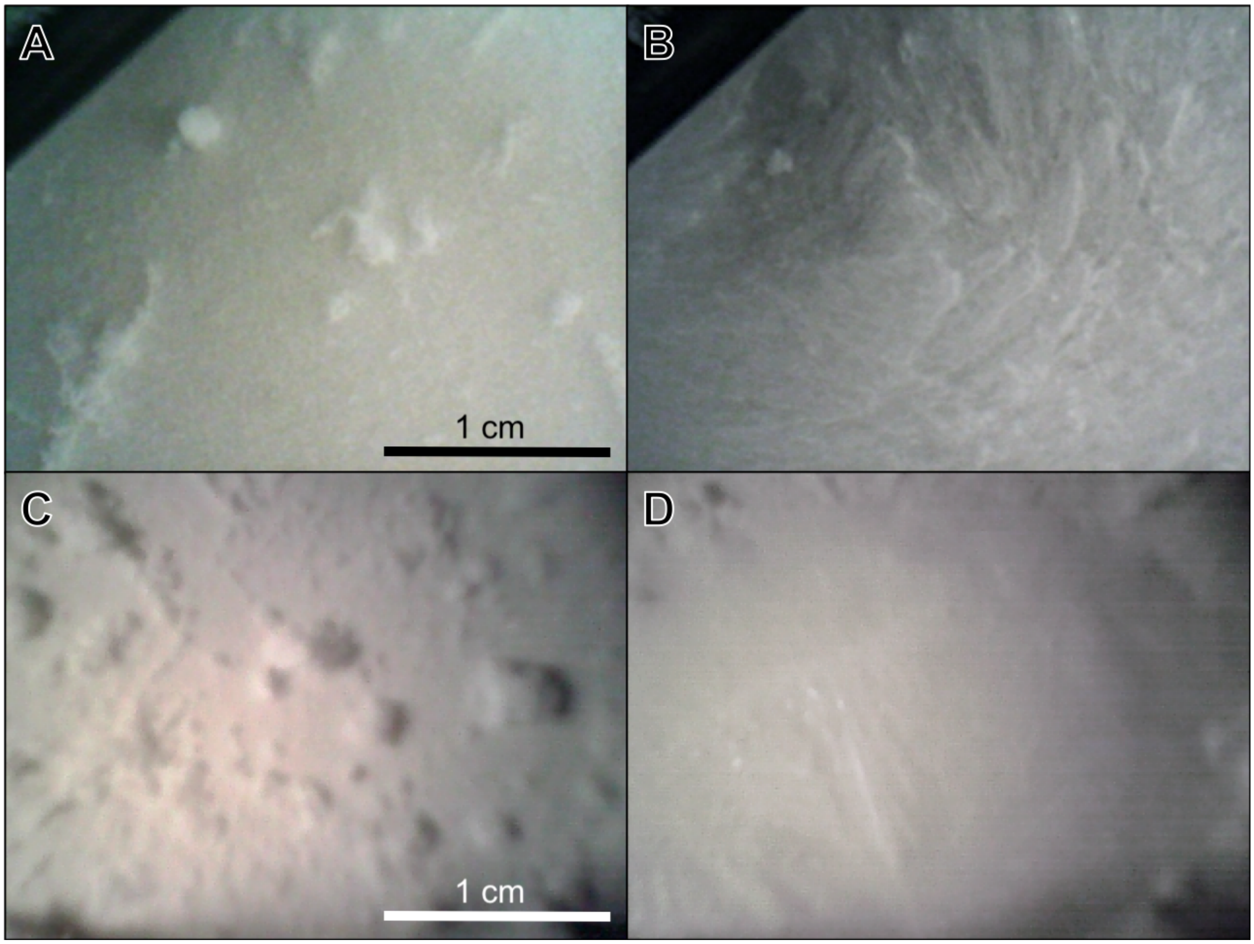

Figure A9. Top-down view of C_2H_2-C_6H_6 mixture from repeat experiment 2 in sample dish showing two different optical camera views: (a) and (b) being one, and (c) and (d) being the other. Panels (a) and (c) were taken at t = 138 and t = 139 minutes at 185 K and 184 K, respectively, before C_2H_2 was added to the dish. Panels (b) and (d) were taken at t = 257 minutes at 112 K, after C_2H_2 was added to the C_6H_6 on the dish. Notice the difference in sample appearance and morphology structure from (a) to (b) and from (c) to (d). The progressed sample has a more complex structure and appears to have increased in reflectance. The white color of the sample is due to the Spectralon® IR reflectance material upon which the sample is deposited.

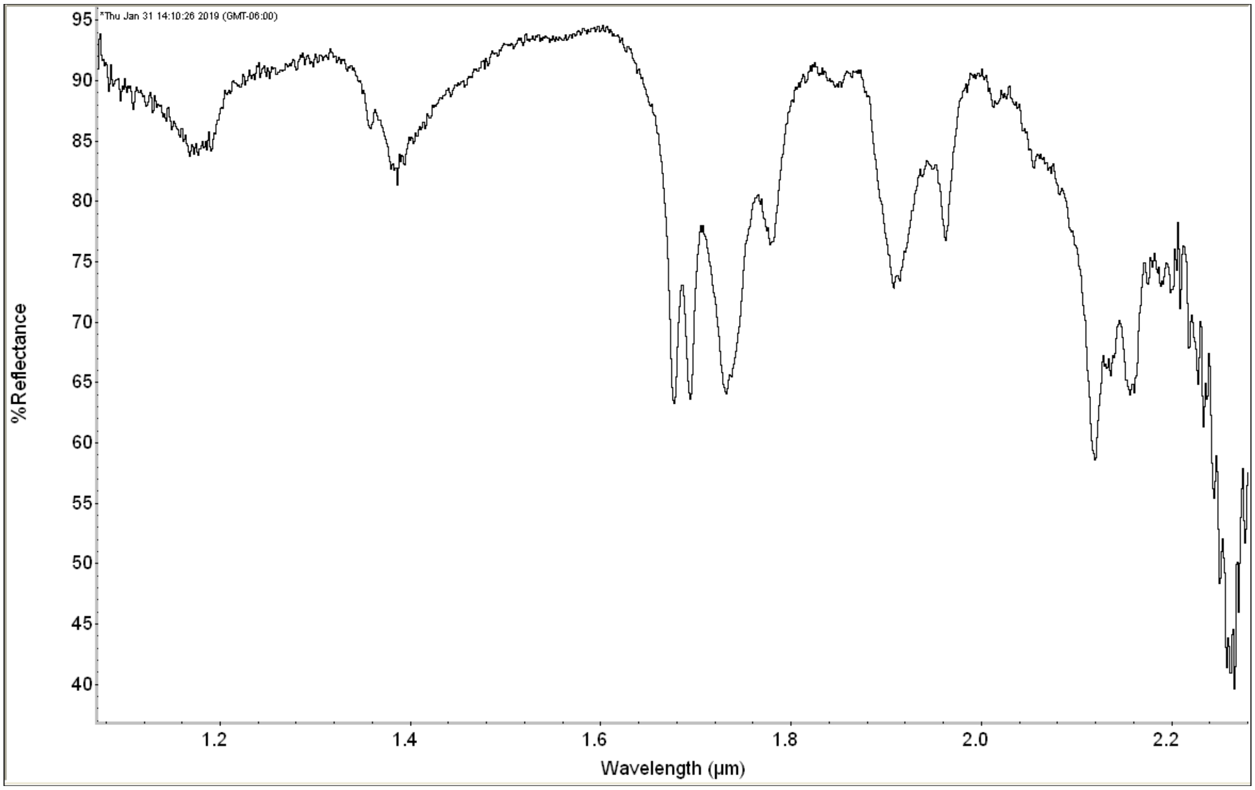

Figure A10. Spectrum of acetone $(CH_3)_2O$ taken at room temperature and pressure

CHAPTER 3. CHARACTERIZING THE NEAR-INFRARED SPECTRAL PROPERTIES OF THE ACETONITRILE-ACETYLENE CO-CRYSTAL IN TITAN-RELEVANT HYDROCARBON MIXTURES

Ellen Czaplinski and Vincent Chevrier

Arkansas Center for Space and Planetary Sciences, University of Arkansas, Fayetteville, AR 72701, USA

Keywords: NIR spectroscopy, nitriles, experimental techniques, surface ices

Highlights:

- Confirmed the formation and detection of the acetonitrile-acetylene co-crystal using NIR spectroscopy under Titan temperatures and pressure
- Co-crystal identified based on a new band at 1.676 µm, spectral shifts, and band splitting
- Formation temperature between 118 and 174 K, and is stable at 90 K

1. Abstract

Recent atmospheric observations of Titan, Saturn's largest moon with a thick atmosphere, have revealed enhanced abundances of acetonitrile (CH_3CN) at Titan's north pole, strengthening the argument that CH_3CN may be an abundant nitrile species at the surface and/or in Titan's liquids. CH_3CN also closely matches spectra of Titan's surface in regions where an undetermined feature centered at 5.01 µm has been identified. Using an experimental Titan surface chamber, we conducted experiments to characterize the near-infrared spectra of CH_3CN in solutions with methane (CH_4) and ethane (C_2H_6), as well as characterizing the NIR spectral signatures of co-crystal formation between CH_3CN and acetylene (C_2H_2). Results from this study show CH_3CN evaporite formation with CH_4, including a CH_4 band at 1.666 µm which may be leftover gas in contact with the evaporite layer. Here, the C_2H_2-CH_3CN co-crystal forms between 118 and 174 K, is stable at Titan surface temperatures (~90 K), and we observe several instances of spectral shifts, band splitting of certain vibrational modes, and possible phase trapping of

C_2H_2. The results from this study confirm NIR detection of the co-crystal, enhancing the techniques that can be used to detect Titan-relevant co-crystals. The upcoming *Dragonfly* mission will explore Titan's surface up close, and may have the opportunity to detect and observe these types of co-crystals in situ.

2. Introduction

Acetonitrile (CH_3CN), a product of ion-neutral reactions induced by UV photolysis of the upper atmosphere, was first discovered in Titan's atmosphere via ground-based measurements from the 30-m telescope operated by the Institut de Radioastronomie Millimétrique (Bézard et al., 1993). CH_3CN has been estimated to exist as a few ppb in the upper atmosphere (Marten et al., 2002), and saturation ratios in the lower atmosphere may approach that required for condensation (60-90 km), potentially explaining a necessary sink to help model the abundances of the gas phase in the lower atmosphere (Ennis et al., 2017). Additional models estimate a constant precipitation flux of 1.27×10^7 molecules/cm^2/s (Krasnopolsky, 2009; Vuitton et al., 2008; Molina-Cuberos et al., 2002). As CH_3CN molecules travel through Titan's atmosphere, they may combine into ordered clusters or precipitates and fall to the surface; alternatively, they may aggregate during fluvial transport of condensed CH_3CN deposits on Titan's surface (Corrales et al., 2017). Recent abundance measurements of CH_3CN in Titan's atmosphere from the Atacama Large Millimeter/submillimeter Array (ALMA) show enhanced abundances at high latitudes, especially at the north pole (Fig. 1, Thelen et al., 2019), which is indicative of a winter enrichment of CH_3CN, and may be advected to lower latitudes post northern winter (Thelen et al., 2019).

On Titan's surface, it has been proposed that CH_3CN may comprise some of the darker areas of the surface, where the *Cassini* Visible and Infrared Mapping Spectrometer (VIMS) spectra imply the surface may be akin to a wet sand (water ice, solid organics, mixture) with liquid methane/ethane incorporated (Clark et al., 2010). Additionally, the study by Clark et al. (2010) observed that the infrared spectrum of acetonitrile has the most similar shape and position to the 5.01 µm feature and also has similar features to the 5.05 µm feature, however slightly shifted.

Recent experimental studies performed under Titan conditions have confirmed the existence of two co-crystals that form with CH_3CN: CH_3CN-C_2H_2 and C_6H_6-CH_3CN (Cable et al., 2020; McConville et al., 2020, respectively). In the former paper, the authors identified the co-crystal via micro-Raman spectroscopy and suggest that the CH_3CN-C_2H_2 co-crystal may be a major component of Titan's organic geological units (e.g., labyrinth terrains – similar to karst on Earth) due to the differential solubility of acetonitrile and acetylene in liquid hydrocarbons (nonpolar C_2H_2 being more soluble and polar CH_3CN being less soluble; Cable et al., 2020). In the latter, the authors report how the mole fraction of CH_3CN changes with temperature and solved the co-crystal structure with X-ray diffraction (XRD) measurements, highlighting the unique compositional diversity of Tian "minerals" (McConville et al., 2020).

Given the enhancement in CH_3CN abundance over Titan's north polar lakes/seas, the fact that CH_3CN closely matches an important VIMS signature, and that acetonitrile is involved in at least two recently studied Titan-relevant co-crystals, we decided to augment these laboratory studies by characterizing the solubility of CH_3CN in liquid CH_4, C_2H_6, and the CH_3CN-C_2H_2 co-crystal stability under Titan temperature and pressure using infrared spectroscopy.

3. Methods

In order to investigate the formation and stability of CH_3CN as an evaporite, we conduct laboratory experiments in the Titan Surface Simulation Chamber (TSSC; Wasiak et al., 2013).

The specific details and general protocol for the TSSC were provided in section 2 of the Introduction: General Methodology. Here, we provide relevant details for the set of experiments in this chapter.

Because CH_3CN is a liquid at standard ambient temperature and pressure (SATP), we follow the “cold trap” protocol to introduce CH_3CN to the condenser (similar to the protocol for working with benzene in chapter 2; Czaplinski et al., 2020). Proper safety precautions should always be followed when working with CH_3CN including wearing: a lab coat, splash goggles, appropriate impermeable gloves, an organic vapor respirator, and working within the glove box or under the fume hood with sufficient ventilation in the room. When the LN_2 flow to the chamber is initiated, the flow to the condenser is restricted so that only the temperature control box (TCB) begins cooling significantly (since the condenser is located inside of the TCB, the condenser still cools slightly when LN_2 is restricted to the TCB). Inside a custom-built glovebox, an Erlenmeyer flask is filled with ~100 mL of avantor™ Baker Analyzed® acetonitrile (CH_3CN, ≥99.9%). Nitrogen gas is continuously bubbled through the CH_3CN-filled flask through the building’s exhaust system at 3 psi for ~5 minutes. This flow of N_2 through the flask causes the CH_3CN to rapidly effervesce. After the flask reaches N_2 saturation and the sample dish reaches ~183 K (any temperatures colder than acetonitrile’s melting point, 228 K), we then open the solenoid valve, close the exhaust valve, and open the exterior condenser inlet so that the N_2-CH_3CN saturated mixture is carried through the condenser at ~6 psi where it deposits onto the sample dish as a solid. The CH_3CN deposits onto the sample dish for ~20 minutes. Deposition is verified via optical cameras and FTIR measurements (Nicolet 6700 FTIR spectrometer that is equipped with a TEC InGaAs 2.6 μm detector, a CaF_2 beam-splitter, spectral range of 1 to 2.6 μm, spectral sampling of 4 cm^{-1}, spectral resolution of 0.01 cm^{-1}, connected to a fiber optic probe above the sample dish). After deposition, the N_2 bubbling through the Erlenmeyer flask is stopped, and the external condenser outlet is closed. We leave the solenoid valve open for an additional 5 minutes to prevent any blockages from solid CH_3CN. As the chamber cools, additional FTIR measurements of the pure CH_3CN are taken for comparison to the pure spectra later in the experiment.

After the sample dish has reached 173 K, we begin flowing C_2H_2 (Airgas, 99.6%, acetone added as stabilizer) through the condenser at 50 kPa for 20 minutes, where it deposits on the sample dish in solid phase. Deposition is confirmed by optical TCB cameras and FTIR spectra. After we stop the C_2H_2 gas flow, the solenoid valve is left open for 5 minutes to prevent blockages.

After both compounds are deposited onto the sample dish (sample thickness on the order of a few mm), the LN_2 flow to the condenser is turned on. Note that at this point, we are finished adding compounds to the condenser; the condenser LN_2 flow merely contributes to the rest of the TCB successfully attaining Titan surface temperatures (89–90 K). Depending on the experiment, the TCB temperatures may be warmed later in the experiment in an attempt to increase reaction times or, in the case of C_2H_2, to identify how the IR spectra changes with regards to temperature. The mole fraction for the acetylene– benzene experiment was calculated using the same methods reported in Czaplinski et al. (2019; see Spectral Unmixing Model section), a Python code (see Czaplinski et al., 2019) that decomposes a given spectrum into a best fit of linear combinations of the pure spectra (taken at corresponding temperatures) added together. The mole fraction is reflected in the linear weights that each raw component spectrum is given to fit the experimental data.

4. Results

Here, we outline three types of experiments: C_2H_6-CH_3CN (liquid-solid), CH_4-CH_3CN, (liquid-solid) and the C_2H_2-CH_3CN co-crystal (solid-solid). Vibrational modes and band assignments of pure CH_3CN are presented in Table 1.

Table 1. Vibrational modes and band assignments of CH_3CN from a previous study compared with the band positions in this study.

Literature band positions[a] (cm^{-1})	This study[b] (cm^{-1})	This study[b] (µm)	Band assignment[a]
4321.8	4321.1	2.314	$\delta_s CH_3 + v_s CH_3$
4366.6	4366.9	2.290	$\delta_s CH_3 + v_{as} CH_3$
4396.6	4403.7	2.271	$v_{as} CH_3 + \delta_{as}' CH_3$
4438.6	4440.4	2.252	$v_{as} CH_3 + \delta_{as} CH_3$
4948.3	4949.4	2.020	$v_s CH_3 + 2_{vs} CH_3$
4996.5	4999.6	2.000	$v_s CH_3 + 2_{\rho}' CH_3$
5064.2	5057.3	1.977	$v_s CH_3 + 2_{\rho} CH_3$
	5070.0	1.972	
5195.2	5188.6	1.927	$v_s CH_3 + {}_{v}CN$
5252.7	5249.3	1.905	$v_{as} CH_3 + {}_{v}CN$
5383.4	5288.0	1.891	$v_{as}' CH_3 + {}_{v}CN$
5671.4	5673.4	1.762	$v_s CH3 + 2_{\delta s} CH_3$
5707.6	5712.1	1.751	$v_s CH_3 + \delta_{as}' CH_3 + \delta_{as}' CH_3$
	5766.4	1.734	
5831.6	5829.1	1.715	$v_{as} CH_3 + v_{as} CH_3$
5953.7	5945.4	1.682	$v_{as}' CH_3 + v_{as}' CH_3$
6277	5989.8	1.669	$v_s CH_3 + vCN + vCC$

[a] Beć et al., 2019 (303 K)
[b] 100 K (9/2/2020, 16:08)

4.1. C_2H_6 - CH_3CN

In the C_2H_6-CH_3CN (liquid-solid) experiment, we first added CH_3CN to the condenser following the procedure described in the Methods section, then condensed liquid ethane on top of the solid layer of CH_3CN and allowed the sample to warm to 143 K. Figure 1 shows the resulting spectra from this experiment. We do not observe obvious or drastic changes to the spectra after cooling the mixture to 93 K and then warming to 143 K (Figure 1). This is confirmed by band depth measurements (Figure 2) which show an average value of 3.9% throughout the experiment for the CH_3CN band at 1.928 µm (this band was chosen, as it does not overlap with C_2H_6 C–H stretching bands in the 1.7 – 1.8 µm region). After C_2H_6 was condensed, it remained in the liquid phase throughout the duration of the experiment, as we do not observe a significant increase in reflectance at the coldest temperature, which aligns with the fact that C_2H_6 does not freeze until ~90 K (Farnsworth et al., 2020). Figure 3 highlights the sample's appearance when liquid C_2H_6 partially dissolves the solid CH_3CN layer underneath. The two panel photos were taken 30 seconds apart and in that time, one can observe the perimeter of the liquid C_2H_6 layer that spreads outwards towards the upper part of the photo.

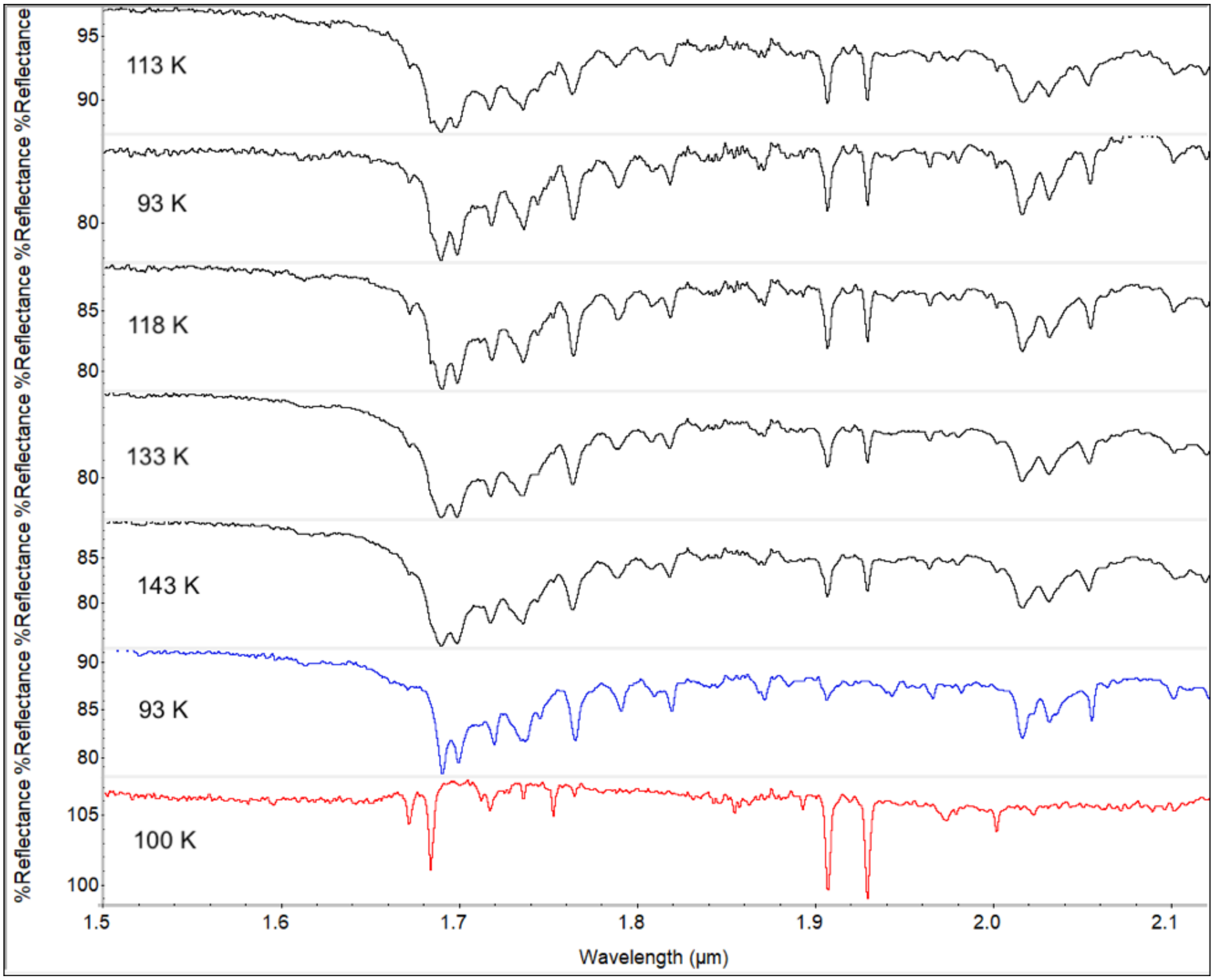

Figure 1. FTIR spectra of C_2H_6 and CH_3CN from 113 K to 143 K. For comparison, a spectrum of pure C_2H_6 (liquid) at 93 K and CH_3CN (solid) at 100 K are shown in blue and red, respectively for comparison. Experimental time increases from top to bottom. Notice how there are no drastic changes to the C_2H_6 bands throughout the experiment

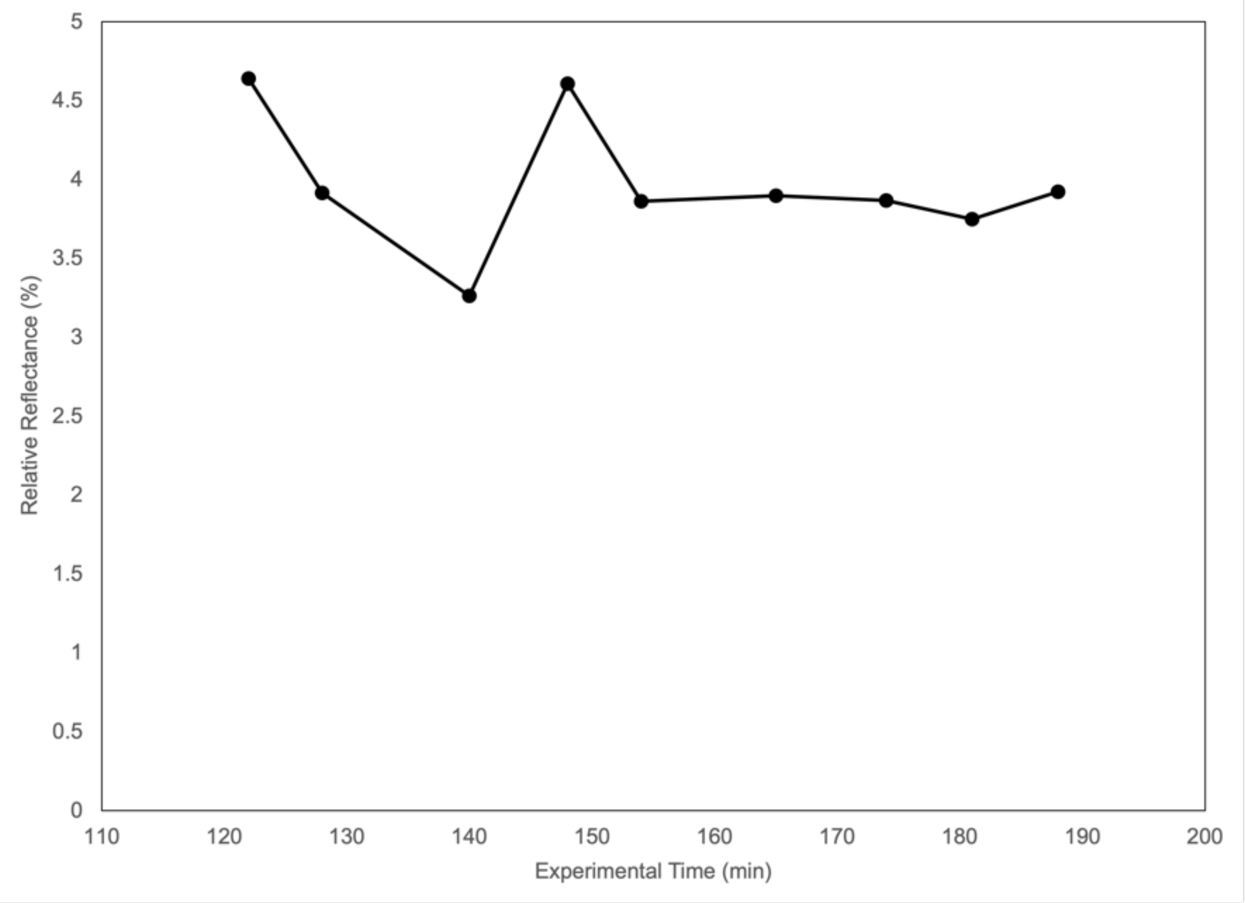

Figure 2. Band depths of the 1.928 µm band of CH_3CN showing no drastic change in band depth as a function of time or temperature. The lowest reflectance value of 3.263 % corresponds to when the sample was coldest (93 K). Temperatures ranged from 93 – 143 K (corresponding with Figure 1 above).

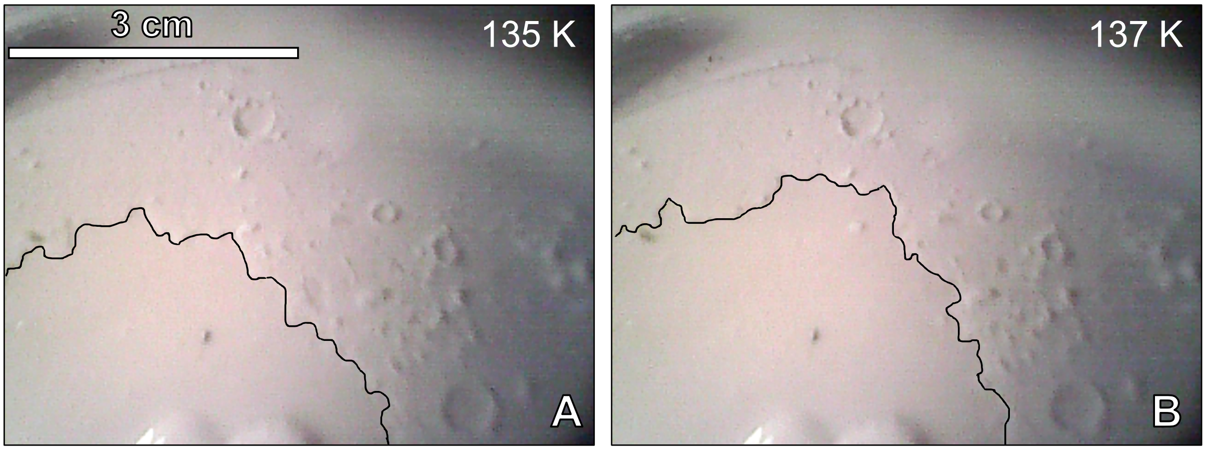

Figure 3. Top-down view of the C_2H_6-CH_3CN mixture in the sample dish. (A) and (B) were taken 30 seconds apart. Liquid C_2H_6 dissolved part of the solid CH_3CN layer, as evidenced by the increase in the liquid portion from (A) to (B), indicated by the black outline.

4.2. CH_4 - CH_3CN

In the CH_4-CH_3CN (liquid-solid) experiment, CH_3CN was added to the condenser initially, following the procedure described in the Methods section, then liquid CH_4 was condensed on top of the solid CH_3CN layer at ~94 K. Temperatures within 94 – 98 K (slightly warmer than Titan surface temperatures) were maintained, because CH_4 readily evaporates at these temperatures (Czaplinski et al., 2019; Farnsworth et al., 2020). Figure 4 shows the corresponding FTIR spectra. An enhanced view of the pure CH_3CN spectrum is compared to the residual CH_4-CH_3CN spectrum after liquid CH_4 had evaporated (Figure 5). Notice the subtle differences in spectral bands in Figure 5, most notably the band at 1.666 μm (associated with the first overtone region of pure CH_4), which persists after all liquid CH_4 has been evaporated. This band has been reported to persist in previous experiments with CH_4 evaporites (Czaplinski et al., 2019; Chapter 1), and in our experience with this experimental setup, is present when the temperature of the sample is well above the boiling point of pure CH_4 (125 K; Friend et al., 1991).

Band depth calculations were performed on the CH_4 triplet (1.668 µm, 1.722 µm, 1.794 µm, respectively) which corresponds to the $2\nu_3$, $\nu_1/\nu_3 + \nu_2 + \nu_4$, and $\nu_1 + 2\nu_4$ vibrational modes, respectively (Czaplinski et al., 2019). By plotting these band depths as a function of experimental time, we provide secondary confirmation of complete CH_4 evaporation by the end of the experiment, as the band depth values from all three CH_4 bands decreased to a value of zero by 190 minutes (Figure 6).

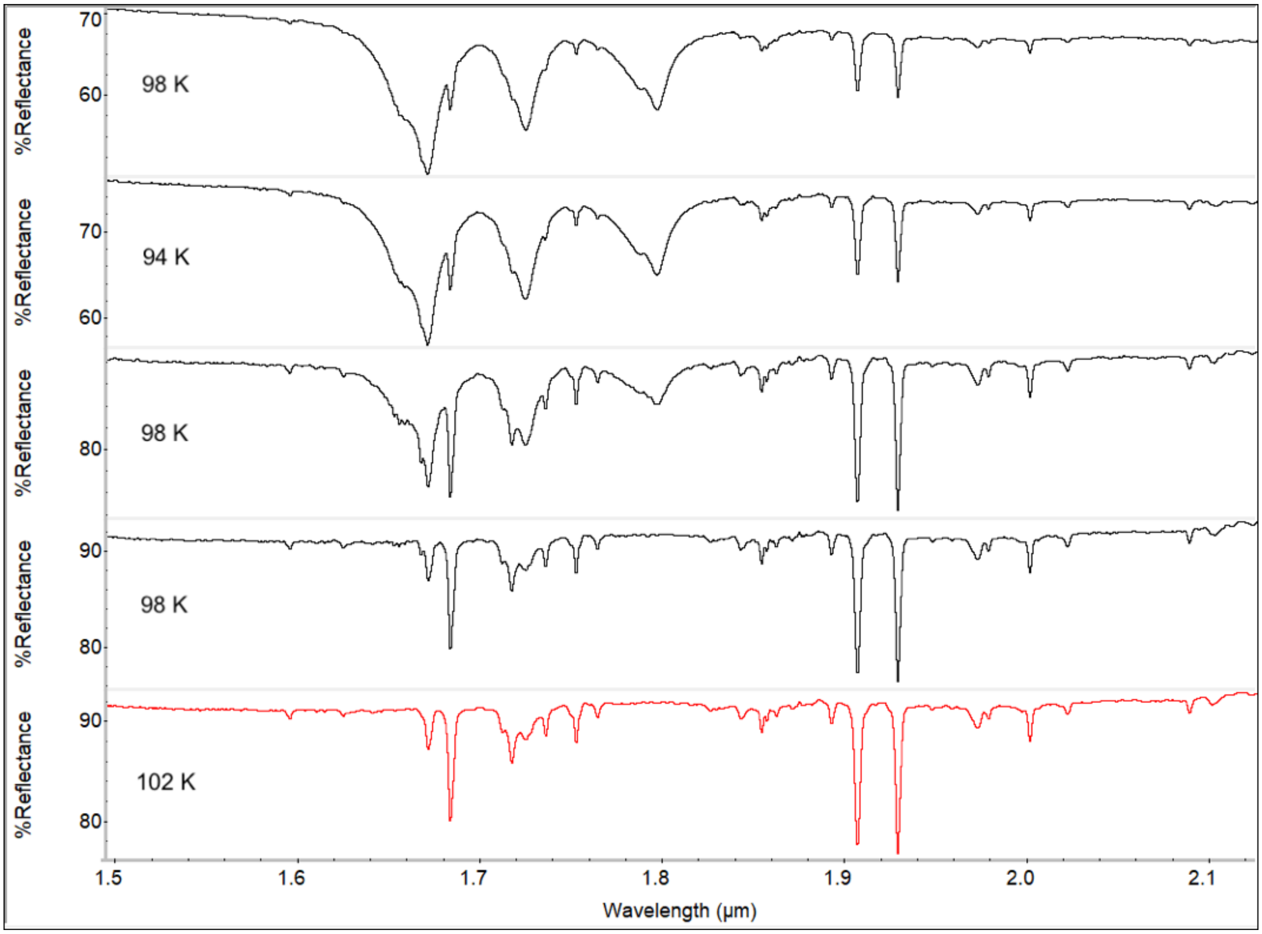

Figure 4. FTIR spectra from the CH_4-CH_3CN (liquid-solid) experiment at different temperatures, along with pure CH_3CN at 102 K in red. Experimental time increases from top spectrum to second from the bottom, as characterized by the CH_4 bands disappearing with evaporation. Notice the increase in reflectance as the sample changes from a liquid (when CH_4 is present) to a solid (after CH_4 has evaporated and only solid CH_3CN is left).

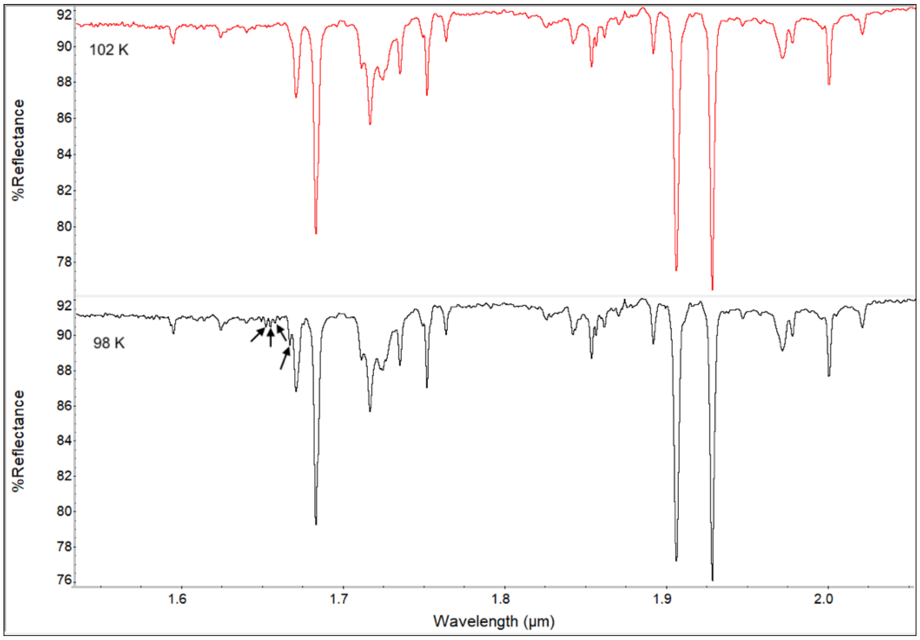

Figure 5. Pure CH_3CN (red) compared with the final (residual) spectrum from the CH_4-CH_3CN experiment. This enhanced view details the differences between the two spectra, most notably the band at 1.666 µm and three small bands just before it (denoted by arrows), which are associated with CH_4.

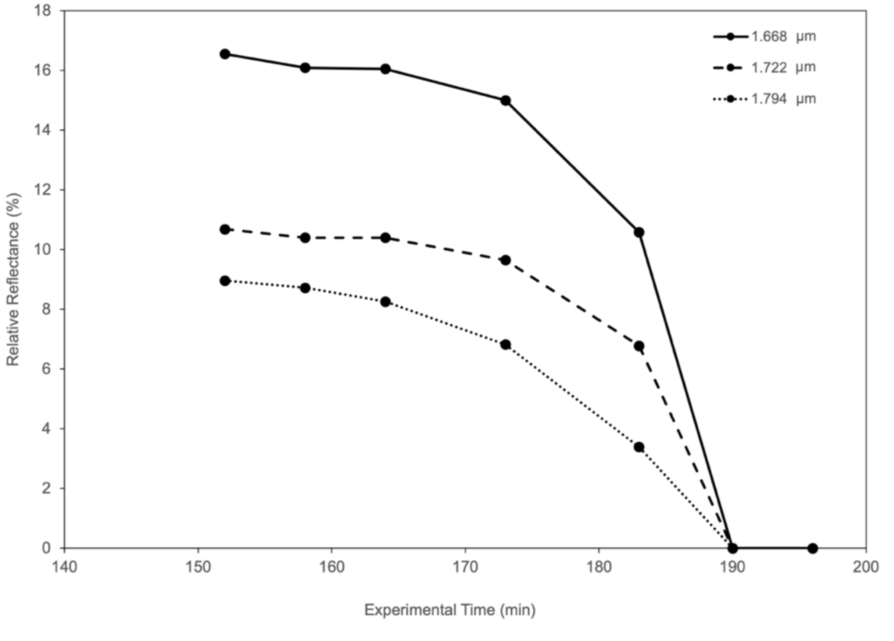

Figure 6. Band depths of the CH_4 triplet (1.668, 1.722, and 1.794 µm; $2\nu_3$, $\nu_1/\nu_3 + \nu_2 + \nu_4$, and $\nu_1 + 2\nu_4$ vibrational modes, respectively) showing complete evaporation after 196 minutes had elapsed.

4.3. CH_3CN - C_2H_2 Co-Crystal

Here, we present three separate experiments with C_2H_2 and CH_3CN, where the C_2H_2-CH_3CN co-crystal was formed in all three via solid-solid interactions. In all three experiments, CH_3CN was first deposited onto the sample dish, as described in the Methods section, then C_2H_2 was deposited on top of the CH_3CN layer. The sample was first cooled down to Titan-relevant temperatures, then allowed to warm up in order to observe any changes in sample morphology, structure, or phase.

4.3.1. Experiment 1

During the first experiment (Figure 7), a lower concentration of C_2H_2 was added, which resulted in very minor differences to the spectra (when compared to experiments 2 and 3). Upon analysis of the spectra in Figure 7, we observe the appearance of a band at 1.676 µm when the sample was cooled to 174 K, which is neither present in pure C_2H_2 nor pure CH_3CN, supporting the claim that the co-crystal formed. Additionally, the spectra show some slight differences in reflectance after solid C_2H_2 was added to solid CH_3CN (Figure 7).

Further spectral changes of the $\nu_1 + \nu_3$ (1.552 µm) vibrational mode include splitting into a unique doublet when the sample is at 108 K, 151 K, and 177 K (Figure 7, second, fourth, and sixth spectra), and a single band centered at 1.551 µm at 97 K. These observations differ from pure C_2H_2 spectra at the same temperatures, which has only a single band when the sample is less than 140 K and four bands when the sample is below 97 K. Further, the $5\nu_4 + 3\nu_5$ (trans and cis bend) vibrational mode (centered around 1.93 µm) shows band shifts and unique band splitting when compared with pure C_2H_2 and pure CH_3CN. Upon cooling to 108 K, the $5\nu_4 + 3\nu_5$ mode splits into two separate bands at 1.926 and 1.932 µm. The 1.927 µm band of pure CH_3CN blue shifts by 0.001 µm (4.44 cm^{-1}) and the 1.932 µm band corresponds to the 1.932 µm band of the $5\nu_4 + 3\nu_5$ mode of pure C_2H_2. This doublet persists until the sample is heated to 188 K, and does not change shape at the orthorhombic to cubic C_2H_2 transition (~139 K), as the pure C_2H_2 bands do.

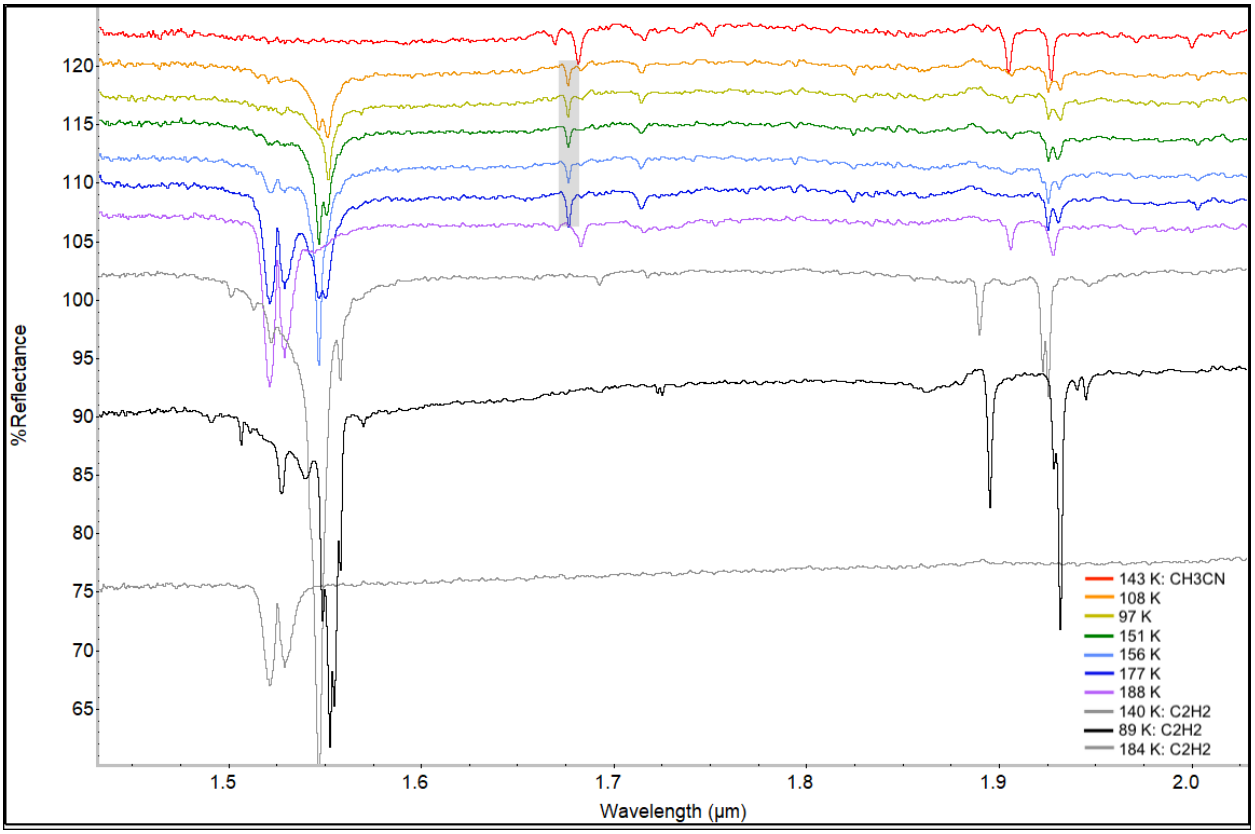

Figure 7. FTIR spectra from the first C_2H_2-CH_3CN experiment showing a pure CH_3CN spectrum from this experiment in red on top and pure C_2H_2 spectra in black and gray (From Chapter 2; Czaplinski et al., 2020) on the bottom (see Figure legend). Experimental time increases from top to bottom. Y-axis is offset for clarity. Notice the band at 1.676 µm (highlighted by gray box), indicating formation of the co-crystal upon cooling.

4.3.2. Experiment 2

The second C_2H_2-CH_3CN experiment shows the addition of a new band at 1.676 µm which appeared at 118 K, upon cooling the sample. Moreover, the band depth of the 1.676 µm band gradually increases throughout the experiment (as the sample is warmed), relative to the CH_3CN bands on either side of the 1.676 µm band (1.671 and 1.683 µm; $\nu_sCH_3 + \nu CN + \nu CC$ and $\nu_{as}'CH_3 + \nu_{as}'CH_3$ and vibrational modes, respectively; Table 1). Baseline reflectance also increases as the sample is warmed. In general, C_2H_2 bands in this experiment more closely match with pure C_2H_2 spectra, however when the sample is warmed to 151 K, the C_2H_2 $\nu_1 + \nu_3$ band splits into a doublet centered at 1.547 and 1.551 µm, unlike what is observed in pure C_2H_2 (Figure 8). At warmer temperatures (~186 K), the C_2H_2 $\nu_1 + \nu_3$ vibrational mode maintains the band at 1.551 µm, while a broad doublet at 1.521/1.529 µm persists even past the boiling point of C_2H_2 (185 K). This is not observed in pure C_2H_2 and is further discussed in the Discussion section. We also observe band splitting and band shifts of the $5\nu_4 + 3\nu_5$ vibrational mode, similar to the first co-crystal experiment above. However, in this experiment the changes were more drastic. The C_2H_2 $5\nu_4 + 3\nu_5$ mode splits into three distinct bands upon cooling to 101 K (Figure 8). These bands are located at 1.925, 1.929, and 1.932 µm and show differences when compared to pure C_2H_2 and CH_3CN. As the sample is warmed to 151 K, the triplet structure becomes less defined, then splits again when the sample was further warmed to 157 K. When warmed to 171 K, the band splits into a doublet at 1.926 and 1.931 µm with a similar appearance to the doublet presented in the first co-crystal experiment. At 186 K (warming), the C_2H_2 begins to evaporate and the band ends up as a single band at 1.925 µm.

Optical observations of the sample (Figure 9) show a noticeable difference in the co-crystal morphology at colder temperatures (~100 K to 156 K). The sample exhibits a “fluffy”, bright texture at these colder temperatures (Figure 8A-D). However, when the sample is warmed to 160 K, the sample loses that snow-like texture, and reverts to individual accumulations of solid sample (Figure 8E,F). Note that we do not include a panel for 160 K in Figure 8, as we wanted the temperatures from Figures 8 and 9 to correspond with each other, however one can still observe the lack of snow-like texture in Figure 9E. Additionally, we observe a “wetting” effect as the sample was warmed to 185 K (Fig. 9F). This is most likely due to the sample partially transitioning into the liquid phase, thus dissolving the surrounding solid portion of the sample (Figure 9F).

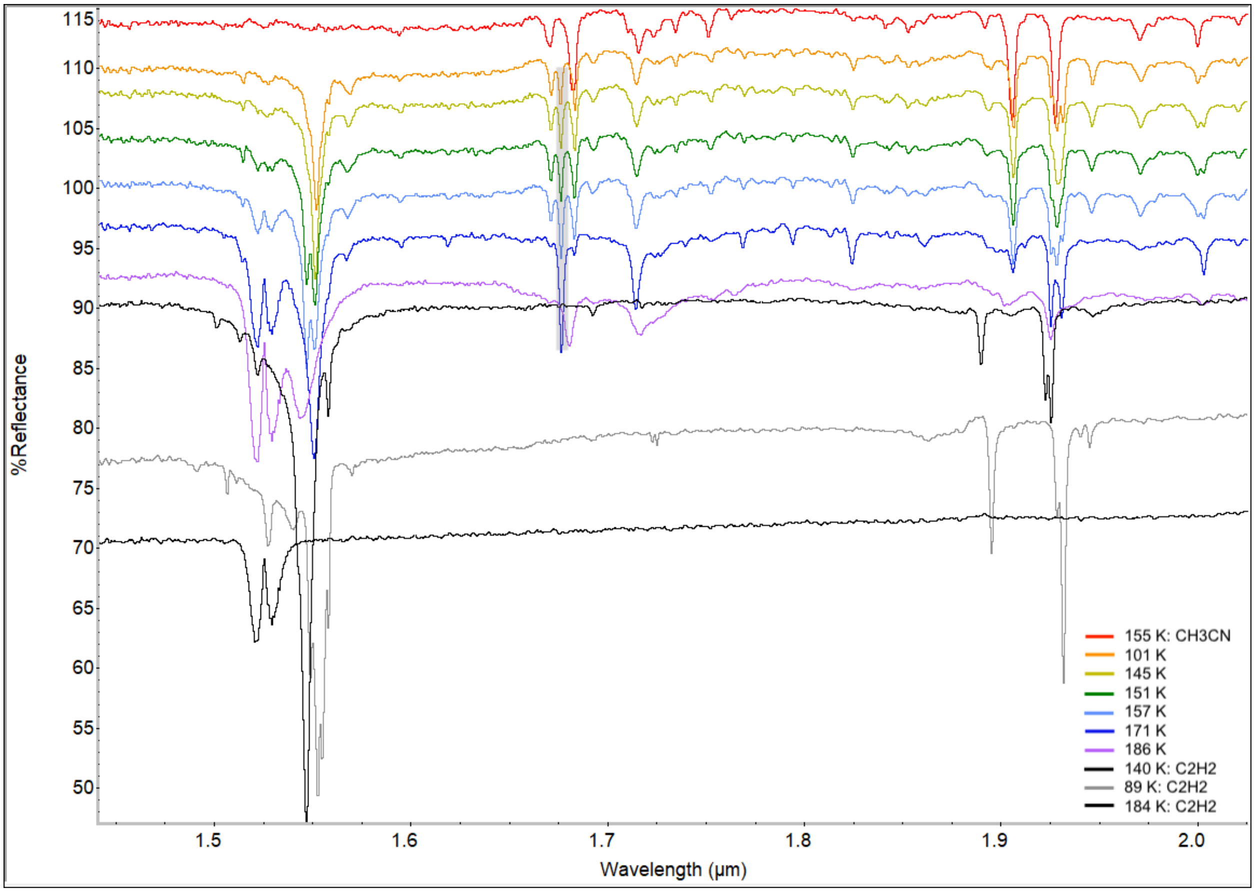

Figure 8. FTIR spectra from the second CH_4-CH_3CN experiment showing a pure CH_3CN spectrum from this experiment in red and pure C_2H_2 spectra in black and gray (From Chapter 2; Czaplinski et al., 2020) on the bottom; see Figure legend. Experimental time increases from top to bottom. Y-axis is offset for clarity. Notice the appearance of the 1.676 µm band (highlighted by gray box) in the 101 K spectrum, indicating formation of the co-crystal upon cooling. The reflectance of this feature increases as the sample is warmed. In the C_2H_2 $\nu_1 + \nu_3$ vibrational mode (1.552 µm), the band shape corresponds to the cubic structure even when the temperature of the sample is in the orthorhombic structural stability range (below 133 K).

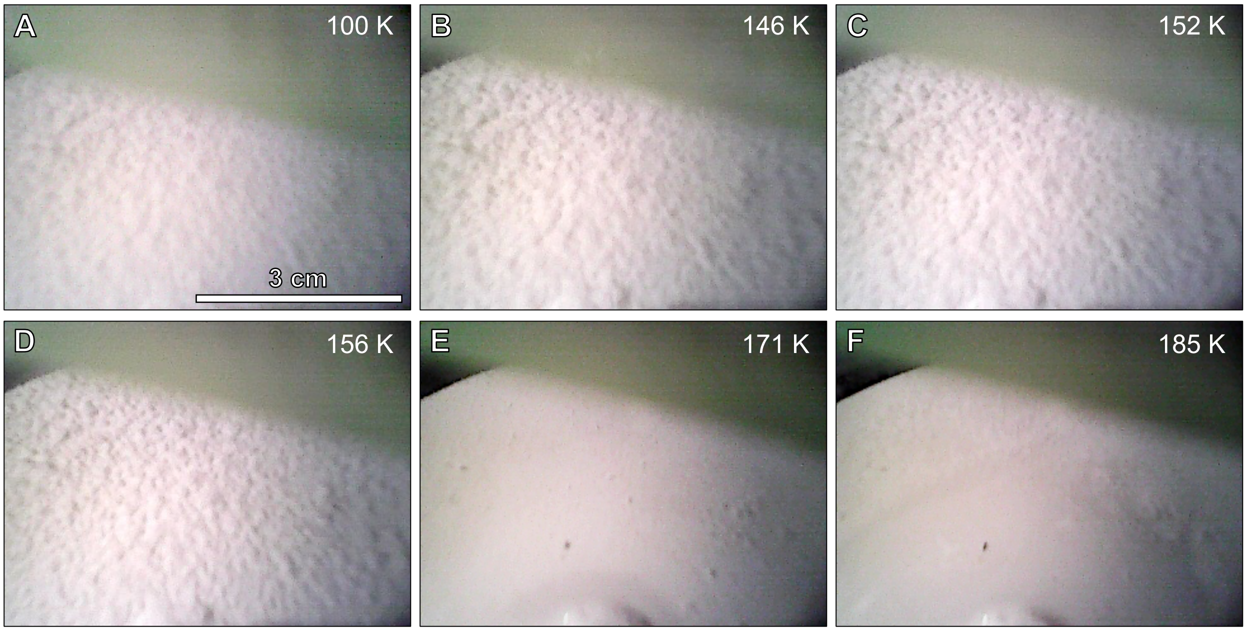

Figure 9. Top-down view of the second C_2H_2-CH_3CN mixture in the sample dish. The sample was warmed from (A)-(F). Temperatures correspond with the temperature labels in Figure 8 above. Notice the drastic difference in sample morphology from (A)-(D) compared with (E) and (F). The co-crystal is stable in (A)-(D), but starts to change phase at 160 K (not pictured), through 185 K.

4.3.3. Experiment 3

We also observe the 1.676 µm band in the third C_2H_2-CH_3CN experiment (Figure 10). This band first appears at 150 K upon cooling and changes reflectance based on temperature and C_2H_2 phase. The $v_1 + v_3$ mode is a single band from 150 K to 93 K, which differs from pure C_2H_2 (a quadruplet band). The $v_1 + v_3$ mode preserves the feature at 1.551 µm while the broad doublet at 1.521/1.529 µm persists, which is also unlike pure C_2H_2. As with the second experiment, we observe the same unique splitting of the $5v_4 + 3v_5$ vibrational mode into three bands (1.925, 1.929, and 1.932 µm) upon cooling, which persist from 101 K until the sample reaches 171 K (Figure 10). The bands revert to a doublet at 1.926 and 1.931 µm when warmed to 171 K.

Optical views of the sample (Figure 11) show that the sample maintains overall morphology throughout the experiment. We observe slight changes, such as an increase in solid clusters of the sample when panel (A) is compared with panel (D).

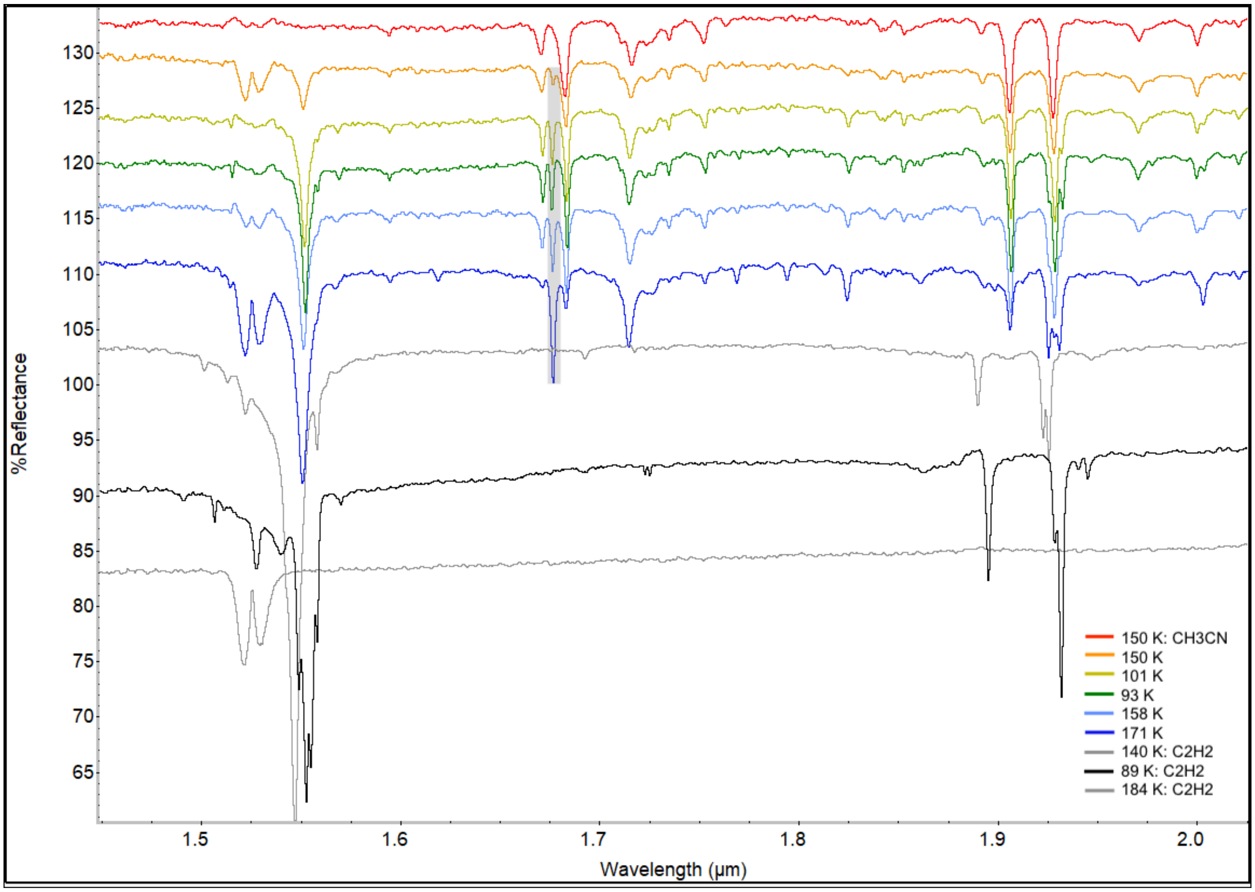

Figure 10. FTIR spectrum from the third CH_4-CH_3CN experiment showing pure CH_3CN from this experiment in red and pure C_2H_2 spectra in black and gray (From Chapter 2; Czaplinski et al., 2020) on the bottom; see Figure legend. Experimental time increases from top to bottom. Y-axis is offset for clarity. Notice the appearance of the 1.676 µm band (highlighted by gray box) in the 150 K spectrum, indicating formation of the co-crystal upon cooling. The reflectance of this feature increases as the sample is warmed. The C_2H_2 $v_1 + v_3$ vibrational mode (1.552 µm) maintains the cubic structure in warmer temperatures, just as in the second experiment.

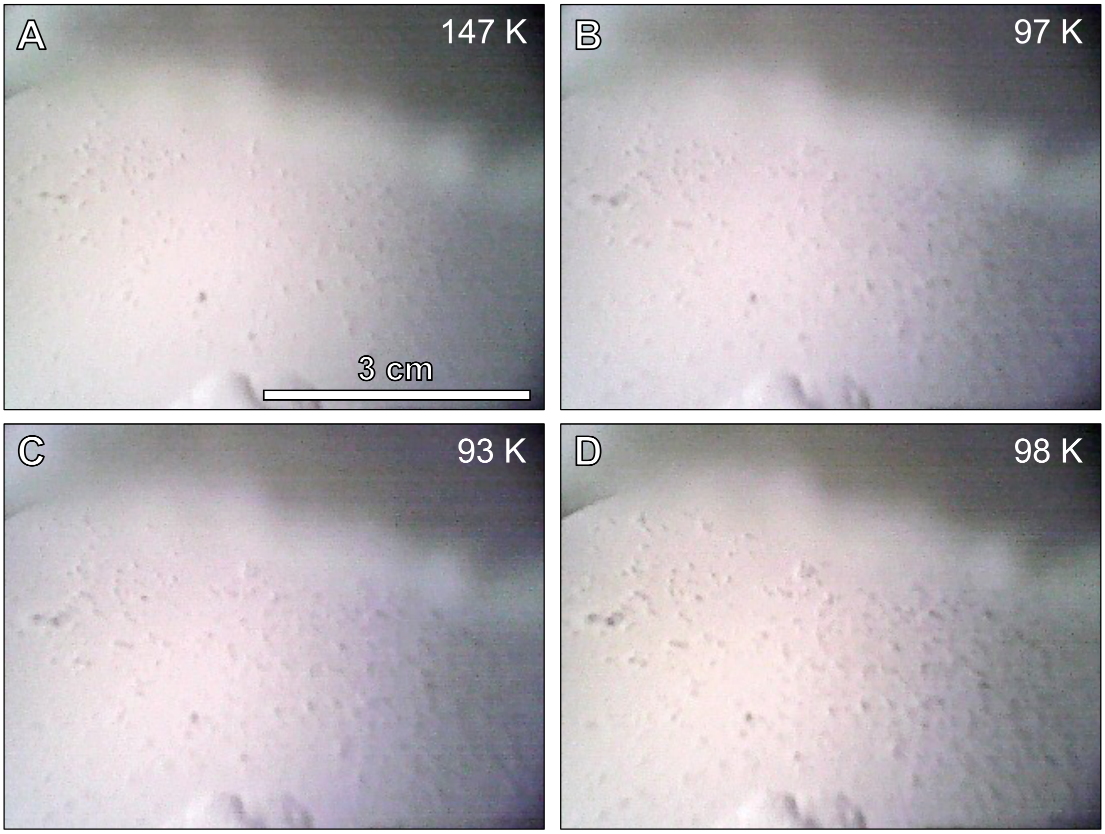

Figure 11. Top-down view of the third C_2H_2-CH_3CN mixture in the sample dish. Note how the sample morphology maintains consistency even though the temperature was cooled from 147 K to 93 K (A)-(C). We observe an increase in solid particles on the dish from (A) to (D).

Band depth measurements of the 1.676 μm co-crystal feature from all three co-crystal experiments are displayed in Figure 12. The color of each datapoint corresponds to the temperature of the sample at the corresponding time. Experiment 1 shows lower relative reflectance values on average when compared with experiments 2 and 3 (Figure 12). We infer that this is due to the lower concentrations of C_2H_2 and CH_3CN, therefore less volume of the co-crystal was formed in experiment 1. Experiments 2 and 3 show the same general shape from the beginning of the experiment to ~220 minutes, after which, the band depths in experiment 2 sharply decrease to zero by the end of the experiment, whereas the band depths in experiment 3 continue to increase.

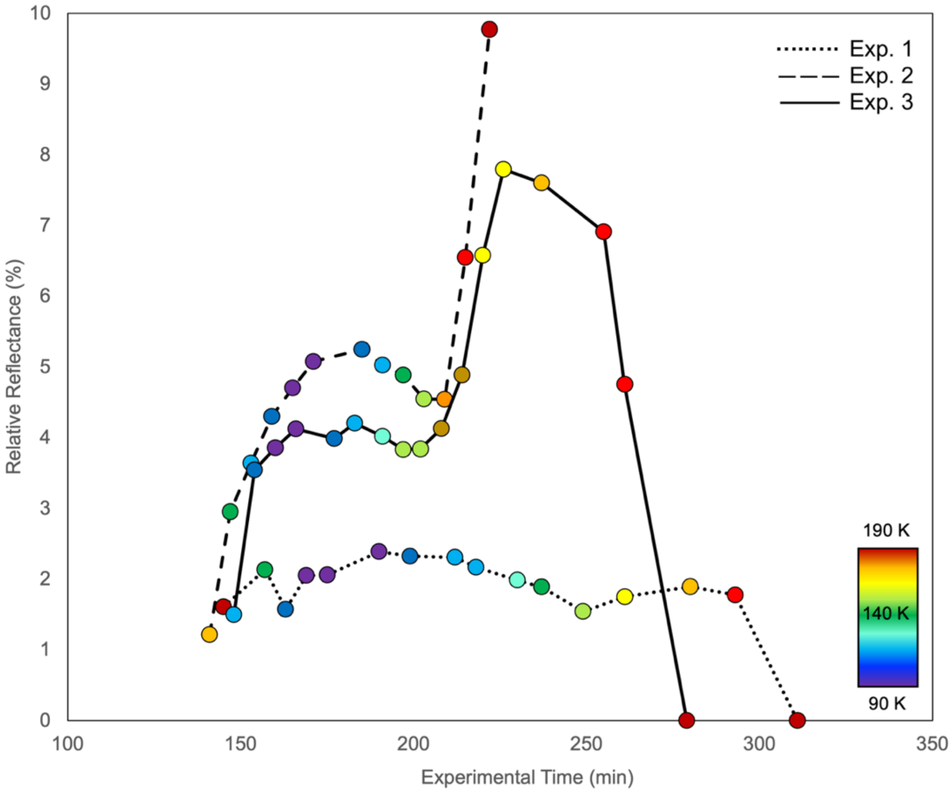

Figure 12. Band depths of the 1.676 μm feature from all three co-crystal experiments as a function of experimental time and temperature. Band depths in experiment 1 are lower in relative reflectance on average, due to the lower amount of C_2H_2 in the sample. The average band depth does not change drastically with temperature in experiment 1. Band depths in experiment 2 increase as the sample is warmed to 165 K, then decrease to zero. Experiment 3 has almost an identical line shape to experiment 2 until ~200 minutes, after which the band depths continue to increase as temperature increases to 171 K.

5. Discussion

We observe the persistence of the 1.666 μm CH_4 band in the CH_4-C_2H_2 experiment. Although difficult to determine using solely FTIR data, we assume that this band represents some residual CH_4 that remains in contact with the CH_3CN evaporite layer. This band was first reported in our previous studies with ethylene (C_2H_4) and CH_4 (Czaplinski et al., 2019; Chapter 1), and is even present when the temperature of the sample is above the boiling point of CH_4. Further, it is possible that a residual amount of CH_4 gas remained above the sample dish after the liquid CH_4 evaporated (i.e., CH_4 fog), as the 1.666 μm band aligns with CH_4 gas. Compounds have different spectra depending on if they are in a gas, liquid, or solid phase, due to a decrease in molecular motion at lower temperatures (Harris and Bertolucci, 1978; Abramczyk and Paradowska-Moszkowska, 2001). This could be determined in future experiments by positioning a gas analyzer above the sample to detect any trace amounts of CH_4 that remains above the sample, for example.

Based on when the 1.676 μm feature appeared, the C_2H_2-CH_3CN co-crystal formed between 174 K and 118 K during our experiments. In general, the 1.676 μm band increases as the sample temperature increases, to a certain point (Figure 12). Because the $v_1 + v_3$ vibration mode preserves the 1.551 μm feature beyond the boiling point of C_2H_2, and the $v_1 + v_3$ mode shows differences at Titan temperatures when compared with pure C_2H_2 (i.e., a single band in the co-crystal spectrum compared with a quadruplet in C_2H_2), this leads us to consider that phase trapping may have occurred in these experiments. For reference, both C_2H_2 and CH_3CN have two solid phases below their melting points (193 K and 230 K, respectively), which are both temperature dependent. In C_2H_2, the high temperature cubic phase is stable from 133 to 193 K, while the low temperature orthorhombic phase exists below 133 K (Sugawara et al., 1952; Bottger et al., 1964; van Nes et al., 1979). For CH_3CN, the high temperature monoclinic phase is stable from 217 to 230 K, while the low temperature orthorhombic phase is stable below 217 K. Recent experiments have indicated that the high temperature monoclinic phase of CH_3CN can be trapped when rapidly cooled to Titan conditions (Choi et al., 2020). Based on this information and the results from the co-crystal experiments reported herein, we believe that the warmer cubic phase of C_2H_2 has been trapped at cooler temperatures, because all three co-crystal experiments show only a single band centered at 1.551μm ($v_1 + v_3$ mode), as opposed to the typical orthorhombic phase of pure C_2H_2 at these temperatures, which has four distinct bands (e.g., Czaplinski et al., 2020).

The splitting of the C_2H_2 $5\nu_4 + 3\nu_5$ mode into three distinct bands upon cooling was observed in both the second and third co-crystal experiments. This splitting may be due to alterations of lattice parameters and symmetry of the crystal structure of CH_3CN (Ennis et al., 2017). For example, broadening and merging of peaks causes a loss of band structure, sometimes indicating a transition to a more amorphous solid (Ennis et al., 2017). This theory is supported with the data from the second and third co-crystal experiments, where the $5\nu_4 + 3\nu_5$ mode transitions from a sharp, triplet band at the coldest temperatures (101 K and 93 K, experiments 1 and 2, respectively) to a broad, wide band (~150 K), and ultimately changes to a doublet at 171 K (both experiments).

A previous study on the C_2H_2-CH_3CN co-crystal by Cable et al. (2020) reported differences in band positions between the co-crystal and the pure compounds using Raman spectroscopy. The authors observed red and blue shifts up to 9.3 cm^{-1} in most prominent vibrational modes (Cable et al., 2020). Here, we report the most significant shifts, in the $5\nu_4 + 3\nu_5$ vibrational mode, in association with the splitting of that band into a triplet of three separate bands. Table 2 outlines these shifts, which range from a blue shift of 0.1 cm^{-1} to a red shift of 3.3 cm^{-1} (values are reported in cm^{-1} for easier comparison to the values reported in the literature). These band shifts are similar in magnitude to those reported in previous studies for the same type of experiment (Cable et al., 2020), as well as additional Titan-relevant co-crystal studies (Vu et al., 2014; Cable et al., 2018; Cable et al., 2019; Czaplinski et al., 2020).

Table 2. Band centers from pure CH_3CN (orthorhombic) and C_2H_2 (cubic and orthorhombic) compared with co-crystal band shifts.

		Band Center (cm^{-1})			
Experiment	Vibrational Mode Assignment	Pure CH_3CN	Pure C_2H_2	Co-crystal	$\Delta\nu$ between pure and co-crystal
1	$5\nu_4 + 3\nu_5$ (band 1)		5193.6	5193.8	0.2
	$5\nu_4 + 3\nu_5$ (band 2)	5189.6			
	$5\nu_4 + 3\nu_5$ (band 3)		5176.8	5174.6	-2.2
2	$5\nu_4 + 3\nu_5$ (band 1)		5193.6	5193.7	0.1
	$5\nu_4 + 3\nu_5$ (band 2)	5188.2	5186.2	5184.9	-3.3
	$5\nu_4 + 3\nu_5$ (band 3)		5176.8	5177.2	0.4
3	$5\nu_4 + 3\nu_5$ (band 1)		5193.6	5193.6	0
	$5\nu_4 + 3\nu_5$ (band 2)	5188.0	5186.2	5184.8	-3.2
	$5\nu_4 + 3\nu_5$ (band 3)		5176.8	5174.5	-2.3

5.1. Relevance to Titan

Recent evaporite models predict that nitriles (in particular CH_3CN) have a good probability for contributing to Titan's evaporites. For example, lake-atmosphere equilibrium model by Cordier et al. (2009) shows that the composition of Titan's lakes contain minor compounds (solutes) much lower than 1%, including CH_3CN. The non-saturated lake mole fraction of CH_3CN was calculated to be 9.89×10^{-4} at the poles (90 K), in comparison with the saturated lake mole fractions of CH_4, 9.69×10^{-2}, and C_2H_6, 7.64×10^{-1} (Cordier et al., 2009). Additional work by Cordier and colleagues found that butane (C_4H_{10}) and C_2H_2 are most likely the main components of the external layers of Titan's evaporites (Cordier et al., 2009), and a further study speculates that less soluble compounds, such as CH_3CN may compose the layers immediately under the top layer of C_4H_{10}-C_2H_2 (Cordier et al., 2016). Furthermore, differences in the RADAR loss tangent (a quantifiable way to describe a dielectric material's inherent dissipation of electromagnetic energy) between Ligeia Mare (north pole) and Ontario Lacus (south pole), observed by Mastrogiuseppe et al. (2014) and Hayes et al. (2010), respectively, could be explained by the solvation of more absorbing compounds, such as nitriles (Mastrogiuseppe et al., 2014).

An unidentified absorption in the *Cassini* Visible and Infrared Mapping Spectrometer (VIMS) 5.01 μm window indicates a yet-to-be-identified compound on Titan's surface. A study by Clark et al. (2010) claimed that solid CH_3CN may be a candidate for this 5.01 μm feature. By studying the infrared spectrum of solid CH_3CN (80 K) in the 5.01 μm window, the authors concluded that CH_3CN has the best match in spectral shape and position to the 5.01 μm feature out of any organic compound measured in reflectance, however it was still not a perfect match (Clark et al., 2010). These imperfections could be due to temperature differences between the lab measured CH_3CN (80 K) and Titan's surface temperature near the equator (~94 K; used to compare to the CH_3CN spectrum), which may result in slight red or blue shifting of bands. VIMS identified the 5.01 μm feature in several "dark" areas on Titan's surface near the equator (58°W, 8°S), so CH_3CN may preferentially accumulate in the dark terrain, implying that liquid may have once existed there (or may still exist today), if the CH_3CN is in the form of an evaporite. The future Titan rotorcraft lander, *Dragonfly*, may be able to investigate the dark terrain, as its current proposed landing site will be in the interdune material near Selk Crater (199°W, 7°N; Lorenz et al., 2020).

6. Conclusions

In summary, we report experimental results on three types of experiments with acetonitrile: C_2H_6-CH_3CN, CH_4-CH_3CN, and the C_2H_2-CH_3CN co-crystal. The main points from each experiment are summarized as follows:

- C_2H_6-CH_3CN: C_2H_6 remained in the liquid phase, as expected, and the sample was stable throughout the experiment. No significant changes to the spectra were observed.

- CH_4-CH_3CN: CH_4 evaporated throughout the experiment, forming the CH_3CN evaporite. However, a CH_4 band at 1.666 μm remained present in the spectra after CH_4 band depths indicate complete evaporation. We interpret this as leftover CH_4 gas being in contact with the evaporite layer.
- C_2H_2-CH_3CN co-crystal: The co-crystal formed in all three experiments, as evidenced by a unique band at 1.676 μm. In general, this band increases band depth throughout experiments. Band splitting and shifting is observed in the C_2H_2 $5v_4 + 3v_5$ vibrational mode (~1.93 μm), which is indicative of changes to the crystal structure of the sample. We observed differences in the C_2H_2 $v_1 + v_3$ vibrational mode (1.55 μm) of the co-crystal compared to this mode in pure C_2H_2, which may be related to the phase trapping nature of CH_3CN. Optical images of the sample confirm the observed phase changes by showing drastic differences in morphology between colder and warmer temperatures.

The results from this study are relevant to the *Dragonfly* mission (a rotorcraft lander) to Titan, which will study the surface up close in the 2030's. Because signatures of CH_3CN have been implied to exist in dark terrains near Titan's equatorial dune belt, it is very likely that *Dragonfly* will have the opportunity to investigate or sample these materials up close for the first time to confirm these types of measurements made in the laboratory.

7. Acknowledgements

This work was supported by NASA Headquarters under the NASA Earth and Space Science Fellowship Program – Grant #80NSSC17K0603. We would also like to thank Woodrow Gilbertson for assistance with mol fraction calculations, Walter Graupner for assistance in the lab, and Troy Williams for support with experiments.

8. References

Abramczyk, H., Paradowska-Moszkowska, K., 2001. The correlation between the phase transitions and vibrational properties by Raman spectroscopy : liquid-solid B and solid B-solid a acetonitrile transitions. Chem. Phys. 265, 177–191. https://doi.org/https://doi.org/10.1016/S0301-0104(01)00271-3

Beć, K.B., Karczmit, D., Kwaśniewicz, M., Ozaki, Y., Czarnecki, M.A., 2019. Overtones of νC ≡ N Vibration as a Probe of Structure of Liquid CH3CN, CD3CN, and CCl3CN: Combined Infrared, Near-Infrared, and Raman Spectroscopic Studies with Anharmonic Density Functional Theory Calculations. J. Phys. Chem. A 123, 4431–4442. https://doi.org/10.1021/acs.jpca.9b02170

Bézard, B., Marten, A., G, P., 1993. Detection of Acetonitrile on TItan, in: Proceedings of the AAS/Division for Planetary Sciences Meeting Abstracts #25. Bulletin of the American Astronomical Society 25. p. 25.09.

Bottger, G.L., Eggers, D.F., 1964. Infrared Spectra of Crystalline C2H2, C2HD, and C2D2. J. Chem. Phys. 40, 2010–2017.

Cable, M.L., Vu, T.H., Malaska, M.J., Maynard-casely, H.E., Choukroun, M., Hodyss, R., 2020. Properties and Behavior of the Acetonitrile − Acetylene Co-Crystal under Titan Surface Conditions. https://doi.org/10.1021/acsearthspacechem.0c00129

Cable, M.L., Vu, T.H., Malaska, M.J., Maynard-casely, H.E., Choukroun, M., Hodyss, R., 2019. A Co-Crystal between Acetylene and Butane: A Potentially Ubiquitous Molecular Mineral on Titan. ACS Earth Sp. Chem. 3, 2808–2815. https://doi.org/10.1021/acsearthspacechem.9b00275

Cable, M.L., Vu, T.H., Maynard-Casely, H.E., Choukroun, M., Hodyss, R., 2018. The Acetylene-Ammonia Co-crystal on Titan. ACS Earth Sp. Chem. 2, 366–375. https://doi.org/10.1021/acsearthspacechem.7b00135

Choi, K.Y., Duyker, S.G., Maynard-Casely, H.E., Kennedy, B.J., 2020. Phase Trapping in Acetonitrile, a Metastable Mineral for Saturn's Moon Titan. ACS Earth Sp. Chem. 4, 1324–1331. https://doi.org/10.1021/acsearthspacechem.0c00105

Clark, R.N., Curchin, J.M., Barnes, J.W., Jaumann, R., Soderblom, L., Cruikshank, D.P., Brown, R.H., Rodriguez, S., Lunine, J., Stephan, K., Hoefen, T.M., Le Mouélic, S., Sotin, C., Baines, K.H., Buratti, B.J., Nicholson, P.D., 2010. Detection and mapping of hydrocarbon deposits on Titan. J. Geophys. Res. E Planets 115. https://doi.org/10.1029/2009JE003369

Cordier, D., Cornet, T., Barnes, J.W., MacKenzie, S.M., Le Bahers, T., Nna-Mvondo, D., Rannou, P., Ferreira, A.G., 2016. Structure of Titan's evaporites. Icarus 270, 41–56. https://doi.org/10.1016/j.icarus.2015.12.034

Cordier, D., Mousis, O., Lunine, J.I., Lavvas, P., Vuitton, V., 2009. An estimate of the chemical composition of titan's lakes. Astrophys. J. 707, L128-131. https://doi.org/10.1088/0004-637X/707/2/L128

Corrales, L.R., Yi, T.D., Trumbo, S.K., Shalloway, D., Lunine, J.I., Usher, D.A., 2017. Acetonitrile cluster solvation in a cryogenic ethane-methane-propane liquid: Implications for Titan lake chemistry. J. Chem. Phys. 146, 104308. https://doi.org/10.1063/1.4978395

Czaplinski, E., Yu, X., Dzurilla, K., Chevrier, V., 2020. Experimental Investigation of the Acetylene–Benzene Cocrystal on Titan. Planet. Sci. J. 1, 16. https://doi.org/10.3847/PSJ/abbf57

Czaplinski, E.C., Gilbertson, W.A., Farnsworth, K.K., Chevrier, V.F., 2019. Experimental Study of Ethylene Evaporites under Titan Conditions. ACS Earth Sp. Chem. 3, 2353–2362. https://doi.org/10.1021/acsearthspacechem.9b00204

Ennis, C., Auchettl, R., Ruzi, M., Robertson, E.G., 2017. Infrared characterisation of acetonitrile and propionitrile aerosols under Titan's atmospheric conditions. Phys. Chem. Chem. Phys. 19, 2915–2925. https://doi.org/10.1039/C6CP08110J

Farnsworth, K., 2020. An Experimental Investigation of Liquid Hydrocarbons in a Simulated Titan Environment. University of Arkansas.

Friend, D.G., Ingham, H., Ely, J.F., 1991. Thermophysical Properties of Ethane. J. Phys. Chem. 20, 275–347.

Harris, D.C., Bertolucci, M.D., 1978. Symmetry and Spectroscopy. Oxford University Press, New York.

Hayes, A.G., Wolf, A.S., Aharonson, O., Zebker, H., Lorenz, R., Kirk, R.L., Paillou, P., Lunine, J., Wye, L., Callahan, P., Wall, S., Elachi, C., 2010. Bathymetry and absorptivity of Titan's Ontario Lacus. J. Geophys. Res. 115, E09009. https://doi.org/10.1029/2009JE003557

Krasnopolsky, V.A., 2009. A photochemical model of Titan's atmosphere and ionosphere. Icarus 201, 226–256. https://doi.org/10.1016/j.icarus.2008.12.038

Lorenz, R.D., Mackenzie, S.M., Neish, C.D., Gall, A. Le, Turtle, E.P., Barnes, J.W., Trainer, M.G., Werynski, A., Hedgepeth, J., Karkoschka, E., 2021. Selection and Characteristics of the Dragonfly Landing Site near Selk Crater, Titan. Planet. Sci. J. 2, 24. https://doi.org/10.3847/PSJ/abd08f

Marten, A., Hidayat, T., Biraud, Y., Moreno, R., 2002. New Millimeter Heterodyne Observations of Titan: Vertical Distributions of Nitriles HCN, HC3N , CH3CN , and the Isotopic Ratio 15N/14N in Its Atmosphere. Icarus 158, 532–544. https://doi.org/10.1006/icar.2002.6897

Mastrogiuseppe, M., Poggiali, V., Hayes, A., Lorenz, R., Lunine, J., Picardi, G., Seu, R., Flamini, E., Mitri, G., Notarnicola, C., Paillou, P., Zebker, H., 2014. The bathymetry of a

Titan sea. Geophys. Res. Lett. 41, 1432–1437. https://doi.org/10.1002/ 2013GL058618. Received

McConville, C.A., Tao, Y., Evans, H.A., Trump, B.A., Lefton, J.B., Xu, W., Yakovenko, A.A., Kraka, E., Brown, C.M., Ručevski, T., 2020. Peritectic Phase Transition of Benzene and Acetonitrile into a Cocrystal Relevant to Titan, Saturn's Moon. Chem. Commun. 56, 13520–13523. https://doi.org/10.1039/D0CC04999A

Molina-Cuberos, G.J., Schwingenschuh, K., López-Moreno, J., Rodrigo, R., Lara, L.M., Anicich, V., 2002. Nitriles produced by ion chemistry in the lower ionosphere of Titan. J. Geophys. Res. 107, 5099. https://doi.org/10.1029/2000JE001480

Sugawara, T., Kanda, E., 1952. The Crystal Structure of Acetylene. Sci. Reports Res. Institutes, Tohoku Univ. 4, 607–614.

Thelen, A.E., Nixon, C.A., Chanover, N.J., Cordiner, M.A., Molter, E.M., Teanby, N.A., Irwin, P.G.J., Serigano, J., Charnley, S.B., 2019. Abundance measurements of Titan's stratospheric HCN, HC3N, C3H4, and CH3CN from ALMA observations. Icarus 319, 417–432. https://doi.org/10.1016/j.icarus.2018.09.023

van Nes, G.J.H., van Bolhuis, F., 1979. Single-Crystal Structures and Electron Density Distributions of Ethane, Ethylene and Acetylene. II.* Single-Crystal X-ray Structure Determination of Acetylene at 141 K. Acta Crystallogr. 35, 2580–2593.

Vu, T.H., Cable, M.L., Choukroun, M., Hodyss, R., Beauchamp, P., 2014. Formation of a new benzene-ethane co-crystalline structure under cryogenic conditions. J. Phys. Chem. 118, 4087–4094. https://doi.org/10.1021/jp501698j

Vuitton, V., Yelle, R. V, Cui, J., 2008. Formation and distribution of benzene on Titan. J. Geophys. Res. 113, E05007. https://doi.org/10.1029/2007JE002997

Wasiak, F.C., Luspay-Kuti, A., Welivitiya, W.D.D.P., Roe, L.A., Chevrier, V.F., Blackburn, D.G., Cornet, T., 2013. A facility for simulating Titan's environment. Adv. Sp. Res. 51, 1213–1220. https://doi.org/10.1016/j.asr.2012.10.020

9. Appendix

Here, we provide mole fraction calculations for experiments in this chapter (Tables A1-A5). We used the same methods as described in Chapter 1, Section 3.3 Spectral Unmixing Model. We only include values for the corresponding spectra presented in this chapter.

Table A1. Mole fractions (%) from the CH_3CN-C_2H_6 experiment.

Spectrum	Temperature (K)	CH_3CN	C_2H_6
1	113.15	60.55	39.45
2	93.15	85.24	14.76
3	118.15	71.07	28.93
4	133.15	24.89	75.11
5	143.15	25.58	74.42

Table A2. Mole fractions (%) from the CH_3CN-CH_4 experiment.

Spectrum	Temperature (K)	CH_3CN	CH_4
1	102.15	100	0
2	98.15	62.47	37.53
3	94.15	63.32	36.68
4	98.15	72.91	27.09
5	98.15	99*	1*

* values approximated based on band depth calculations

Table A3. Mole fractions (%) from the first C_2H_2-CH_3CN experiment.

Spectrum	Temperature (K)	C_2H_2	CH_3CN
1	143.15	4.29	95.71
2	108.15	33.58	66.42
3	97.15	29.33	70.67
4	151.15	47.19	52.81
5	156.15	44.77	55.23
6	177.15	64.65	35.35
7	188.15	90.09	9.91

Table A4. Mole fractions (%) from the second C_2H_2-CH_3CN experiment.

Spectrum	Temperature (K)	C_2H_2	CH_3CN
1	155.15	8.78	91.22
2	101.15	35.88	64.12
3	145.15	24.98	75.02
4	151.15	37.99	62.01
5	157.15	32.77	67.23
6	171.15	76.24	23.76
7	186.15	67.8	32.2

Table A5. Mole fractions (%) from the third C_2H_2-CH_3CN experiment.

Spectrum	**Temperature (K)**	**C_2H_2**	**CH_3CN**
1	150.15	0	100
2	150.15	14.67	85.33
3	101.15	22.51	77.49
4	93.15	23.98	76.02
5	158.15	22.46	77.54
6	171.15	40.11	59.89

CHAPTER 4. BINARY COMPOUND EVAPORITES: STABILITY WITH LIQUID METHANE AND ETHANE UNDER TITAN CONDITIONS

Ellen Czaplinski and Vincent Chevrier

Arkansas Center for Space and Planetary Sciences, University of Arkansas, Fayetteville, AR 72701, USA

Keywords: evaporites, binary mixtures, NIR spectroscopy

Highlights:

- Spectral band shifts and splits when multiple evaporite species are involved
- Acetylene-acetonitrile co-crystal is stable after exposure to methane-ethane
- Morphology changes to the sample upon warming

1. Abstract

Models of Titan's evaporite composition predict multiple evaporite species may be present in the deposits. Because performing experiments with ten or more evaporite compounds is too complex for a single experiment, we present a series of binary evaporite studies that include two potential Titan-relevant evaporites (acetylene-ethylene and acetylene-acetonitrile) combined in methane-ethane solvents. We find that these mixtures produce interesting changes to the spectra and morphology of the sample upon warming/cooling the sample. In particular, the acetylene-acetonitrile co-crystal band depths show an inverse relationship with temperature when compared to the methane band at 1.666 μm. We also observe a unique trend with acetylene after methane evaporation. The results from these experiments have implications as to observations of Titan's evaporites from *Cassini* data, as well as what we might expect to observe in future missions to Titan's surface with the *Dragonfly* mission.

2. Introduction

On Titan, multiple hydrocarbon and/or nitrile species (on the order of 10 or more) may be dissolved in the methane/ethane-dominated, polar lakes and seas. As the liquid component (methane and/or ethane) evaporates, this may give the various species an opportunity to precipitate out of solution as evaporite deposits (Cordier et al., 2009; 2013; 2016). Although studying multiple (six or more) evaporite species (along with methane, ethane, and dissolved molecular nitrogen) is relatively accessible in a modeling framework, this process is too complex to be studied in a single experiment. Therefore, we present a simplified starting point towards studying these more complex mixtures within a laboratory framework; running experiments with two evaporite-relevant species in conjunction with the methane-ethane-nitrogen solvent (hereafter referred to as binary experiments). We acknowledge that this is a gross simplification of the probable processes occurring in Titan's lakes and seas, however the objective of studying these binary experiments is to identify which compound(s) consistently dominate the spectral signatures across experiments. For example, modeling of Titan's evaporite composition by Cordier et al. (2013, 2016) revealed that acetylene and butane consistently dominated the upper (surface) evaporites layer due to their high solubilities. Unsurprisingly, evaporite composition depends on the initial composition of dissolved liquids and the mole fraction at saturation of the solutes in solution (Cordier et al., 2013). Thus, species with the highest solubilities and mol fraction at saturation will remain dissolved in the liquid longer and ultimately dominate the composition of the final evaporite layer, while species with lower solubilities and mol fractions will be the first to precipitate out as evaporites (Cordier et al., 2013). A more recent study by Cable et al. (2019) confirmed the formation and presence of a co-crystal between acetylene and butane, providing further insight into the preferred existence and orientation of these two molecules in terms of Titan's evaporites. The same compounds that dominate the spectral signatures in these binary experiments may be expected to also dominate spectra involving more realistic, complex compositions of evaporites, especially when comparing molecules that are highly soluble in liquid methane/ethane (e.g., acetylene) to molecules that are barely soluble in these solvents (e.g., acetonitrile; Stevenson et al. 2015).

The previous chapters herein investigated single (C_2H_4), binary (C_2H_2-C_6H_6), and binary with methane and/or ethane (C_2H_2-CH_3CN-CH_4-/C_2H_6) evaporites. These studies introduced evaporite experiments and how to analyze the data for the simplest cases. In this chapter, we present two types of binary evaporite experiments with both methane and ethane: C_2H_2-C_2H_4-CH_4-C_2H_6 and C_2H_2-CH_3CN-CH_4-C_2H_6. By taking this binary approach, this work can be used to inform Cassini Visible and Infrared Mapping Spectrometer (VIMS) data analysis of which spectral features may dominate and be the most identifiable in a given evaporite spectrum (e.g., evaporites in the equatorial basins Tui and Hotei Regions; MacKenzie et al., 2014, 2016). Additionally, because these organic species reach solidification temperatures in Titan's atmosphere, they may form exotic organic snows, which have the opportunity to form new molecular minerals (i.e., co-crystals) or other crystalline solids (Cordier et al., 2016; Maynard-Casely et al., 2018). Thus, the binary experiments presented here are essential for understanding how evaporite molecules behave and evolve on a molecular level when existing together as a layer (or layers) of evaporites.

We began by testing C_2H_2-C_2H_4, two of the most simple hydrocarbon species on Titan (and relatively straightforward for testing in our laboratory setup). The C_2H_2-CH_3CN experiments were slightly more complicated due to the fact that CH_3CN is a liquid at SATP (described in detail below). Indeed, we presented an in-depth study of the C_2H_2-CH_3CN co-crystal in the previous chapter, however we sought to reevaluate the C_2H_2-CH_3CN co-crystal as a binary evaporite by testing the stability of the co-crystal after adding methane and ethane to the mixture.

3. Methods

In this set of experiments, we follow the same general experimental protocol, as described in section 2 General Methodology. Briefly, the chamber and condenser are purged with N_2 gas, then liquid nitrogen (LN_2) is flowed through the condenser and/or the temperature control box (TCB) to cool these portions of the chamber to Titan-relevant temperatures (89-94 K). When the condenser is at an appropriate temperature for condensation of the compounds being tested, the gaseous compounds (methane, ethane, ethylene) are individually added to the condenser and allowed to condense for ~5 minutes.

A different procedure (the "cold trap" method, described in section 2 General Methodology) is used for adding acetylene and acetonitrile to the TCB. Because acetylene's liquid phase has a relatively small temperature range (189 to 193 K), this makes it extremely difficult to add acetylene to the condenser in the same way as the other gases (described above). Therefore, we use the cold trap method here, which means the condenser LN_2 is restricted from flowing at the beginning of the experiment, while LN_2 flows to the TCB as normal. When the temperature of the sample dish reaches ~150 K (significantly below acetylene's melting point of 189 K), acetylene flows through the condenser while the solenoid valve is open, which allows acetylene to deposit (phase change from gas to solid) onto the sample dish relatively easily. We also use the cold trap method for acetonitrile, however since acetonitrile is a liquid at SATP, we must utilize an Erlenmeyer flask filled with 100 mL of acetonitrile (connected to both the N_2 cylinder and the exhaust/condenser interchangeable connections on the chamber exterior) inside of a custom built glove box (for safety because acetonitrile vaporizes quickly and is toxic upon inhalation). N_2 is bubbled through the flask while the exhaust valve connection to the flask remains open, allowing the flowing N_2 gas in the flask to become saturated with acetonitrile (~10-15 minutes). Next, the exhaust valve is closed at the same time that the condenser valve is opened (with solenoid valve already open), allowing the acetonitrile-nitrogen mixture to pass directly through the approximately room temperature condenser and deposit onto the sample dish (~193 K).

From this point, we initiate LN_2 flow to the condenser, and cool the TCB to Titan-relevant surface temperatures while collecting FTIR spectra. LN_2 flow to the TCB is either decreased or increased in order to warm or cool the temperature of the sample. Warming the sample speeds up evaporation of the liquid (methane and ethane), and also allows us to characterize the phase change of acetylene (cubic to orthorhombic phase transition at 135 K).

We would like to note that in these experiments, the solid species are deposited first, followed by condensation of the liquid (methane and ethane) on top of the solid component. This represents a scenario not unlike that which is speculated to occur on Titan, where there is a wet period followed by a dry period. Specifically, the wet period is characterized by methane and/or ethane rains dissolving solid organics on the ground and filling topographical depressions (i.e., lakes), whereas the dry period is characterized by the liquid component evaporating and producing the evaporites (Cordier et al., 2016). Thus, the precipitation/deposition of solid organics is assumed to have taken place prior to the wet period.

4. Results

Two general categories of binary evaporite experiments were performed: acetylene-ethylene and acetylene-acetonitrile. Within each category, the stability of the binary evaporite compounds after liquid methane and/or ethane were added to the sample dish was tested. A summary of all experiments are reported in Table 1.

4.1. C_2H_2-C_2H_4 Binary Experiments

4.1.1. Experiment 1: C_2H_2-C_2H_4-CH_4

In the C_2H_2-C_2H_4-CH_4 experiment, C_2H_2 was first added to the sample dish following the cold trap method described in the Methods section, then C_2H_4 and CH_4 were sequentially condensed at ~137 K and ~100 K, respectively. After all species were added to the sample dish, Titan surface temperatures (89-94 K) were maintained in the TCB for 165 minutes, after which the LN_2 was turned off to observe the sample as temperatures increased. Figure 1 shows the spectra from this experiment. When the sample is warmer (128 K and 108 K), we observe an additional band on the left portion of the 1.55 µm C_2H_2 band ($v_1 + v_3$ vibrational mode) at 1.542 µm. This is not observed in pure C_2H_2 spectra.

In general, the C_2H_4 bands have a comparable band depth than the C_2H_2 bands (Figure 2; 13% compared to 12%, respectively), and these band depths do not vary drastically when temperature is altered. The band depth of the CH_4 band (1.666 µm) starts at ~0.7% and decreases to zero by the end of the experiment, confirming complete CH_4 evaporation. This 1.666 µm band is relatively small (less reflective) compared to the other bands in this study, however, it is the only measurable CH_4 band in these binary experiments, because the CH_4 triplet bands (1.669, 1.723, 1.796 µm) are overlapped by both C_2H_6 and C_2H_4 bands.

Optical views of the sample (Figures 3 and 4) show a difference in sample brightness and texture between warmer (~140 K) and cooler (~90 K) temperatures. At warmer temperatures, one can observe the light from the lightbulb reflecting off the liquid portion of the sample. In the last panel on each figure (Figures 3(F) and 4(F)), new crystals can be seen spread across the camera view. We interpret these crystals to be excess sample that originated from the filter (just outside of view from the camera panels), based on additional camera views not included in Figures 3-4. Notice the larger crystal size of the sample in this instance (146 K, end of experiment after CH_4 evaporation), and "fluffy," snow-like texture. Observations of view 2 (Figure 4(F)) show that the snow-like crystals originate at the perimeter of the sample dish (upper half of figure panel), but are also observed from the solid sample collapsing onto the center of the dish (lower right portion of figure panels in view 2).

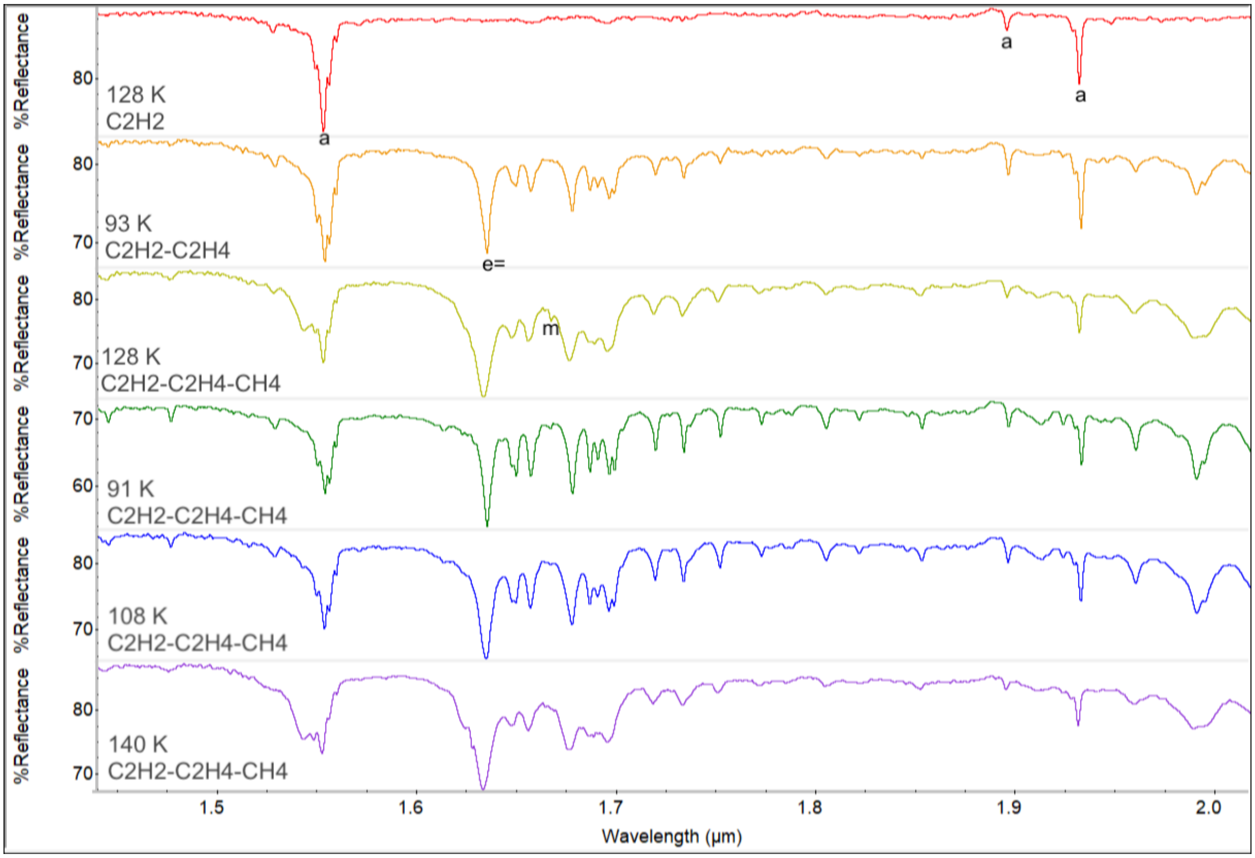

Figure 1. FTIR spectra from the C_2H_2-C_2H_4-CH_4 experiment from 91 K to 140 K. Experimental time increases from top to bottom. C_2H_2 bands are labeled with "a", the C_2H_4 band is labeled with "e=" (to denote the double bond), and the CH_4 band is labeled with "m." Note that the bands are only labeled on the spectrum where the compound is first introduced to avoid clutter, however, one can observe each of these bands in the additional spectra from the experiment. Notice the broad shoulder of the C_2H_2 $\nu_1 + \nu_3$ vibrational mode (1.55 µm region) that is only observed in warmer spectra (128 K and 140 K).

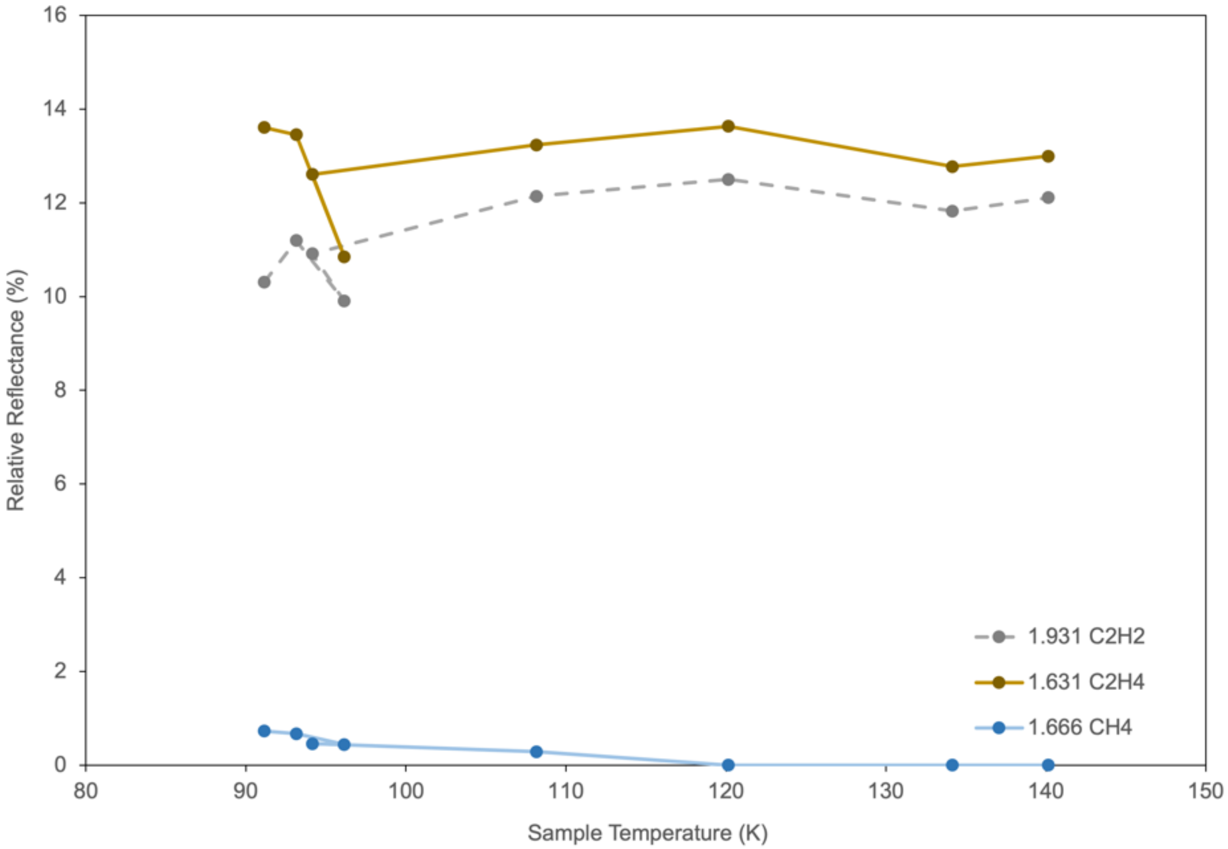

Figure 2. Band depths from the C_2H_2-C_2H_4-CH_4 experiment. Here, we only show band depths after all three species were added to the sample dish, which corresponds to when the sample was warmed from 91 K to 140 K over a period of 80 minutes. C_2H_2 and C_2H_4 bands stay relatively constant over this temperature range, and the CH_4 bands decrease to 0% due to evaporation.

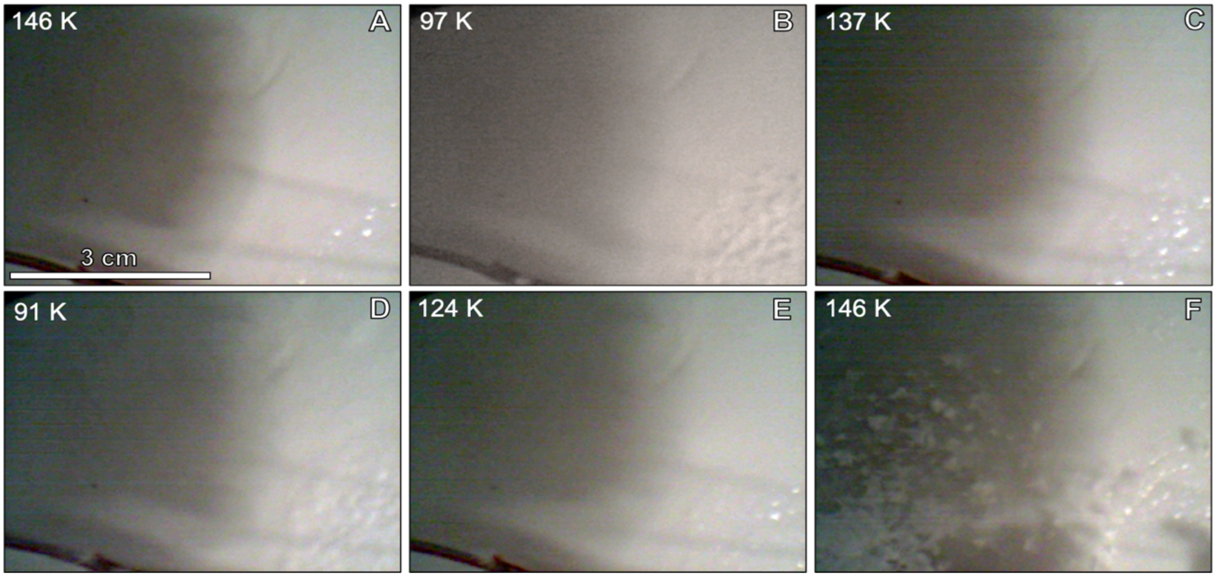

Figure 3. Top-down view of the C_2H_2-C_2H_4-CH_4 mixture in the sample dish (view 1). The sample underwent a warming and cooling cycle, as denoted by the temperatures. The black line in the bottom-left is a portion of the filter, which is attached directly beneath the condenser. The shadow of the filter can be seen covering the left half of each panel. The lower-right corner of each panel is where the sample exits the bottom of the filter. Notice the reflected light from the lightbulb that is seen in panels (A), (C), and (E; when the sample is warmer). Part of the frozen sample can be observed in (F), after part of the sample had fallen from the filter onto the dish (see explanation in text).

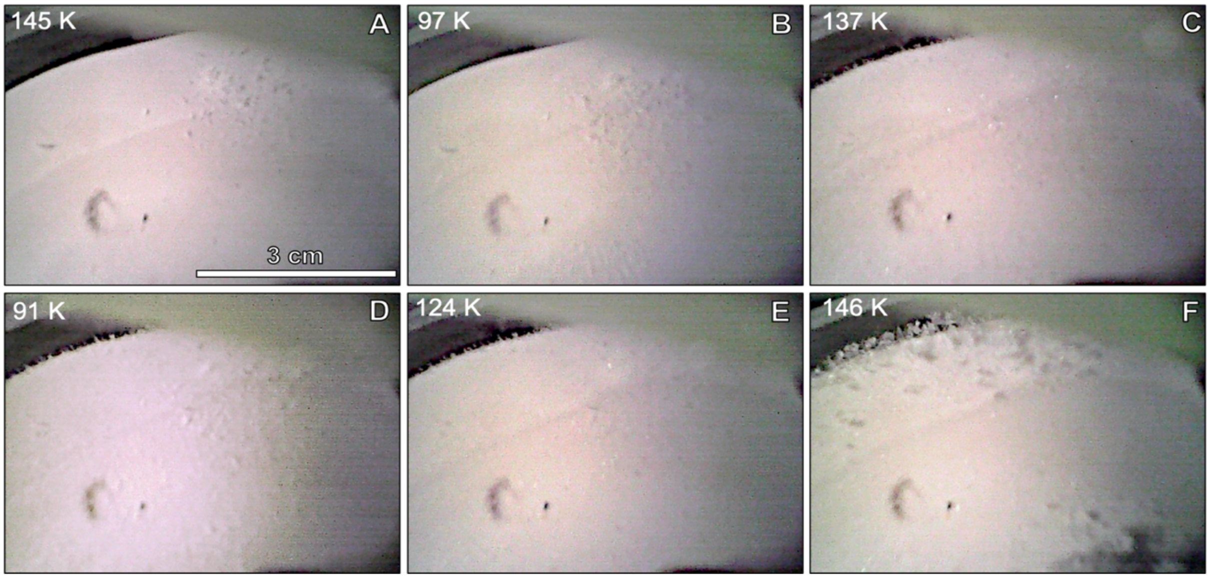

Figure 4. Top-down view of the C_2H_2-C_2H_4-CH_4 mixture in the sample dish (view 2). Temperatures correspond to those shown in Figure 3. The lower-right corner of each panel is where the sample exits the bottom of the filter. Notice the boundary in the upper part of each image that separates the dark and light portion of the Spectralon; this boundary corresponds to the extent of the liquid CH_4 pour. In panel (F), the crystallized sample can be observed.

4.1.2. Experiment 2: C_2H_2-C_2H_4-C_2H_6

In the C_2H_2-C_2H_4-C_2H_6 experiment, C_2H_2 was first added to the sample dish following the cold trap method, then C_2H_4 and C_2H_6 were sequentially condensed at ~126 K and 104 K, respectively. FTIR spectra from this experiment are shown in Figure 5. After all species were added to the sample dish, we subjected the sample to a warming phase, followed by a cooling phase, the purpose of which is to increase the rate of any C_2H_6 evaporation that may occur. This is important for these types of experiments, as we are more concerned with the evaporite species, as opposed to the liquid portion of the sample (CH_4/C_2H_6). Nonetheless, the combined spectra is a good representation of which species are more dominant when liquid remains. The spectra shows splitting of C_2H_6 bands at 1.688 μm and 1.697 μm at 123 K and 92 K, as well as a more broad shape of these bands at 98 K (Fig. 5), which is different from pure C_2H_6. We do not observe the C_2H_2 shoulder at 1.542 μm, as we did in the previous experiment.

C_2H_2 and C_2H_4 have comparable band depths (Figure 6) which have a twofold increase from ~6% at 105 K to ~12% at 92 K. C_2H_6 band depths increase slightly as temperature decreases (~1% at 105 K to ~3% at 92 K). These increases are expected, as in previous studies, the increase is most likely due to changes in grain size and reflectance as temperature decreases.

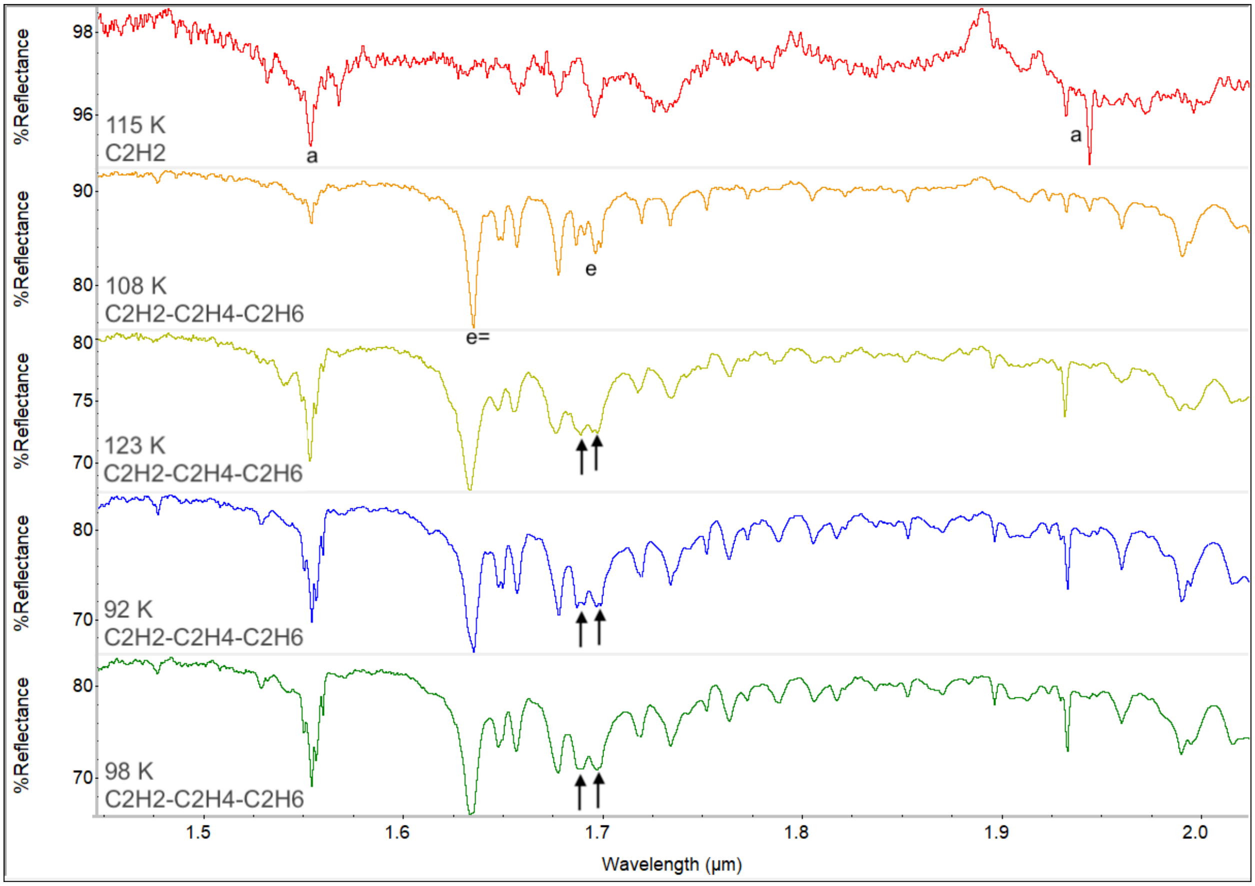

Figure 5. FTIR spectra from the C_2H_2-C_2H_4-C_2H_6 experiment from 92 K to 123 K. Experimental time increases from top to bottom. C_2H_2 bands are labeled with “a”, the C_2H_4 band is labeled with “e=”, and C_2H_6 bands are labeled with “e.” Note that the bands are only labeled on the spectrum where the compound is first introduced, to avoid clutter, however, one can observe each of these bands in the additional spectra from the experiment. Notice the splitting of the C_2H_6 doublet (1.688 µm and 1.697 µm) at 123 K, which is preserved until the final spectrum at 98 K. This splitting of the C_2H_6 doublet results in wider bands by the end of the experiment.

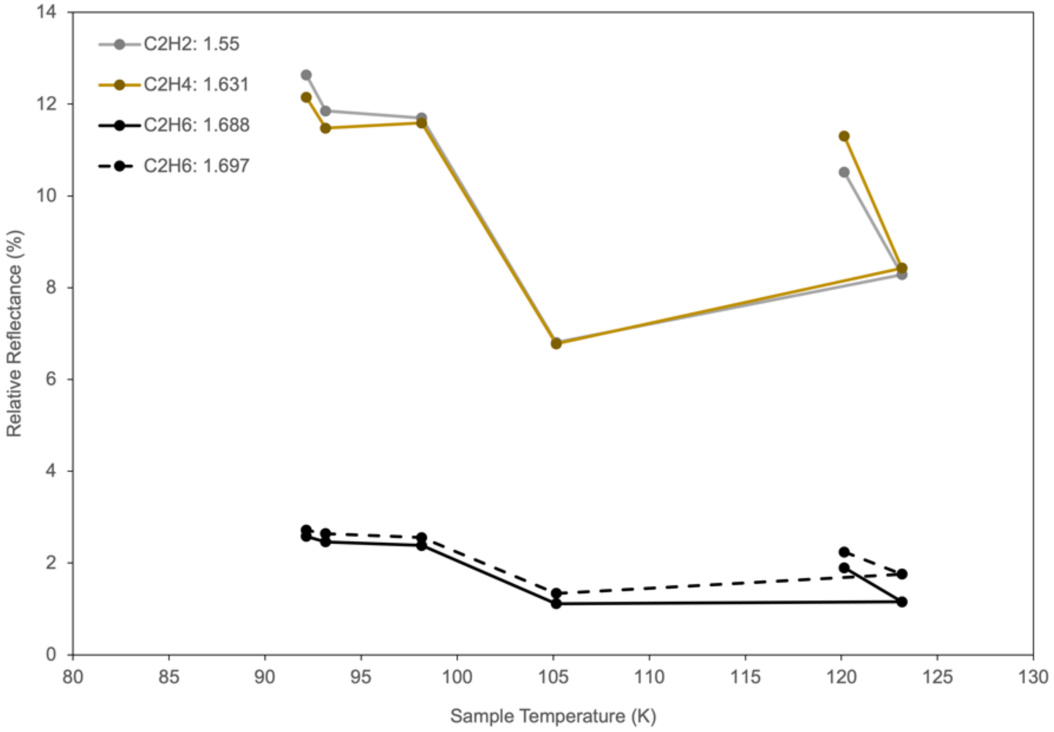

Figure 6. Band depths from the C_2H_2-C_2H_4-C_2H_6 experiment. Here we show band depths after all three species were added to the sample dish, which corresponds to when the sample was cooled from 120 K to 92 K over a period of 41 minutes. C_2H_2 and C_2H_4 bands increase as temperature decreases, as expected. C_2H_6 bands also increase slightly with decreasing temperature.

4.1.3. Experiment 3: C_2H_2-C_2H_4-CH_4-C_2H_6

In the C_2H_2-C_2H_4-CH_4-C_2H_6 experiment, C_2H_2 was added to the sample dish using the cold trap method, then C_2H_6 was condensed at 112 K and CH_4 and C_2H_4 were co-condensed at ~104 K. FTIR spectra from this experiment are shown in Figure 7. Notice how at 159 K, C_2H_2 bands are no longer present. This is confirmed by the band depth (Figure 8), which shows a drastic decrease in C_2H_2 bands from ~7% to 0% in less than 10 K. Interestingly, this decrease in the C_2H_2 band corresponds with the CH_4 band (1.666 μm) also disappearing. By the last spectrum, the 1.666 μm band decreases from ~1% at 90 K to 0% at 150 K. In the last hour of the experiment, the C_2H_4 band (1.631μm) decreases from ~5% at 132 K to 3% at 159 K, whereas the C_2H_6 band (1.688 μm) decreases from 2.7% at 132 K to 1.6% at 159 K (Figure 8).

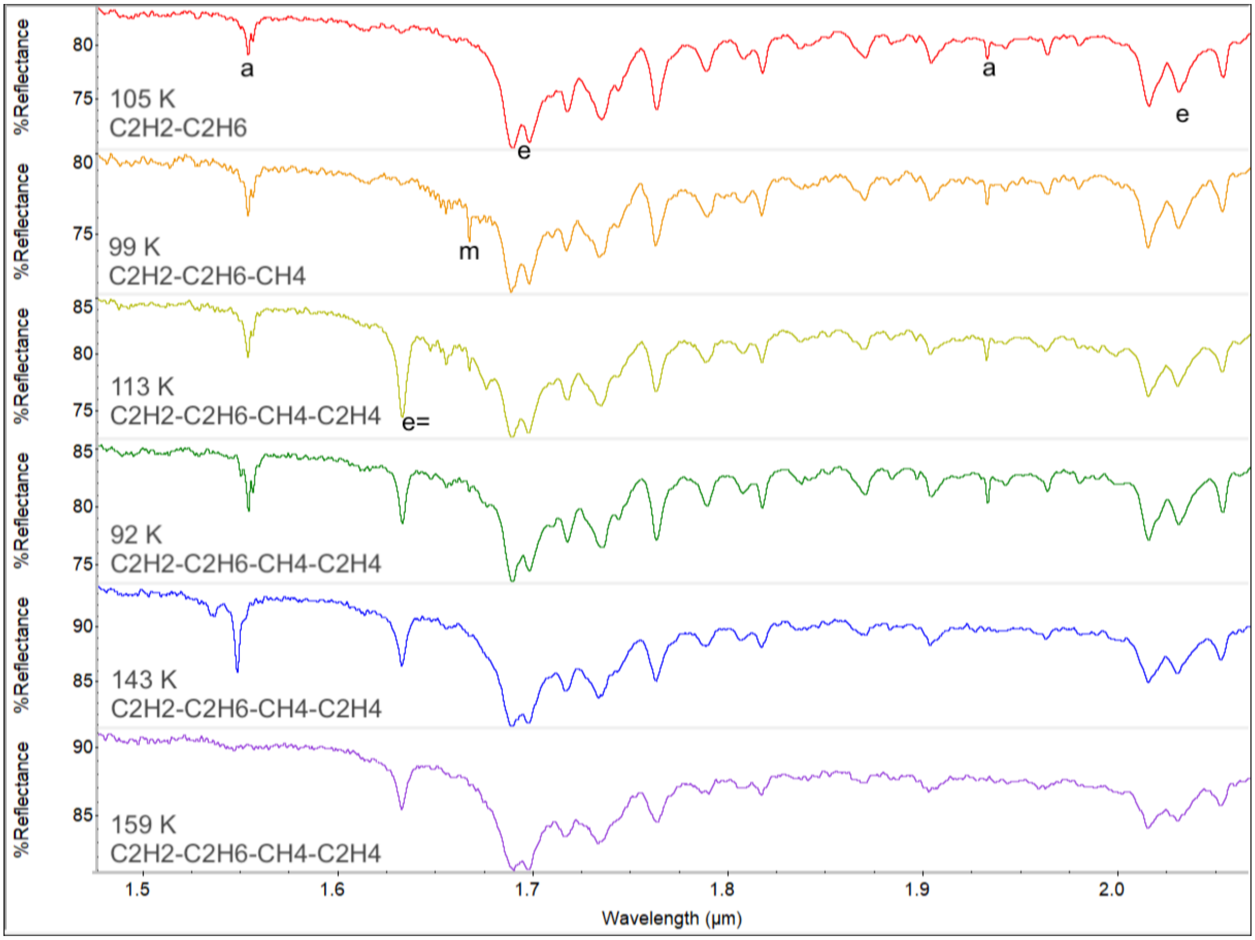

Figure 7. FTIR spectra from the C_2H_2-C_2H_4-C_2H_6-CH_4 experiment from 92 K to 159 K. Experimental time increases from top to bottom. C_2H_2 bands are labeled with "a", the C_2H_4 band is labeled with "e=", C_2H_6 bands are labeled with "e", and the CH_4 band is labeled with "m." Note that the bands are only labeled on the spectrum where the compound is first introduced, to avoid clutter, however, one can observe each of these bands in the additional spectra from the experiment. Notice the increase in C_2H_2 reflectance until the 143 K spectrum, after which it disappears (along with the CH_4 band at 1.666 µm). C_2H_2 bands are more reflective than C_2H_4 bands throughout the experiment.

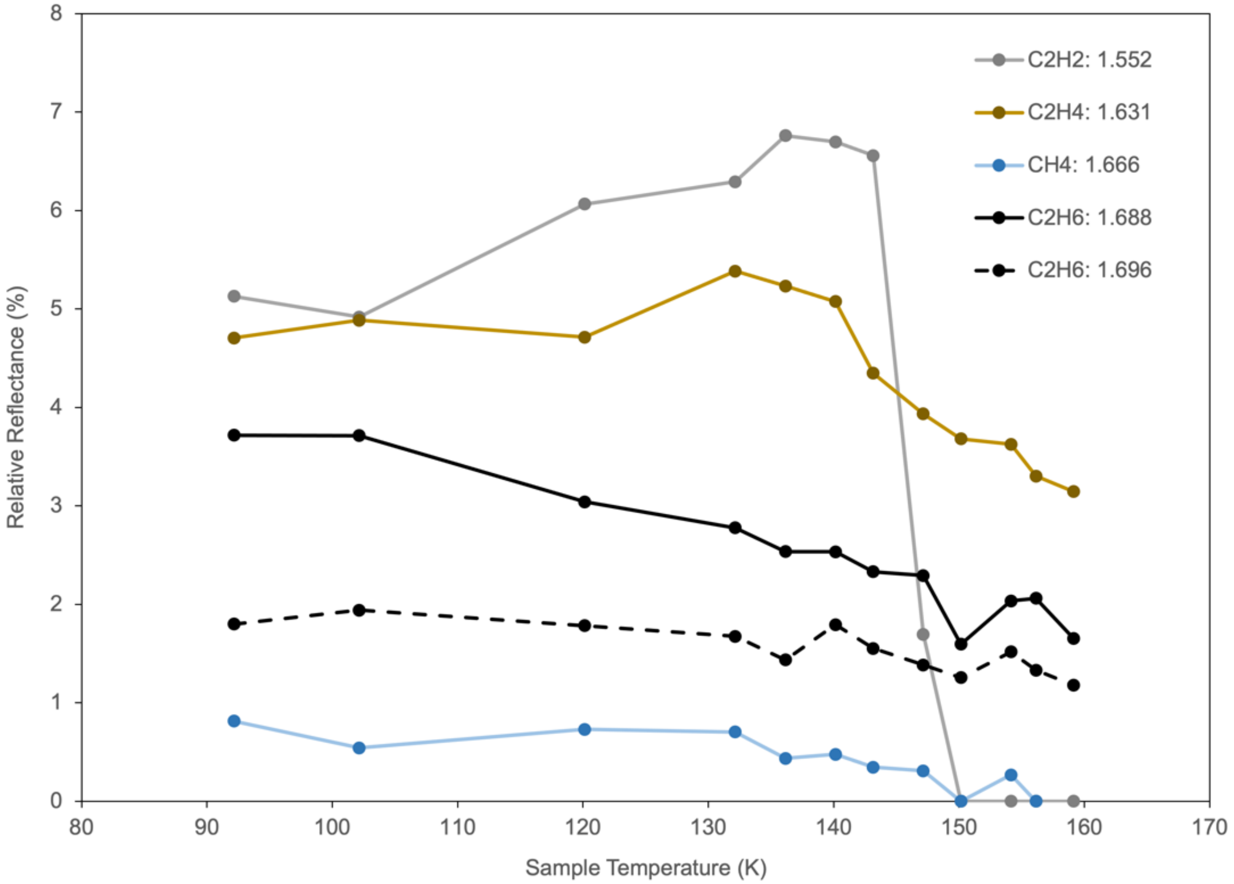

Figure 8. Band depths from the C_2H_2-C_2H_4-C_2H_6-CH_4 experiment. Here we show band depths after all four species were added to the sample dish, which corresponds to when the sample was warmed from 92 K to 159 K over a period of 57 minutes. C_2H_2 and C_2H_4 bands increase as temperature increases to ~140 minutes, after which both species' band depths decrease sharply. C_2H_2 band depths decrease to 0% at the same temperature that CH_4 band depths decrease to 0%. C_2H_6 band depths gradually decrease over the course of the warming period.

4.2. C_2H_2-CH_3CN Binary Experiments

4.2.1. Experiment 4: C_2H_2-CH_3CN-CH_4

In the C_2H_2-CH_3CN-CH_4 experiment, CH_3CN was added to the sample dish via the Erlenmeyer flask/cold trap method at ~192 K. C_2H_2 was added at ~144 K using the cold trap method, and CH_4 was added to the sample dish at 104 K. FTIR spectra from this experiment are shown in Figure 9. Notice the co-crystal band at 1.676 µm (described in Chapter 3), which persists throughout the experiment, including before, during, and after CH_4 evaporation. The methane band at 1.666 μm is clearly observed and decreases throughout the experiment as CH_4 evaporates.

Band depths of the co-crystal (1.676 μm) and CH_4 (1.666 μm) are shown in Figure 10. Here, we see an interesting inverse (1/x; see Fig. A5) relationship between these two bands. This relationship is also seen in the repeat experiment, shown in the Appendix (Figure A4). From cold to warm temperatures, the CH_4 band depth increases to a maximum of ~10% at 120 K, then steadily decreases as it evaporates, ending at ~1%. Alternatively, the C_2H_2-CH_3CN co-crystal band consistently remains around 2.5% until CH_4 evaporates, at which point the co-crystal band increases to a maximum value of 7.3% at 165 K, then decreases to ~1% by 184 K (Figure 10). This is the clearest relationship observed in the band depth data from all the binary experiments.

Optical views of the sample in Figures 11 and 12 show the distinct co-crystal morphology at 91 K. When the sample is warmed, the morphology changes after the sample reaches 152 K, and the solid sample appears to completely disappear above 180 K (Figure 11 (E), (F), Figure 12 (F)), which is near the sublimation point of C_2H_2 (189 K).

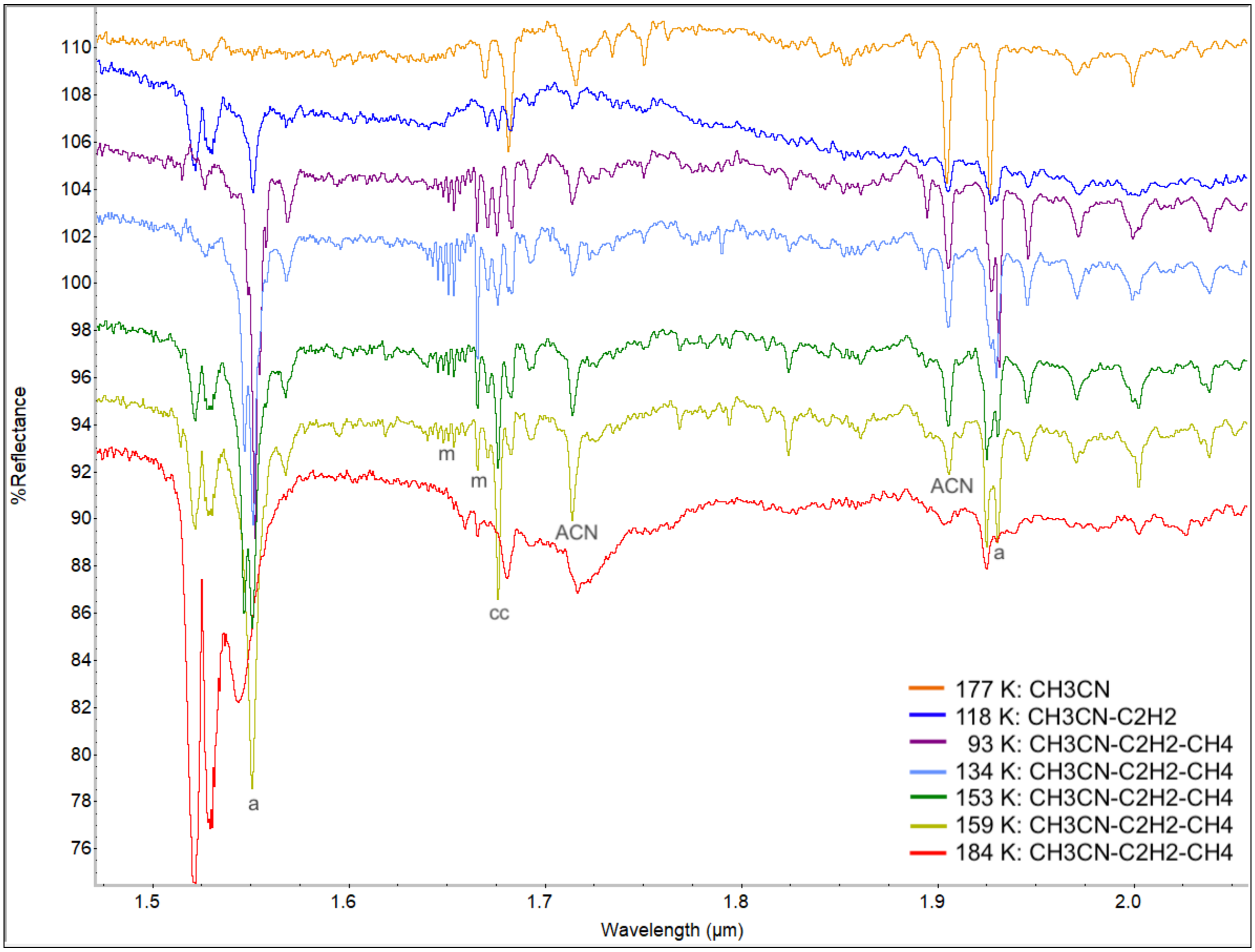

Figure 9. FTIR spectra from the C_2H_2-CH_3CN-CH_4 experiment from 93 K to 184 K. Experimental time increases from top to bottom. C_2H_2 bands are labeled with “a”, the CH_3CN bands are labeled with “ACN” (acetonitrile abbreviation), and the CH_4 band is labeled with “m.” Note that the bands are only labeled on the bottom spectrum for clarity, however, one can observe each of these bands in the additional spectra from the experiment. Notice the increase in reflectance of the CH_4 band until 153 K when it decreases due to evaporation. The co-crystal band shows the inverse of the CH_4 band trend, in that reflectance stays relatively constant until 134 K, after which it increases in reflectance to be greater than the two bands on either side of it.

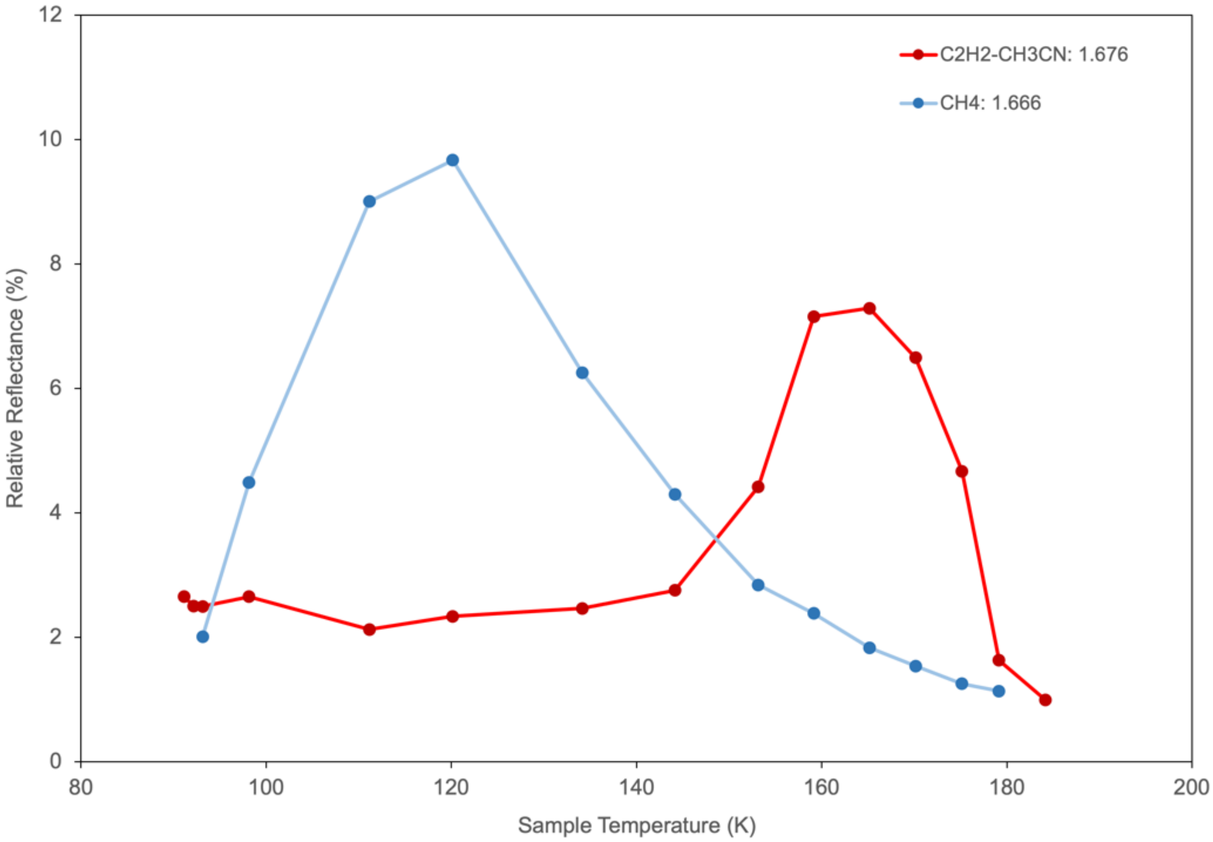

Figure 10. Band depths from the C_2H_2-CH_3CN-CH_4 experiment. Here we show band depths of the C_2H_2-CH_3CN co-crystal band (1.676 µm) and the CH_4 band (1.666 µm) after all three species were added to the sample dish, which corresponds to when the sample was warmed from 91 K to 184 K over a period of 204 minutes. There is a clear inverse relationship between these two bands. As temperature increases, the CH_4 band depth sharply increases to ~10% at 120 K, then steadily decreases to 1% at 180 K during evaporation. The opposite trend is observed in the co-crystal band, as it remains at ~2.5% until the CH_4 begins decreasing, then peaks at 7.3% (165 K) before decreasing to ~1% by 184 K.

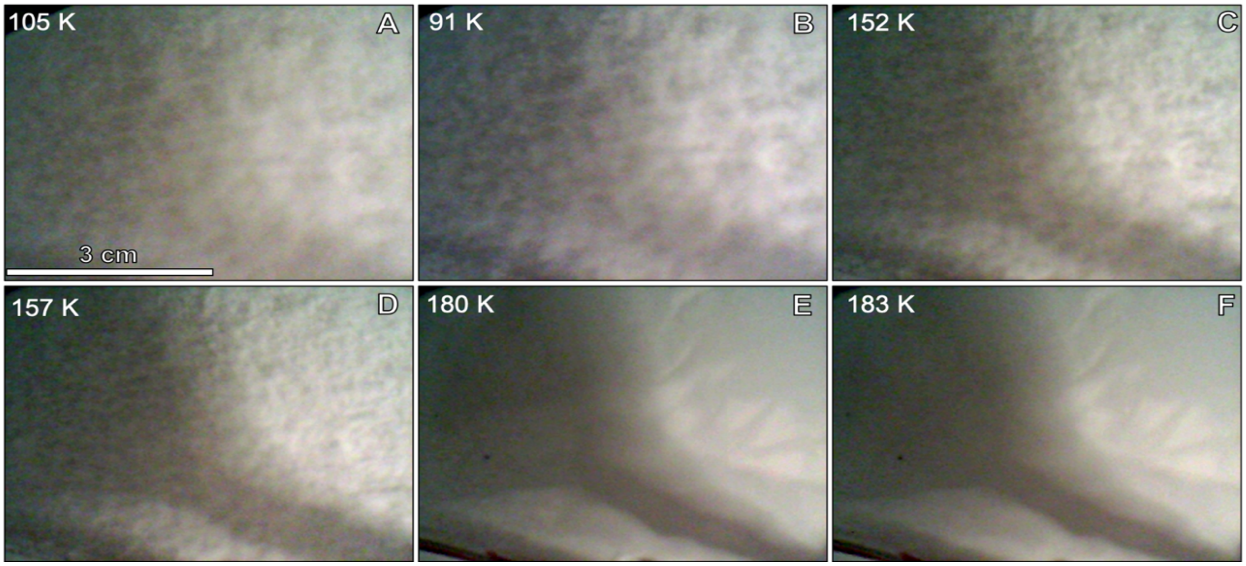

Figure 11. Top-down view of the C_2H_2-CH_3CN-CH_4 experiment in the sample dish (view 1). The sample underwent a cooling and warming cycle, as denoted by the temperatures, which closely represent those shown in the spectra of Figure 9. The shadow of the filter can be seen covering the left half of each panel. The lower-right corner of each panel is where the sample exits the bottom of the filter. Notice the difference in texture between 91 K (B) and when the sample is at warmer temperatures ((C)-(F)). The morphology of the co-crystal appears to lose structure and completely disappears when the sample is ≥180 K, which is near the sublimation point of C_2H_2 (189 K).

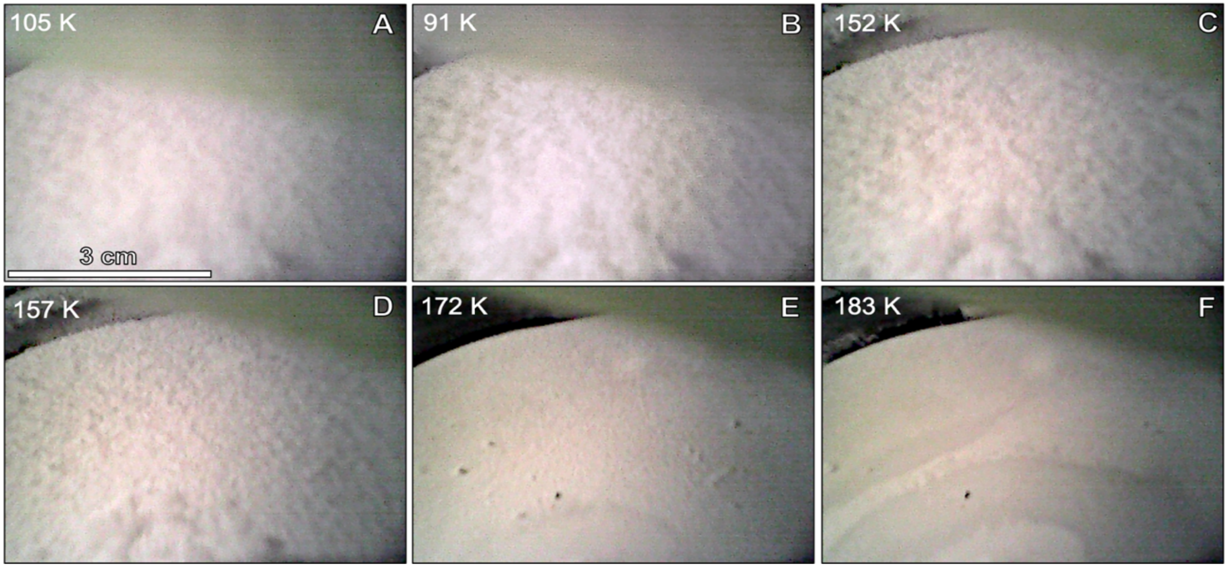

Figure 12. Top-down view of the C_2H_2-CH_3CN-CH_4 mixture in the sample dish (view 2). Temperatures correspond to those shown in Figure 11, except for panel (E; we were not able to collect a photo of view 2 at that temperature). The lower-right corner of each panel is where the sample exits the bottom of the filter. Notice the liquid-solid boundary in panels (E) and (F). The white light source from the FTIR probe can be seen in the upper central part of panels (E) and (F). The co-crystal texture change is observed when comparing cooler ((B)) to warmer ((C) and (D)) panels. The co-crystal has mostly sublimated by panels (E) and (F), corresponding with the band depths in Figure 10.

4.2.2. *Experiment 5: C_2H_2-CH_3CN-CH_4-C_2H_6*

In the C_2H_2-CH_3CN-CH_4-C_2H_6 experiment, CH_3CN was added to the sample dish via the Erlenmeyer flask/cold trap method at ~160 K. C_2H_2 was added at ~173 K using the cold trap method. CH_4 was added to the sample dish at 115 K, and C_2H_6 at 157 K. FTIR spectra from this experiment are shown in Figure 13. Notice the co-crystal band at 1.676 µm, which persists throughout the experiment, including before, during, and after CH_4 evaporation. C_2H_6 bands appear to evaporate, as well, due to the warmer temperatures during part of the experiment (warming the sample forces the C_2H_6 to evaporate; see Czaplinski et al., 2019; Chapter 1), after which, C_2H_2 appears to dominate the last sample spectrum.

Band depths show a U-like shape with C_2H_6 dominating at ~6.5% at the coldest temperatures, while the C_2H_2-CH_3CN co-crystal band (1.676 µm) dominates at 7% when the sample is warmest. From 92 K to 160 K, CH_4 bands increase, from ~0.3% to 1.5%, respectively.

Optical views of the sample (Figures 15, 16) show the co-crystal morphology at 113 K, and partial melting of the sample at 156 K, as evidenced by the reflected light from the light bulb. After the sample was cooled back down to Titan temperatures (92 K), the large, fluffy, snow-like crystals can be observed in the panel (E) of both camera views.

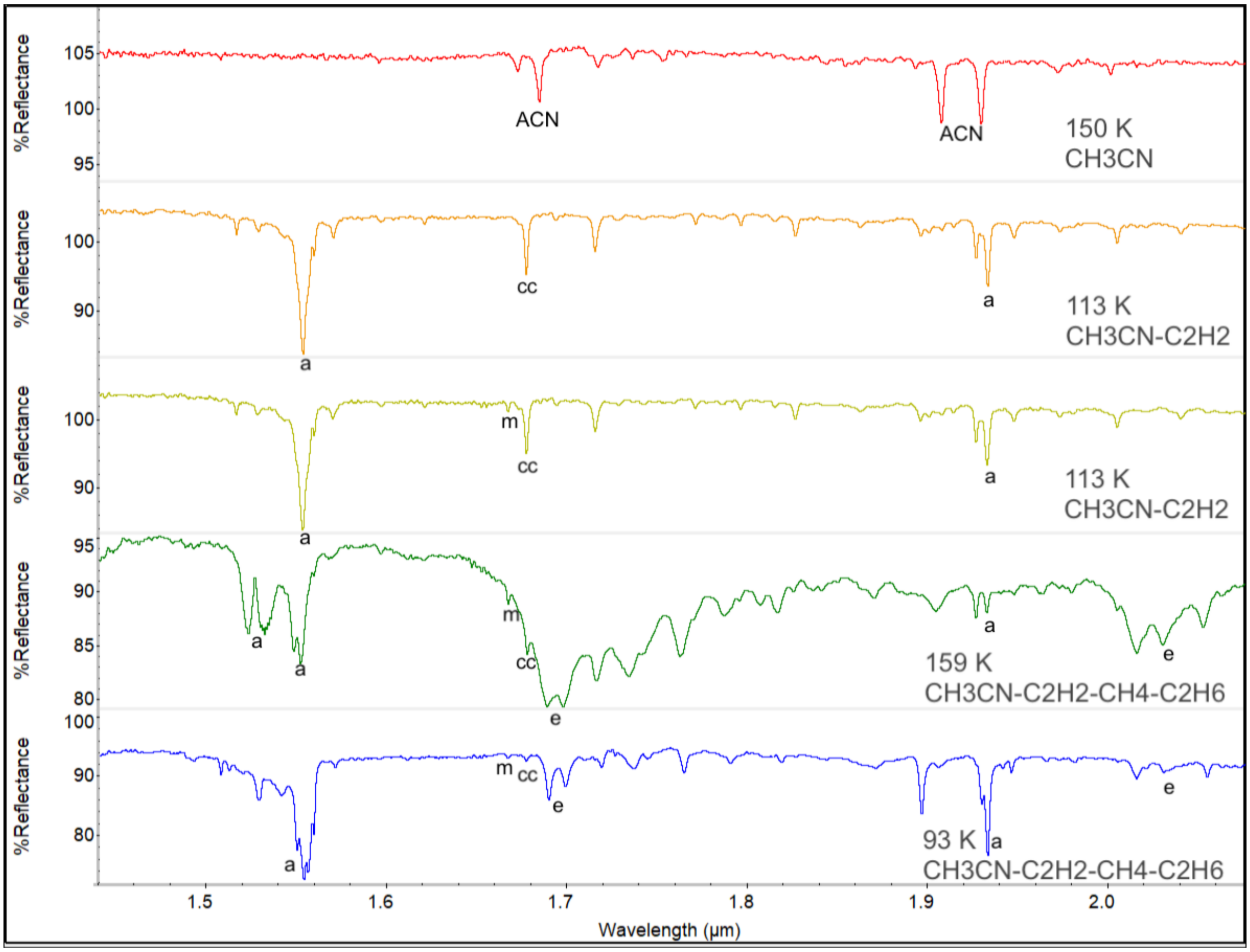

Figure 13. FTIR spectra from the C_2H_2-CH_3CN-CH_4-C_2H_6 experiment from 93 K to 159 K. Experimental time increases from top to bottom. C_2H_2 bands are labeled with "a", the CH_3CN bands are labeled with "ACN", the CH_4 band is labeled with "m", and C_2H_6 bands are labeled with "e." Notice how the C_2H_6 band depths drastically decrease from top to bottom, indicating evaporation. C_2H_2 bands dominate the remaining spectra, in this case. The co-crystal band (1.676 μm) is clearly not as prominent as it was in the previous experiment (Figure 9).

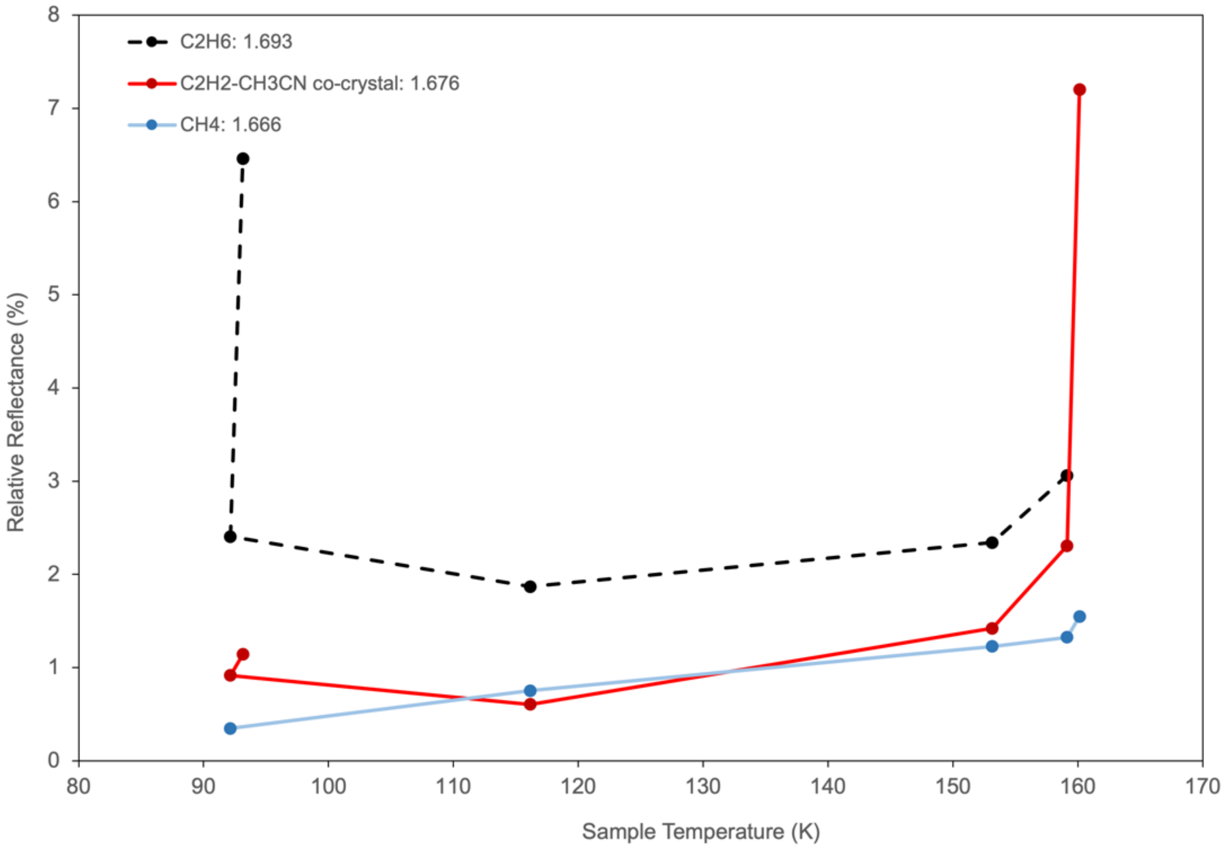

Figure 14. Band depths from the C_2H_2-CH_3CN-C_2H_6-CH_4 experiment. Here we show band depths of C_2H_6 (1.693 µm), the C_2H_2-CH_3CN co-crystal band (1.676 µm), and the CH_4 band (1.666 µm) after all four species were added to the sample dish, which corresponds to when the sample was cooled from 160 K to 93 K over a period of 44 min. Notice the opposite trend of C_2H_6 and the co-crystal band, where C_2H_6 has a greater band depth at ~90 K (6.5%) and C_2H_2 has a greater band depth at 160 K (7.2%). The CH_4 band decreases from 1.5% to 0.3% as the sample is cooled.

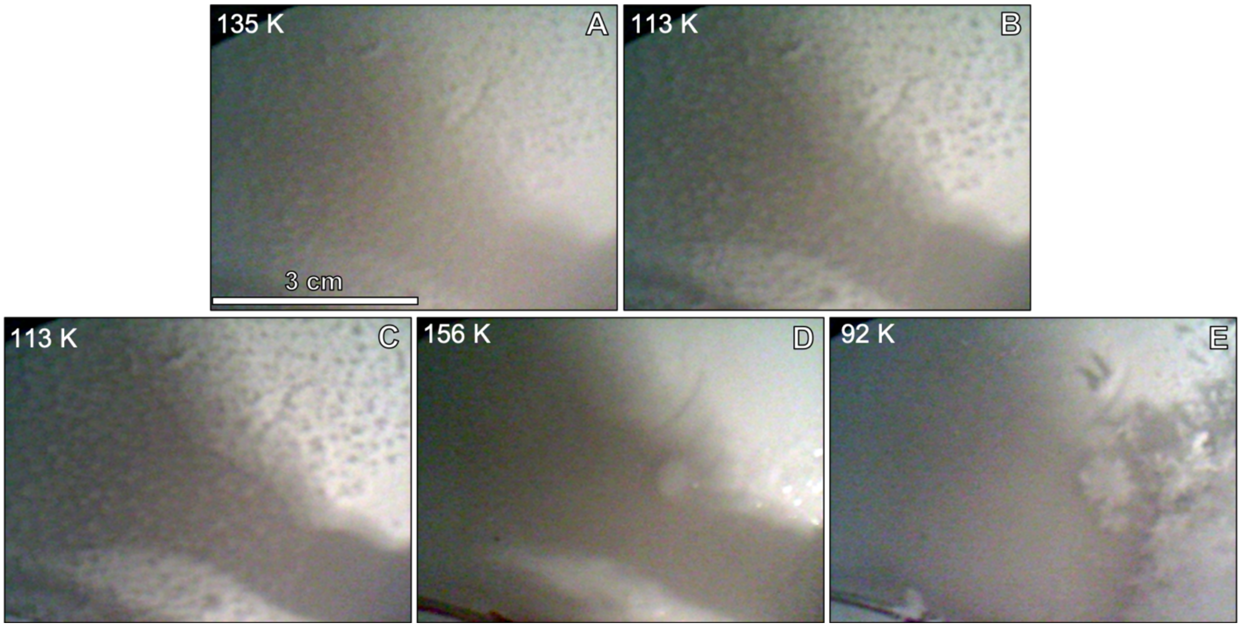

Figure 15. Top-down view of the C_2H_2-CH_3CN-CH_4-C_2H_6 mixture in the sample dish (view 1). The sample underwent a cooling and warming cycle, as denoted by the temperatures, which closely represent those shown in the spectra from Figure 13. The shadow of the filter can be seen covering the left half of each panel. The lower-right corner of each panel is where the sample exits the bottom of the filter. Notice the difference in texture between 113 K (B), (C) and when the sample is at warmer temperatures ((D)-(E)). The morphology of the co-crystal appears to lose structure at these warmer temperatures. Reflected light from the lightbulb is observed on the right side of panel (D), when the sample has melted. Distinct, snow-like crystals formed prior to panel (E), and are enhanced at the coldest temperatures (92 K)

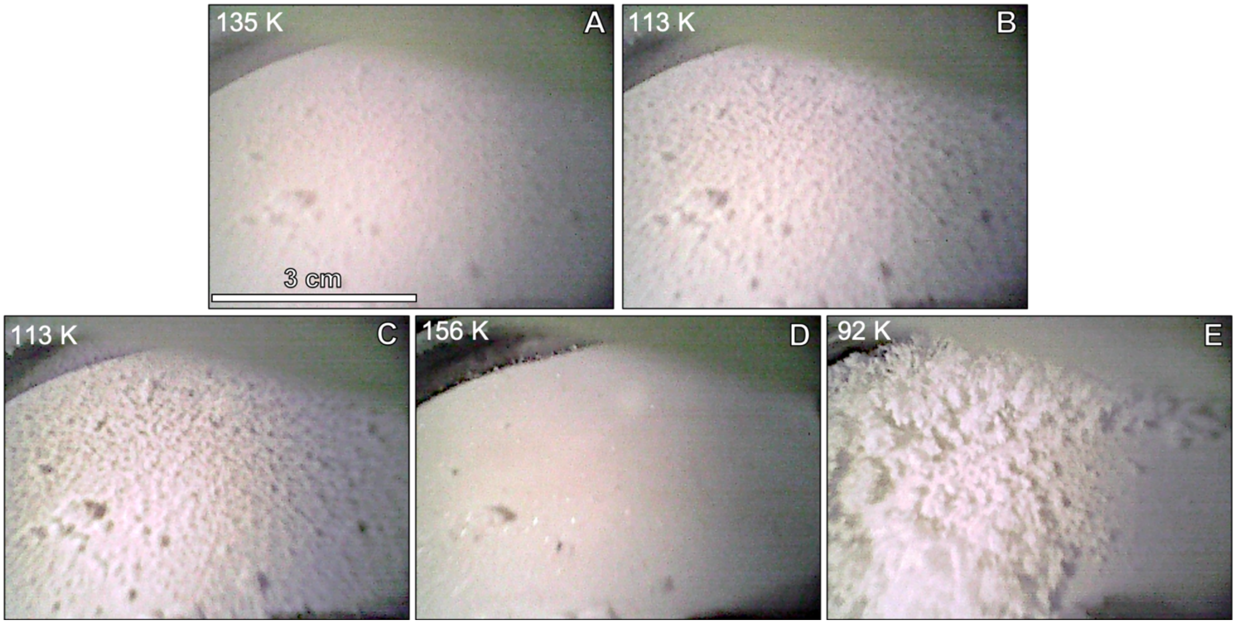

Figure 16. Top-down view of the C_2H_2-CH_3CN-CH_4-C_2H_6 mixture in the sample dish (view 2). Temperatures correspond to those shown in Figure 15. The lower-right corner of each panel is where the sample exits the bottom of the filter. The white light source from the FTIR probe is most clearly seen in the upper central part of panel (D). The co-crystal texture change is observed when comparing cooler ((B) and (C)) to warmer ((A) and (D)) panels. The fluffy, snow-like crystals are observed in panel (E), after cooling the sample back down to Titan temperatures.

Table 1. Summary of binary evaporite experiments

Exp.	Compounds	Temperature Range (K)	Important Notes		
			Spectra	Band Depths	Camera Views
1	C_2H_2, C_2H_4, CH_4	91 - 143	1.542 µm C_2H_2 band – C_2H_4 dominant	C_2H_2/C_2H_4 constant – CH_4 decreases to zero	Large, snow-like crystals at warmer temperatures
2	C_2H_2, C_2H_4, C_2H_6	92 – 135	Splitting of C_2H_6 bands	Increase with decreasing temperature	n/a
3	C_2H_2, C_2H_4, CH_4, C_2H_6	92 - 159	C_2H_2 disappears with CH_4	Decrease with increasing temperature	n/a
4	C_2H_2, CH_3CN, CH_4	91 – 184	Co-crystal band persists before, during, and after CH_4	Clear, inverse relationship	Co-crystal morphology at Titan temps
5	C_2H_2, CH_3CN, CH_4, C_2H_6	92 - 160	Co-crystal band persists before, during, and after adding liquid C_2H_6/CH_4 – C_2H_6 evaporation	C_2H_2 dominates after C_2H_6 evaporation	Large, snow-like crystals at warmer temperatures

5. Discussion

5.1. Highlights from each Experiment

Experiment 1 shows the only occurrence of the broad shoulder at 1.542 µm. This band is associated with the $v_1 + v_3$ vibrational mode of C_2H_2 and is seen when the sample is at 128 K and 140 K. C_2H_2 undergoes a crystal structure phase change around 139 K (Czaplinski et al., 2020). We interpret that the 1.542 µm band is most likely due to this phase change and may represent a metastable state of the molecule. When the 128 K spectrum in Figure 1 was taken (one spectrum takes 6 minutes to acquire), it is likely that because the sample was cooled relatively quickly, the first minute or so of spectral acquisition was when C_2H_2 was in the high temperature cubic phase and then phase transition to orthorhombic C_2H_2 occurred in the later portion of spectral acquisition (i.e., the molecule had not fully transitioned to the next phase when the spectrum was taken). This can be avoided by holding the sample at a certain temperature point long enough for the sample to equilibrize, however, this is not possible to do with our setup upon cooling the sample. The band depths are as expected; evaporite species stay relatively constant, while CH_4 evaporates throughout the duration of the experiment. The fluffy, snow-like texture of the sample at the end of the experiment is most likely a result of thermal expansion as the sample warms. We assume there was some excess sample in the filter, which, during expansion, began building up, then collapsed onto the dish (imagine a drinking glass that has been overfilled with liquid). This expansion may also be related to the C_2H_2 phase change – the higher temperature, cubic phase has larger spacing between molecules (e.g., Vu et al., 2020).

In experiment 2, the slight changes to the C_2H_6 spectra (mainly the double at 1.688 and 1.693 μm) align well with C_2H_4 bands that overlap with this C_2H_6 doublet. It is interesting to view a spectrum of this mixture in which C_2H_6 is not saturated, as it allows us to see which portions of the spectrum the evaporite species are most apparent. We note additional observations, such as the C_2H_6 bands appearing broader (i.e., not as sharp), due to the lack of saturation. Both evaporite species have almost identical band depths throughout the experiment, which increase with decreasing temperature. We also see this trend in the C_2H_6 bands, however at lower band depths than C_2H_2 and C_2H_4. The close match of C_2H_2 and C_2H_4 band depths may be related to their almost equal solubility in C_2H_6 (Singh et al., 2017), hence, band depth is highly dependent on initial concentration of the solute(s)/solvent(s).

Experiment 3 combined all four species: C_2H_2-C_2H_4-CH_4-C_2H_6. Here, the main observation is the clear disappearance of C_2H_2 in the spectra which corresponds with complete CH_4 evaporation (however, a repeated experiment showed the opposite trend between C_2H_2 and CH_4; Figs. A1, A2). The band depth and reflectance data also confirm this, as can be seen by the drastic decrease in C_2H_2 band depths which correspond to the decrease in CH_4 band depths (less C_2H_2 added to the dish initially). We interpret that the disappearance of C_2H_2 in the spectra may be related to evaporation of the solvent (CH_4-C_2H_6). C_2H_2 has a high solubility in CH_4 (Singh et al., 2017), and increases by a factor of 3 when dissolved in C_2H_6 (Glein and Shock, 2013). Additionally, geochemical modeling work by Glein and Shock (2013) indicate that the solubility of C_2H_2 may respond to changes in the composition of the solvent (i.e., the solvent composition changed after CH_4 evaporated). All of these factors combined may contribute to the decrease in C_2H_2 band depths in this experiment.

In Experiment 4, the co-crystal band at 1.676 µm is stable throughout the entire experiment. We observe an interesting inverse relationship between the CH_4 band and the co-crystal band; CH_4 is prominent at lower temperatures, whereas the co-crystal band is more prominent at higher temperatures. We interpret this as the evaporation of CH_4 allows the co-crystal band to become more prominent and increase in reflectance. This relationship also may be a function of temperature. We also see this same relationship in a repeated experiment presented in the Appendix (Figure A4). Additionally, we would like to point out that the extent of the liquid portion of the sample does not always reach all the way out to where the FTIR probe white light footprint is located (this can be observed in Figure 12 (F). The FTIR probe location only represents one portion of the sample in time, and not the entire dish. This is important to note, as evaporite processes (and evaporation in general) is often location dependent; meaning that evaporation in one location does not equate to the same degree of evaporation in a different location on the other side of the sample dish (or lake, in the case of Titan). This will be important to keep in mind if future missions to Titan (i.e., *Dragonfly*) encounter evaporite deposits. This is also why we include the optical views of the sample, as they can help interpret the general processes occurring in an experiment, while the FTIR probe gives more accurate information, but only for a minimized point of view, because it is a fiber optic probe. A hyperspectal camera would be needed to cover the entire surface area of the sample dish. Camera views from this experiment confirm the co-crystal formation morphology of the C_2H_2-CH_3CN co-crystal (outlined in Chapter 3).

Experiment 5 combined the C_2H_2-CH_3CN co-crystal with both CH_4 and C_2H_6. Here, because the sample was kept at warmer temperatures, this allowed a majority of the C_2H_6 to evaporate, revealing what the spectrum may look like in a scenario where C_2H_6 is depleted. Here, C_2H_2 is the most prevalent species when C_2H_6 is no longer dominant. The co-crystal band persists throughout the experiment. The uncommon shape of the band depth relationships may be from the fact that the sample was warmed and cooled several times in order to properly add all four components to the dish. As more species are introduced, the experimental procedure becomes more complicated and more difficult to reproduce. We once again observed the fluffy, snow-like texture of the solid components (the co-crystal), assumed to be due to lattice expansion as the solid increases in temperature.

5.2. Relevance to Titan's Evaporites

As predicted from thermodynamic modeling of Cordier et al. (2013, 2016), C_2H_2 is indeed the most prominent evaporite species (as evidenced by the band depths) in the majority of our experiments. However, this is an expected result, as our experiments simulate a situation that assumes an evaporite layer (i.e., the solid portion of the sample) is already present before liquid deposition and secondary evaporation (a dry period followed by a wet period). We chose to model our experiments this way, due to the difficulties in condensing C_2H_2 as a liquid (small temperature range as a liquid; 189 to 193 K), therefore requiring us to utilize the cold trap method. Nonetheless, we are still able to study acetylene's reactivity and ability to form a co-crystal even with the cold trap method.

Additionally, C_2H_2 forms many different co-crystals with Titan-relevant molecules (Kirchner, Bläser, and Boese, 2010; Cable et al., 2018, 2019, 2020; Maynard-Casely et al., 2018), so it will be important for future Titan missions to distinguish between the pure C_2H_2 spectral signatures and that of the co-crystal. These distinctions will be highly dependent on the wavelength range utilized. For example, the NIR spectral region excites overtone and combination bands, while the MIR excites the fundamental vibrations of molecules, which are generally much deeper absorptions than in the NIR.

Regarding the 5-μm-bright signature that is strongest in Titan's equatorial Tui and Hotei Regios (MacKenzie and Barnes, 2016), our set of experiments provide new insights as to the complexity surrounding this signature. MacKenzie and Barnes (2016) point out that a signature that is highly reflective in one wavelength range may not necessarily show the same trends in other wavelength ranges. For example, in our study we focus on the NIR, where C_2H_2 plays a prominent role in our evaporite spectra. However, a previous spectral survey of organic compounds in the 5 μm region (Clark et al. 2010) showed that CH_3CN most closely resembles an uncharacterized feature at 5.01 μm. This highlights the need for future studies of experimental evaporites that include a wider wavelength range (specifically, the MIR). Additionally, MacKenzie and Barnes (2016) indicate that not all 5-μm-bright terrains possess a certain feature at 4.92 μm, and the locations that do have this feature may not always appear in all observations of Titan's surface. This transience may be explained by differences in grain size or even phase changes that may occur on Titan's surface. As seen in several of our binary evaporite experiments with C_2H_2, at warmer temperatures the crystal shape completely changes, expanding into snow-like ice crystals. These crystals may cause longer optical path lengths and higher reflectance of the corresponding compound. Indeed, the process of solids precipitating from evaporating saturated liquids may create crystals with long optical path lengths and deep absorption features (Barnes et al., 2011). Additionally, our experiments highlight how multiple sample compositions of various concentrations can still produce an evaporite deposit – alluding to an instance on Titan where not every evaporite deposit has the same ratio and concentration of compounds, therefore, only certain compounds/phases of these compounds/concentrations may be creating the 5-µm-bright signature. This was suggested in MacKenzie et al. (2016), where the authors note that material variability such as grain size differences may cause the difference in signals between Tui and Hotei Regios.

Clearly, different and additional processes are at play on Titan when compared to our laboratory experiments. Sintering (a process whereby porosity is removed from compacted particles/grains, decreasing the volume of the system) could create larger grain sizes of certain compounds and redefine how the compound behaves/interacts with other organics (i.e., co-crystals). Winds on Titan may introduce additional mixing of liquids in Titan's lakes and seas. Precipitation would indeed complicate the evaporation process by introducing additional solvent (e.g., CH_4) to the system during evaporation, causing precipitation of solids to become re-dissolved and potentially recrystallize after a second (or third, etc.) round of evaporation. Infiltration of liquids from surrounding channels into a lake may introduce additional solutes/sediments or even more solvent. For example, Ligeia Mare (north pole) does not show a bright feature at 4.92 µm, whereas Kraken Mare (north pole, further south from Ligeia) does MacKenzie et al., 2016). This dichotomy could be due to Ligeia's watershed introducing different solutes (or different amounts of solutes) into Ligeia Mare when compared to Kraken Mare (MacKenzie et al., 2016).

6. Conclusions

To conclude this evaporite study, we ran a set of binary evaporite experiments that include two candidate evaporite species (along with methane and ethane) in order to work towards replicating a more accurate scenario as to what may occur in Titan's evaporitic environments. Acetylene-ethylene-methane-ethane experiments show an interesting relationship between acetylene and methane after methane evaporation where acetylene band depths also decreased. However, a repeat experiment showed the opposite trend in acetylene. Clearly, initial concentrations of each species are an important factor here. Acetylene-acetonitrile-methane-ethane experiments show that the acetylene-acetonitrile co-crystal still forms and is stable when exposed to methane and ethane. Many spectral band shifts/splits and changes to the sample morphology (such as differing crystal structure and size) are noted across all experiments. These experiments emphasize the importance of expanding the wavelength range, compounds studied, and external environmental factors for future, multi-species evaporite studies in order to maximize relevance with *Cassini* VIMS spectral comparison.

7. Acknowledgement

This work was supported by NASA Headquarters under the NASA Earth and Space Science Fellowship Program – Grant #80NSSC17K0603. We would also like to thank Woodrow Gilbertson for assistance with mol fraction calculations, Walter Graupner for assistance in the lab, and Troy Williams for support with experiments.

8. References

Barnes, J.W., Bow, J., Schwartz, J., Brown, R.H., Soderblom, J.M., Hayes, A.G., Vixie, G., Le Mouélic, S., Rodriguez, S., Sotin, C., Jaumann, R., Stephan, K., Soderblom, L.A., Clark, R.N., Buratti, B.J., Baines, K.H., Nicholson, P.D., 2011. Organic sedimentary deposits in Titan's dry lakebeds: Probable evaporite. Icarus 216, 136–140. https://doi.org/10.1016/j.icarus.2011.08.022

Cable, M.L., Vu, T.H., Malaska, M.J., Maynard-casely, H.E., Choukroun, M., Hodyss, R., 2019. A Co-Crystal between Acetylene and Butane: A Potentially Ubiquitous Molecular Mineral on Titan. ACS Earth Sp. Chem. 3, 2808–2815. https://doi.org/10.1021/acsearthspacechem.9b00275

Clark, R.N., Curchin, J.M., Barnes, J.W., Jaumann, R., Soderblom, L., Cruikshank, D.P., Brown, R.H., Rodriguez, S., Lunine, J., Stephan, K., Hoefen, T.M., Mouélic, S. Le, Sotin, C., Baines, K.H., Buratti, B.J., Nicholson, P.D., 2010. Detection and mapping of hydrocarbon deposits on Titan. J. Geophys. Res. Planets 115, E10005. https://doi.org/10.1029/2009JE003369

Cordier, D., Barnes, J.W., Ferreira, A.G., 2013. On the chemical composition of Titan's dry lakebed evaporites. Icarus 226, 1431–1437. https://doi.org/10.1016/j.icarus.2013.07.026

Cordier, D., Cornet, T., Barnes, J.W., MacKenzie, S.M., Le Bahers, T., Nna-Mvondo, D., Rannou, P., Ferreira, A.G., 2016. Structure of Titan's evaporites. Icarus 270, 41–56. https://doi.org/10.1016/j.icarus.2015.12.034

Cordier, D., Mousis, O., Lunine, J.I., Lavvas, P., Vuitton, V., 2009. An estimate of the chemical composition of titan's lakes. Astrophys. J. 707, L128-131. https://doi.org/10.1088/0004-637X/707/2/L128

Czaplinski, E., Yu, X., Dzurilla, K., Chevrier, V., 2020. Experimental Investigation of the Acetylene–Benzene Cocrystal on Titan. Planet. Sci. J. 1, 16. https://doi.org/10.3847/PSJ/abbf57

Glein, C.R., Shock, E.L., 2013. A geochemical model of non-ideal solutions in the methane–ethane–propane–nitrogen–acetylene system on Titan. Geochim. Cosmochim. Acta 115, 217–240. https://doi.org/10.1016/j.gca.2013.03.030

Kirchner, M.T., Bläser, D., Boese, R., 2010. Co-crystals with Acetylene: Small Is not Simple! Chem. A Eur. J. 16, 2131–2146. https://doi.org/10.1002/chem.200901314

MacKenzie, S.M., Barnes, J.W., 2016. Compositional Similarities and Distinctions between Titan's Evaporitic Terrains. Astrophys. J. 821, 17.

MacKenzie, S.M., Barnes, J.W., Sotin, C., Soderblom, J.M., Le Mouélic, S., Rodriguez, S., Baines, K.H., Buratti, B.J., Clark, R.N., Nicholson, P.D., McCord, T.B., 2014. Evidence of Titan's climate history from evaporite distribution. Icarus 243, 191–207. https://doi.org/10.1016/j.icarus.2014.08.022

Maynard-Casely, H.E., Cable, M.L., Malaska, M.J., Vu, T.H., Choukroun, M., Hodyss, R., 2018. Prospects for mineralogy on Titan. Am. Mineral. 103, 343–349. https://doi.org/10.2138/am-2018-6259

Singh, S., Combe, J.-P., Cordier, D., Wagner, A., Chevrier, V.F., McMahon, Z., 2017. Experimental determination of acetylene and ethylene solubility in liquid methane and ethane: Implications to Titan's surface. Geochim. Cosmochim. Acta 208, 86–101. https://doi.org/10.1016/j.gca.2017.03.007

Stevenson, J.M., Fouad, W.A., Shalloway, D., Usher, D., Lunine, J., Chapman, W.G., Clancy, P., 2015. Solvation of nitrogen compounds in Titan's seas, precipitates, and atmosphere. Icarus 256, 1–12. https://doi.org/10.1016/j.icarus.2015.04.019

Vu, T.H., Maynard-Casely, H.E., Cable, M.L., Hodyss, R., Choukroun, M., Malaska, M.J., 2020. Anisotropic thermal expansion of the acetylene–ammonia co-crystal under Titan's conditions. J. Appl. Crystallogr. 53, 1524–1530. https://doi.org/10.1107/S1600576720014028

9. Appendix

Here, we show repeated experiments for C_2H_2-C_2H_4-CH_4-C_2H_6 (Fig. A1, A2) and C_2H_2-CH_3CN-CH_4 (Fig. A3, A4). Notice how in the C_2H_2-C_2H_4-CH_4-C_2H_6 experiment, the C_2H_2 band depths *increase* after CH_4 evaporation, which is opposite of the trend from figure 8 in the main text. In the C_2H_2-CH_3CN-CH_4 experiment, we observe a similar inverse relationship between the CH_4 and C2H2-CH_3CN co-crystal band depths.

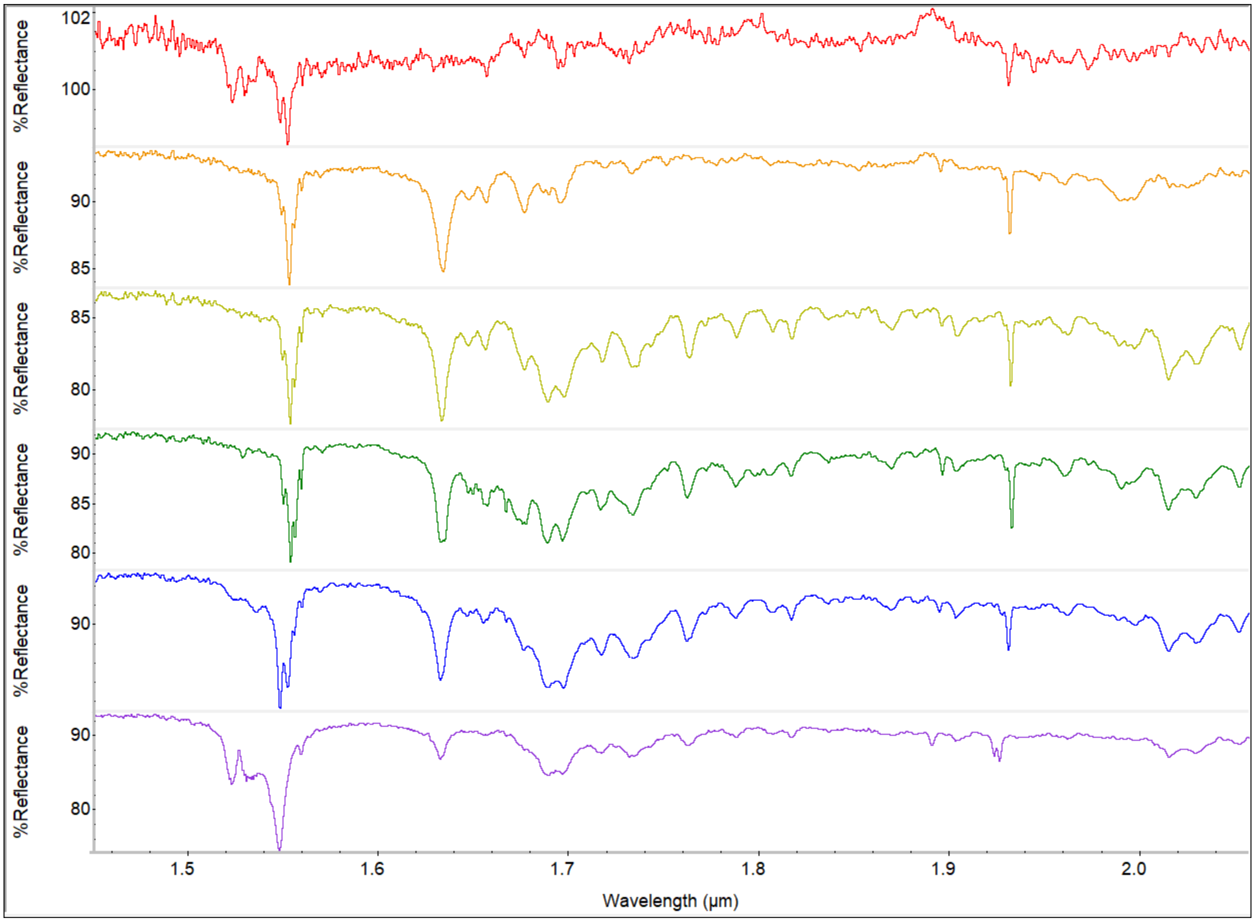

Figure A1. FTIR spectra from the repeated C_2H_2-C_2H_4-CH_4-C_2H_6 experiment.

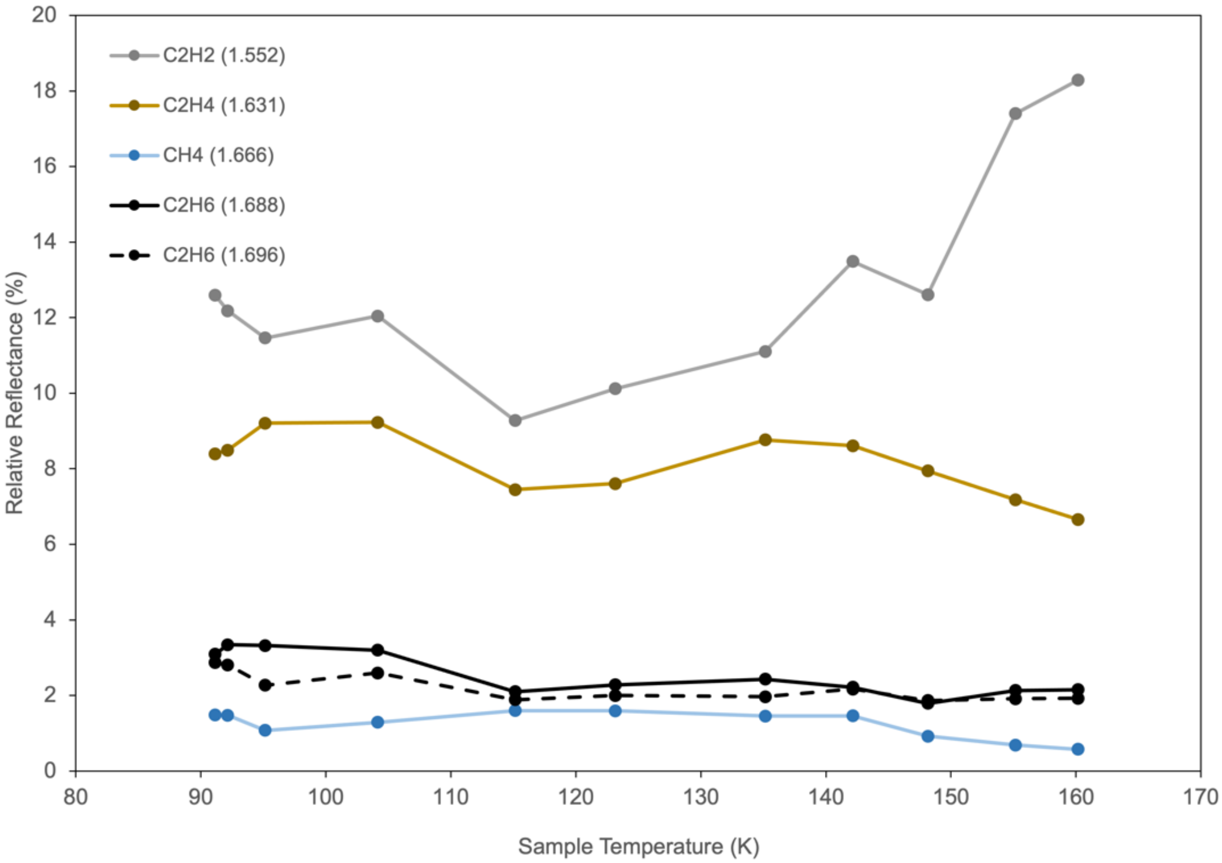

Figure A2. Band depths from the repeated C_2H_2-C_2H_4-CH_4-C_2H_6 experiment. Notice how the C_2H_2 band depths (gray) increase after CH_4 evaporation.

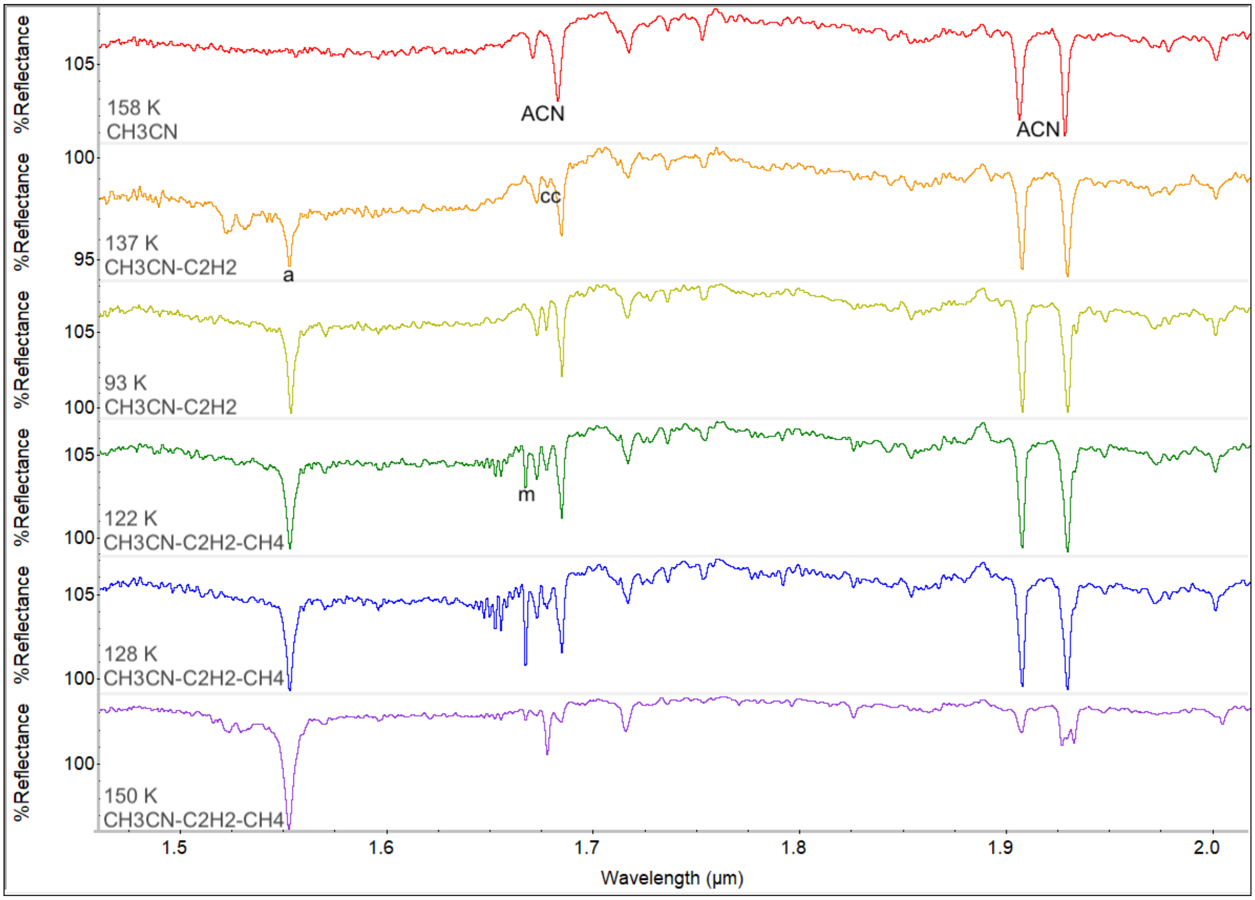

Figure A3. FTIR spectra from the repeated C_2H_2-CH_3CN-CH_4 experiment from 93 – 158 K. Experimental time increases from top to bottom. C_2H_2 bands are labeled with “a”, the CH_3CN bands are labeled with “ACN” (acetonitrile abbreviation), and the CH_4 band is labeled with “m.” Note that the bands are only labeled on the spectrum where the compound is first introduced, to avoid clutter, however, one can observe each of these bands in the additional spectra from the experiment.

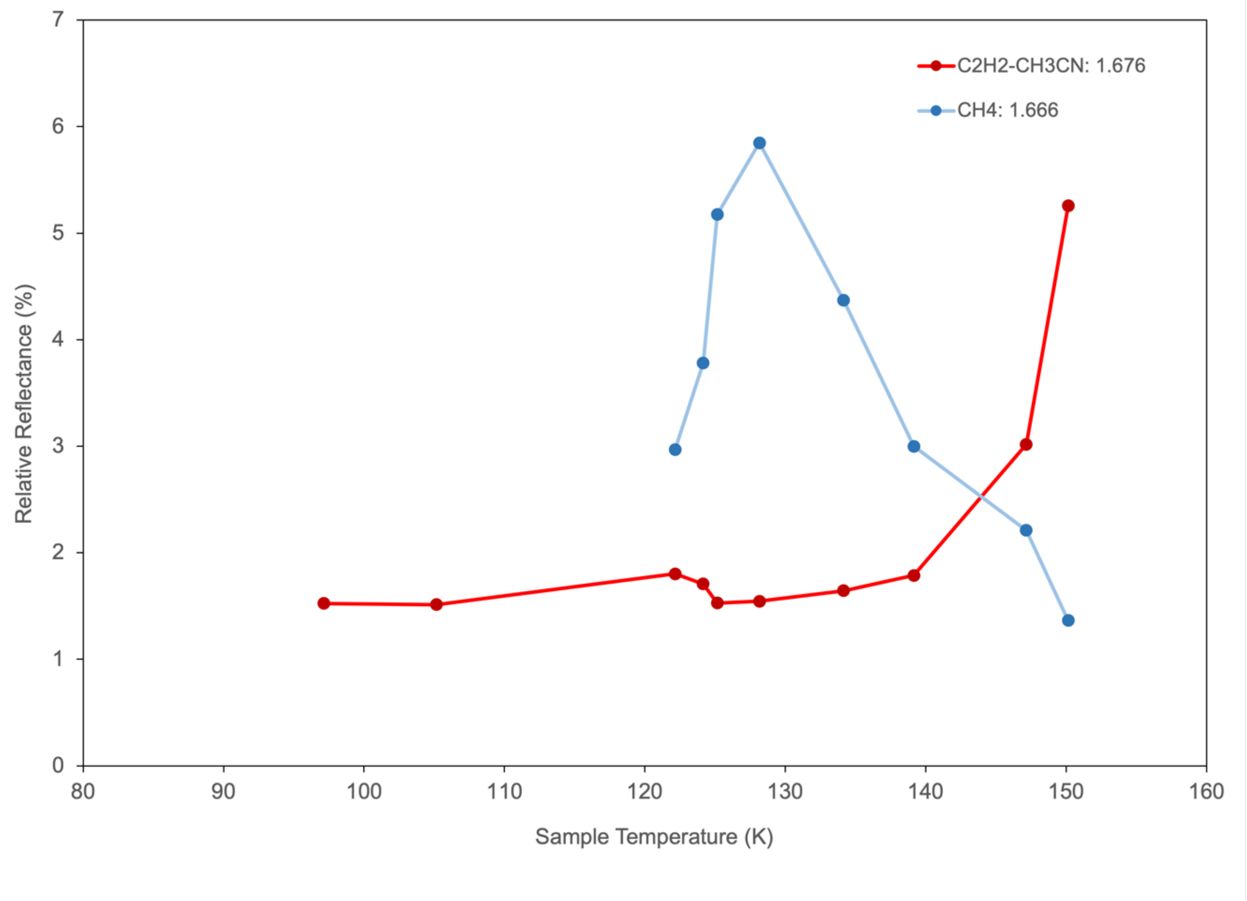

Figure A4. Band depths from the repeated C_2H_2-CH_3CN-CH_4 experiment. Notice the inverse relationship between the co-crystal band (1.676 µm) and the CH_4 band (1.666 µm).

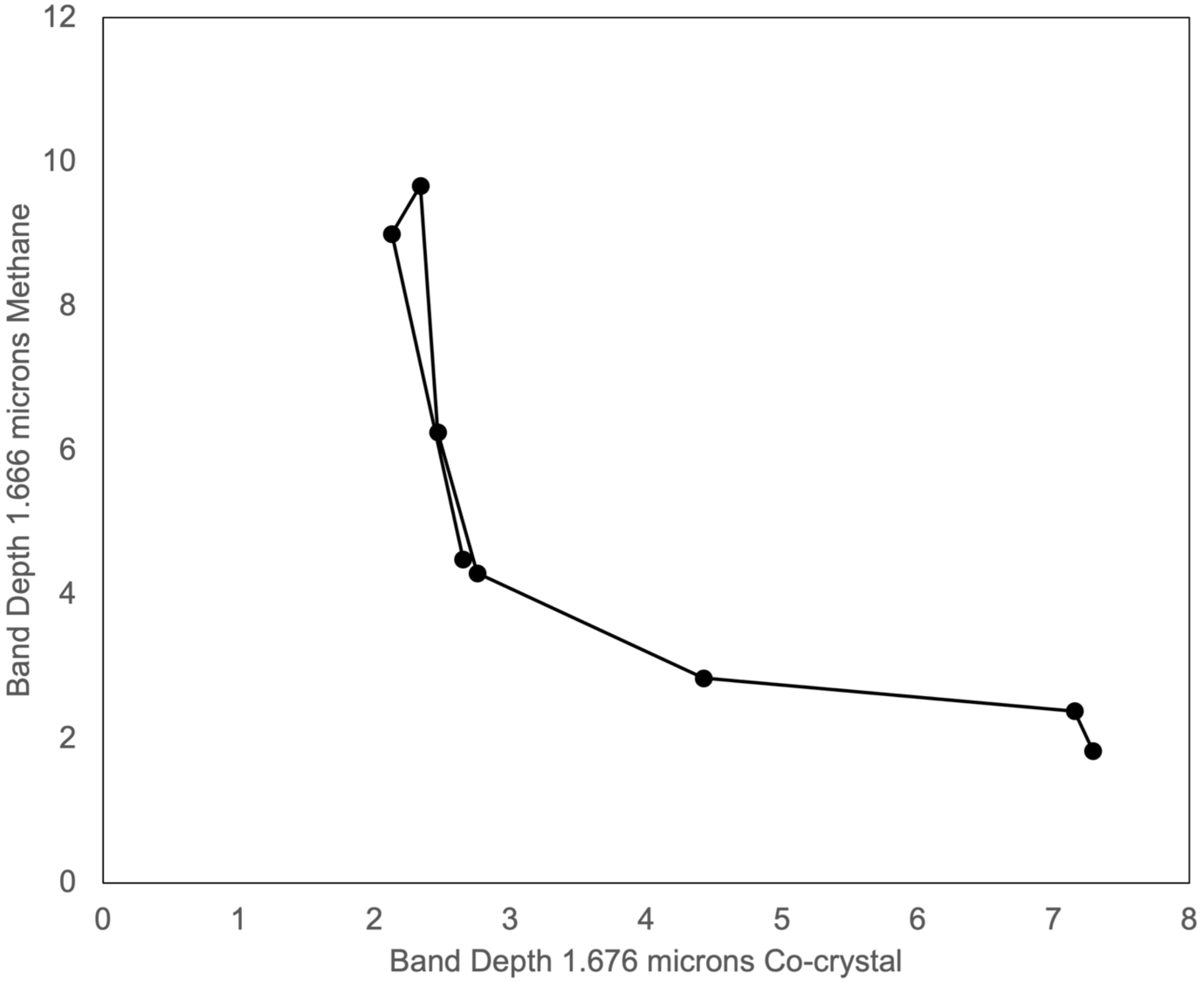

Figure A5. Plot of the band depth of the 1.676 µm C_2H_2-CH_3CN co-crystal band and the 1.666 µm CH_4 band from 98 – 165 K in the C_2H_2-CH_3CN-CH_4 experiment showing an approximately inverse relationship between the two bands.

DISSERTATION CONCLUSIONS AND SYNTHESIS

This dissertation was motivated by the discovery of 5-µm-bright sediments in filled and empty basins at the north pole (Barnes et al., 2011a), the dry equatorial deposits of Tui and Hotei Regios (MacKenzie et al., 2014), and the "bathtub" rings along the perimeter of Ontario Lacus (Barnes et al., 2009; Moriconi et al., 2010). The 5-µm-bright deposits in all three locations have been interpreted as evaporitic in origin. Over the last decade, many experimental efforts have attempted to answer fundamental questions associated with the discovery of evaporites on Titan, such as: What is the specific identity of the organic evaporites? Why do only certain regions show the 5-µm-bright signature? A new type of molecular mineral called a co-crystal, which is a unique crystalline structure of two or more species in a set stoichiometric ratio (Cable et al., 2014, 2018, 2019, 2020; Czaplinski et al., 2020; Maynard-Casely et al., 2018; McConville et al., 2020; Vu et al., 2014) may be the key to understanding these questions regarding Titan's evaporites, as they can potentially be a hydrocarbon reservoir. Additionally, some co-crystal compositions may be the dominant form of certain molecules such as benzene (Cable et al., 2014). Co-crystals require a specific ratio of molecules and specific formation temperatures, which can in part explain why certain regions/areas on Titan exhibit the 5-µm-bright feature, while others do not.

Our experimental Titan chamber provides a unique, in situ surface environment that is in direct contact with a large atmosphere, promoting atmosphere-dominated kinetics due to the large atmospheric volume compared to a smaller liquid volume. This differs from other laboratory facilities that utilize a liquid-dominated experimental design (e.g., Cable et al., 2014; Engle et al., 2020). Liquid exchange with the atmosphere would be a dominant process occurring on Titan, and our chamber allows for these types of interactions due to the large relative atmospheric portion. Further, we are able to directly measure mass change over time via the balance, as well as taking in situ FTIR spectra at a fixed point within the TCB. On the other hand, the fact that all of our instruments are located in situ (a finite amount of space in the TCB) makes sample modifications inaccessible, as the chamber must be entirely taken apart, opened, and closed any time changes are desired; a process that takes a week for simple changes and longer depending on the modifications being made. Easier accessibility may be desired in the case of certain types of experiments where the researcher(s) wish to remove a sample for analysis outside of the chamber (e.g., external tholins analysis; Nna-Mvondo et al., 2015). Nevertheless, the current setup remains desirable for experiments focusing on liquid processes (Farnsworth et al., 2020) and evaporite formation from a liquid solution (Czaplinski et al., 2019; 2020).

1. Summary of Results

1.1. Chapter 1

In Chapter 1, we investigated the ability of evaporites to form in liquid methane, ethane, and methane-ethane solvents. Ethylene was directly dissolved into the solvent inside of the condenser, allowing the dissolved solution to be studied on the sample dish.

In the methane-ethylene experiment, nearly all methane evaporated by the end of the experiment, leaving behind a residual ethylene evaporite. We can clearly track the methane evaporation via all three dataset types: spectra (methane triplet disappeared), mass vs. time plot (mass decreased as methane evaporated), and band depth measurements (methane bands decrease while ethylene bands increase). Additionally we note the persistence of a methane band at 1.666 μm, potentially representing trapped in the evaporite layer or evaporated methane in the atmosphere between the FTIR probe and the sample. Ethylene bands show a noticeable shift upon changing phase from dissolved liquid to evaporated solid.

The ethane-ethylene 90 K experiment showed no drastic changes in spectra, mass, or band depths, as ethane is not volatile (does not readily evaporate due to its vapor pressure) as methane does under these conditions. Therefore, we then force-evaporated ethane-ethylene via warming the sample to show what the evaporite may look like if ethane were to evaporate under Titan conditions. However, due to ethylene's high solubility in ethane, both species disappeared by the end of the experiment.

The methane-ethane-ethylene experiment showed methane evaporation, as expected, leaving behind ethane-ethylene spectra. Band depths of ethane and ethylene were stable after complete methane evaporation. No evaporite was formed in this experiment.

By utilizing a spectral unmixing model, we determined the solubility (agrees with previously reported values), methane and ethane evaporation rates (which closely align with previously reported values), and the mole fraction at saturation (for the methane-ethylene experiment), which was slightly higher than previous values, indicating supersaturation. Assuming ethylene saturation, we also calculated the time of evaporation (~5 years) and thickness (upper limit of 9 m) of an ethylene evaporite deposit in a methane-dominated north polar lake on Titan. Ethylene may be a probable candidate for evaporites on Titan, owing to its high solubility and simple molecular structure.

1.2. Chapter 2

Taking advantage of acetylene's ease of forming co-crystals (Kirchner et al., 2010) chapter 2 determined to what extent the acetylene-benzene co-crystal is detectable using FTIR spectroscopy. Both acetylene and benzene are relatively abundant photochemical products in Titan's atmosphere, therefore we would expect that they also may be dominant species at the surface, as well. Here, we utilized two new experimental methods to introduce benzene and acetylene to the sample dish: the Erlenmeyer flask/glove box method, and the cold trap method. These new methods were used due to complications of working with a liquid (benzene) and species with a small amount of time in the liquid range (acetylene).

We report pure spectra of acetylene ice, showing the cubic to orthorhombic phase transition occurring around 139 K, as well as pure benzene ice, which does not change phase within the temperature range of these experiments (~85 K to 185 K). We note that the acetylene cylinder contained acetone as a stabilizer, therefore, the cold trap method helped ensure that no acetone made its way to the sample dish.

We show spectra in both cold (93 – 94 K) and warm (135 – 151 K) temperature ranges, (as temperature drastically affects how the acetylene behaves), as well as its spectral properties under Titan-relevant conditions. The most prominent evidence of the co-crystal formation is the appearance of new spectral bands from 1.569 to 1.598 µm and 1.943 to 2.122 µm. These bands are more clearly visible in the spectra taken under colder temperatures, as the colder sample reflects light differently compared to the warmer sample. Additionally, several bands shift upon co-crystal formation, and we observe drastic changes to the sample morphology (more structure to the sample) upon co-crystal formation.

These results can potentially be applied to the search for acetylene in Titan's clouds, as portions of the atmosphere are within the range of the acetylene phase change. Under Titan conditions, we report a slightly warmer acetylene phase change (139 K) compared to previous studies (133 K), possibly a result of different experimental setups. Solid-solid interactions are a proven path to co-crystal formation, as noted here and in previous co-crystal studies (Cable et al., 2018; 2020). The IR spectral shifts observed here match closely to previous studies of the acetylene-benzene co-crystal, although at different wavelengths. Experimental limitations preclude us from determining the crystal structure or mechanical properties of the co-crystal on a microscopic scale, however this will be an important aspect of future co-crystal studies. Familiarization of the morphological changes upon co-crystal formation will be important for when *Dragonfly* images and studies Titan's surface in situ. We verify that co-crystals form relatively easily under the right conditions (and even a range of temperatures/concentrations). On Titan, co-crystallization may be possible in the stratosphere (~130 – 140 K), introducing the plausibility of co-crystals in Titan's equatorial dune fields, as well as co-crystals with more than two species. We provide a rough estimation on the thickness of the acetylene-benzene co-crystal that may have accumulated on Titan's surface over 1 Gyr: ~5 cm.

1.3. Chapter 3

In Chapter 3, we introduced evaporite experiments with a compound that has enrichments near Titan's north pole, acetonitrile (CH_3CN). Nitriles are organic compounds with a CN group, and they represent an important group of molecules on Titan, due to their association with prebiotic processes. Acetonitrile may be associated with dark regions on Titan's surface and is a prime candidate for matching the 5-μm-bright features discussed earlier. It is known that acetylene and acetonitrile form a co-crystal under Titan conditions and is detectable via Raman spectroscopy (Cable et al., 2020), therefore we sought to test co-crystal identification with FTIR spectroscopy. Because acetonitrile is a liquid at room temperature, we utilized the glove box/Erlenmeyer flask method (and the cold trap method for acetylene) again to introduce both species to the sample dish.

We started with straightforward experiments of combining acetonitrile with ethane and methane separately. Acetonitrile bands are easily detectable in both solvents, and a residual spectrum was produced after methane evaporation. We observed several differences in this residual spectrum due to small methane gas bands being present. As expected, ethane bands were stable at Titan temperatures and even with warming the sample.

We then performed three experiments in which the acetylene-acetonitrile co-crystal formed. In all three experiments, a new band appeared at 1.676 μm that is neither seen in pure acetylene nor pure acetonitrile. We also observed band shifts and band splitting, as well as drastic changes to sample morphology upon co-crystal formation. Band depths of the 1.676 μm co-crystal band show that they increase as the sample warms.

The co-crystal formed between 174 K and 118 K and we believe that phase trapping may have occurred during these experiments due to changes in some of the acetylene bands. Band shifts observed are similar in magnitude to previous Raman studies (Cable et al., 2020). Nitriles may contribute to differences in RADAR signal between Ligeia Mare (north pole) and Ontario Lacus (south pole), as well as the unidentified 5.01 μm absorption in *Cassini* VIMS data. This set of experiments is important for understanding some of the minute spectral differences that occur upon co-crystal formation, providing constraints for when *Dragonfly* studies the surface in the 2030's.

1.4. Chapter 4

Here, we further complicate our evaporite experiments by studying "binary" samples (two evaporite species mixed with methane *and* ethane solvents) in order to proceed towards giving a more accurate view of Titan's evaporitic processes. In reality, Titan's lakes may have 6 or more species of minor concentrations, which drastically complicates the evaporite picture. Even the binary experiments are a vast oversimplification, however the goal is to determine which species consistently dominate the spectral signatures. We tested acetylene and ethylene, two simple hydrocarbon species, combined with methane and ethane, followed by the acetylene-acetonitrile co-crystal combined with methane and ethane. The cold trap method was used for adding acetylene, while the glove box/Erlenmeyer flask method was used to add acetonitrile. Then methane and ethane were condensed in the condenser and poured as a liquid on top of the solid sample.

We began by running an acetylene-ethylene-methane experiment, where methane evaporated and left behind a deposit of acetylene and ethylene. Camera views show the differences in sample morphology as the sample was cooled and warmed. Next, we tested acetylene-ethylene-ethane, where the spectra showed splitting of some ethane bands and clear signatures of acetylene and ethylene. Lastly, we combined all four species for an acetylene-ethylene-methane-ethane experiment. Here, we tracked spectral differences as methane evaporated, and acetylene bands also disappeared after methane evaporation.

The next set of experiments started with acetylene-acetonitrile-methane, showing that the co-crystal was stable after adding methane and after evaporation. The band depths of the co-crystal and methane bands show an interested inverse relationship as a function of temperature. Camera views also confirm co-crystal formation. The last experiment combined all four species: acetylene-acetonitrile-methane-ethane. We warmed and cooled the sample to force evaporate some ethane, which produced interesting spectra that clearly shows acetylene after ethane evaporation. Camera views also show ice crystals expanding as temperature increases.

These experiments simulate a situation that begins with a dry period (solid is deposited on the dish) followed by a wet period (liquid methane and ethane are condensed on top of the solid) due to experimental limitations. We show the difficulty in distinguishing between pure acetylene and the co-crystal, as well as the need to perform these types of experiments in the mid-infrared range to compare with VIMS results. These experiments also show how differences in concentration can drastically affect the spectra, which can be related to Titan where only certain regions show the bright signature. Different geological processes on Titan may also affect the evaporites such as sintering, winds, and grain sizes.

2. Potential Evaporite Studies with Future Titan Missions

The *Cassini* mission gave us a glimpse as to the spatial extent and variability of Titan's evaporite deposits. The *Cassini* Radar (RADAR) and Visible and Infrared Mapping spectrometer (VIMS) were integral in identifying and characterizing the evaporites. RADAR gives topographical and geographical context and identified dry and partially filled lakes (Hayes et al., 2008; Barnes et al., 2011), which are still referenced as prime examples of Titan's evaporites. RADAR data can be taken in either Synthetic Aperture RADAR (SAR) or high altitude Synthetic Aperture RADAR (HiSAR), which spatially coincide with the 5-µm-bright spectral unit identified by VIMS (MacKenzie et al., 2014). Additionally, some 5-µm-bright material also correspond with lake shorelines as viewed by RADAR, illustrating the advantage of utilizing both instruments to study the evaporites (MacKenzie et al., 2014). Although *Cassini* unveiled a multitude of Titan's geological secrets, many post-*Cassini* mission concepts have been proposed since the mid 2000's to re-visit Titan so we can delve deeper into understanding its history.

In 2006, the Titan Prebiotic Explorer (TiPEx) was proposed, which consisted of an orbiter, a hot air balloon (Montgolfière), and surface investigations (Elliott et al., 2007). The orbiter would provide global observations of Titan's atmosphere and surface with instruments such as a radar imager/altimeter, NIR imaging spectrometer, and radio science (Elliott et al., 2007). The Montgolfière would use waste heat from its energy source, Multi-Mission Radioisotopic Thermoelectric Generators (MMRTG), to float in Titan's dense atmosphere while drifting with the prevailing winds as it changed altitudes. Instruments on the Montgolfière, such as a NIR spectrometer, gas chromatograph mass spectrometer (GCMS), and subsurface sounder would give enhanced views of the surface from 10 km altitude. Surface investigations would be carried out via a harpoon system attached to the Montgolfière gondola. The harpoon (including sampler) would be dropped to the surface where it would collect a sample to be winched back up to the gondola for further study via the science instruments. Using this method would allow for investigations of the surface chemistry, including the search for prebiotic molecules. With the use of a sample microscope imager and NIR spectrometer, *this mission concept could in theory collect a sample of an evaporite (or co-crystals) and determine their organic composition.*

Also utilizing the Montgolfière concept in 2007 was the Titan Explorer Flagship (Lorenz et al., 2008). The mission architecture consisted of an aero-captured orbiter, a Montgolfière balloon, and a lander. The orbiter would provide in situ measurements of the ionosphere, mapping of the surface at 1700 km, and would assume a near polar orbit capable of altimetric mapping of the polar lakes/seas. Similar to TiPEx, the Titan Explorer Flagship Montgolfière would achieve neutral buoyancy at ~10 km altitude, enabling a high resolution surface survey with descents improving image resolution/spectra. The lander element would address the surface chemistry and internal structure with an instrument package including a sampling arm with a microscope camera, spectral measurements, fluorescence detection, and a chemical analyzer. *The orbiter's polar orbit would give ample opportunities to characterize Titan's evaporites via remotely sensed data, and given the instruments of the lander and capability for collecting samples, the lander may also be able to study the chemical makeup of evaporite-related materials*, depending on its equatorial landing site.

Later, in 2009, the Titan Saturn System Mission (TSSM) concept was proposed (Reh and

Elliott, 2010), which used similar elements from the Titan Explorer mission. Mission architecture included a *Cassini*-like orbiter with 6 instruments, a Montgolfière equipped with an imaging spectrometer (1 – 5.6 μm) and visual imaging system for detailed geomorphology, as well as a lake lander which would chemically analyze the lakes via isotopic measurements, provide context images of the lakes, and characterize their physical properties. Here, the lake lander would be key in providing a detailed story of the evaporites. A 5-hour descent to the surface would allow imaging from above, as well as atmospheric measurements, followed by 3 – 4 hours of lake measurements after landing. A lake lander such as this one *could give the highest scientific output for studying Titan's evaporites (and compositional variation of the lakes) up close, given the abundance of evaporites in Titan's northern lake district*.

The next Titan mission concept came in 2010, Aerial Vehicle for In-situ and Airborne Titan Reconnaissance (AVIATR), and moved away from including a Montgolfière as the aerial unit (Barnes et al., 2012). Instead, the main element for AVIATR is an airplane that would fly continuously in the atmosphere, providing global mapping and imaging capabilities. This mission concept is more focused, as it is constrained to accomplishing the best and most appropriate science that can be carried out from an airplane, while leaving other science objectives open for platforms that are better suited for addressing them (Barnes et al., 2012). AVIATR would be able to explore from pole-to-pole, furthering our understanding of the surface and lower atmosphere. Having no latitudinal restrictions, AVIATR would study the polar lakes/seas, methane hydrology, equatorial dunes, mountains, winds, atmospheric structure, clouds, rain, haze, and also identify potential landing sites of interest for future missions. Instruments include two NIR cameras, one NIR spectrometer, a RADAR altimeter, an atmospheric structure suite, a haze sensor, and a raindrop detector. *While AVIATR could* *potentially give a complete (remotely sensed) picture of Titan's evaporites at both poles (and the equator), no landing element means that no direct samples could be taken for compositional analysis*. However, a future follow-up lander mission to the evaporites could ground-truth the data collected by AVIATR.

Also in 2010, the Titan Mare Explorer (TiME) was selected for a Phase A study in the 2010 Discovery missions solicitation (Stofan et al., 2013). The mare explorer is a capsule that would land in Ligeia Mare, Titan's second largest northern sea. The capsule would drift with the wind and waves, allowing for detailed liquid compositional measurements, imaging and sonar surveys, as well as meteorological observations. The main objectives would be to measure the sea chemistry, sea depth, constrain marine processes, determine sea surface meteorology, and constrain prebiotic chemistry in the sea (Stofan et al., 2013). These objectives would be completed using instruments such as a mass spectrometer, camera suite, and meteorology/physical properties packages. Over time, the capsule may float to the shoreline, causing it to "beach," where the mission would continue to monitor shoreline processes. Here, the capsule may encounter evaporative processes, however on a slower scale than a lake lander would monitor at a lake shoreline. Nonetheless, the scientific output from TiME would give the *most detailed compositional analysis of one of Titan's largest lakes, informing us greatly about what potential evaporite compounds are present, as well as their spatial variability as the capsule drifts towards the shoreline*. A logical follow-up mission to TiME would be some sort of Titan submarine to explore the depths of Titan's seas.

In the 2017 New Frontiers Program Solicitation, two Titan missions concepts were submitted: Oceanus and Dragonfly. Oceanus is an orbiter concept that would investigate specific features that were identified by *Cassini*, such as potential cryovolcanic features, impacts, and other tectonic processes (Sotin et al., 2017). Oceanus would have the capability to study Titan's surface through the 5 µm window at 25 m/pixel, and would also characterize the habitability of the surface using an instrument suite including: an IR camera, a radar altimeter, and a mass spectrometer. Although Oceanus would investigate the surface chemistry and geology from orbit, *there would be no in situ element to give a closer look at any evaporites.*

Dragonfly, on the other hand, is a quadcopter that will land directly in the equatorial dune fields and has the capability to fly or "hop" to locations up to 60 km away from its landing site to scout out areas of high scientific interest (Lorenz et al., 2018). *Dragonfly* combines elements of the previously proposed aerial and lander units, as it can provide atmospheric measurements during flight, and directly sample in situ material when it is on the surface. However, *Dragonfly* will be restricted in latitude to areas that allow for direct to Earth communication (DTE), meaning that it will not have the opportunity to fly to the polar lakes/seas for compositional measurements. Though, the equatorial evaporite deposits (e.g., Tui and Hotei Regios), as well as theoretical crater lake deposits (S. Birch, personal comm.) may provide an opportunity for sampling. Further, co-crystals may not be restricted to regions around filled lakes/seas, so it is entirely possible for *Dragonfly* to collect in situ co-crystalline material for analysis, as well. *Dragonfly's* payload includes a laser-desorption ionization (LDI) mass spectrometer, a gamma-ray and neutron spectrometer, and a camera suite with UV source (detects organics via fluorescence). *Combined, sample analysis using these instruments will give a detailed understanding and identification of Titan's surface organics as a whole.*

In the next decade, at least two Titan mission concept white papers have already been suggested in regards to the 2023-2032 decadal survey. First, a New Frontiers Titan Orbiter (Barnes et al., 2020) to compliment *Dragonfly* has been proposed. This orbiter would give a global view of Titan's energy, geophysics, and atmosphere, as well as the surface by using instruments such as RADAR, a NIR laser for altimetry, a wide angle NIR camera for weather imaging, gravity tracking, and a NIR camera/SAR for surface imaging. *No in situ opportunities would permit close-up studies of the evaporites.* However, a flagship orbiter with probes (Nixon et al., 2020) has also been proposed, with key goals of permitting global, multi-spectral surface/subsurface mapping, temporal atmospheric measurements, and in situ measurements of the polar regions. The orbiter would achieve elliptical polar orbit and give global coverage with instruments such as: VIS/NIR cameras/spectrometers, a sub mm sounder, a multi-stage mass spectrometer, an aerosol mass spectrometer, and a plasma/electric field probe. Two probes would land in Titan's northern seas to measure compositional differences between Kraken and Ligeia Maria with instruments such as a color camera, a surface science package, and a mass spectrometer. Again, *these landed probes would give extremely high resolution information as to the compositional variability and structure of Titan's seas, which directly relate to evaporite studies*.

3. Future Work

Future experiments should focus on increasing our knowledge of evaporite candidates by testing additional systems including: C_2H_4-C_6H_6, C_2H_6-C_6H_6, additional nitrile experiments with CH_3CN, acrylonitrile (CH_2CHCN), and cyanoacetylene (C_3HN), as well as incorporating butane (C_4H_{10}) and propane (C_3H_8) into experiments. A solubility study of CH_3CN and toluene (C_7H_8) in CH_4 and C_2H_6 solvents, as well as determining the solubility of multiple species (i.e., binary experiments) would also be beneficial. Further, being able to model these evaporite experiments will give a better understanding of the dynamic processes at play during evaporite formation and/or co-crystal formation, and can potentially shed light on topics such as spatial extent of evaporites, thickness of an evaporite layer, and how much of a particular evaporite may have accumulated on Titan's surface.

When *Dragonfly* lands on Titan's surface in the next decade, there is a high chance that the mission encounters either evaporite deposits or co-crystals at some point in the mission. Therefore, the results from this study (and from future evaporite studies) will be of high importance for interpreting the discoveries of *Dragonfly* with regards to surface evaporite deposits, furthering our understanding of the fascinating chemical evolution that Titan's solid organics undergo.

4. References

Barnes, J.W., Bow, J., Schwartz, J., Brown, R.H., Soderblom, J.M., Hayes, A.G., Vixie, G., Le Mouélic, S., Rodriguez, S., Sotin, C., Jaumann, R., Stephan, K., Soderblom, L.A., Clark, R.N., Buratti, B.J., Baines, K.H., Nicholson, P.D., 2011. Organic sedimentary deposits in Titan's dry lakebeds: Probable evaporite. Icarus 216, 136–140. https://doi.org/10.1016/j.icarus.2011.08.022

Barnes, J.W., Brown, R.H., Soderblom, J.M., Soderblom, L.A., Jaumann, R., Jackson, B., Le Mouélic, S., Sotin, C., Buratti, B.J., Pitman, K.M., Baines, K.H., Clark, R.N., Nicholson, P.D., Turtle, E.P., Perry, J., 2009. Shoreline features of Titan's Ontario Lacus from Cassini/VIMS observations. Icarus 201, 217–225. https://doi.org/10.1016/j.icarus.2008.12.028

Barnes, J.W., Hayes, A.G., Soderblom, J.M., Mackenzie, S.M., Hofgartner, J., Lorenz, R.D., Turtle, E.P., Radebaugh, J., Burr, D., Lora, J., Neumann, G., Vance, S., Lopes, R., Nixon, C., Corlies, P., Regoli, L., Sciamma-O'Brien, E., Schindhelm, R., Rodriguez, S., 2020. New Frontiers Titan Orbiter, White paper for the NRC Decadal Survey for Planetary Science and Astrobiology.

Barnes, J.W., Lemke, L., Foch, R., Mckay, C.P., Beyer, R.A., Radebaugh, J., Atkinson, D.H., Lorenz, R.D., Le, S., Sebastien, M., Jay, R., Giannini, F., Bain, S., Flasar, F.M., Hurford, T., Anderson, C.M., Merrison, J., Ádámkovics, M., Kattenhorn, S.A., Mitchell, J., Burr, D.M., Colaprete, A., Schaller, E., Friedson, A.J., Edgett, K.S., Coradini, A., Adriani, A., Sayanagi, K.M., Malaska, M.J., Morabito, D., Reh, K., 2012. AVIATR — Aerial Vehicle for In-situ and Airborne Titan Reconnaissance. Exp. Astron. 33, 55–127. https://doi.org/10.1007/s10686-011-9275-9

Cable, M.L., Vu, T.H., Hodyss, R., Choukroun, M., Malaska, M.J., Beauchamp, P., 2014. Experimental determination of the kinetics of formation of the benzene-ethane co-crystal and implications for Titan. Geophys. Res. Lett. 41, 5396–5401.

https://doi.org/10.1002/2014GL060531

Cable, M.L., Vu, T.H., Malaska, M.J., Maynard-casely, H.E., Choukroun, M., Hodyss, R., 2020. Properties and Behavior of the Acetonitrile − Acetylene Co-Crystal under Titan Surface Conditions. https://doi.org/10.1021/acsearthspacechem.0c00129

Cable, M.L., Vu, T.H., Malaska, M.J., Maynard-casely, H.E., Choukroun, M., Hodyss, R., 2019. A Co-Crystal between Acetylene and Butane: A Potentially Ubiquitous Molecular Mineral on Titan. ACS Earth Sp. Chem. 3, 2808–2815. https://doi.org/10.1021/acsearthspacechem.9b00275

Cable, M.L., Vu, T.H., Maynard-Casely, H.E., Choukroun, M., Hodyss, R., 2018. The Acetylene-Ammonia Co-crystal on Titan. ACS Earth Sp. Chem. 2, 366–375. https://doi.org/10.1021/acsearthspacechem.7b00135

Czaplinski, E., Yu, X., Dzurilla, K., Chevrier, V., 2020. Experimental Investigation of the Acetylene–Benzene Cocrystal on Titan. Planet. Sci. J. 1, 16. https://doi.org/10.3847/PSJ/abbf57

Czaplinski, E.C., Gilbertson, W.A., Farnsworth, K.K., Chevrier, V.F., 2019. Experimental Study of Ethylene Evaporites under Titan Conditions. ACS Earth Sp. Chem. 3, 2353–2362. https://doi.org/10.1021/acsearthspacechem.9b00204

Elliott, J.O., Reh, K., Spilker, T., 2007. Concept for Titan Exploration Using a Radioisotopically Heated Montgolfiere, in: IEEEAC. p. 1380.

Engle, A.E., Hanley, J., Dustrud, S., Thompson, G., Gerrick, E., Grundy, W.M., Tegler, S.C., 2021. Phase Diagram for the Methane-Ethane System and its Implications for Titan's Lakes. Planet. Sci. J. 1–21.

Farnsworth, K., 2020. An Experimental Investigation of Liquid Hydrocarbons in a Simulated Titan Environment. University of Arkansas.

Hayes, A., Aharonson, O., Callahan, P., Elachi, C., Gim, Y., Kirk, R., Lewis, K., Lopes, R., Lorenz, R., Lunine, J., Mitchell, K., Mitri, G., Stofan, E., Wall, S., 2008. Hydrocarbon lakes on Titan: Distribution and interaction with a porous regolith. Geophys. Res. Lett. 35, L09204. https://doi.org/10.1029/2008GL033409

Kirchner, M.T., Bläser, D., Boese, R., 2010. Co-crystals with Acetylene: Small Is not Simple! Chem. A Eur. J. 16, 2131–2146. https://doi.org/10.1002/chem.200901314

Lorenz, R.D., Leary, J.C., Lockwood, M.K., Waite, J.H., 2008. Titan Explorer: A NASA Flagship Mission Concept, in: AIP Conference Proceedings. pp. 380–387.

Lorenz, R.D., Turtle, E.P., Barnes, J.W., Trainer, M.G., Adams, D.S., Hibbard, K.E., Sheldon, C.Z., Zacny, K., Peplowski, P.N., Lawrence, D.J., Ravine, M.A., Mcgee, T.G., Sotzen, K.S., Mackenzie, S.M., Langelaan, J.W., Schmitz, S., Wolfarth, L.S., Bedini, P.D., 2018. Dragonfly: A Rotorcraft Lander Concept for Scientific Exploration at Titan. APL Tech.

Dig. 34, 374–387.

MacKenzie, S.M., Barnes, J.W., Sotin, C., Soderblom, J.M., Le Mouélic, S., Rodriguez, S., Baines, K.H., Buratti, B.J., Clark, R.N., Nicholson, P.D., McCord, T.B., 2014. Evidence of Titan's climate history from evaporite distribution. Icarus 243, 191–207. https://doi.org/10.1016/j.icarus.2014.08.022

Maynard-Casely, H.E., Cable, M.L., Malaska, M.J., Vu, T.H., Choukroun, M., Hodyss, R., 2018. Prospects for mineralogy on Titan. Am. Mineral. 103, 343–349. https://doi.org/10.2138/am-2018-6259

McConville, C.A., Tao, Y., Evans, H.A., Trump, B.A., Lefton, J.B., Xu, W., Yakovenko, A.A., Kraka, E., Brown, C.M., Ručevski, T., 2020. Peritectic Phase Transition of Benzene and Acetonitrile into a Cocrystal Relevant to Titan, Saturn's Moon. Chem. Commun. 56, 13520–13523. https://doi.org/10.1039/D0CC04999A

Moriconi, M.L., Lunine, J.I., Adriani, A., Aversa, E.D., Negrão, A., Filacchione, G., Coradini, A., 2010. Characterization of Titan's Ontario Lacus region from Cassini/VIMS observations. Icarus 210, 823–831. https://doi.org/10.1016/j.icarus.2010.07.023

Nixon, C.A., Abshire, J., Ashton, A., Barnes, J.W., Carrasco, N., Choukroun, M., Coustenis, A., Couston, L.-A., Edberg, N., Gagnon, A., 2020. The Science Case for a Titan Flagship-class Orbiter with Probes, White paper for the NRC Decadal Survey for Planetary Science and Astrobiology.

Nna-Mvondo, D., Singh, S., Chevrier, V.F., Tobie, G., Mège, D., 2015. Complex organics in Titan lakes: Spectral detection and Chemical behavior, in: European Planetary Science Congress.

Reh, K.R., Elliott, J., 2010. Preparing for a Future In Situ Mission to Titan.

Sotin, C., Hayes, A., Malaska, M., Nimmo, F., Trainer, M., Mastrogiuseppe, M., Soderblom, J., Tortora, P., Hofgartner, J., Aharonson, O., Barnes, J.W., Hodyss, R., Iess, L., Kirk, R., Lavvas, P., Lorenz, R., Lunine, J.I., Mazarico, E., McEwen, A., Neish, C., Nixon, C., Turtle, E., Vuitton, V., Yelle, R., 2017. Oceanus: A New Frontiers Orbiter to Study Titan's Potential Habitability, in: LPSC XLVIII. p. 2306.

Stofan, E., Lorenz, R., Lunine, J., Bierhaus, E.B., Clark, B., Martin, L., 2013. TiME – The Titan Mare Explorer 1–10.

Vu, T.H., Cable, M.L., Choukroun, M., Hodyss, R., Beauchamp, P., 2014. Formation of a new benzene-ethane co-crystalline structure under cryogenic conditions. J. Phys. Chem. 118, 4087–4094. https://doi.org/10.1021/jp501698j

5. Appendix

Primary Author Contribution Statement – Chapter 1

Chapter 1: Experimental Study of Ethylene Evaporites Under Titan Conditions

By signing this document, I verify that I am a **co-author** in Chapter 1 of Ellen Czaplinski's dissertation and corresponding publication. Further, I certify that the primary author, Ellen Czaplinski, has completed at least 51% of the presented work.

5/31/21

Woodrow Gilbertson Date

Kendra Farnsworth 6/1/21

Kendra Farnsworth Date

6/1/2021

Vincent Chevrier Date

Primary Author Contribution Statement – Chapter 2

Chapter 2: Experimental Investigation of the Acetylene–Benzene Cocrystal on Titan

By signing this document, I verify that I am a **co-author** in Chapter 2 of Ellen Czaplinski's dissertation and corresponding publication. Further, I certify that the primary author, Ellen Czaplinski, has completed at least 51% of the presented work.

06/01/2021

Xinting Yu (余馨婷) Date

6-1-2021

Katherine Dzurilla Date

6/1/2021

Vincent Chevrier Date

Primary Author Contribution Statement – Chapter 3

Chapter 3: Characterizing the Near-Infrared Spectral Properties of the Acetonitrile-Acetylene Co-Crystal in Titan-Relevant Hydrocarbon Mixtures

By signing this document, I verify that I am a **co-author** in Chapter 3 of Ellen Czaplinski's dissertation. Further, I certify that the primary author, Ellen Czaplinski, has completed at least 51% of the presented work.

6/1/2021

Vincent Chevrier Date

Primary Author Contribution Statement – Chapter 4

Chapter 4: Binary Compound Evaporites: Stability with Liquid Methane and Ethane under Titan Conditions

By signing this document, I verify that I am a **co-author** in Chapter 4 of Ellen Czaplinski's dissertation. Further, I certify that the primary author, Ellen Czaplinski, has completed at least 51% of the presented work.

6/1/2021

Vincent Chevrier Date

Primary Author Curriculum Vitae

ELLEN CZAPLINSKI

EDUCATION

PH.D. IN SPACE AND PLANETARY SCIENCES (Defense date: June 2021)
University of Arkansas, Fayetteville, AR • June 2021
Relevant courses: planetary geology, astrobiology, remote sensing
GPA: 4.0

BACHELOR OF SCIENCE IN PLANETARY SCIENCE
Purdue University, West Lafayette, IN • May 2016
Concentrations: planetary geology, martian surface geomorphology
Major GPA: 3.58

PUBLICATIONS

Czaplinski, E. C., Harrington, E. M., Bell, S. K., Tolometti, G. D., Farrant, B. E., Bickel, V. T., Honniball, C. I., Martinez, S. N., Rogaski, A., Sargeant, H. M., Kring, D. A. (2021) Geologic Map and Rover Traverses for Human-Assisted Sample Return Missions to the Schrödinger Basin, Lunar Farside. *The Planetary Science Journal*, *2*, 51. DOI:10.3847/PSJ/abdb34

Czaplinski, E. C., Yu. X., Dzurilla, K., Chevrier, V. F. (2020) Experimental Investigation of the Acetylene-Benzene Co-Crystal on Titan, *The Planetary Science Journal*, *1*, 76. DOI:10.3847/PSJ/abbf57

Czaplinski, E. C., Gilbertson, W. A., Farnsworth, K. K., Chevrier, V. F. (2019) Experimental Study of Ethylene Evaporites under Titan Conditions. *ACS Earth and Space Chemistry*, *3*, 2353-2362. DOI:10.1021/acsearthspacechem.9b00204

MacKenzie, S. M. et al., including **Czaplinski, E. C.** (2021) Titan: Earth-like on the Outside, Ocean World on the Inside. *The Planetary Science Journal*, *2*, 112. DOI:10.3847/PSJ/abf7c9

Moore, K., Courville, S., Ferguson, S., Schoenfeld, A., Llera, K., Agrawal, R., Buhler, P., Brack, D., Connour, K., **Czaplinski, E.**, DeLuca, M., Deutsch, A., Hammond, N., Kuettel, D., Marusiak, A., Nerozzi, S., Stuart, J., Tarnas, J., Thelen, A., Castillo, J., Smythe, W., Landau, D., Mitchell, K., Budney, C. (2021) Bridge to the stars: A mission concept to an interstellar object, *Planetary and Space Science, 197*, 105137 DOI:10.1016/j.pss.2020.105137

Sargeant, H. M., Bickel, V. T., Honniball, C. I., Martinez, S. N., Rogaski, A., Bell, S. K., **Czaplinski, E. C.**, Farrant, B. E., Harrington, E. M., Tolometti, G. D., Kring. D. A. (2020) Using Boulder Tracks as a Tool to Understand the Bearing Capacity of Permanently Shadowed Regions on the Moon. *JGR: Planets, 125*, e2019JE006157. DOI:10.1029/2019JE006157

Bickel, V. T., Honniball, C. I., Martinez, S. N., Rogaski, A., Sargeant, H. M., Bell, S. K., **Czaplinski, E. C.**, Farrant, B. E., Harrington, E. M., Tolometti, G. D., Kring. D. A. (2019) Analysis of Lunar Boulder Tracks: Implications for Trafficability of Pyroclastic Deposits. *JGR: Planets, 124,* 1296-1314. DOI:10.1029/2018JE005876

EXPERIENCE

GRADUATE RESEARCH – **TITAN EVAPORITE EXPERIMENTS**
University of Arkansas • June 2016 – June 2021 (expected)

Performed evaporite/co-crystal experiments using hydrocarbons relevant to Titan's lakes. Analyzed resulting mixtures via FTIR spectroscopy and mass to determine saturation values, evaporation rates, and sample thickness. Proficient in analyzing band depth, band area, peak positions, and phase transitions. Updated/engineered several systems (electronics, cooling, etc.) on the Titan chamber. Implemented a Raman spectrometer into the chamber. Oral presentations at LPSC 2017-2020, Titan Surface Meetings, and DPS 2018-2019. Poster presentations at AGU 2017-2020, Titan After Cassini-Huygens 2019. Awarded the 2017 NASA Earth and Space Sciences Fellowship (NESSF) for this research.

NASA AUTONOMOUS ROBOTICS RESEARCH FOR OCEAN WORLDS (ARROW) – **SCIENCE CONSULTANT**
February 2020 – present

Provided input to roboticists/engineers regarding the geologic processes, chemical compounds, and surface environments on ocean worlds such as Europa, Enceladus, and Titan. Assisted with testing Resource Adaptive Software Purpose-Built for Extraordinary Robotic Research Yields – Science Instruments (RASPBERRY – SI) in both virtual and physical ocean worlds testbeds.

JPL **PLANETARY SCIENCE SUMMER SEMINAR** – PARTICIPANT
NASA Jet Propulsion Laboratory • May – Aug 2019

Helped plan a spacecraft mission concept to study an interstellar object. Determined how to best study object's molecular composition. Designed spacecraft in mechanical/structures role. Worked directly with JPL Team X mentors and Architecture Team.

MARS DESERT RESEARCH STATION – **CREW GEOLOGIST**
Hanksville, UT • Dec 2018 – Jan 2019

Performed 10 field expeditions in a simulated space suit. Measured and analyzed spectra of geologic samples using a TREK visible/IR portable spectrometer. Observed the Sun using the Musk Observatory. Collected and identified ~100 samples of clay, fluvial, and evaporite minerals.

EXPLORATION SCIENCE SUMMER INTERN – **LUNAR GEOLOGY**
The Lunar and Planetary Institute • May 2018 – Aug 2018

Explored future robotic mission sites in the Schrödinger basin, lunar south pole, farside. Created a geologic map of the SW Schrödinger peak ring. Used geologic map as a guide to design robotic traverses in SW peak ring. Served as a beta tester and implemented improved Lunar Reconnaissance Orbiter imagery for JPL's Moon Trek software for exploring lunar datasets.

TEACHING ASSISTANT – **MICROBIOLOGY**
University of Arkansas • Aug 2016 – May 2017

Taught the lab portion of the course for 2 semesters. Topics taught include: identifying unknown bacteria, preparing various stains (Gram, acid-fast, endospore, capsule), microscopy techniques, aseptic technique, and *Staphylococcus/Streptococcus* identification.

UNDERGRADUATE RESEARCH – **MARTIAN GEOMORPHOLOGY**
Purdue University • Feb 2014 – May 2016

Performed a planet-wide survey of slipface features on Martian dune fields. Categorized slipface features based on morphology. Determined most probable origination environment. Presented research at LPSC 2016 – 2018.

AWARDS & OPPORTUNITIES

NASA Postdoctoral Program Fellowship • 2021

UArk Women's Giving Circle Award for a new Planetarium ($15,000) • 2021

Early Career Observer for the Europa Clipper science team meeting • 2020

ICARUS Journal Peer Reviewer • 2020

Zonta International Amelia Earhart Fellowship • 2020

Science Org. Committee – Experimental Outer Solar System Workshop • 2020

Student Representative for the UArk Space Center • 2019 – 2020

Senior Division Judge – Northwest AR Regional Science Fair • 2019-2020

Judge – NASA "Name the Rover" contest for Mars 2020 Rover • 2019

Hartmann Student Travel Grant – Division for Planetary Sciences • 2019

Executive Secretary – NASA ROSES Panel • 2019

3 Minute Thesis Runner-Up over Titan research • 2018

American Geophysical Union Volunteer Grant/Travel Grant • 2017/2020

Arkansas Space Grant Consortium STEM/Minority Grant • Arkansas, 2017, 2021

NASA Earth and Space Science Fellowship (Titan research) • 2017

Learning Beyond the Classroom Certificate (Purdue) • 2016

Ascarelli Research Scholarship (Purdue) • 2012

Presidential Scholarship (Purdue) • 2012

CONFERENCE PUBLICATIONS

First-Authored Abstracts:

E. Czaplinski, X. Yu, K. Dzurilla, V. Chevrier. Experimental Investigation of the Acetylene-Benzene Co-Crystal on Titan. *AGU Fall Meeting 2020,* P067-0004. (Poster)

E. Czaplinski, K. Farnsworth, X. Yu, K. Dzurilla, V. Chevrier. Experimental Study of Evaporites on Titan. *DPS 52,* 408.01D. (Oral – Dissertation Talk)

E.C. Czaplinski, V.F. Chevrier, X. Yu, K. Dzurilla. (2020). Experimental Study of C_2H_2 Crystal Structure Changes Under Titan Conditions. *LPSC LI*, Abstract #1694. (Oral – cancelled due to the pandemic).

E.C. Czaplinski, W.A. Gilbertson, K.K. Farnsworth, V.F. Chevrier. (2019). Characterizing Evaporites on Titan Using an Experimental Chamber. *EPSC-DPS Joint Meeting*, Abstract #1132. (Oral)

E.C. Czaplinski, W.A. Gilbertson, K.K. Farnsworth, V.F. Chevrier. (2019). Characterizing Evaporites on Titan Using an Experimental Chamber. (2019). *Titan After Cassini Huygens Workshop.* (Poster).

E.C. Czaplinski, K.K. Farnsworth, V.F. Chevrier. (2019). Experimental study of ethylene and benzene evaporites under Titan conditions. *LPSC L,* Abstract #1153. (Oral)

E.C. Czaplinski, C.J. Ahrens, V.F. Chevrier. (2019). Comparitive morphologies between dune slope streaks and recurring slope lineae on Mars. *LPSC L,* Abstract #1160. (Poster)

E. Czaplinski, K. Farnsworth, V. Chevrier. (2018). An Experimental Study of Evaporites on Titan. *Experimental Analysis of the Outer Solar System Workshop*. Abstract #3009. (Oral)

E. Czaplinski, K. Farnsworth, V. Chevrier. (2018). Experimental Studies of Benzene and Acetylene Evaporites on Titan. *Titan Surface Meeting, Cornell University*. (Oral)

E. Czaplinski, K. Farnsworth, V. Chevrier. (2017). Experimental simulations of ethylene evaporites on Titan. *AGU,* Abstract #213124. (Poster)

E. Czaplinski, K. Farnsworth, V. Chevrier. (2017). Experimental Simulations of Ethylene Evaporites. *Titan Surface Meeting, MIT.* (Oral)

E. Czaplinski, K. Farnsworth, D. Laxton, V. Chevrier, S. Singh. (2017). Experimental results of evaporite deposits on Titan using a surface simulation chamber. *Titan Through Time IV Workshop, NASA Goddard.* (Oral)

E. Czaplinski, K. Farnsworth, D. Laxton, V. Chevrier, M. Heslar, S. Singh. (2017). Experimental results of evaporite deposits on Titan using a surface simulation chamber. *LPSC XLVIII*, Abstract #1537. (Oral)

E.C. Czaplinski, C.J. Ahrens, B.H.N. Horgan. V. F. Chevrier. (2017). Dune Slipface Feature Morphologies and Their Relationship to Mineralogy. *LPSC XLVIII,* Abstract #2049. (Poster)

E. Czaplinski and B. Horgan. (2016). Constraining the Mechanisms of Slipface Failure on Martian Sand Dunes from a New Global Survey. *LPSC XLVII,* Abstract #2006. (Poster)

Co-Authored Abstracts:

E.M. Harrington, S.K. Bell, **E.C. Czaplinski**, B.E. Farrant, G.D. Tolometti , V.T. Bickel, C.I. Honniball, S.N. Martinez, A. Rogaski, H.M. Sargeant, and D.A. Kring. (2021). Proposed human-assisted robotic traverses in the northwest peak ring of the Schrödinger basin. *International Astronautical Congress – 21*, (Upcoming Conference).

E.M. Harrington, **E.C. Czaplinski**, S.K. Bell, G.D. Tolometti, B.E. Farrant, V.T. Bickel, C.I. Honniball, S.N. Martinez, A. Rogaski, H.M. Sargeant, and D.A. Kring. (2021). Geologic Map of a Segment of the Schrödinger Peak Ring and Potential Rover Traverses. *NASA Exploration Science Forum*, (Upcoming Conference).

G.D. Tolometti, V.T. Bickel, **E.C. Czaplinski**, and H.M. Sargeant. (2020). Using Temperature Constraints to Identify Potentially Traversable Permanently Shadowed Regions at the Lunar South Pole. *NASA Exploration Science Forum*, NESF2020-073. (Poster)

V.T. Bickel, C.I. Honniball, S.N. Martinez, A. Rogaski, H.M. Sargeant, S.K. Bell, **E.C. Czaplinski**, B.E. Farrant, E.M. Harrington, G.D. Tolometti, and D.A. Kring. (2019). Analysis of Lunar Boulder Tracks: Implications for Rover Mobility on Pyroclastic Deposits. (2019). *LPSC L*, Abstract #1587. (Poster)

K. Farnsworth, V. Chevrier, **E. Czaplinski**, and J.M. Soderblom. (2019). Freezing Points of Methane-Ethane-Nitrogen Mixtures under Titan Surface Pressure. *LPSC L*, Abstract #2672 (Oral)

K. Farnsworth, J.M. Soderblom, S. Rodriguez, **E. Czaplinski**, and V. Chevrier. (2019). Constraining Ethane Concentration in Titan's Lakes and Seas. *LPSC L*, Abstract #1488 (Poster)

B.E. Farrant, S.K. Bell, **E.C. Czaplinski**, E.M. Harrington, G.D. Tolometti, V.T. Bickel, C.I. Honniball, S.N. Martinez, A. Rogaski, H.M. Sargeant, and D.A. Kring. (2019). Geologic Map and Potential Rover Traverses for Human-Assisted Sample Return Missions to the Schrödinger Basin, Lunar Farside. *LPSC L*, Abstract #1790. (Poster)

H.M. Sargeant, V.T. Bickel, C.I. Honniball, S.N. Martinez, A. Rogaski, S.K. Bell, **E.C. Czaplinski**, B.E. Farrant, E.M. Harrington, G.D. Tolometti, and D.A. Kring. (2019). Determining the Bearing Capacity of Permanently Shadowed Regions of the Moon Using Boulder Tracks. *LPSC L,* Abstract #1792. (Oral)

K. Farnsworth, Z. McMahon, D. Laxton, **E. Czaplinski**, V. Chevrier, A. Luspay-Kuti, and S. Singh. (2017). Experimental Study of Nitrogen Dissolution in Methane-Ethane Mixtures under Titan Surface Conditions. *LPSC XLVIII,* Abstract #1932. (Poster)

M. Heslar, K. Farnsworth, V. Chevrier, **E. Czaplinski**, and D. Laxton. (2017). Simulations of Titan Lakes: Potential Methane-Ethylene Evaporitic Deposits. *LPSC XLVIII,* Abstract #2657. (Oral)

S. Singh, T. McCord, J-P. Combe, G. Singh, K. Farnsworth, D. Laxton, E. Czaplinski, and V.F. Chevrier. (2017). Impact of Acetylene and Tholins Mixtures on 1.55 μm Absorption Band. *LPSC XLVIII,* Abstract #2951 (Poster)

EXTRACURRICULARS

SPACE HOGS, ASTRONOMY OUTREACH GROUP – **V.P.**
University of Arkansas • Aug 2018 – Present

Present space science educational lectures to ~2,000 people a year from the community. Travel to local community groups to present mobile planetarium shows. Run hands-on space science activities for K-12 students. Lead a successful fundraising campaign to purchase a new, mobile StarLab planetarium. Awarded a $15,000 grant from UArk Women's Giving Circle towards the new planetarium.

ROCK CLIMBING
Feb 2017 – Present

ATC, GriGri, and Lead climbing/belaying certified. Climbed the height of El Capitan during Feb 2019 and Feb 2020. Outdoor expeditions in AK, AR, AZ, WA.

PURDUE BANDS AND ORCHESTRAS - **PERCUSSION**
Purdue University • 2013 – 2016

Marched snare drum. Proficient in various concert percussion instruments in the Wind Ensemble, Percussion Ensemble, and Orchestra.